Technische Universität München
Institut für Energietechnik

Lehrstuhl für Thermodynamik

# High Frequency Transverse Thermoacoustic Instabilities in Swirl and Reheat Combustors

**Frederik Magnus Berger**

Vollständiger Abdruck der von der Fakultät für Maschinenwesen der Technischen Universität München zur Erlangung des akademischen Grades eines

DOKTOR – INGENIEURS

genehmigten Dissertation.

Vorsitzender:

Prof. Dr. Rudolf Neu

Prüfer der Dissertation:

1. Prof. Dr.-Ing. Thomas Sattelmayer
2. Prof. Dr.-Ing. Christian O. Paschereit
3. Rudolf Diesel Fellow (TUM) Bruno Schuermans, Ph.D.

Die Dissertation wurde am 03.07.2019 bei der Technischen Universität München eingereicht und durch die Fakultät für Maschinenwesen am 11.12.2019 angenommen.

## Acknowledgements

This thesis summarizes the results of my research project at the Institute of Thermodynamics, Technical University of Munich, under the supervision of Prof. Thomas Sattelmayer. The project was bi-laterally funded by GE Power (former Alstom Power) and the German Federal Ministry of Economic Affairs and Energy (BMWi) within the framework of the AG Turbo COOREFLEX-TURBO research association (project no. 03ET7021T), which is gratefully acknowledged.

First and foremost, I would like to thank my supervisor Prof. Thomas Sattelmayer for your outstanding support and advice, for giving me this opportunity as well as for providing an excellent work environment both in terms of the infrastructure and the team at the Institute of Thermodynamics. My special thanks also goes to Bruno Schuermans for the inspiring collaboration in Munich and Baden. The discussions with you, the ideas developed in the process, and the lively team spirit have given the project a great deal of momentum. Thank you to Prof. Rudolf Neu for taking over the examination chairmanship and to Prof. Thomas Sattelmayer, Prof. Christian O. Paschereit, and Bruno Schuermans for examining my work.

I look back at my time at the Institute of Thermodynamics with very positive memories. The team dynamics as well as the support of the whole administration have contributed to this. At this point I would like to especially emphasize Tobias Hummel. The joint project work with you and the different perspectives on challenges and new results have always been a pleasure and contributed significantly to the success of the work. In addition, I am very grateful for your commitment in proof-reading my thesis. Thank you to Helga Bassett and Sigrid Schulz-Reichwald for supporting me with the organizational and administrative work as well as to Jens Hümmer and Gerhard Giel, representing the workshop team, for your help in setting up the combustor test rigs as the basis of all experimental insight. In addition, I was particularly pleased about the interest and motivation of the students who contributed to the project through various theses and research assistant activities and I always enjoyed working with you. Jan Kaufmann, Andreas Ewald, and Michael

Bertsch, you deserve special thanks here for your great effort and collaboration in the course of your master projects.

The close collaboration in joint projects has also turned respected colleagues into very good friends, most notably Georg Fink, Nicolai Stadlmair, Noah Klarmann, and Tobias Hummel. The breaks with you, be it in the coffee kitchen or on the journeys together, were always a great time with enlightening extracurricular discussions. Even though we are going different ways now, I hope that we will continue to keep these precious times together in the future.

The last lines are reserved for my dearest ones! Ina, I thank you from the bottom of my heart for all your support, your confidence and that we have mastered this time with so many changes and challenges so wonderfully. My daughter Aurélie, if you can read this sometime, I am overjoyed and proud that we have you and that you have always given me the necessary creative breaks in the final phase of the work by your beautiful way of distracting me! My parents deserve the greatest respect and thanks for always supporting me and enabling me a great education.

Munich, January 2020 Frederik Berger

## Abstract

For transforming the global energy infrastructure towards sustainable and $CO_2$ neutral technologies, load flexible and low-emission gas turbines in CCGT are considered as a key technology. This is due to the fact that, on the one hand, such power plants are base load capable, and on the other hand can balance load fluctuations of regenerative sources efficiently. Moreover, there are concepts to operate such power plants with regenerative fuels $CO_2$ neutral. One engineering challenge in the development of modern gas turbine burners that meet the above requirements is the occurrence of thermoacoustic instabilities in the combustion chamber. These deteriorate the efficiency of the machine, and lead to accelerated wear or even destruction of machine components. Suppression of such instabilities in existing machines is particularly expensive and its prediction for new systems complex or limited.

This thesis deals with feedback phenomena of flame and acoustics in swirl and reheat flames as found in two-stage/sequential gas turbine combustors. The specific focus of the investigations is on high frequency transversal instabilities. In the high frequency range (the beginning of the frequency range is defined by the specific cut-off frequency for transverse acoustic modes of the combustion chamber) local interaction of the flame with the transverse pressure field is observed. In contrast to longitudinal LF instabilities, the flame can therefore no longer be assumed as compact compared to the acoustic wavelength. This non-compactness of the flame must be taken into account in new prediction methods. In order to study the phenomena occurring in a first combustion stage, a readily available aerodynamically stabilizing swirl burner was used. For the investigation of the phenomena in the second-stage of sequential gas turbines, a new test bench was designed, constructed and used for first experiments of high-frequency flame dynamics. For the swirl flame it could be shown that the flame is periodically displaced and deformed by the acoustic field. This modulation of the flame shape leads to a driving thermoacoustic feedback. Furthermore, the reheat combustor experiment shows an additional modulation of the reactive shear layer and the auto-igniting flame zone. Especially the modulation of the auto-ignition delay in combination with the flame displacement and deformation is seen as another

basic driving mechanism for the occurring high-frequency and transverse instability in the newly developed reheat experiment.

Experimental results presented in this thesis confirm theoretically derived driving mechanisms and generated new insight into the nature of high frequency instabilities. These help to improve tools for predicting thermoacoustic interactions in gas turbine combustors. In addition, the reheat experiment provides a framework for further comprehensive investigations of high-frequency, non-compact flame response, which are of particular interest for the development of novel combustion chambers with axial fuel and air staging.

## Kurzfassung

Für die Transformation der globalen Energieinfrastruktur hin zu nachhaltigen und $CO_2$-neutralen Technologien werden lastflexible und emissionsarme Gasturbinen in Gas- und Dampfkraftwerken als Schlüsseltechnologie gesehen. Diese Schlüsselrolle liegt darin begründet, dass solche Kraftwerke grundlastfähig sind sowie im Teillastbetrieb Lastschwankungen regenerativer Quellen effizient ausgleichen können. Ferner gibt es Ansätze, solche Kraftwerke mit regenerativen Brennstoffen $CO_2$-neutral zu betreiben. Eine ingenieurstechnische Herausforderung bei der Entwicklung moderner Gasturbinenbrennern, welche den obigen Anforderungen an schnelle Lastwechsel und große Lastbereiche gerecht werden, ist das Auftreten von thermoakustischen Instabilitäten in der Brennkammer. Diese verschlechtern die Effizienz der Maschine und führen zu einem beschleunigten Verschleiß oder gar zur Zerstörung von Maschinenkomponenten. Eine Unterdrückung solcher Instabilitäten in bestehenden Maschinen durch entsprechende Hardwarenachrüstungen ist häufig mit hohen Kosten verbunden und dessen Vorhersage für neue Systeme komplex oder nur eingeschränkt möglich.

Die vorliegende Arbeit beschäftigt sich mit Rückkopplungsphänomenen von Flamme und Akustik in Drall- und Reheat-Flammen, wie sie in emissionsarmen und flexiblen zweistufigen/sequenziellen Gasturbinen zu finden sind. Ein besonderer Aspekt dieser Untersuchung ist der Fokus auf hochfrequente, transversale Instabilitäten. Im Hochfrequenzbereich (der Anfang des Frequenzbereichs wird durch die spezifische Grenzfrequenz für transversale akustische Moden der Brennkammer definiert) wird eine gleichphasige, lokale Interaktion der Flamme mit dem transversalen Druckfeld beobachtet. Im Gegensatz zu longitudinalen, niederfrequenten Instabilitäten kann die Flamme aus diesem Grund nicht mehr als kompakt, verglichen zur akustischen Wellenlänge, angenommen werden. Diese Nicht-Kompaktheit der Flamme muss in neuen Vorhersagemethoden berücksichtigt werden. Um die auftretenden Phänomene in einer ersten Verbrennungsstufe zu studieren, wurde ein bereits bestehender aerodynamisch stabilisierender Drallbrenner herangezogen. Für die Untersuchung der Phänomene in der zweiten Stufe sequenzieller Gasturbinen wurde im Rahmen der Arbeit

ein neuer Prüfstand konzipiert, aufgebaut und für erste Experimente der hochfrequenten Flammendynamik genutzt. Für die Drallflamme konnte gezeigt werden, dass die Flamme sich mit dem akustischen Feld periodisch verschiebt und verformt wird. Diese oszillierende Änderung der Flammenform führt zu einer Rückkopplung mit dem akustischen Feld und wirkt damit als thermoakustischer Treibmechanismus. Ferner zeigt sich für die Reheat Brennkammer eine zusätzliche Modulation der reaktiven Scherschicht, sowie der selbstzündenden Flamme. Insbesondere die Modulation der Selbstzündzeit in kombination mit der Flammenverschiebung und -verformung wird als weiterer grundlegender Treibmechanismus für die auftretende hochfrequente und transversale Instabilität in dem neu entwickelten Reheat-Experiment gesehen.

Anhand der Untersuchungen in der vorliegenden Arbeit konnten theoretisch gezeigte Treibmechnismen für hochfrequente Instabilitäten experimentell bestätigt und neue Einblicke gewonnen werden. Diese helfen, Werkzeuge zur Vorhersage thermoakustischer Wechselwirkungen in Gasturbinenbrennern zu verbessern und Modellentwicklungen zu validieren. Überdies wurde mit dem Reheat-Experiment eine Plattform geschaffen, mit welcher weitere umfassende Untersuchungen des hochfrequenten, nicht-kompakten Flammentreibens ermöglicht werden, welche für die Entwicklung neuartiger Brennkammern mit axialer Stufung von besonderem Interesse sind.

# Contents

**List of Figures** xx

**Nomenclature** xxiii

**List of Tables** xxiii

**1 Introduction** 1
- 1.1 Sequential Gas Turbine Systems . . . 2
  - 1.1.1 Working Principle . . . 4
  - 1.1.2 Part Load Flexibility . . . 5
  - 1.1.3 Emission Reduction . . . 8
- 1.2 High-Frequency Thermoacoustic Instabilities in Gas Turbines 9
  - 1.2.1 Thermoacoustic Feedback in Gas Turbines . . . 10
  - 1.2.2 High Frequency and Transverse Thermoacoustic Instabilities . . . 14
  - 1.2.3 Recent Research Activities and Findings . . . 17
- 1.3 Research Objectives and Thesis Structure . . . 20

**2 Experimental Setup** 23
- 2.1 Swirl Combustor Setup . . . 23
  - 2.1.1 Swirl Combustor Velocity Flow Field . . . 26
- 2.2 Reheat Combustor Concept . . . 27
  - 2.2.1 Combustion Regime . . . 29
  - 2.2.2 Acoustic Characteristics . . . 31
  - 2.2.3 Pressure Scaling . . . 33
- 2.3 Reheat Combustor Setup . . . 34
  - 2.3.1 Vitiator Design . . . 35
  - 2.3.2 Reheat Combustor Design . . . 37
  - 2.3.3 Reheat Combustor Flow Field . . . 42
- 2.4 Diagnostics . . . 46
  - 2.4.1 Dynamic Pressure . . . 47

2.4.2 Flame Chemiluminescence . . . . . 48

**3 Methods** **51**
3.1 Time Series Analysis . . . . . 52
3.1.1 Band-limited Hilbert Transform . . . . . 53
3.1.2 Identification of Thermoacoustic Stability States and Modal Dynamics . . . . . 55
3.2 Investigation of the Non-Compact Flame Response . . . . . 59
3.2.1 Decomposition of the Oscillating Heat Release Field . 60
3.2.2 Tomographic Cut-Plane Reconstruction of the Swirl Flame . . . . . 63
3.2.3 Quantification of the Flame Response . . . . . 64
3.2.4 Amplitude Dependent Flame Response . . . . . 66
3.3 Reconstruction of Flame Displacement . . . . . 68
3.3.1 Spatial Covariance of Subsequent Flame Images . . . 69
3.3.2 Reconstruction of the Oscillatory Displacement Field 71
3.3.3 Reconstruction of the Heat Release Modulations . . . 73

**4 Acoustic Combustor Response to Unsteady Heat Release** **75**
4.1 Swirl Combustor . . . . . 75
4.1.1 Thermoacoustic Stability States . . . . . 76
4.1.2 Effect of Swirl on the Acoustic Response . . . . . 78
4.1.3 Combined Effects of Swirl and Thermal Power on the Acoustic Response . . . . . 80
4.1.4 Acoustic Mode Dynamics . . . . . 81
4.1.5 Summary and Conclusions - Swirl Combustor Response . . . . . 82
4.2 Reheat Combustor . . . . . 83
4.2.1 Acoustic Response at the $\mathbf{T_{1y}}$ Resonance Frequency . 83
4.2.2 Limit-Cycle Oscillations at the $\mathbf{T_{1z}}$ Resonance Frequency . . . . . 87
4.2.3 Effect of Reheat Combustor Configuration on the Thermoacoustic Instability Propensity . . . . . 88
4.2.4 Summary and Conclusions - Reheat Combustor Response . . . . . 90

**5 Non-Compact Flame Response** **93**
5.1 Swirl Stabilized Flame . . . . . 93
5.1.1 General Observations . . . . . 93
5.1.2 Phase-Conditional Heat Release Oscillations . . . . . 97
5.1.3 Tomographic Reconstruction of the Distributed Heat Release Oscillations . . . . . 100
5.1.4 Extraction of the Flame Displacement . . . . . 102
5.1.5 Thermoacoustic Response due to Flame Displacement and Deformation . . . . . 106
5.1.6 Impact of the Swirl Number on Non-Compact Flame Response . . . . . 108
5.1.7 Analytical Source Term Expressions and Their Validation . . . . . 109
5.1.8 Summary and Conclusions - Swirl Flame Response . 115
5.2 Partly Auto-Ignition Stabilized Reheat Flame . . . . . 115
5.2.1 General Reheat Flame Characteristics . . . . . 116
5.2.2 Non-Compact Flame Response at the $\mathbf{T_{1y}}$ Resonance Frequency . . . . . 121
5.2.3 Non-Compact Flame Response at the $\mathbf{T_{1z}}$ Resonance Frequency . . . . . 126
5.2.4 Summary and Future Work - Reheat Flame Response 129

**6 Influence of Flame Shape Effects on Swirl Combustor Dynamics** **133**
6.1 Pulsation Amplitude Dependent Swirl Flame Response . . . 134
6.1.1 Amplitude Dependent Heat Release Distribution . . . 135
6.1.2 Quantification of the Amplitude Dependent Driving Rate . . . . . 139
6.1.3 Summary and Conclusions - Pulsation Amplitude Dependent Swirl Flame Response . . . . . 142
6.2 Impact of Macroscopic Swirl Flame Structure on the Thermoacoustic Response . . . . . 143
6.2.1 Combustor Geometry Impact on Mean Heat Release Distribution . . . . . 144
6.2.2 Impact of the mean Heat Release Distribution on Thermoacoustic Stability . . . . . 147

6.2.3 Summary and Conclusions - Impact of Macroscopic Swirl Flame Structure on the Thermoacoustic Response . . . . . 149

**7 Summary and Outlook** **151**

**A Temperature Field Approximation** **155**

**B External Forcing of High-Frequency Pressure Pulsations** **157**

**Bibliography** **165**

# List of Figures


1.1 Schematic of the Ansaldo GT24/GT26 and GT36 sequential heavy duty gas turbine engines. . . . 3
1.2 Thermodynamic cycles of single and sequential/staged GT24/26 GT36 gas turbine systems. . . . 4
1.3 Auto-ignition delay for natural gas fuel and fuel blends with propane or hydrogen, as a function of temperature and pressure. . . . 7
1.4 Qualitative part load operation scheme of a sequential gas turbine. . . . 7
1.5 Thermoacoustic feedback mechanisms in a gas turbine combustor. . . . 10
1.6 Thermoacoustic stability states illustrated by evolution of a limit-cycle oscillation as well as by flame driving and acoustic damping over the pulsation amplitude. . . . 13
1.7 Schematic representation of compact vs. non-compact thermoacoustic systems. . . . 15

2.1 Sketch of the $A^2EV$ swirl-stabilized gas turbine burner experiment with details of the face-plate, swirler and diffusor. 24
2.2 Mean axial flow velocity fields retrieved from CFD simulations of the $A^2EV$ lab-scale combustor. . . . 26
2.3 Schematic of the desired combustion characteristics of the reheat combustor experiment. . . . 30
2.4 Schematic of the desired acoustic characteristics of the reheat combustor experiment for the $T_{1y}$ and $T_{2y}$ acoustic modes with expected flame response mechanisms. . . . 32
2.5 Schematic of the elements for the vitiator and reheat combustor setup with indication of relevant control parameters. 35
2.6 Vitiator combustor setup with sectional view of swirl burners and air dilution pipes. . . . 36

2.7 Reheat combustor setup with magnified sectional views of the vortex generator arrangement and combustion chamber. 37
2.8 Transverse fuel stating in the reheat combustor by shifting the VG tip off its center position. . . . . 39
2.9 Detailed view of the diffusor geometry highlighting the different diffusor edge geometries as well as the diffusor opening angle $\alpha$. . . . . 40
2.10 Mean axial flow velocity and fuel mass fraction fields retrieved from CFD simulations of the laboratory reheat combustor. . . . . 44
2.11 Flow velocity range for high and low thermal power from 1D calculations as well as cross sectional area over the reheat combustor length. . . . . 45
2.12 Schematic of the diagnostic setup to synchronously capture the flame images with the acoustic pressure pulsations. . . . 47

3.1 Analytic signal representation showing the real and imaginary signal as well as the phasor along with sample time series of raw and analytical signals. . . . . 54
3.2 Probability density distributions $P(p')$ and $P(A_{p'})$ for three thermoacoustic stability states. . . . . 56
3.3 Probability density distributions of the Fourier coefficients for stable and unstable combustor operation along with the probability density distribution of the spin-ratio. . . . . 58
3.4 Analytical signal of the acoustic pressure along with image acquisition signals and sample flame CL images. Details show the association of flame CL data to the acoustic pressure. 61
3.5 Proportionality of measured $OH^*$ CL intensity with thermal power of the swirl-stabilized flame run in perfectly premixed mode. . . . . 65
3.6 Sample pressure signal with probability density distribution of the envelope amplitude for specification of different pulsation amplitude ranges. . . . . 67
3.7 Image pre-processing and subsequent cross-correlation of two subsequent flame images with indication of windowing. 70

3.8 Sample vector fields from the covariance analysis of flame CL measurements showing distributions of the phase-locked average, time average and their difference. . . . . 71
3.9 Evaluation of displacement scaling factors and illustration of the distribution of the maximum coherent flame front motion. . . . . 73
3.10 Evaluation of the oscillating heat release field from the displacement vector field based on the time averaged and inverse Abel transformed flame CL data. . . . . 74

4.1 Acoustic pressure from thermoacoustically stable, marginally unstable, and self-sustained limit-cycle oscillations of the A$^2$EV swirl combustor. . . . . 77
4.2 Acoustic pressure time series analyses for comparison of two swirl configurations of the A$^2$EV combustor at otherwise equal operation conditions. . . . . 79
4.3 Bifurcation diagram for air-fuel equivalence ratio over the pulsation amplitude for the LS and HS configuration as well as spin-ratio of the reconstructed first transverse mode. 80
4.4 Frequency spectrum of the dynamic pressure for a marginal (in)stability of the reheat combustor and phase difference of the pulsation probes. . . . . 84
4.5 Acoustic pressure time series analysis for comparison of the low frequency $L_1$ and high frequency $T_{1y}$ reheat combustor response. . . . . 86
4.6 Frequency spectrum, phase portrait and pressure time series data for $T_{1z}$ limit-cycle oscillations of the reheat combustor. . . . . 87
4.7 Bifurcation diagram of air-fuel equivalence ratio over the pulsation amplitude for different propane blends with natural gas fuel. . . . . 90

5.1 Frequency profile of the pressure and heat-release oscillations of the A$^2$EV combustor. . . . . 94
5.2 Integral flame heat release intensity oscillations from OH$^\star$ CL recordings over the pressure phase and heat release oscillation amplitude over the pulsation amplitude. . . . . 96

5.3 Example line-of-sight integrated and time averaged OH* CL recording of the swirl flame and its deconvolution via inverse Abel transform. . . . . 97
5.4 Phase-locked ensemble averaged OH* CL images for four different phase bins of the associated acoustic pressure signal. 98
5.5 Oscillation intensity and standard error from phase-locked averaged OH* CL distributions. . . . . 99
5.6 Real part and amplitude weighted phase of the distributed Fourier coefficient as well as the tomographic reconstruction of the modulated swirl flame. . . . . 100
5.7 Oscillation cycle of the line-of-sight integrated heat release superposed with related velocity vector fields $\mathbf{u}' = \delta\Delta'/\delta t$ indicating the flame displacement/motion. . . . . 103
5.8 Flame displacement oscillations from OH*CL image covariance analysis over the pressure phase as well as the displacement amplitude over the pressure envelope amplitude. 103
5.9 Distributed heat release oscillations resulting from local flame displacement of the mean heat release field. . . . . 104
5.10 Spatial heat release oscillations based on OH*CL recordings and acoustic PIV data along with sample acoustic pressure distribution to indicate regions of flame acoustics interaction. . . . . 105
5.11 Heat release oscillation fields obtained via tomographic reconstruction, covariance analysis, and substraction of the former two fields. . . . . 107
5.12 Distributed Rayleigh indices for the LS and HS configuration along with the distributed heat release and the pressure field of the first transverse acoustic mode. . . . . 108
5.13 Illustration of the non-compact thermoacoustic driving mechanisms via flame displacement and deformation throughout an oscillation cycle. . . . . 110
5.14 Comparison of experimentally and numerically obtained fields of the oscillating heat release from non-compact swirl flame response to transverse pressure pulsations. . . . . 113
5.15 Comparison of the heat release fields from experiments and computations for the high-swirl $A^2EV$ combustor configuration. . . . . 114

5.16 Time averaged CH* CL recording of a the xy-projection and yz-projection of the reheat flame for a representative operation point with respective standard deviation of the mean. . 117
5.17 Raw CH* CL image sectionized in propagation and auto-ignition dominate flame stabilization zones along with the probability density distribution of the auto-ignition and propagation ratio. . . . . 119
5.18 Probability density distribution of the axial position $P(x_{ai})$ of the auto-ignition flame zone as well as associate conditional averages of the CH* CL data for different axial flame positions. . . . . 120
5.19 Heat release oscillations from CH* CL measurements of the perturbed reheat flame related to the unstable $T_{1y}$ frequency. 121
5.20 Phase-locked ensemble averages for six phase situations $\varphi 1 - 6$ of the $T_{1y}$ thermoacoustic oscillation cycle. . . . . 123
5.21 Integral flame heat release intensity oscillations from CH* CL data over the phase from synchronous acoustic pressure measurements. . . . . 124
5.22 Distributed Rayleigh index $ri(\mathbf{x})$ along with local Rayleigh integrals $\mathrm{RI}_{\Delta_a}$ and their cumulative sum $S_c$ for integration sub-windows in $ri(\mathbf{x})$. . . . . 125
5.23 Oscillation cycle of the flame CH* CL recordings from backwards facing view via ensemble averages from six phase conditions $\varphi_{I'} 1 - \varphi_{I'} 6$. . . . . 127
5.24 Line-of-sight distribution of the oscillating flame CH* CL signal $I'$ from lateral (xy-projection) and backwards view (yz-projection). . . . . 129

6.1 Mean line-of-sight integrated, deconvoluted, and oscillating swirl flame CL distributions for different pulsation amplitude levels. . . . . 136
6.2 Integral heat release of the amplitude locked flame $\bar{Q}_A$ and integral heat release of the flame oscillations $\dot{Q}'_A$ along with the frequency response over the pulsation amplitude. . . . . 137
6.3 Mean flame CL distributions for minimal and maximal pressure amplitude level for LS1-4, as well as their difference images. . . . . 139

6.4 Amplitude dependent driving rates for flame deformation $\beta_\rho(A)$, flame displacement $\beta_\Delta(A)$ and their superposition $\beta_{\rho,\Delta}(A)$ for LS and HS configuration results. . . . . 141
6.5 Schematic of acoustic pressure $p'$ and velocity $u'$ over the combustor radius and indicative flame positions 1-3 that lead to different contributions of thermoacoustic driving. . . 142
6.6 Flame opening angle $\gamma_f$ and the axial position of the flame stagnation point $x_f$ for an example image of the A$^2$EV swirl flame. . . . . 145
6.7 Swirl flame opening angle $\gamma_f$ dependent on the swirl number from altering the A$^2$EV swirler's tangential slot height $h$ along with flame shape dependence of flow stagnation position $x_f$ for different area blockages $\Delta_{A,SC}$. . . . . 146
6.8 Linear thermoacoustic driving rate $\beta_{\rho+\Delta}$ by flame deformation and displacement for different flame shapes. . . . . 147
6.9 Oscillation frequency and thermoacoustic stability vs. thermal power density for different flame shapes. . . . . 148

A.1 Sample flame CL distribution indicating the mean heat release $\bar{q}$ and reconstructed temperature distribution $\bar{T}_{\mathrm{CFD}}$ from the CFD reference. . . . . 156

B.1 Sketch of the reheat combustor with external forcing applied to the upper and lower combustor liner with detailed view of the forcing unit. . . . . 158
B.2 Comparison of a non-forced/forced reheat combustor response. . . . . 159

# List of Tables

2.1 Summary of the geometrical and flow parameters varied to obtain different operational conditions of the $A^2EV$ combustor for investigation of the non-compact flame response to high-frequency pressure pulsations. . . . . 25
2.2 Summary of the operation parameters of the sequential reheat combustor setup for investigation of the non-compact rehaeat flame response to HF pressure pulsations. . . . . 42

# Nomenclature

### Latin Letters

| | | |
|---|---|---|
| $A$ | [$m^2$] | Area |
| $A$ | [Pa] | Envelope Amplitude |
| $ai$ | [$-$] | auto-ignition ratio |
| $c$ | [m/s] | Speed of sound |
| $D$ | [$N^2$/ms] | Damping |
| $E$ | [N/$m^2$] | Modal Energy Density |
| $f$ | [Hz] | Frequency |
| $F$ | [Pa] | Slowly varying amplitude CCW rotating mode |
| $G$ | [Pa] | Slowly varying amplitude CW rotating mode |
| $h$ | [m] | Height |
| $I$ | [$-$] | Intensity distribution |
| $K$ | [$-$] | Proportionality factor |
| $l$ | [m] | Length |
| $l_{min}$ | [$-$] | Minimal air requirement |
| $\dot{m}$ | [kg/s] | Mass flow rate |
| $M$ | [kg/kmol] | Molar mass |
| $N$ | [$-$] | Total number of samples |
| $p$ | [Pa] | Pressure |
| $P$ | [$-$] | Probability density function |
| $P_{GT}$ | [W] | Gas Turbine load |
| $pr$ | [$-$] | propagation ratio |
| $\dot{q}'$ | [W/$m^3$] | Volumetric heat release |
| $\dot{Q}'$ | [W] | Unstead heat release |
| $\dot{Q}, \dot{Q}_1, \dot{Q}_2$ | [W] | Head addition |
| $r$ | [m] | Radius |
| $S$ | [$-$] | Spinratio |
| $T$ | [K] | Temperature |
| $t$ | [s] | Time |
| $u$ | [m/s] | Velocity component |

| | | |
|---|---|---|
| $V$ | [m$^3$] | Volume |
| $\dot{W}_C$ | [W] | Compression work |
| $\dot{W}_E$ | [W] | Expansion work |
| $x$ | [m] | Spatial coordinate |
| $x_{C_3H_8}$ | [−] | Propane mass ration |
| $x_a$ | [−] | Air mass ratio |
| $\mathbf{x}$ | [m] | Spatial coordinate vector |
| $x_f$ | [m] | x-position of the flame stagnation point |
| $y$ | [m] | Spatial coordinate |
| $z$ | [m] | Spatial coordinate |

### Greek Letters

| | | |
|---|---|---|
| $\alpha_d$ | [deg] | Diffusor opening angle |
| $\alpha$ | [rad/s] | Acoustic damping rate |
| $\beta$ | [rad/s] | Flame driving rate |
| $\Delta_{A,SC}$ | [−] | Swirler cone tip area ratio |
| $\delta_{fl}$ | [m] | Flame thickness |
| $\eta$ | [Pa] | Complex Fourier coefficient signal |
| $\gamma_{O_2}$ | [−] | Volumetric oxygen ratio |
| $\gamma$ | [−] | Ratio of specific heats |
| $\gamma_f$ | [deg] | Flame opening angle |
| $\lambda$ | [−] | Air-fuel equivalence ration |
| $\lambda_a$ | [m] | Wave length |
| $\nu$ | [rad/s] | Thermoacoustic growth rate |
| $\sigma$ | [−] | Standard error |
| $\tau$ | [s] | Delay time |
| $\omega$ | [rad/s] | Angular (Eigen-)frequency |
| $\varphi$ | [deg] | Phase angle |
| $\phi$ | [−] | unsteady quantitiy |
| $\Phi$ | [−] | Complex analytical signal representation |

### Subscript

| | |
|---|---|
| $(\dots)_a$ | Acoustic |
| $(\dots)_{ad}$ | Adiabatic |
| $(\dots)_C$ | Combustor |
| $(\dots)_\Delta$ | flame displacement |
| $(\dots)_E$ | Exhaust gas tube |
| $(\dots)_f$ | Fuel |
| $(\dots)_{fl}$ | Flame |
| $(\dots)_{ign}$ | Ignition |
| $(\dots)_{max}$ | Maximum |
| $(\dots)_{min}$ | Minimum |
| $(\dots)_{ox}$ | Oxidizer |
| $(\dots)_{pre}$ | Preheated |
| $(\dots)_\rho$ | flame deformation |
| $(\dots)_s$ | sample |
| $(\dots)_{T1}$ | First transversal |
| $(\dots)_{VG}$ | Vortex Generator |
| $(\dots)_x$ | x-direction |
| $(\dots)_\infty$ | Ambient |

### Superscript

| | |
|---|---|
| $(\bar{\dots})$ | Steady/Mean value |
| $(\dots)'$ | Oscillation/Disturbance/Perturbation |
| $(\tilde{\dots})$ | Stochastic Disturbance |

### Dimensionless Numbers

| | |
|---|---|
| He | Helmholtz number |
| Ma | Mach number |

### Abbreviations

| | |
|---|---|
| 1D | One-dimensional |
| 2D | Two-dimensional |
| 3D | Three-dimensional |
| $A^2EV$ | Advanced$^2$ EnViromental Burner |
| $\mathcal{A}$ | Abel transform |
| C | Combustor |
| $\mathcal{C}$ | Correlation matrix |
| CCGT | Combined Cycle Gas Turbine |
| CFD | Computational Fluid Dynamics |
| CL | Chemiluminescence |
| EV | EnViromental |
| $\mathcal{F}$ | Fourier coefficient |
| FEM | Finite Element Method |
| FS | Flame Sheet |
| GT | Gas Turbine |
| $\mathcal{H}$ | Hilbert transform |
| HF | High-Frequency |
| HP | High Pressure |
| HS | High swirl |
| IRZ | Inner recirculation zone |
| LF | Low-Frequency |
| LIF | Laser Induced Fluorescence |
| LS | Low swirl |
| N | Nozzle |
| ORZ | Outer recirculation zone |
| P | Sensor position |
| PD | Power Density |
| PIV | Particle Image Velocimetry |
| RI | Rayleigh Integral |
| ri | Rayleigh index |
| $\mathcal{R}$ | Radon transform |
| SEV | Sequential EnViromental |
| TTL | Transistor-transistor logic |
| VG | Vortex Generator |

# 1 Introduction

The transformation of the global energy infrastructure towards enhanced sustainability and zero net $CO_2$ emissions on the long-term perspective is one of the crucial challenges to achieve the objectives of the United Nation's Paris Agreement to counteract climate change and the 2030 Agenda for Sustainable Development [1]. Momentarily, the energy sector represents one of the largest sources of anthropogenic $CO_2$ and other greenhouse gas emissions [2]. At the same time, technological developments allow to forecast substantial sustainability improvement along with $CO_2$ reduction for the future energy infrastructure. For example, it can be expected that renewable sources will account for more than 70% of the gross electricity production in 2050 [3], which is already reflected in a robust growth of installed solar and wind capacity in recent years [3,4]. A major challenge regarding this development trend is the mismatching intermittency of volatile renewable sources and electricity demand. Hence, advanced systems and strategies that allow for efficient energy conversion, distribution, and usage are necessary [5]. Possible future scenarios comprise international collaborations for technology exchange and shared infrastructures for diverse exploitation of renewable energy sources [6]. Thus, various locations for efficient use of e.g. wind, sun, hydro, and biomass need to be identified for respective conversion, storage and distribution in a demand-actuated manner across borders utilizing modern power plants, storage technologies and smart power grids [5].

A key role in the implementation of the foregoing strategies is attributed to combined cycle gas turbine (CCGT) power plants [7,8]. These are able to supply base-load electricity at high efficiency, but in particular to flexibly and efficiently compensate demand to supply deviations associated with increasing shares of renewable energy sources. This translates into requirements and development drivers for heavy duty gas turbine combustion systems of (i) low pollutant (most notably $CO_2$, $NOx$, and CO) emissions in compliance with strict regulative frameworks, (ii) high part

load efficiency and turndown capability to provide reserve power, (iii) fast load ramp and high peak load performance, and (iv) fuel flexibility to allow for e.g. power to gas incorporation [9–11]. An approach to meet these requirements in modern gas turbine engines is the use of (i) lean-premixed combustion technologies [12–14] along with (ii) axial fuel and air staging via e.g. a sequential arrangement of two combustion systems in series [9–11, 15–19]. However, besides the significant performance advantages over conventional non-premixed diffusive combustion [12], a regularly encountered problem specifically with the lean-premixed technology is the occurrence of thermoacoustic instabilities [11, 20]. These instabilities result from the constructive interference of the unsteady flame with an acoustic eigenmode of the combustion chamber and can lead to significant pressure pulsations [21]. Emerging consequences are (i) accelerating wear and fatigue of the combustor hardware, (ii) a restricted operational range, or (iii) the damage of hardware components [20]. All these drawbacks are associated with substantial cuts in the technical and economic efficiency of the system. Hence, an a-priori predictive assessment and avoidance of thermoacoustic pulsations represents a major engineering challenge in the design and operation of modern gas turbine engines. A particular challenge for this task is above all the consideration of various operating points, which may constitute thermoacoustic responses at different frequencies [22, 23]. Hence, for the development of effective mitigation strategies and stabilizing combustor designs, a detailed understanding of the system dynamics and thermoacoustic feedback mechanisms is necessary [20]. Thus, a wide field of engineering research on thermoacoustic instabilities in gas turbine engines has established in which the present thesis is allocated.

## 1.1 Sequential Gas Turbine Systems

The main motivation for the employment of axial fuel and air staging systems in heavy duty gas turbines are the improved part load efficiencies within the regulatory emission limits in contrast to single stage counterparts [9–11]. In general, staged/sequential systems can be operated in both, single stage and two-stage sequential mode for reduced and nomi-

nal power output, respectively. This controllability represents an effective measure to respond to volatile renewable energy sources and to stabilize the electricity grid [10]. The real world sequential systems to which this work references is the GT24/GT26/GT36 heavy duty gas turbine family of the company Ansaldo Energia[1]as schematically provided in Figure 1.1. The GT24/26 gas turbine architecture (cf. Fig. 1.1 (a)) comprises two burners in series, which are interconnected by a high-pressure turbine [17], whereas the burners of the GT36 connect through an air dilution stage (cf. Fig. 1.1 (b)) [11]. Moreover, the GT24/26 annular combustor geometry is replaced by a can-annular system in the GT36 for improved maintenance capability [11]. The following Sections 1.1.1-1.1.3 provide an overview of the working principles, part load capabilities and emission characteristics of the GT24/26 and GT36 systems.

[1]The GT24/26 gas turbine engine was originally developed by ABB [16, 17] and further improved by Alstom Power after acquiring ABB's gas turbine business [15, 18, 24].

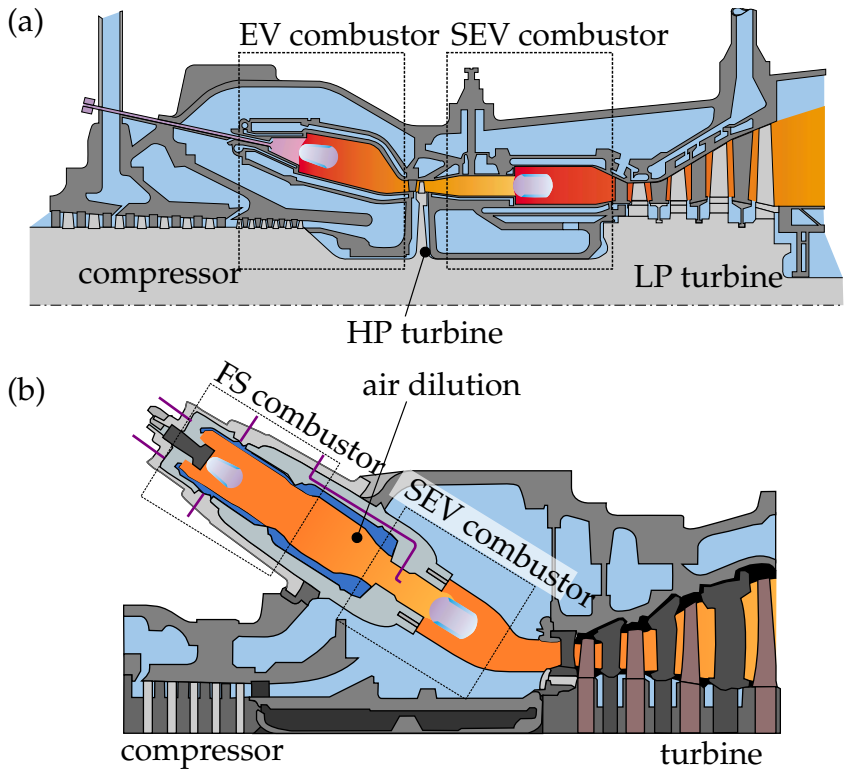


**Figure 1.1:** Schematic of the Ansaldo GT24/GT26 and GT36 sequential heavy duty gas turbine engines (adapted from [11, 16]).

### 1.1.1 Working Principle

The working principle of the sequential combustion technology is summarized in Figure 1.2 with help of the related thermodynamic cycle in a h-s diagram compared to a single-stage gas turbine. All cycles show the typical processes of compression work $\dot{W}_C$, addition of heat $\dot{Q}_1$, $\dot{Q}_2$ and expansion work $\dot{W}_E$ of the fluid with the ultimate aim of generating net mechanical work for transformation into electrical energy. From a first glance, the multistage systems illustrate the improved turndown flexibility by modifying the heat addition $\dot{Q}_2$ over the single-stage counterpart. For this thesis, the addition of heat, i.e. the combustion systems within this thermodynamic cycle are of interest. The working principle of these combustion systems (cf. Fig. 1.1) are as follows: Compressed air enters the first lean and technically premixed combustion stage. In the GT24/26 and GT36 gas turbine systems, this comprises either a so called EnVironmental (EV) [14, 25] or a Flame Sheet$^{TM}$ (FS) [26, 27] combustor, respectively. Both systems stabilize the flame be means of aerodynamic effects [12, 28]. Stable combustion in terms of flash-back and blow-off limits is substantially influenced by global flow parameter and air-fuel equivalence ratio, which implicitly specifies the load flexibility range [9, 26, 27].

After this first combustor stage, the hot exhaust gas stream expands in a high-pressure turbine for the GT24/26 or is dilluted at constant pressure with compressed air in the GT36 system. This temperature staging

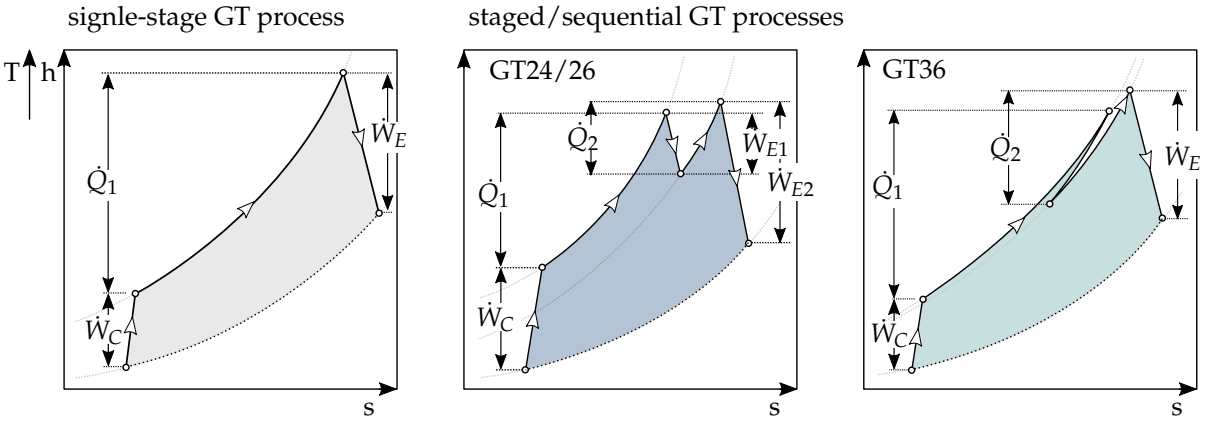


**Figure 1.2:** Thermodynamic cycles of single and sequential/staged GT24/26 GT36 gas turbine systems.

is a unique aspect over other sequential systems for improved emission and turndown performance, as further detailed in Sec. 1.1.3. For both systems, the inlet temperatures at the second-stage Sequential EnVironmental[2] (SEV) combustor range above 1300 K with an $O_2$-content of about $10 - 15\,\text{Vol} - \%$ [15, 17, 24]. Hence, the air-fuel mixture is at temperature levels at which auto-ignition within the fluid's residence time in the combustor occurs. Thus, the SEV combustor reveals (i) flame propagation and (ii) auto-ignition as flame stabilization mechanisms. Specifically, after a sudden area expansion at the combustion chamber inlet, shear layer formation and recirculation of hot combustion products lead to an increased reactivity, and flame propagation stabilized combustion manifests in this region. In the core flow, auto-ignition reaction occur as the dominating flame stabilization mechanism [30, 31]. Accordingly, temperature, pressure and mixture quality directly impact the auto-ignition delay, and hence influence the SEV combustion rather than global flow parameters (as for the EV/FS systems). This renders the SEV combustor particularly efficient and stable for part load operation [9,16,17]. In addition, short residence times of the reacting stream in the SEV system (e.g. $\tau_{\text{EV/FS}} \approx 30\,\text{ms}$ vs. $\tau_{\text{ign,SEV}} \approx 5\,\text{ms}$) effectively lower $NO_x$ formation [11, 15]. The exhaust gases are then finally expanded in the turbine.

### 1.1.2 Part Load Flexibility

In order to describe the part load capability of the sequential combustion systems, further details on flame stabilization mechanisms are necessary. For the first-stage EV/FS combustors, the deflagrative flame speed is the main parameter that specifies the physical flame stabilization mechanism. The oxidation reaction propagates through molecular and turbulent transport processes from the hot combustion products towards the cold reactants [28]. The reactivity depends primarily on the fuel kinetics and its transport properties at temperatures close to the adiabatic flame temperature. Increasing the fuel-air equivalence ratio, and thus the adiabatic flame temperature, leads to an elevated reactivity of the heat release

[2]The available literature refers to the GT36 second-stage sequential combustor as *Sequential Burner* (SB) [11]. Both combustors, the newest SEV generation with multiple fuel lances and vortex generators and the SB combustor work with the same fundamental principles [11, 29]. Hence, for this thesis, both combustors are referred to as SEV for better readability.

zone. Hence, a stable combustion regime is limited by the minimal and maximum reactivity by lean flame extinction (blow off) and flashback, respectively [11, 12, 28]. With the use of the aerodynamic stabilization, the EV/FS combustion can be maintained over a considerable range of deviating reactivities by parallel adjustment of flow features [14, 26].

As already outlined above, SEV flame stabilization is dominated by auto-ignition, which occurs after the elapse of the ignition delay $\tau_{ign}$. This stabilization mechanism mainly depends on the temperature of the inflowing gas stream, and therefore effectively on the flame temperatures of the EV/FS combustion. The SEV flame position is thus rather independent of its own adiabatic flame temperature. Further to this, pressure and fuel composition impact the auto-igniting SEV combustion, but can again be controlled/counterbalanced by adjustment of the EV/FS flame temperature. These effects on the auto-ignition delay $\tau_{ign}$ and thereby on the flame location in the combustion chamber are exemplarily summarized in Figure[3] 1.3. Hence the controllability of the reheat combustion via the auto-ignition delay yield important advantages in terms of possible operation conditions and flexibility of the system [9, 11], as outlined below.

The use of various fuel composition (cf. Fig. 1.3) with increased auto-ignition tendency allows for extension of the stable combustion limit in the low load regime. For example, for a given flame temperature, the addition of e.g. hydrogen and higher hydrocarbons leads to a higher flame speed of the EV/FS flame and shortened ignition delay times in the SEV combustor result [28, 29, 32]. The shortened ignition delay would, however, lead to an increased flash back propensity in the SEV combustor. Employed countermeasures are the simultaneous reduction and increase of the respective fuel mass flow rate in the EV/FS and SEV combustors. This decreased EV/FS fuel mass rate leads to a reduction of the adiabatic flame temperature, and consequently a reduction of the SEV inlet temperature. Thereby, the overall higher fuel reactivity is compensated without shortening the auto-ignition delay. The overall power conversion remains constant, which represents an advantage of sequential system com-

[3] The figure shows a $p = 1\,\text{bar}$ situation as it is of interest for the experimental investigations presented in this work. The temperature dependence of the auto-ignition delay reveals the same general trend at elevated, i.e. engine, pressures.

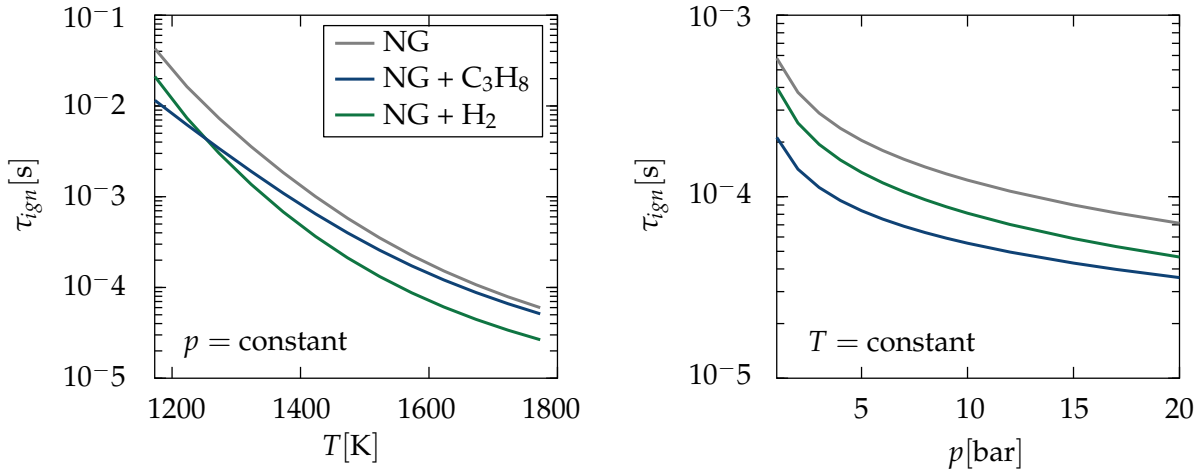


**Figure 1.3:** Auto-ignition delay $\tau_{ign}$ for natural gas fuel (NG) and fuel blends of 90 % natural gas with 10 % propane or hydrogen, as a function of temperature $T$ with constant pressure $p = 1\,\text{bar}$ (left) and as a function of pressure $p$ at constant temperature $T = 1473\,\text{K}$ (right).

pared to the single-stage gas turbine counterpart. Specifically, the alignment of both combustion stages represents the central feature for flexible part load operation. Figure 1.4 illustrates a representative operation scenario of a sequential combustion system from low load operation towards nominal power output. In this figure the 10 % and 100 % relative gas turbine load $P_{GT}$ correspond to the lower and upper bounds of the power output, respectively. In order to reach the lower 10 % load point, the turbine is operated solely using the first-stage EV/FS combustor by increas-

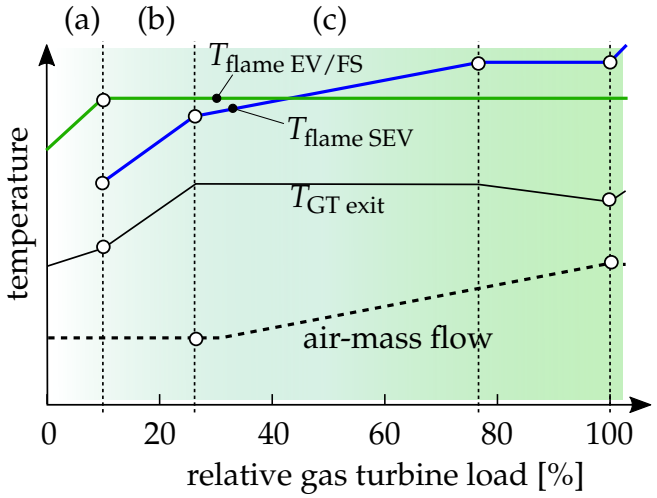


**Figure 1.4:** Qualitative part load operation scheme of a sequential gas turbine [9, 13].

ing the flame temperature via increasing the fuel mass flow rate (a). In order to quickly respond to grid load fluctuations, the gas turbine can be efficiently parked at this condition to allow for a fast power ramp. Moreover, at the 10 % load point, auto-ignition and stable combustion conditions for the second-stage combustor are reached, and thus, the SEV combustor can be/is started. The gas turbine power output is further ramped up towards 25 % (b) by increasing the SEV flame temperature by means of adding fuel to the SEV. Further ramp up of the power output to 100 % is then achieved by adjusting the fuel and air mass flows in both combustors (c) [9]. It is important to note that the EV/FS temperature remains constant while the SEV increases due to the respective reactivity characteristic, as above described [13]. In this context, the described behavior of EV/FS and SEV flame temperatures (2nd stage is always operated at higher flame temperatures than 1st stage) is additionally utilized to minimize pollutant emissions [9, 11] as described in the next paragraph.

### 1.1.3 Emission Reduction

The emission characteristic is a further advantage of sequential combustion compared to single stage engines due to three main emission reduction mechanisms: (i) low maximum combustion temperatures, (ii) low combustor residence times due to high flow velocities and (iii) reduced oxygen content in the EV/FS exhaust gases entering the SEV combustor [9, 11, 13].

**Low maximum combustion temperatures** are maintained due to the temperature drop across the high-pressure turbine and air dilution in the GT24/26 and GT36 system, respectively. This allows to decouple power output from an increase of the maximum temperature. Physically, the oxygen-radical formation, and thereby the formation of $NO_x$ rises sharply with temperature [12, 28]. Hence, a reduction of the maximum combustion temperatures is accompanied by a decrease of $NO_x$ emissions [9]. Further to this, the second-stage SEV combustor can always be operated at higher temperature levels compared to the first-stage EV/FS combustion. This promotes a low $NO_x$ and CO EV/FS combustor footprint, while short residence times of the reacting stream and reduced $O_2$ content in

the SEV combustor counterbalance possible thermal $NO_x$ formation at increased temperatures in the second-stage as is detailed below.

**Low combustor residence times and high turbulence levels** of the reacting mixture in the SEV combustor optimize flame stabilization and mixing of fuel with hot exhaust gases from the EV/FS combustor [15,18]. Auto-ignition occurs in areas of sufficient mixture quality, which reduces presence of fuel-rich zones. Thereby, temperature distributions are homogenized and related $NO_x$ production rates reduced [11]. In addition, the high flow velocity in the SEV combustor compared to the EV/FS system comprise another favouring condition in terms of mixture homogeneity. High flow velocities result in reduced residence times in the combustor and thereby lead to reduced $NO_x$ formation.

**Reduced oxygen content** and increased $H_2O$ content in the SEV inflow gas, originating from the EV/FS exhaust, hamper $NO_x$ formation. In combination with short combustor residence times, reduced oxygen content in the reacting stream is presumed to drastically decrease the oxidation path of $N_2$ to $NO_x$ [9] compared to the first-stage combustion. Consequently, the overall emissions are considerably reduced by sequential systems over the entire operational range.

## 1.2 High-Frequency Thermoacoustic Instabilities in Gas Turbines

This thesis focusses on high-frequency (HF) and transverse thermoacoustic instabilities in gas turbines. The present section provides the relevant background of thermoacoustic instabilities in gas turbine combustors. First, an introduction of the general feedback phenomenology between flame and acoustics is provided in Section 1.2.1. Second, specific aspects on HF and transverse thermoacoustic instabilities with a respective comparison to their low-frequency (LF) and longitudinal counterpart are given in Section 1.2.2. The last Section 1.2.3 provides an overview of recent research activities and findings in this field that raise open questions and lead to the research objective of this thesis.

### 1.2.1 Thermoacoustic Feedback in Gas Turbines

Thermoacoustic oscillations are caused by a constructive feedback between the flame's distributed heat release rate $\dot{Q}'(\mathbf{x}, t)$ and the resonant combustion chamber acoustics $p'(\mathbf{x}, t)$ as schematically illustrated in Figure 1.5. The unsteady heat release of the flame in the combustion chamber can be considered as a volume source, which emits acoustic waves into the system. These waves impinge on the chamber walls, inlets and outlets where they are either absorbed or reflected. As a result, small acoustic perturbations interact with the flame to cause heat release fluctuations, which establishes the thermoacoustic feedback loop. In addition to this, acoustic oscillations may also excite e.g. fuel feed modulations or vortical structures by interaction of the resulting acoustic field with the mean flow. These perturbations are then convectively transported to the flame and lead to additional heat release fluctuations. Thermoacoustic pulsations in gas turbines occurring at low frequencies (LF) are commonly governed by longitudinal and azimuthal modes [20,34,35]. A usually valid assumption for this regime is, that burner and flame are compact with respect to

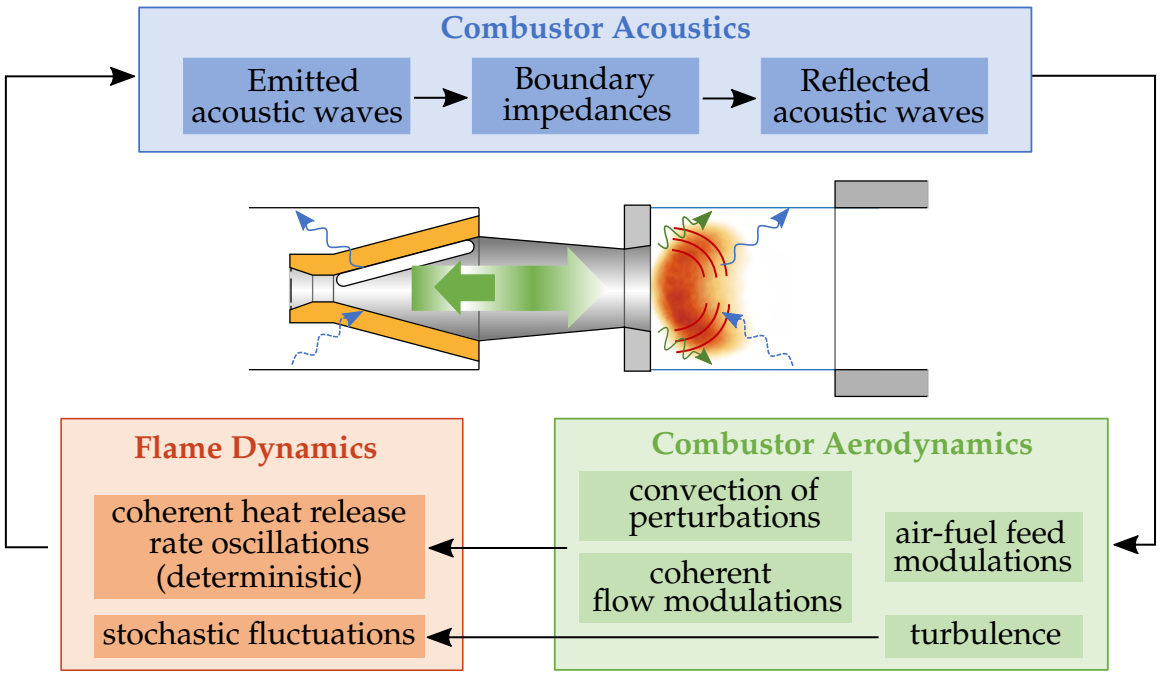


**Figure 1.5:** Thermoacoustic feedback mechanisms in a gas turbine combustor [adapted from [33]]

the acoustic wavelength (cf. details in Sec. 1.2.2) [34]. Flame responses are dominated by convective driving effects, while driving mechanisms associated with azimuthal pulsations add additional complexity compared to the longitudinal case, mainly due to the interacting multi burner setup in an annular combustion chamber [36–39]. The focus of this work is on HF combustion instabilities, often referred to as screech, as the unstable frequencies are found in the kilohertz regime [11, 22]. At this frequency levels, the flame is non-compact compared to the acoustic wavelength and the dominance of flame driving mechanisms differ compared to the LF counterpart, which is why established methods to describe the LF thermoacoustic feedback may not be applicable to HF systems (cf. details in Sec. 1.2.2).

**Rayleigh's criterion** defines whether the thermoacoustic feedback is of constructive nature, which depends on the relative phases between the oscillating heat release field and the pressure distribution. This can be quantified using the Rayleigh integral [40]

$$\mathrm{RI} = \int_V \oint p'(\mathbf{x},t)\dot{Q}'(\mathbf{x},t)dtdV > 0, \tag{1.1}$$

where $t$ and $V$ denote time and volume, respectively. For a phase difference of less than $90\,^\circ$ a constructive feedback between flame and acoustics occurs, which implies that acoustic energy is added [41]. One main focus associated with this work is the assessment of the driving behavior of a given unsteady heat release distribution and the respective acoustic field of the combustion chamber. For this purpose, the so called Rayleigh index is used, which is given by the spatial integrand of Equation 1.1, i.e.

$$\mathrm{ri}(\mathbf{x}) = \oint p'(\mathbf{x},t)\dot{Q}'(\mathbf{x},t)dt, \tag{1.2}$$

which provides a local field of acoustic sources and sinks across the given flame volume due to thermoacoustic interactions.

**Thermoacoustic stability states** of a combustor, i.e. whether it is stable or unstable, are assessed by accounting for acoustic damping in addition to the flame driving given by the Rayleigh integral (cf. Eq. 1.1). These mechanisms comprise the attenuation of acoustic energy $D$ due to mean flow effects [38,42,43] and dissipation at the system boundaries [21]. Ther-

moacoustic energy generation and acoustic dissipation are commonly described quantitatively by the so called flame driving rate $\beta_n[\mathrm{rad/s}]$ and acoustic damping rate $\alpha_n[\mathrm{rad/s}]$ of the n-th acoustic mode of the combustor, respectively. The superposition of these former quantities yields the growth rate

$$\nu_n = \beta_n - \alpha_n. \tag{1.3}$$

A positive growth rate $\nu_n$ thus implies that flame driving quantitatively outperforms acoustic damping and results in a linearly unstable thermoacoustic system (and vice versa) [21, 38].

The driving and damping rate can be linked to the energy transfer due to flame driving and acoustic dissipation by

$$\beta_n \sim \frac{1}{2}\frac{RI}{E_n}, \alpha_n \sim \frac{1}{2}\frac{D}{E_n} \tag{1.4}$$

where $E_n$ denotes the modal energy density [38]. The linear stability of a gas turbine combustor can be assessed by quantifying the growth rate $\nu_n$ at the mode of interest. Hence, driving and damping rates (cf. Eq. 1.3) of this mode need to be obtained, which requires knowledge about (i) the modal energy density $E$, (ii) the Rayleigh integral $RI$ as well as (iii) the damping $D$. The former quantity is retrieved numerically by solving the Helmholtz equations in Finite Element framework, e.g. presented in [38, 44]. The values for $E$ and $RI$ rely on explicit formulations of the oscillation heat release field (subject of this work), while formulations of the damping term $D$ can be found in e.g. [38, 43, 45]. Performing these linear stability assessments are of relevance for analysis, design, operation and control of thermoacoustic systems. Hence, a comprehensive understanding of the flame response mechanisms and derivation of respective linear source term expressions, which can be prescribed to the acoustic governing equations, represents a core research and engineering challenge to improve the robustness of the aforementioned stability assessment tools [37].

**The evolution of a thermoacoustic instability** is illustrated in Figure 1.6. The development of considerable pulsation amplitudes over time are shown in Figure 1.6 (a) by means of experimentally obtained acoustic pressure data. Thermoacoustically unstable conditions are reached by in-

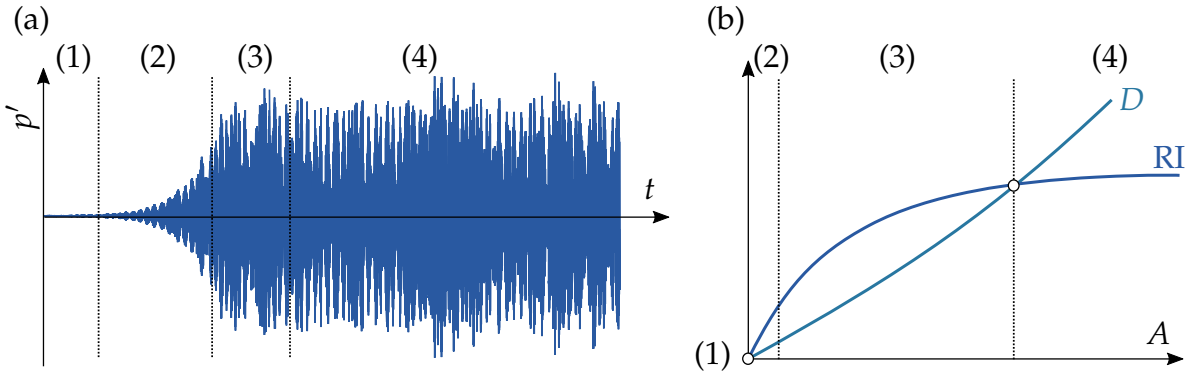


**Figure 1.6:** (a) Acoustic pressure time series of a combustor during evolution of a limit-cycle oscillation from initially stable conditions, (b) flame driving RI, acoustic damping $D$, driving rate $\beta$ and damping rate $\alpha$ over the pulsation amplitude indicating different stability states (1)-(4) of the thermoacoustic system.

creasing the thermal power of the combustion during recording of the pressure pulsations. Figure 1.6 (b) presents the energy due to heat release oscillations $RI$ and acoustic damping $D$ as a function of the pulsation amplitude. State (1) shows thermoacoustically stable combustor operation, where low amplitude pressure fluctuations originate from broadband flow and combustion noise. Initiation of a positive thermoacoustic feedback can e.g. be induced by a change of the combustor operation mode, which leads to state (2). Here a feedback establishes between small heat release perturbations and the oscillating pressure, which leads to an exponential amplification of the pressure amplitudes with $p' \sim e^{\nu_n t}$ [21] at mode $n$. Physically, flame driving RI is positive, i.e. is in the right phase relation with the acoustic mode, and exceeds the system damping $D$. This situation portrays the initial growth of a self-excited thermoacoustic instability, and is referred to as linear regime as the flame driving increases linearly with the pressure pulsations. Eventually, non-linear driving saturation effects limit the growth (3) and the system settles into a limit-cycle oscillation (4) [20,21,46]. At this state, the energy gain equals the losses of the system and thermoacoustic pulsation amplitudes remain at constant level.

**Non-linear saturation mechanisms of the heat release** define the pulsation amplitudes of the limit-cycle oscillation. Knowledge of these amplitudes is of technical relevance for e.g. the efficient design of countermeasures such as damping devices [22,23]. Qualitatively accounting for

the flame saturation in analysis tools is typically realized by adding a non-linear cubic saturation function to the linear flame driving source that reflects the physical flame saturation behavior [47,48]. For LF thermoacoustic instabilities, experimental studies exist, which specifically investigate the flame saturation mechanisms responsible for the non-linear flame driving capability. Proposed mechanisms are (i) characteristic phase lags between the flame modulations by acoustics, i.e. such that the Rayleigh criterion for acoustic energy generation [40] is not fulfilled, (ii) local quenching of the flame as well as kinematic effects, and (iii) convective flow-flame behavior [46,49–51]. For HF systems, the non-linear saturation mechanisms are sparsely researched and understood (cf. Sec. 1.2.3). In this work, such investigations are initiated by means of amplitude dependent characterization of the flame driving behavior to derive directions for future research on these.

### 1.2.2 High Frequency and Transverse Thermoacoustic Instabilities

In the following, specific differences in regard to LF thermoacoustic instabilities are discussed to establish the typical characteristics of the less investigated HF transversal counterparts. Specifically, (i) the compactness of the flame, (ii) the acoustic mode type associated with HF transverse instabilities, and (iii) associated flame response phenomena are assessed.

**Non-compact flames** are the first specific feature of the HF flame response due to the typical length scales of flame and acoustics. The LF flame dynamics can be described as a spatially compact discontinuity (point source) as flame length scales $\delta_x$ are much smaller than the acoustic wavelength $\lambda_L$, i.e. $\delta_x \ll \lambda_L$. Conversely, with increasing frequencies, the wavelength of an HF acoustic mode $\lambda_T$ and typical flame length scales $\delta_{y,z}$ have the same order of magnitude, i.e. $\delta_{y,z} \approx \lambda_T$. Hence, the heat release oscillations are spatially distributed across a multi-dimensional acoustic field (cf. details below). As a consequence, the benefit of the flame description as a compact point source is no longer applicable. Due to equal length scales of the flame and acoustic wavelength, HF thermoacoustic feedback needs to be considered as spatially non-compact. This condition

is schematically shown in Figure 1.7 by means of $\delta$ and $\lambda$, which define the Helmholtz numbers

$$He_L = \frac{\delta_x}{\lambda_L} << 0.1, \qquad He_T = \frac{\delta_{y,z}}{\lambda_T} > 0.1 \tag{1.5}$$

for longitudinal $He_L$ and transversal $He_T$ systems. For the combustor experiments treated in this work, typical Helmholtz numbers of flame and acoustics are $He_T > 0.1$.

**Multi-dimensional modes** present the second characteristic of the HF thermoacoustic system. Figure 1.7 (a) shows a sample low-frequency longitudinal mode in a can-combustor configuration concerned in this work. The longitudinal acoustic mode occurs in the direction of mean flow and is characterized by comparably large wavelengths $\lambda_L$ and constant pressure over the combustor cross-section. In contrast, the HF mode in Figure 1.7 (b) occurs beyond the cut-on frequency of the concerned system and is distributed over the combustor cross-section. With respect to typical can, can-annular, or annular gas turbine combustors, HF acoustic modes are of transverse, radial, or longitudinal (azimuthal) character as well as combinations thereof. Note that, depending on the oscillation frequency, the characteristic of a multi-dimensional mode can also appear at LF conditions. A typical example are azimuthal acoustic modes in an annular

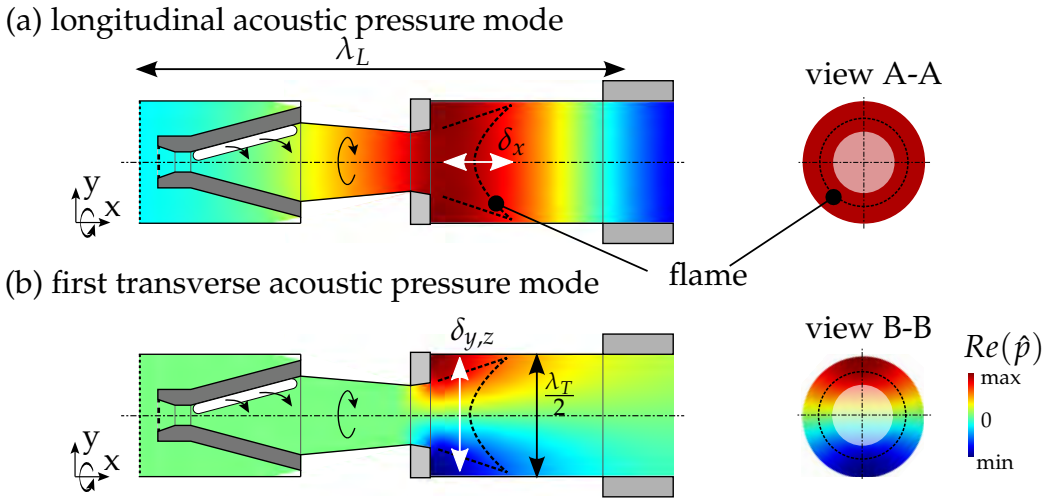


**Figure 1.7:** Schematic representation of compact vs. non-compact thermoacoustic systems.

combustor, which transversely interacts with the flame. However, the specific focus of this work is on HF acoustic oscillations of the first or second transverse mode in can-type combustors (or conceptually in transverse direction of an annular system) and non-compact flames, as schematically shown in Figure 1.7 (b).

**Flame response mechanisms** associated with LF longitudinal modes with wave propagation in the direction of the mean flow are dominated by convective effects. These emerge from acoustic perturbations of e.g. velocity or equivalence ratio, which are convectively transported to the flame region and result in heat release rate fluctuations. Principally, these convective effects are characterized by a low pass behavior [37,52], which is why the resulting flame driving reduces with increasing oscillation frequencies. Whether or not these convective mechanisms prevail in HF thermoacoustic systems depends on the convective time and length scales in relation to the specific combustor geometry and flame shape as discussed in [38]. A possible condition under which convected modulations impact the local HF and non-compact heat release oscillations can be found in the reheat system. First, the transversal mode in the combustor might have a longitudinal extend into the upstream mixing section. As fuel injection, fuel-oxidizer mixing, and auto-ignition occur within a rather small zone of the combustor, modulations thereof can result in heat release perturbation, if dispersion occurs on larger time scales. Second, a modulation of e.g. the auto-ignition delay of a transverse acoustic mode in upstream direction towards the face-plate would have an impact on the auto-ignition flame location further downstream. A specific characteristic of the HF multi-dimensional transverse mode is a local flame acoustics interaction. It was found for a swirl-type can-combustor (also treated in this work) that the flame is both locally displaced with the acoustic velocity and locally responds to the distributed pressure fluctuations. As these mechanisms occur on small scale, they are often disregarded in LF systems but represent dominating driving mechanisms in HF thermoacoustic instabilities of gas turbine combustors.

The following section summarizes the state-of-the art comprehension of HF thermoacoustic instabilities in gas turbine combustors and highlights open questions to specify the research objective of this work (cf. Sec. 1.3).

### 1.2.3 Recent Research Activities and Findings

The thermoacoustic response and system dynamics of LF combustion instabilities have been subject to numerous experimental, theoretical, and numerical studies and a comprehensive understanding exists, as e.g. summarized by Lieuwen in [20,36]. However, the occurrence of HF combustion instabilities due to the development trends of modern gas turbine combustors (cf. Sec. 1.1) represent a further engineering challenge [11,22]. This is why research efforts have recently been intensified to understand the HF flame acoustics interactions during unstable combustion and develop respective modeling and analysis frameworks.

A comprehensive review on transverse instabilities in gas turbine combustors is provided by O'Connor *et al.* [39], which also covers recent works on HF non-compact thermoacoustics. While flow and flame interactions with transverse acoustic modes have been researched experimentally in the context of annular combustor geometries [53–56] (these studies can be allocated to the LF instability regime), experimental investigations of HF and non-compact thermoacoustic instabilities are rare. The first experimental test facility in the context of industrial gas turbine combustors was a lean-premixed swirl stabilized combustor in a can-type chamber, which exhibits a self-excited HF screech instability of the first transverse acoustic mode in the 3 kilohertz regime (this experiment is also used for investigations presented in this thesis). Schwing *et al.* [57–60] reported on the phenomenological observations and physical understanding of the occurring HF thermoacoustic feedback mechanisms. Periodic vortex shedding at the mean flow separation point with the unstable frequency was initially expected to cause the positive thermoacoustic feedback [57]. However, further detailed investigations unveiled that this shedding-effect attenuates with changing operation conditions while the pulsation magnitude was increased. Thus, it was concluded that vortex induced heat release perturbations cannot be considered as a driving mechanism in the concerned system [58]. This is supported by the findings in [61], which show that the shear layer in the wake of the face-plate of this combustor reveals no significant reaction due to local quenching phenomena. In the further course of the investigations, flame displacement induced by the acoustic velocity was found to constitute the root cause for high-

frequency flame modulations [58, 60]. Specifically, the flame moves with the acoustic oscillation towards the high-pressure region of the transverse mode and thereby modulates the combustion heat release off its mean quantity in a non-compact fashion. Based on these findings, Schwing *et al.* [58] proposed a mathematical model for the displacement flame driving for a simplified dirac shaped heat release zone [58].

Utilizing the same experimental setup, Hertweck *et al.* [62, 63] extended the phenomenological investigation of the self-excited HF instability focussing on the effect of different operation conditions and geometrical burner configurations on the instability intensity. Specifically, a relation of heat release distribution with flame driving was studied via a quantitative evaluation of the Rayleigh integral in a respective analysis framework. A further focus of this work was the assessment and comparison of different feedback model propositions describing the non-compact flame driving by displacement and deformation (details on a flame deformation driving are introduced below).

Besides this atmospherically operated swirl-combustor experiment, Buschhagen *et al.* [64, 65] recently reported a premixed single burner jet flame of a generic gas turbine combustor operated at elevated pressure, which drives a weak thermoacoustic instability in the 5 kilohertz regime. Similar to this work, vortex shedding processes and local heat release oscillations counter-phased to the burner's central axis are observed. However, further physical implications on the HF thermoacoustic feedback are missing in the presented research and left open for future work.

Parallel to the works by Schwing *et al.* and Hertweck *et al.*, Zellhuber *et al.* [66–69] investigated HF thermoacoustic phenomena of a generic reheat combustor by means of computational LES[4] studies with focus on the first and second transverse acoustic mode. Extending the combustion regime towards partly auto-igniting reheat flames adds the pressure sensitivity of chemical formation rates as a physical effect that can couple with the acoustic field. On a theoretical basis, different source term expressions were proposed for flame driving by displacement, deformation, and pressure sensitivity. LES studies revealed, as a further consequence of the known flame displacement effect and the given combus-

[4] Large Eddy Simulations

tor boundaries, that the flame experiences a deformation by compression. This means that the heat release increases in the region of increased local fluid density. Consequently, a flame expansion is observed at the opposite low-acoustic pressure region. This heat release oscillation by flame deformation adds a second HF non-compact modulation effect. Further to this, a pressure dependence of the auto-igniting flame is proposed with a respective source term expression. However, neither the deformation nor the auto-ignition HF and non-compact driving mechanism was demonstrated on the basis of experimental observations.

Besides of the work by Zellhuber *et al.* [66–69], further investigations on HF dynamics of reheat flames are rare even though the underlying physical processes characterizing the flame response mechanisms within this frequency regime are not yet comprehensively understood. Especially, to the author's knowledge, no experimental research facility of HF thermoacoustic in reheat flames exists, which could provide a profound insight into the HF reheat flame dynamics to extend their comprehension and to ultimately confirm/adjust hypothesized physical mechanisms and proposed feedback models. In contrast to that, a considerable research effort on investigations of LF reheat flame dynamics has been reported, both, on an experimental and on a theoretical basis. Based on numerical simulations of the reheat flame dynamics, the LF flame response was extracted and analyzed by means of a flame transfer function approach by various authors [70–72]. All studies reveal a significant gain of the flame transfer function for pressure and temperature fluctuations, which are strong indicators of a fundamental influence of auto-ignition on the flame driving. In comparison to this, velocity and equivalence ratio perturbations are rendered less significant for the reheat flame dynamics [70]. Parallel to the present work, a sequential combustor experiment with two burners in series have been commissioned in the research group of Noiray [73–75], tailored towards the study of LF combustion dynamics and synchronization phenomena of the two combustors.

Beyond the field of power generating gas turbine combustors, extensive research reports exist on HF thermoacoustic instability occurrence in rocket combustors [21] and afterburners for power augmentation [76–79]. These works are interesting in terms of developed physical understanding and established analysis methods, which are partly appli-

cable also to gas turbine combustor thermoacoustics. A comprehensive report including fundamental understanding towards physical details of unsteady combustor physics in respective propulsion systems is provided by Culick [21].

## 1.3 Research Objectives and Thesis Structure

The scope of this thesis is to experimentally unveil the physical mechanisms behind the thermoacoustic feedback of HF, transverse, and non-compact thermoacoustic instabilities in combustors associated with sequential gas turbine systems. These systems consist of a conventional first stage with aerodynamically stabilized flames followed by a partly auto-ignition stabilized flame in the second reheat stage. The scope of this thesis unfolds into the following main research objectives:

1. Extension of the experimental infrastructure with the development of a sequential reheat combustor experiment featuring a partly auto-ignition stabilized flame that develops an HF thermoacoustic instability.

2. Comprehension of the HF acoustic response characteristics of the swirl and reheat combustors.

3. Visualization of the flame feedback phenomena with HF transverse acoustic modes within swirl and reheat combustors from experimental data as well as interpretation of the underlying physical mechanisms.

The first objective to develop a sequential reheat combustor for the investigation of HF transverse thermoacoustic instabilities in such systems is motivated by two reasons: (i) The increasing technical relevance of fuel and air staging concepts in gas turbine engines for performance enhancement (cf. Sec. 1.1). (ii) A lack of understanding of HF phenomena that hamper a smooth engine operation in general, and of the effect of the pressure and temperature sensitive auto-ignition induced combustion on the HF flame response in particular (cf. Sec. 1.2). The specific requirements of a lab-scale combustor environment that houses a partly auto-ignition sta-

bilized reheat flame and allows to excite an HF thermoacoustic instability are specified in Chapter 2. This chapter also describes the commissioned reheat combustor experiment and provides details on hardware components.

Provision of experimental data and insight from the combustors to unveil the HF thermoacoustic feedback requires respective diagnostics and analysis methods. The employed diagnostic techniques to spatio-temporally capture acoustic and heat release quantities is discussed in Chapter 2. Visualization and interpretation of physical mechanisms behind the HF thermoacosutic feedback loop generally relies on relating synchronously sampled data of the unsteady heat release and acoustic oscillations. From these data, system dynamics are identified and oscillating heat release distributions reconstructed. The corresponding post-processing methods applied are discussed in Chapter 3.

For the second objective of this thesis, i.e. to comprehend the acoustic response characteristics of both combustors, dynamic pressure time series of representative operation conditions are analysed in Chapter 4. By means of statistical approaches, different thermoacoustic stability states are characterized first. Specifically, the system behavior at stable, marginally unstable and limit-cycle conditions is concerned. The second part of the system response investigation is the discussion of (i) the acoustic behavior and (ii) the operation parameter dependence of the self-excited HF pulsations with respect to both combustors.

Chapters 5 and 6 comprise the investigation of the non-compact swirl and reheat flame response in order to fulfill the third objective. Specifically, Chapter 5 concerns the visualization and discussion of underlying physical mechanisms of generally observable flame response phenomena to an HF transverse acoustic mode in both flame types. In the following Chapter 6, the comprehension of the swirl flame response mechanisms is extended by the assessment of the effect of pulsation amplitude and macroscopic flame structure. These experimental investigations aim at providing physical insight into the non-compact swirl and reheat flame response mechanisms for the validation of corresponding theoretical models. The thesis closes with concluding remarks as well as recommendations for future work in Chapter 7.

It is worthwhile to point out that this thesis is part of a collaborative research initiative on HF transverse thermoacoustic phenomena in heavy duty gas turbine combustors. The present work focusses on the experimental investigation of these non-compact flame acoustics interferences alongside with the development of diagnostic and post-processing strategies. In parallel works e.g. [38, 42, 80], HF thermoacoustic instabilities are assessed and analysed from a theoretical, analytical and numerical viewpoint.

# 2 Experimental Setup

Non-compact thermoacoustic feedback mechanisms (cf. Ch. 1) in sequential gas turbine combustors are studied for two different flame types: (i) a swirl-stabilized and (ii) a partly auto-ignition stabilized reheat flame. These studies are conducted with two experimental setups, which are specifically designed for investigating the HF flame dynamics of the respective flame types. This chapter provides details of both experiments. The swirl combustor was readily available for this work. On the one hand, this combustor served for investigations on the thermoacoustic feedback, and on the other hand, to derive design rules for a new setup that hosts the reheat flame. This latter reheat combustor has been specifically conceptualized, designed, commissioned, and utilized for investigations during the course of this work. The following Section 2.1 provides a brief description of the swirl combustor setup. The reheat combustor concept and realized setup are described in Sections 2.2 and 2.3, respectively. Section 2.4 closes the chapter with a discussion of the diagnostics used to capture the non-compact flame and acoustic responses within these combustors.

## 2.1 Swirl Combustor Setup

Investigations of first-stage HF flame dynamics are conducted with the A$^2$EV[1] lean-premixed and swirl-stabilizing gas turbine combustor experiment, a schematic of which is provided in Figure 2.1. This system resembles a modular, lab-scale burner which principal design is based on the industrial AEV[2] burner architecture [14, 25, 81–83]. The burner was developed and first described in the works by Mayer and Sangl [84–87]. Due to its unique occurrence of a self-excited transverse instability at $f_{T1} \approx 3000\,\mathrm{Hz}$, it later served for investigations of the high-frequency

[1] Advanced$^2$ EnVironmental Combustor (A$^2$EV)
[2] Advanced EnVironmental Combustor (AEV)

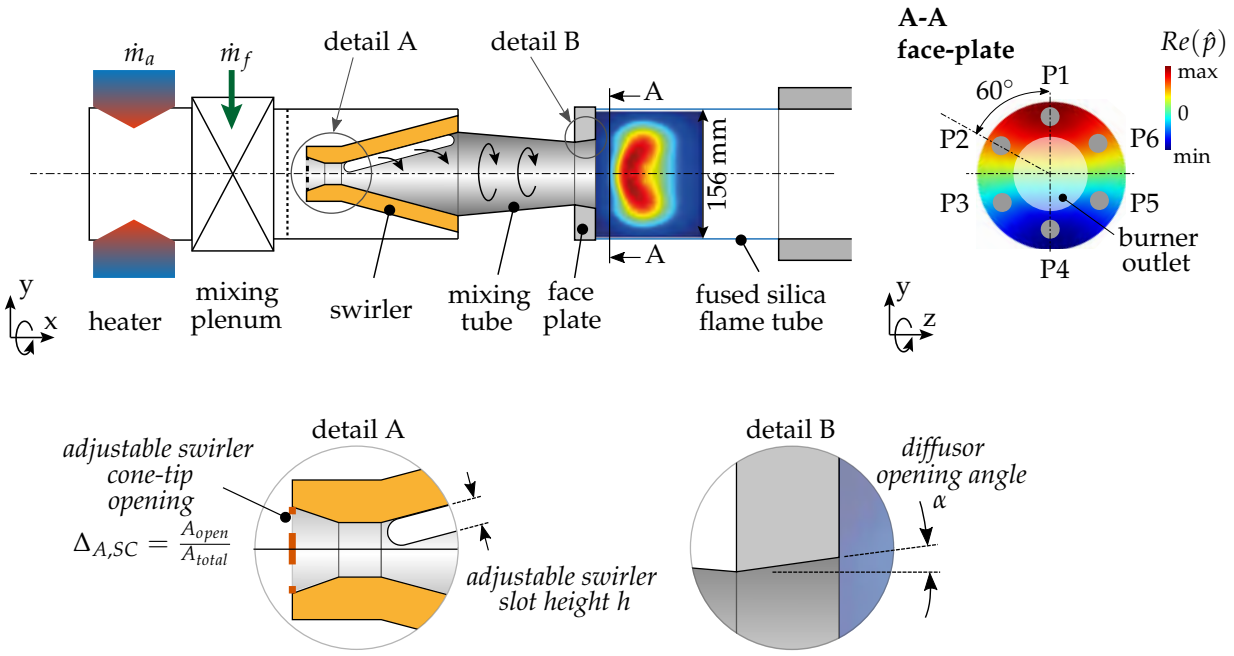


**Figure 2.1:** Sketch of the A$^2$EV swirl-stabilized gas turbine burner experiment with sectional view of the face-plate featuring the instrumentation ports P1-6; contrast level in face plate detail indicates instantaneous pressure for acoustic T1 mode distribution. Details A and B show swirler and diffusor specific geometrical parameters.

thermoacoustic feedback by Schwing *et al.* [57–60, 69] and Hertweck *et al.* [62, 63].

The system is operated at ambient pressure. In main flow direction, the air mass flow $\dot{m}_a$ is first preheated to $T_{pre} = 393 - 693\,\mathrm{K}$ and then mixed with natural gas fuel mass flow $\dot{m}_f$ in a static mixer. For the studies presented in this work, only perfect fuel-air mixtures are applied, while the setup is principally capable to also be operated in technically premixed mode [59]. The air-fuel mixture with a specified air-fuel equivalence ratio $\lambda$ is then guided into the plenum in which the cone shaped swirler is mounted. The swirling flow is induced by four tangential slots, which produce a tangential flow momentum [85, 87]. Swirl intensity is adjusted via variable slot heights of $h = 9 - 14\,\mathrm{mm}$ (cf. detail A in Fig. 2.1). Decreasing $h$ leads to an increasing tangential flow momentum, i.e. swirl intensity. An opening at the swirler cone tip (cf. detail A in Fig. 2.1) allows for slight modification of the axial flow momentum in the core flow [87, 88]. Adjusting the pressure loss of this opening via an orifice plate with a blocking

ratio of either $\Delta_{A,SC} = 0, 0.37, 0.49$, or 0.7 allows to impact the axial position of the stabilizing flame root. A high blocking ratio, i.e. high pressure loss, translates into a decreased axial flow momentum at the burner central axis. Downstream of the swirler, the air-fuel mixture passes the mixing tube and a diffusor whereafter it expands into a quartz glass flame tube with a radius of $r = 0.078\,\mathrm{m}$ and a length of $l_C = 0.2\,\mathrm{m}$. The swirling flow and the sudden area expansion at the face-plate result in strong inner and outer flow recirculation zones that stabilize the flame at the diffusor shaped burner outlet. For the experiments in this work, the diffusor has a fixed opening angle of $\alpha = 10^\circ$ (cf. detail B in Fig. 2.1). The face-plate is water cooled and houses six azimuthally distributed instrumentation ports for damping/driving and measurement equipment. Further details on diagnostics are provided in the diagnostics Section 2.4. The exhaust gases are released to the environment via a duct of the same radius as the flame tube and an approximate length of $l_E = 2\,\mathrm{m}$. Table 2.1 summarizes the swirl-combustor operation parameters that are varied to conduct the presented experiments.

**Table 2.1:** Summary of the geometrical and flow parameters varied to obtain different operational conditions of the A$^2$EV combustor for investigation of the non-compact flame response to high-frequency pressure pulsations.

| parameter | abbrevation | range | unit |
|---|---|---|---|
| **geometrical burner modification** | | | |
| swirler cone tip area blockage | $\Delta_{A,SC}$ | 0, 0.37, 0.49, 0.7 | $[-]$ |
| swirler slot height | $h$ | 9,11,14 | [mm] |
| **flow parameters** | | | |
| air mass flow rate | $\dot{m}_a$ | 0.1, 0.12 | [kg/s] |
| air-fuel equivalence ratio | $\lambda$ | 1 - 2.2 | $[-]$ |
| air preheat temperature | $T_{pre}$ | 200 | [K] |

### 2.1.1 Swirl Combustor Velocity Flow Field

An example steady state isothermal velocity flow field of the A$^2$EV combustor experiment retrieved from numerical CFD[3] simulations (details outlined in [89]) is shown in Figure 2.2. The velocity flow fields visualize the swirling flow (cf. Fig. 2.2 view A-A), as well as the inner (IRZ) and outer (ORZ) recirculation zones in the flame tube after the sudden area expansion. As a result of these, both, shear layers from the flow recirculation and a flow stagnation at the burner centerline occur. These are important features for aerodynamic flame stabilization. The flame root stabilizes in the vicinity of the stagnation point and propagates in the turbulent inner shear layer along the local direction of flow. As a result, the flame heat release is mainly distributed along this inner shear layer trajectory (further details in [28]). The outer shear layer principally behaves in a similar fashion in terms of the fluid dynamic and combustion processes. However, the A$^2$EV lab-scale burner features high stretch ratios and heat losses at the recirculating flow to the combustor wall, which lead to local quenching of the reaction as demonstrated in [61]. This is why the outer shear layer of this swirl flame only shows marginal or even no reaction in the close vicinity of the face-plate.

As the A$^2$EV combustor flow features with flow recirculation and stagnation point determine (among other factors) the flame's heat release

[3]Computational Fluid Dynamics (CFD)

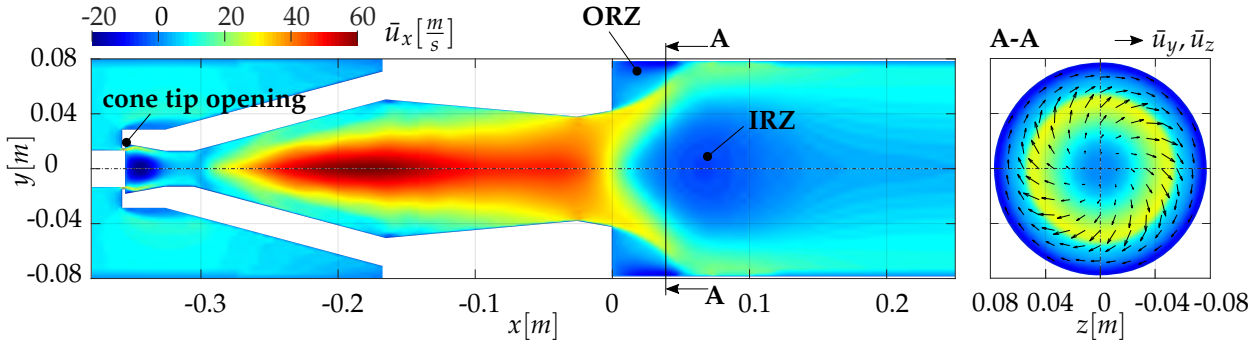


**Figure 2.2:** Mean axial flow velocity $\bar{u}_u$ field retrieved from CFD simulations of the A$^2$EV lab-scale combustor geometry and sectional view A-A with mean axial flow velocity $\bar{u}_u$ superposed with vector field of the velocity components in y- and z-direction $\bar{u}_y$ and $\bar{u}_z$, respectively, indicating swirling flow.

zone, these can be used to alter the flame shape. Thereby, the (i) tangential and (ii) axial flow momentum produced by the swirler can be adjusted to vary the position of the flame root and the spatial compactness of the flame brush. These modifications can be implemented independent of the thermal power governed by the air and fuel control parameters. Thus, these allow to study the effect of the flow velocity field/flame shape onto the burner's propensity to develop a high-frequency thermoacoustic instability. Details and results of this study are discussed in Section 6.2.

## 2.2 Reheat Combustor Concept

The second overall aim of this thesis is the validation and extension of non-compact thermoacoustic feedback mechanisms observed in the $A^2EV$ swirl flame towards reheat flames, as found in sequential gas turbine combustors employing axial fuel and air staging (cf. Fig. 1.1). A part of the research objective of this thesis was the design of an experimental framework to study the reheat flame and system dynamics, the concept of which is outlined in this section. Especially for the high-frequency regime in gas turbine combustors no experimental investigations exist, which could provide deeper insight into the flame acoustics coupling. In order to study these, an entirely new experimental setup is required that combines both, typical reheat flame characteristics on a laboratory scale and the ability to excite HF transverse acoustic modes to which combustion is exposed. The design of this experimental concept requires to consider the following general specifications:

**Establishment of a second-stage reheat flame on laboratory scale:** This requires a high temperature gas stream ($T \sim 1200 - 1700\,\mathrm{K}$) with an oxygen concentration in the range of $\gamma_{O_2} \sim 10 - 16\,\mathrm{Vol\,\%}$. Furthermore, both, the temperature and oxygen profile need to be homogeneous due to their sensitive impact on auto-ignition in the reheat flame. Such conditions are obtained by sequentially arranging a lean first combustion stage and air dilution preceding the reheat combustor. In addition to this, fuel and air premixing of the second combustion stage needs to be accomplished within the short auto-ignition delay, whilst again reaching sufficient levels of mixture homogeneity.

**Investigation of the transverse thermoacoustic feedback:** The combustor ideally needs to provide a mono-frequent flame and system response at the targeted frequency (i.e. first or second transverse mode) with sufficient pulsation amplitude either self-sustained or by forced excitation. Thus, appropriate acoustic boundary and geometrical conditions of the setup need to be fulfilled alongside with maximizing flame driving and minimizing the occurrence of acoustic damping. This requirement constitutes to be the most challenging, as knowledge and information on mechanisms leading to the development of spontaneous transverse-mode HF instabilities in gas-turbines combustors are scarce. To the author's knowledge, the lean-premixed $A^2EV$ combustor is the only experimental setup that has shown self-sustained transverse HF instabilities at atmospheric pressure so far.

**Applicability of high fidelity diagnostics to capture the spatio-temporal flame dynamics and resolve the acoustic mode:** This is required to decompose the non-compact, i.e. locally occurring, flame response to the pressure/velocity oscillations. Particularly challenging for provision of optical accessibility to the flame and measurement of the dynamic pressure in close vicinity to the flame are the extensive thermal power and associated flame temperatures up to $T_{ad} \sim 2200\,\mathrm{K}$. Moreover, the reheat flame stabilizes by both, auto-ignition in the core flow and flame propagation towards the corner recirculation zones. More details on reheat flame characteristics are provided in Section 2.2.1. The realization of both flame stabilization mechanisms on a laboratory scale is advantageous for the transferability of the results to an industrial application. Furthermore, these different zones are expected to exhibit different thermoacoustic response mechanisms. Hence, a decomposition of these different flame zones with available diagnostics is beneficial for analyses of the thermoacoustic feedback.

Thermoacoustic instabilities are commonly researched in lab-scale gas turbine combustors, which are operated at atmospheric pressure but represent the relevant flow parameters as found in the industrial high-pressure counterpart. An atmospheric test environment allows for the necessary geometrical modularity and access for diagnostic equipment in a cost-efficient framework. Besides a testing facility for industrial research on reheat combustion systems for two-stage heavy duty gas tur-

bines [24], academic studies of thermoacoustic experiments with two burners in series exhibiting different combustion regimes are rare and only recent activities focus on these. One other sequential combustor was implemented at ETH Zurich[4] parallel to the development of the herein presented work, although this burner serves for investigations of LF flame dynamics as well as interaction of the two sequentially arranged combustors [73–75, 90]. In contrast, the setup presented in this thesis focusses on HF, transverse dynamics of reheat flames. In order to achieve the overall aim of visualizing such dynamics, a laboratory combustor concept and design is derived building upon (i) lessons learned from the comprehension of non-compact thermoacoustic feedback mechanisms in the A$^2$EV swirl flame and (ii) typical features of rocket combustor experiments focussing on HF combustion instabilities. Existing studies, in which HF instabilities at laboratory-scale are reported, were reviewed for design strategies (e.g. [21, 91–95]).

As this reheat combustor setup was developed in the course of this work, a more detailed description of the design concept is provided. This description comprises a brief discussion of the reheat combustor design considerations in the light of the previously established performance requirements. Specifically, the combustion and acoustic characteristics are presented in (Sec. 2.2.1 and 2.2.2), respectively. Aspects of pressure scaling are given in Section 2.2.3.

Parts of these discussions have been previously published by the author in [80, 96].

### 2.2.1 Combustion Regime

The investigation of the non-compact flame acoustics interactions within the A$^2$EV swirl-combustor (cf. Sec. 5) reveal a dominance of flame response in-phase with the local acoustic pressure. Resulting linear driving rates show a high dependency on the spatial distribution of both the heat release and acoustic mode in the combustion chamber. The reheat flame is expected to couple with the acoustic oscillations in the same way as the swirl stabilizing flame (cf. Fig. 2.4 in Section 2.2.2). This equality is

[4] Eidgenössische Technische Hochschule Zürich, Switzerland

motivated by the observation that the modulation of the local heat release rate depends on combustion parameters such as macroscopic flame structure and power density. In addition, further thermoacoustic sources due to modulation of the auto-ignition delay $\tau_{ign}$ [68,70] as well as convective mechanisms in the reactive shear layer [20,21,76,79] are expected.

From the GT24/26 and GT36 industrial gas turbine reference cases (cf. Ch. 1), it is known that reheat flames are predominantly stabilized by (1) auto-ignition in the core flow as well as (2) propagation in the recirculation zones as schematically shown in Figure 2.3 [11, 15, 30, 72, 90, 97]. These reheat flame characteristics need to be reproduced realistically in the design of the experiment. However, in order to decompose the unknown auto-ignition effect from the total heat release modulation, separated combustion zones are sought to be created in which flame stabilization is dominated by propagation (horizontal zones in Fig. 2.3 (a)) and auto-ignition (vertical zone in Fig. 2.3 (a)). For implementation of this feature, a quasi two-dimensional, flat/rectangular combustion chamber (cf. Fig. 2.3 (b)) is chosen to deliberately induce flow recirculation only in the upper and lower chamber and to yield a homogeneous core flow in which auto-ignition dominates combustion.

Besides obtaining realistic reheat flame features, the ultimate goal is to trigger the occurrence of a high-frequency thermoacoustic instability of a transverse mode. In addition to the impact of heat release and mode distribution relative to each other for high flame driving capability, the

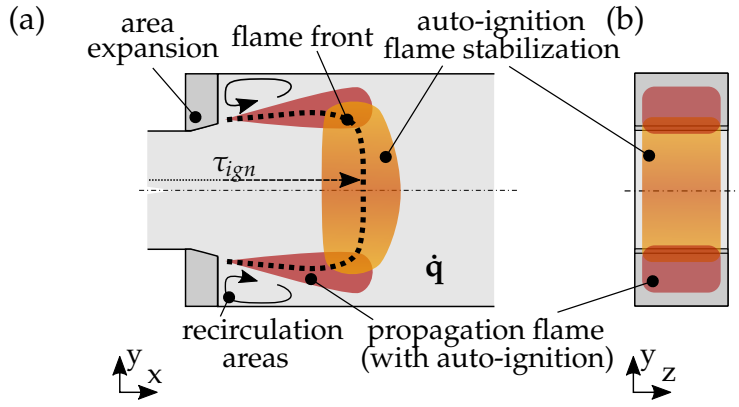


**Figure 2.3:** Schematic of the desired combustion characteristics of the reheat combustor experiment, (a) lateral view, (b) cross-sectional view.

propensity of the combustor to develop such instabilities is associated with high power densities. Comparable lab-scale experiments of gas turbine and rocket combustors that feature HF oscillations have a thermal power density $PD \approx 12 - 20\,\mathrm{MW/m^2/(bar)}$ with respect to the combustion chamber cross section [57, 91–93]. Such high power densities are especially important in atmospheric experiments and in the HF instability regime as damping is enhanced under these conditions. These pressure and frequency effects on the acoustic damping are mainly due to dispersion effects and elevating viscous damping [42]. Hence, it is concluded that comparable thermal power densities need to be realized to intensify local flame modulation, and thereby increase the chance of obtaining a thermoacoustically unstable configuration.

### 2.2.2 Acoustic Characteristics

Published results on research of combustion instabilities in cryogenic rocket combustors (e.g. [91, 93, 94]) indicate that a flat and rectangular combustor geometry favours the occurrence of transverse acoustic pulsations. In combination with the desired spatially separated stabilization regimes of the reheat flame, such a combustor geometry also features beneficial acoustical characteristics, specified as follows:

**Excitation of a single transverse mode** is promoted with the quasi two dimensional, flat, and rectangular combustion chamber setup. In this setting, the term ”single” describes the interest in mono frequent transverse acoustic oscillations as schematically shown in Figure 2.4.

**Interference/overlap with further transversal acoustic modes** at the same frequency but different orientation, e.g. given by degenerate transversal mode pairs in cylindrical combustor geometries [98, 99], is excluded. The same argument applies for purely rotating modes, which are also suppressed by a rectangular combustor cross-section. This requirement would allow for an unambiguous investigation of the specific flame response mechanisms to an acoustic pulsation. In addition to this, the height of the combustor needs to be deliberately chosen to constitute a low cut-on frequency and thereby lower the acoustic damping on associated first or second transverse modes. Note that flame responses associ-

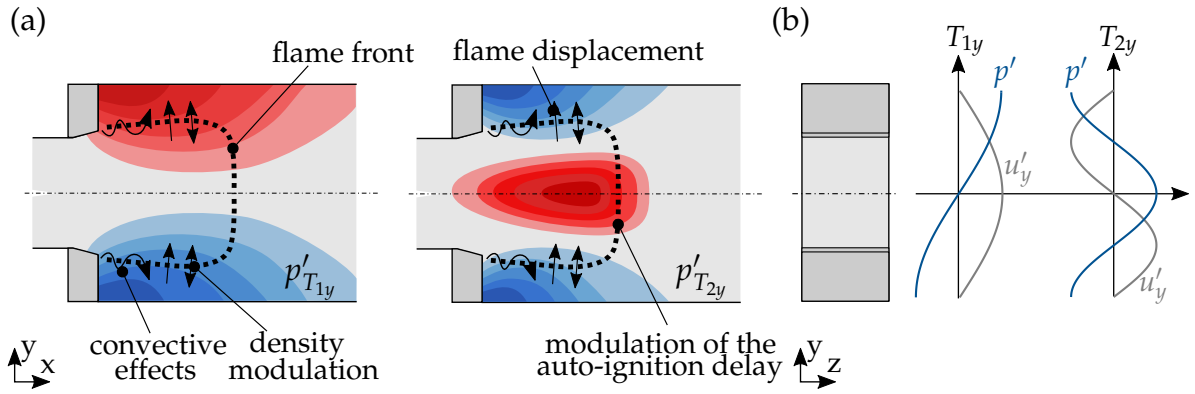


**Figure 2.4:** Schematic of the desired acoustic characteristics of the reheat combustor experiment for the $T_{1y}$ and $T_{2y}$ acoustic modes with expected flame response mechanisms, (a) lateral view, (b) cross-sectional view.

ated to both, the first and second transverse modes are of interest. This is due to the characteristic distribution of the reheat flame (cf. Fig. 2.3) with respect to the nodal lines of the transverse acoustic fields (cf. Fig. 2.4). The high acoustic pressure of the first transverse mode spatially interferes with the outer flame propagation zones. In contrast, the anti-node of the second transverse mode overlaps with the flame's auto-ignition zone, which is why a modulation of the auto-ignition delay is expected to predominate for this mode type. This is because the spatial interference (cf. Fig. 2.4) of heat-release and acoustic pressure is crucial to obtain thermoacoustic driving according to the Rayleigh integral (cf. Eq. 1.1).

**Strong damping of longitudinal modes** is required to avoid any domination of the combustion dynamics by these modes, which would suppress the transverse, HF pulsations. In order to achieve this, the flat setup needs to be supplemented by measures that lead to an increased damping of longitudinal acoustics, which do not affect the transverse acoustic modes. Namely, boundary conditions with high pressure losses at the combustor inlet acoustically decouple the system from the upstream periphery. In downstream direction, a nozzle termination is placed to convectively damp longitudinal oscillations [100, 101]. Note that the transverse mode will be unaffected by the nozzle termination. This is due to an attenuation of the acoustic mode in downstream direction as temperature, and thereby sonic velocity, increase related to combustion [63].

### 2.2.3 Pressure Scaling

In addition to obtaining realistic reheat flame features and triggering a thermoacoustic instability of the first transverse mode, effects of mean pressure scaling on the thermoacoustic feedback require careful consideration. The experiment is operated at atmospheric conditions to allow for a modular geometrical design and simple access to the combustion region for measurement equipment without complex high-pressure engineering. However, a necessary criterion for the experimental concept is the ability to transfer observations from the low-pressure laboratory reheat combustor to derive models that are applicable in the high-pressure regime as present in industrial gas turbines [20, 22, 102]. Ideally, flow velocities, combustor inlet temperatures, and adiabatic flame temperatures can be adapted from high-pressure to atmospheric conditions according to pressure scaling laws [12, 103, 104]. Hence, the Mach number ratio of the incoming hot gas flow to the product gases of the combustion are conserved [12]. If flame and damping properties are then equal for the experiment and the industrial application, thermoacoustic transfer functions and resulting pressure pulsations would scale with the mean pressure via $p'/\bar{p}$ [102, 104].

Investigating the thermoacoustic modulation mechanisms of reheat flames adds the challenge of auto-ignition presence with its pressure dependency of the auto-ignition delay $\tau_{ign}$ [24, 31]. Hence, at inlet temperatures equal to a industrial high-pressure case, the balance between auto-ignition and flame propagation as well as the flame brush thickness would not be conserved, which was comprehensively investigated in [24, 31]. Countermeasures to obtain realistic reheat flame features on laboratory scale are (i) increasing the reheat inlet temperature with increased flow velocity, and (ii) application of fuel compositions with decreased auto-ignition delay compared to natural gas (e.g. increase propane or hydrogen concentrations) [24]. In contrast, elevating the inlet temperature for an increased auto-ignition tendency leads to a changing Mach number of the incoming hot gas and to changing flame temperatures. For the design of thermoacoustic research environments, the Mach numbers are taken into account in order to obtain similar acoustic mode shapes and convective time scales as in the industrial reference system. Research on

transverse instabilities in swirl flames showed that the mode is mainly affected by the flame temperature, which enforces a downstream mode decay and thereby impacts the acoustic power density [63, 105]. Pressure effects on damping mechanisms have negligible influence on the thermoacoustic feedback mechanisms themselves, but might hinder the development of a self-sustained instability. The dominant mechanism for acoustic energy dissipation is vortex shedding, which is pressure independent. Only viscous damping at the combustor walls might have an effect at low pressure and high frequencies due to increased viscosity [42]. To account for the latter loss mechanism, significant levels of thermal power density are realized in the experiment to overbalance damping by flame driving.

Hence, with the given constraints on pressure scaling and possible countermeasures, it can be concluded that the representation of specific combustion regimes is limited for an atmospheric experiment but does not hinder an effective identification of thermoacoustic feedback mechanisms for reheat flames that lead to validated models (i.e. for the high and low pressure regime). Details on the final translation of the aforementioned general setup requirements in terms of combustion, acoustic and pressure scaling properties into the test rig are described in the next section.

## 2.3 Reheat Combustor Setup

This section describes the commissioned reheat combustor experiment, which is used for the studies in this thesis. In order to appropriately model and capture reheat flame dynamics on laboratory scale, a multi-stage setup is implemented. This setup consists of a first combustion and air dilution stage, i.e. the vitiator, and is followed by the reheat combustor. A schematic of these test rig elements, including flow paths, is given in Figure 2.5. The flow paths provide an overview of all parameters that can be controlled for operation of the experiment. The entire setup is operated at near atmospheric and constant pressure. In the upcoming paragraphs, the design details of the vitiator (cf. Sec. 2.3.1) and reheat setup (cf. Sec. 2.3.2) are described, followed by the discussion of the resulting mean flow field characteristics (cf. Sec. 2.3.3).

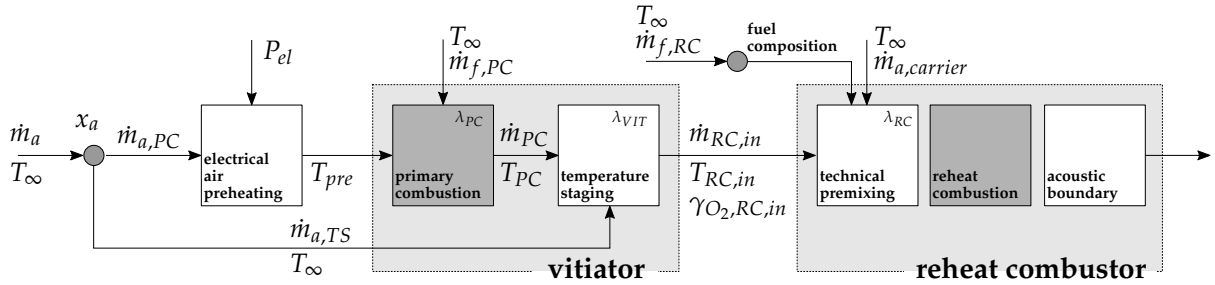


**Figure 2.5:** Schematic of the elements for the vitiator and reheat combustor setup with indication of relevant control parameters.

### 2.3.1 Vitiator Design

The vitiator (cf. Fig. 2.5) is used to provide appropriate reheat inlet conditions at which auto-ignition can occur. These conditions are mainly defined by hot gas temperatures of $T_{RC,in} = 1200 - 1700\,\mathrm{K}$ and necessary air mass flow rates of $\dot{m}_a = 0.35 - 0.65\,\mathrm{kg/s}$. Sufficient air mass flow rates are needed to achieve the required specific thermal power density in the reheat combustor to allow for thermoacoustic investigations. The high reheat combustor inlet temperature levels are reached by a primary combustion (PC) stage, which is operated with a lean fuel-air composition. The hot gas temperature of the primary combustion stage is then further reduced to reheat inlet temperatures by injecting additional cold air into the post flame zone, referred to as temperature staging. The two different air mass flow rates for combustion $\dot{m}_{a,PC}$ and dilution $\dot{m}_{a,TS}$ are related to each other by the staging ratio

$$x_a = \frac{\dot{m}_{a,PC}}{\dot{m}_{a,PC} + \dot{m}_{a,TS}}, \tag{2.1}$$

which is used as a control variable to specify the operation points of the experiment. The process of primary combustion followed by temperature staging with a given air dilution rate can be represented by an overall air-fuel equivalence ratio of the vitiator

$$\lambda_{VIT} = \frac{\frac{\dot{m}_{a,PC}+\dot{m}_{a,TS}}{M_a}}{\dot{m}_{f,PC} \cdot l_{min}}, \tag{2.2}$$

where $M_a$ is the molar mass for air and $l_{min}$ the minimal air requirement for complete fuel consumption.

Figure 2.6 provides a cross-sectional view of the vitiator that shows the design implementation of this multistage concept. First, air entering the primary combustion stage is electrically preheated to $T_{pre} = 493 - 693\,\mathrm{K}$. This improves the aerodynamic flame stabilization in the primary combustion zone and thereby allows to increase the combustion air-fuel equivalence ratio $\lambda_{PC}$. The primary combustion stage then comprises six lean premixed, swirl, and bluff-body stabilized burners. Incoming preheated air is homogeneously distributed to all six burners in the vitiator plenum. A fuel nozzle is placed at each burner entry to inject natural gas fuel into the air co-flow. A high burner pressure drop of $\approx 20\%$ [103] reduces the thermoacoustic instability propensity in the vitiator.

The operation window of the primary combustion stage is limited by lean flame blow off [103]. Hence, applicable air-fuel equivalence ratios are $\lambda_{PC} \leq 2.3$ which result in adiabatic flame temperatures of approximately 1700 K. Each burner provides a thermal power of $35 - 110\,\mathrm{kW}$. Capability to reduce the post flame temperature is implemented by six air dilution pipes, which inject air at six locations per pipe into the swirling mean flow. The injection locations are axially distributed, which also increases acoustic damping, and thereby reduces the thermoacoustic instability propensity of the vitiator as well as increases temperature homogeneity at the reheat combustor inlet. The hot-gas mixture then passes the

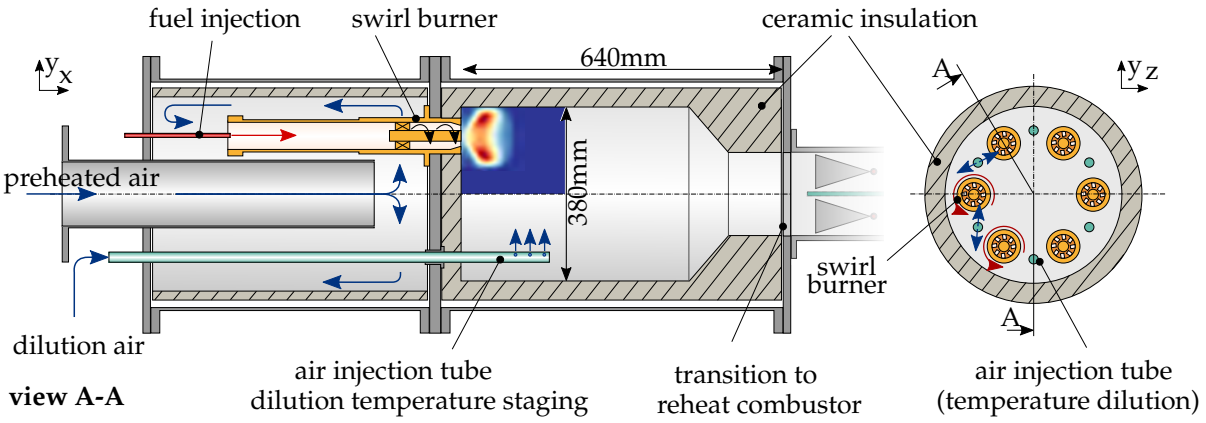


**Figure 2.6:** Vitiator combustor setup with sectional view of swirl burners and air dilution pipes.

remaining combustion chamber, and is guided to the reheat combustor. Overall, vitiator air-fuel equivalence ratios reach $\lambda_{VIT} \leq 3.7$. The entire vitiator is insulated with ceramic layers to the ambience to keep heat losses at a minimum.

### 2.3.2 Reheat Combustor Design

The second-stage combustor is directly attached to the vitiator outlet. In general, the design features a high degree of modularity in terms of (i) changing system in- and outlet conditions, (ii) varying fuel composition, (iii) different mixing section configurations, (iv) changing combustion chamber inlets, as well as (v) a wide range of applicable instrumentation. In addition to this, the overall reheat burner design is geometrically related to the industrial SEV combustor principle of the GT24/26 and GT36 gas turbines [11, 15–18, 106] to ease transferability of observations. Figure 2.7 shows cross-sectional views of the reheat combustor, the specific and modular design features of which are further described as follows.

The reheat burner section consists of two vertically adjacent channels with delta-wing shaped vortex generators (VG) facing each other as

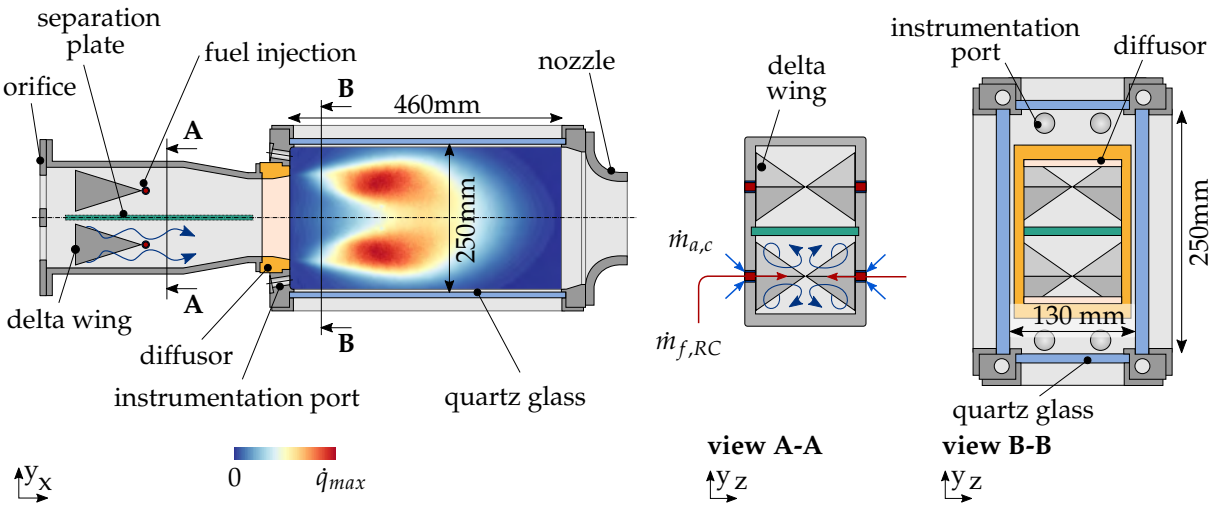


**Figure 2.7:** Reheat combustor setup with magnified sectional views of the vortex generator arrangement (A-A) and combustion chamber (B-B). Colormap indicates example reaction zone.

shown in Figure 2.7. The wall separating the channels is removable and is implemented as one measure to change the upstream acoustic boundary conditions of the combustor. Its purpose is to acoustically decouple the burner and combustion chamber as per increase of the burner channels cut-on frequency[5]. This decoupling seeks to avoid any transverse oscillations in the channels at the frequency of the targeted transverse mode in the chamber, which is of primary interest in this work. A further modifiable upstream boundary condition is the orifice plate at the reheat combustor inlet. This plate increases damping of longitudinal oscillations and homogenizes the incoming vitiator hot gas flow as per local pressure drop.

Each of the VGs in the mixing section generates two counter rotating vortex pairs (cf. Fig. 2.7 view (A-A)), which enhance fuel-oxidizer mixing as well as improves flow recirculation in the combustion chamber after the sudden area expansion [15, 18, 106]. Natural gas fuel is optionally blended with propane by a specified mass ratio $x_{C_3H_8}$ for increased autoignition tendency (cf. Ch. 1). The fuel blend is then injected in a jet in cross flow configuration and with a surrounding air shield via fuel nozzles at the mixing section walls located at the wake of each VG tip (cf. Fig. 2.7 view (A-A)). The air shield functions to adjust the required momentum ratio for optimum fuel-oxidizer mixing irrespective of the hot-gas mass flow. Taking these three streams of exhaust gas, fuel, and air shield into account, results in a representative reheat combustion air-fuel equivalence ratio

$$\lambda_{RC} = \frac{\frac{\dot{m}_{ox}}{\sum_{i=1}^{N} \gamma_{i,ox} \cdot M_i}}{\dot{m}_{f,RC} \cdot ox_{min}}, \tag{2.3}$$

which is used to specify the reheat combustor operation points. In Equation 2.3 the subscript $ox$ denotes the oxidiser, which is composed of the vitiator exhaust and shielding air. Furthermore, $\gamma_{i,ox}$ specifies the individual concentrations of the oxidiser components, $M_i$ the respective molar mass, and $ox_{min}$ the required oxidiser for stoichiometric combustion. An additional functional detail of this VG injector arrangement is given by the possibility to shift the VG tip transversally off the injector centerline. This allows for transverse fuel staging, i.e. to change the vertical equiv-

[5]The burner cut-on frequency doubles with inserted separation wall.

alence ratio profile at the combustion chamber inlet, by either enriching the fuel concentration of the upper or lower vortices as shown in Figure 2.8.

After fuel injection, the mixture passes through a divergent-convergent section before it is released into the combustion chamber (cf. Fig. 2.7). This divergent-convergent section design has the advantage of fostering auto-ignition due to increased local flow velocities, as well as strengthening the corner recirculation zones in the combustion chamber due to the diffusor shaped outlet [15, 66, 90]. Different diffusor types that vary in angle and edge are available to modify the resulting flow field in the combustion chamber. Within this thesis, the diffusor angle $\alpha$ is kept constant, while the diffusor rim is either of rounded or sharp edged geometry as illustrated in Figure 2.9. With this measure, damping and convective driving associated with vortex shedding shall be influenced. A further discussion of the flow design is provided in the following Section 2.3.3.

The expansion ratio between the burner and combustion chamber $A_{chamber}/A_{burner}$ is 2.1, which results from an area expansion mainly in transverse y-direction. The area expansion in transverse z-direction is kept minimal (cf. Fig. 2.7 (c)). As mentioned before, this flat, i.e. quasi two-dimensional, chamber design is chosen to

1. deliberately promote distinct zones of flame stabilization dominated by propagation in the upper and lower corner recirculation zones and auto-ignition in the homogeneous core flow[6],

[6]Flame stabilization at the lateral combustor zones after the minor area expansion in z-direction is assumed to be negligible. This is due to the proximity to the cold walls which causes quenching and prevents combustion to occur.

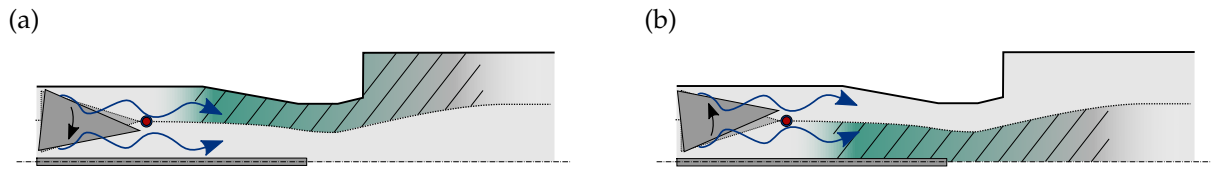


**Figure 2.8:** Transverse fuel staging by (a) shifting the VG tip to the center to increase fuel concentration towards the recirculation zones or (b) shifting the VG tip outwards for increased fuel concentration in the core flow.

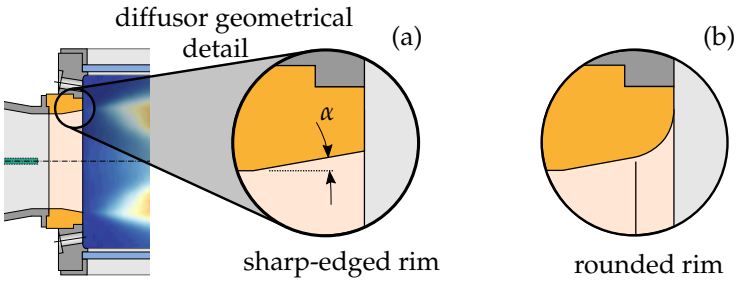


**Figure 2.9:** Detailed view of the diffusor geometry highlighting the different diffusor edge geometries (sharp-edged (a) and rounded rim (b)) as well as the diffusor opening angle $\alpha$.

2. trigger a single transverse acoustic mode in y-direction to which the flame region is exposed (cf. Fig. 2.4),

3. and ultimately excite HF thermoacoustic instabilities of a transverse mode.

Considering the combustion chamber as a rectangular volume with the dimensions $(L, H, W)$ in $(x, y, z)$ direction (cf. Fig. 2.7) and neglecting in- and outlet boundary conditions (diffusor at the sudden area expansion and auxiliary nozzle outlet) leads to the idealized eigenfrequencies [21]

$$f_c(n_x, n_y, n_z) = \frac{c}{2}\left[\left(\frac{n_x}{L_x}\right)^2 + \left(\frac{n_y}{H_y}\right)^2 + \left(\frac{n_z}{W_z}\right)^2\right]^{\frac{1}{2}}, \tag{2.4}$$

where $c = \sqrt{RT\kappa}$ denotes the speed of sound with $R$, $T$, and $\kappa$ being the specific gas constant, temperature, and isentropic exponent, respectively. To retrieve realistic cut-on frequencies of the first and second transverse modes, the temperature $T$ is presumed to be the average of the reheat combustor inlet temperature $T_{RC,in}$ and the adiabatic flame temperature $T_{ad}$.

The combustion chamber height $H_C$ (in transverse y-direction) is set to 0.25 m and thus results in a cut-on frequency in y-direction of

$$f_{c_{1y}} = f_{T_{1y}} = \frac{c}{2H_C} \approx 1600\,\text{Hz}. \tag{2.5}$$

Such relatively low cut-on values should promote thermoacoustic pulsations as acoustic damping effects increase with increasing frequencies [21]. The combustion chamber width (z-direction) $W_C$ of 0.13 m is chosen to avoid the appearance of z-directed transverse modes oscillating in close frequency to the y-directed transverse modes. This accounts for a cut-on frequency in z-direction $f_{c_{1z}} \approx 3000\,\text{Hz}$ being significantly higher than its counterpart in y-direction. In addition to this, $f_{c_{1z}}$ is not an integer factor of $f_{c_{1y}}$ to avoid any overlap with higher harmonics, too. The length of the combustion chamber is selected sufficiently long, such that the transverse modes can naturally attenuate towards the downstream exit. The attenuation of the transverse mode is due to the natural frequency dependence on the local sonic velocity $c(x)$ and thus on the temperature profile $T(x)$, i.e. $c(T(x)) \rightarrow f_c(x)$. Therefore, the transverse acoustic mode does not propagate into the hotter region in axial direction due the increasing temperature caused by the flame heat release [62, 80, 105].

An optional auxiliary nozzle is attached to the combustion chamber to convectively damp longitudinal modes (cf. Fig. 2.7 (a)). Note, that the nozzle remains invisible to transverse oscillations due to the temperature dependent attenuation of the mode in downstream direction, as mentioned above. In order to minimize reflection of LF longitudinal oscillations from the nozzle, its design follows

$$Ma_N \approx \frac{H_C}{H_N} \tag{2.6}$$

with $Ma_N$ and $H_C/H_N$ being the nozzle Mach number and the nozzle area contraction ratio, respectively [100]. A demerit of this feature is that the optimal Mach number to area contraction ratio depends on the operation parameters. This is why a compromise between optimal damping of LF acoustics and operability needs to be accomplished during the experiments, although sufficient damping is expected to occur for all operation points.

Access for pulsation probes, temperature sensors or damping/driving equipment (cf. details in Sec. 2.4) is provided via water cooled instrumentation ports located at the sudden area expansion (face-plate). Optical access to the flow and flame is provided via quartz glass windows to all lateral sides of the combustion chamber. The entire frame is internally water

cooled to optimize thermo-mechanical integrity while keeping heat losses to a minimum and allowing for high local power densities [107]. The side walls of the entire reheat setup are additionally cooled by air impingement if wall temperatures reach critical values. Thermal power densities in the reheat combustor are in the range of $5 - 25\,\mathrm{MW/m^2}$. A comprehensive report from commissioning of the reheat combustor experiment is presented in [96].

Relevant operation parameters utilized to conduct the experiments for this work are summarized in Table 2.2.

**Table 2.2:** Summary of the operation parameters of the sequential reheat combustor setup for investigation of the non-compact rehaeat flame response to HF pressure pulsations.

| parameter | abbrevation | range | unit |
|---|---|---|---|
| **vitiator parameters** | | | |
| primary combustion air mass flow rate | $\dot{m}_{air,PC}$ | 0.3 - 0.48 | [kg/s] |
| air preheat temperature | $T_{pre}$ | 300 | [K] |
| vitiator air-fuel equivalence ratio | $\lambda_{VIT}$ | 1.8 - 2.3 | [−] |
| air-staging ratio | $x_{air}$ | 0.75 - 0.95 | [−] |
| **reheat combustor parameters** | | | |
| reheat combustor air-fuel equivalence ratio | $\lambda_{RC}$ | 1 - 1.8 | [−] |
| propane mass percent blended to natural gas fuel | $x_{C_3H_8}$ | 0 - 0.5 | [kg/s] |

### 2.3.3 Reheat Combustor Flow Field

An essential aspect for the lab-scale reheat combustor design is the mean flow field adjustment so that the above introduced combustion characteristics (cf. Sec. 2.2.1) are achieved as good as possible. Note that the isothermal flow field instead of the reactive counterpart is assessed. This is justified by the assumption that (i) the periphery upstream of the flame

is unaffected by the heat release, (ii) the combustion heat release zone can be deduced from isothermal flow features for the design purposes, and (iii) complexity of computations is greatly reduced. Figure 2.10 provides example mean axial velocity fields $\bar{u}_x$ and fuel-mixture profiles $X_{CH_4}$ for the realized setup. These are retrieved from isothermal CFD simulations employing representative flow conditions at the in- and outlet boundaries of the computation domain. Further details of the CFD setup are outlined in [80].

To illustrate the different reheat combustor flow features, Figure 2.10 (a) and (b) show longitudinal cuts at different axial positions in z-direction. Respective cross sectional views at different axial positions in x-direction are shown in Figure 2.10 (c) and (d). These latter ones are supplemented with the vectorial field of the velocity components in y- and z- direction, $\bar{u}_y$ and $\bar{u}_z$, respectively. In comparison to Section 2.1.1, the results demonstrate the differing flow features between the swirl-stabilized and reheat combustion.

Evaluation of the resulting flow fields in Figure 2.10 shows the following relevant features for design of the reheat combustor:

**Corner recirculation zones (RZ) and vortical flow field from vortex generators** produce beneficial flow features for flame stabilization. These are detectable from the mean axial velocity field $\bar{u}_x$ and the velocity vectors in y- and z-direction $\bar{u}_y$ and $\bar{u}_z$. The corner recirculation zones and resulting shear layers facilitate deflagrative flame stabilization and formation of upper and lower propagation flame zones. Formation of a shear layer and a reattachment point close to the face-plate are promoted by (i) a sufficient area-expansion ratio in y-direction, (ii) a diffusor at the mixing tube outlet, and (iii) the tangential flow momentum from the large-scale vortices (cf. Fig. 2.10 (d)).

**Homogeneous axial velocity in the core flow** occurs towards the center of the combustion chamber. The bulk-like flow pattern minimizes deviances of the local auto-ignition delay $\tau_{ign}$. This is of relevance to promote the occurrence of a distinct auto-ignition flame front at constant axial location over the combustor cross-section.

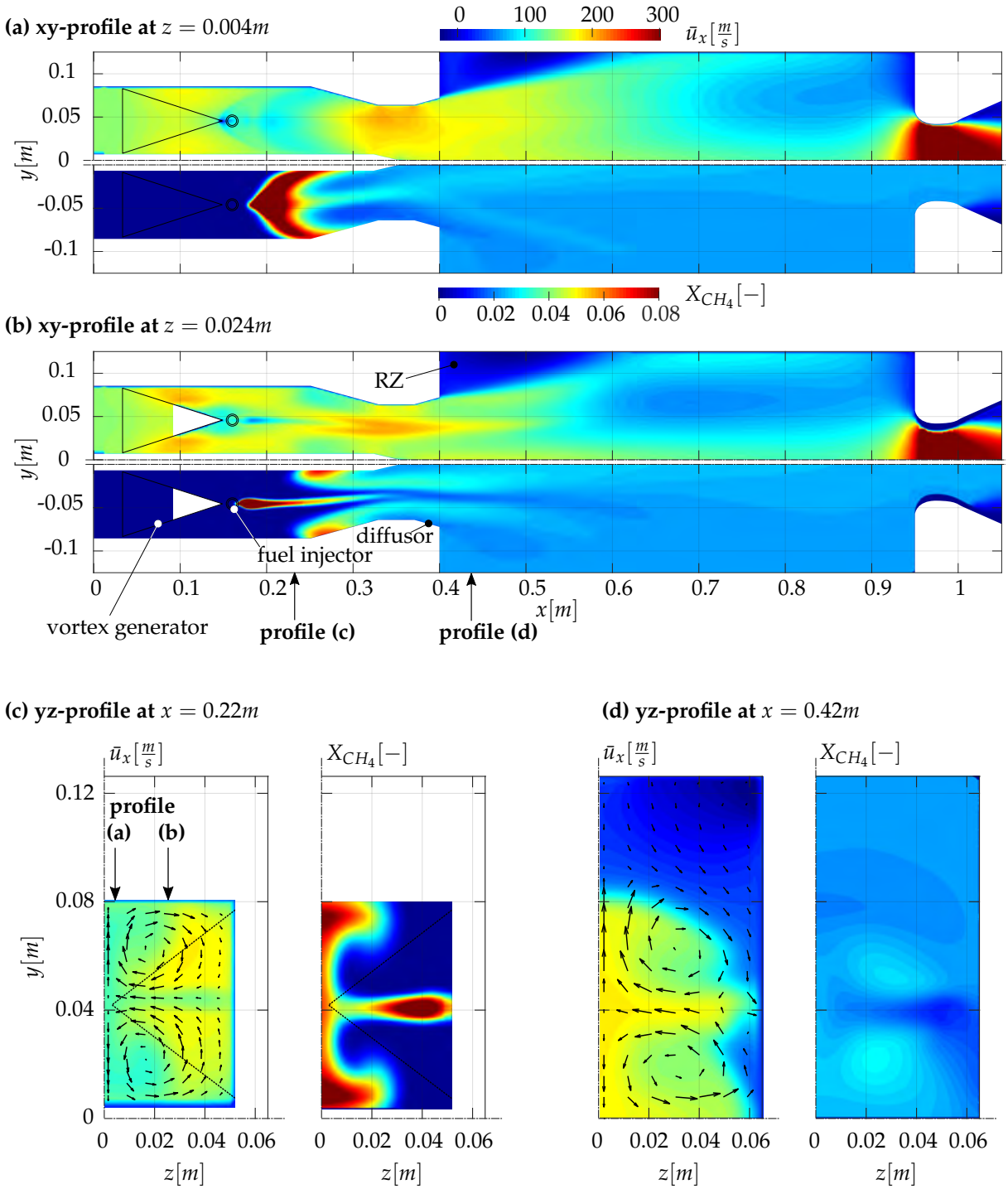


**Figure 2.10:** Cross sectional planes showing the distributions of mean axial velocity $\bar{u}_x$ and fuel mass fraction $X_{CH_4}$ for two xy-planes (a, b) at different z-position, as well as for two yz-planes (c, d) at different x-position (positions are indicated in view (c) and (b), respectively). Vector field in (c, d) show the velocity components in y- and z-direction $\bar{u}_y$ and $\bar{u}_z$, respectively.

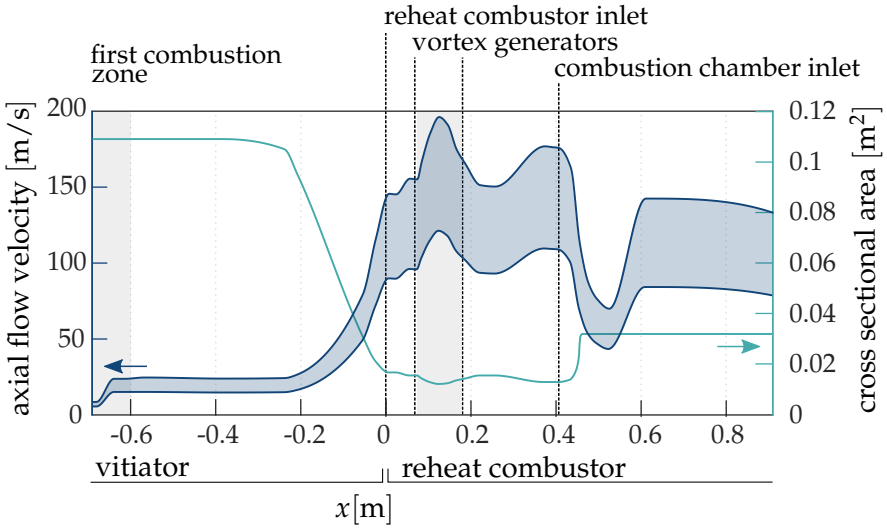


**Figure 2.11:** Flow velocity range for high and low thermal power operation from 1D calculations for the experiment including vitiator and reheat combustor, as well as cross sectional area over the setup length. Lower and upper velocity curve indicate operation at low and high thermal power, i.e. oxidiser mass flow rate, respectively.

**High local flow velocities in the upstream mixing tube** followed by deceleration of the flow after the area expansion in the combustion chamber promote the occurrence and controllability of auto-ignition. A homogeneous flame front in the combustor core flow governed by auto-ignition stabilization is desired. Figure 2.11 additionally shows an approximate range of resulting axial flow velocities over the combustor length for high and low thermal power. The given velocity ranges are estimates from 1D mass-balance calculations and do not consider any turbulence or tangential flow effects. The figure is supplemented with the underlying cross-sectional area along the combustor's x-axis showing the divergent-convergent mixing section. Such high local flow velocities in the mixing tube (cf. Fig. 2.10 (a,b) and Fig. 2.11) are desirable for the following reasons: During operation of the combustor, the axial position of the auto-igniting flame in the combustion chamber is adjusted as a function of the reheat inlet temperature. For thermoacoustic investigations, a compact and steady heat release zone close to the face-plate is desired. Furthermore, the heat release position of the auto-ignition flame front results from $\tau_{ign}$, which is sensitive to temperature, air-fuel equivalence ratio, and pressure. Hence, the reheat inlet temperature cannot be increased

as needed, if a higher auto-ignition tendency is required as this would move the auto-ignition flame either up- or downstream. However, with high flow velocities in the mixing tube, acceptable auto-ignition characteristics at atmospheric conditions can nevertheless be achieved. This is because increasing flow velocities allow to ramp up the combustor inlet temperature while the auto-ignition flame front remains at the desired axial position.

**Homogeneity of the fuel-oxidizer mixture in the combustion chamber** is enhanced via applied vortex generators in the mixing tube. As can be observed from Figure 2.10, the $X_{CH_4}$ concentration deviations are minimal in the combustion chamber (in the presented case $\bar{X}_{CH_4} = 0.022[-]$ with a standard deviation of $\sigma = 0.0023$) and fast mixing is achieved downstream of the fuel injector. Specifically, the vortex generators help to transport the fuel from the centrally located injectors to the side walls and thereby help to provide both, a homogeneous distribution in the core flow and a sufficient fuel concentration towards the outer shear layers. In contrast to the $A^2EV$ swirl system (being perfectly premixed), the reheat combustor experiment is a technically premixed system, which is associated with inhomogeneities in the air-fuel equivalence ratio distribution.

## 2.4 Diagnostics

Diagnostic equipment used to investigate the swirl and reheat combustor thermoacoustics are the same for both, the swirl and reheat combustor setups. To investigate the thermoacoustic feedback, diagnostics for spatio-temporal resolution of the heat release and acoustic quantities are required. In order to obtain experimental data of these quantities, accessibility to the thermoacoustic oscillations within the high temperature environment, as well as proper handling of the diagnostics needs to be considered. The main strategy to analyze the thermoacoustic feedback is to synchronically sample acoustic pressure oscillations and the flame chemiluminescence (indicative for the flame heat release) with high temporal and spatial resolution. These quantities were recorded by dynamic pressure sensors and an intensified high-speed CMOS camera, respectively. Resulting time series are then analysed by post-processing routines which

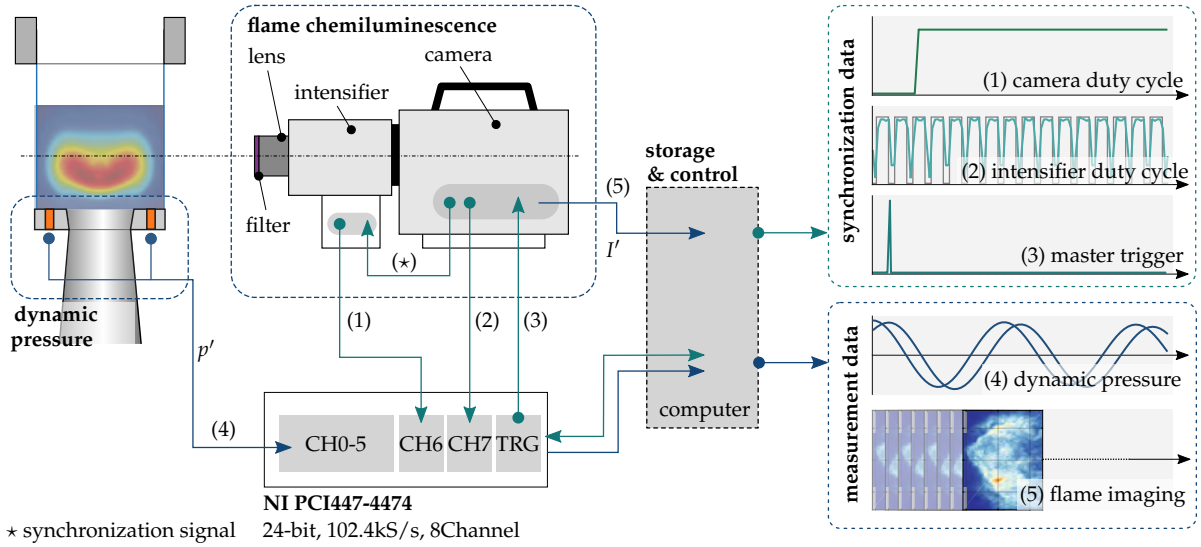


**Figure 2.12:** Schematic of the diagnostic setup to synchronously capture the spatio-temporal flame signal with the acoustic pressure pulsations at the combustor face-plates. Data samples show the duty cycles of the (1) the CMOS high-speed camera and (2) the image intensifier, the (3) master trigger signal, as well as (4) sample pulsation probe data and (5) flame CL images.

are introduced in Chapter 3. These routines allow to decompose the deterministic flame response to acoustic oscillations from other occurring flame and acoustic fluctuations for investigation/interpretation of underlying physical mechanisms. Figure 2.12 schematically shows the arrangement of dynamic pressure sensors and optical measurement equipment with respective data acquisition units. The following Sections 2.4.1 and 2.4.2 provide information on application and handling of the diagnostic equipment.

### 2.4.1 Dynamic Pressure

Recording the dynamic pressure signal of an HF transverse mode requires the placement of sensors at the combustor liner in close vicinity to where these acoustic pulsations occur. The swirl setup houses up to six (cf. Fig. 2.1) and the reheat setup up to four (cf. Fig. 2.7) pulsation probes at the combustor face-plate. These locations are deliberately chosen to resolve the spatial extend of the targeted first or second transverse acoustic mode in y-z-direction. Principally, further pulsation probes distributed along

the longitudinal direction would be required to unambiguously identify the three-dimensional mode structure and dynamics. However, additionally to the conducted experiments, acoustic mode reconstructions by means of FEM methods described in [38,44] helped to surpass the requirement of further pulsation probes. Motivation for this process of assessing the longitudinal dependency by computational means is mainly due to the thermal conditions to which the sensors are exposed. Placing the pressure sensors at the face-plate and in the vicinity of the recirculation zones has the strong advantage that the temperatures there are lower than at downstream liner positions. Dynamic pressure time series can thus be recorded with high sensitivity utilizing standard microphones installed in water-cooled instrumentation ports, as well as water-cooled sensor adaptors. Thermal handling is complicated when placing the sensors at other liner positions as temperatures are significantly higher than in the flow recirculation zones, often exceeding the critical temperature limits to which the sensor can be exposed.

The microphones applied were PCB 106B piezoelectric sensors mounted in PCB 064B06 water-cooled adaptors with a recess cavity working as a heat shield. The recess cavity has a resonant frequency $> 10\,\mathrm{kHz}$ to allow for measurements in the multi kHz regime. An advantage of these pulsation probes over other standard systems is the available IEPE (integrated electronics piezo electric) technology. This means that the piezoelectric high impedance signal is converted within the sensor housing to a low impedance voltage. Thereby, the conditioned signal can be transferred robustly to the recording device (i) without further amplification units and (ii) with minimized occurrence of frequency or phase deviations dependent on the measurement chain. The sensitivity of these types of sensors is in the range of $35 - 45\,\mathrm{mV/kPa}$. All dynamic pressure signals are sampled synchronously with a National Instruments PCI-4472 card. Applied sampling frequencies $f_s$ are $100\,000\,\mathrm{Hz}$.

### 2.4.2 Flame Chemiluminescence

The swirl and reheat flame dynamics, specifically the underlying deterministic oscillations, are analyzed by means of the spatio-temporally re-

solved flame chemiluminescence (CL) signal. Chemiluminescence is the emission of light during the combustion reaction - i.e. light emission from electronically excited radicals during the oxidation. A common method for investigation of hydrocarbon flames is the detection of its intermediate hydroxyl ($OH^\star$) or carbyne ($CH^\star$) radical chemiluminescence signals with an appropriate optical setup [108, 109]. Generally speaking, these radicals appear during the oxidation reaction at the flame front - i.e. in the combustion zone where local heat release is the highest. Due to this, the flame CL signal is often used as an indicator for the spatial occurrence and intensity of the flame's heat release. This is supported by the considerable advantage of a rather simple and non-intrusive optical setup required for measurement of the flame's CL signal compared to complex direct heat release detection methods. Indication of the spatial flame heat release distribution via the CL signal works with good confidence for the swirl burner due to (i) perfectly premixed/homogeneous air-fuel mixture and (ii) occurrence of heat release oscillations close to the inner shear layers, where impact of local strain rate on the $OH^\star$ and $CH^\star$ CL is negligible [109–111]. Further details are outlined in Section 3.2.3.

In contrast to the perfectly premixed $A^2EV$ swirl flame, the reheat flame is run in technically premixed mode. This implicates slight deviations in the local air-fuel equivalence ratio. Additionally, flame stabilization and significant modulation of the heat release is observed in the reactive shear layer in the vicinity of the corner recirculation zones. It can be assumed that flow/flame parameters, such as equivalence ratio inhomogeneities, as well as locally intense curvature and strain lead to underestimated heat release rates in the reactive shear layer of the reheat flame when indicated by the flame CL [112]. This is why interpretations of the thermoacoustic reheat flame modulation in this work is of qualitative nature only. Alternative flame diagnostics to obtain quantitative estimates of heat release fields can be found in [108, 112, 113].

For imaging of the flame's CL signal, an external gated image intensifier unit coupled with a CMOS high speed camera is used. To capture the narrowband $OH^\star$ and $CH^\star$ (superposed by background $CO_2^\star$) radiation only, an optical $307 \pm 10nm$ and $431 \pm 10$ nm interference filter is applied, respectively. These filters are mounted on either a 45 or 100 mm UV camera lens with a maximum aperture of $1 : 1.8$. Images are recorded with

a resolution of $\approx 24\,\mathrm{px/mm^2}$ and sampled with a frequency $f_I$ of up to 15 000 frames/s. Such high frame rates are necessary in order to spatio-temporally resolve the transverse heat release oscillations at frequencies up to 3400 Hz. As lean premixed hydrocarbon-air flames at atmospheric pressure have low values of opacity, the camera captures line-of-sight integrated images of the momentary $OH^\star$ or $CH^\star$ emission. In postprocessing steps explained in Chapter 3, planar cut-planes of the flame through its centerline are determined from the measured 3D projection by Radon and inverse Abel transformations for the swirl flame. A quasi parallel view on the flame should be achieved for best postprocessing results, which is why the optical setup is as follows: (i) The imaging configuration is precisely arranged normal to the burner axis. (ii) A large focal length of the UV lens is needed to reduce optical distortion. (iii) A small aperture of the UV lens is needed to ensure a sufficient depth of field, whereas a sufficiently large aperture is required for enough sensor illumination critical for high-speed measurements. Hence, the optical setup is adjusted in such a way that the entire depth of the combustion chamber is displayed as a sharp image in line-of-sight direction.

# 3 Methods

This chapter outlines the post-processing methods that are employed within the present work to analyze the non-compact thermoacoustic feedback mechanisms in swirl and reheat flames. These methods are tailored to identify the system dynamics and linear thermoacoustic stability characteristics from time series of dynamic pressure and flame chemiluminescence. In addition, the spatio-temporal flame chemiluminescence recordings are processed to visualize deterministic oscillatory patterns within the flame. The methods applied for time series analysis are discussed in Section 3.1. The second part of this chapter then covers the procedures for decomposition of the spatially distributed heat release oscillations, which are used to investigate the physical mechanisms of the non-compact thermoacoustic feedback in the concerned combustors (cf. Sec. 3.2 and 3.3).

The following methods are described with reference to the perturbed $A^2$EV swirl flame. It is important to consider that the swirl and reheat combustors fundamentally differ in terms of geometries and flow fields. The swirl combustor consists of a cylindrical combustion chamber, while the reheat combustor is deliberately designed to be of flat and rectangular shape (cf. Ch. 2). The cylindrical geometry of the $A^2$EV renders the identification methods more extensive in contrast to the reheat setup. This is due to (i) the swirl flame being three-dimensional versus quasi two-dimensional in the reheat case and (ii) the presence of counter-rotating transverse mode pairs in the swirl combustor compared to a single transverse mode in the reheat combustor. While the methods are described with reference to the $A^2$EV combustor, these can be straightforwardly transferred to the reheat setup.

Parts of the following methods discussion have been previously published by the author in [98, 114, 115].

## 3.1 Time Series Analysis

The time series analyzed in this work are retrieved from both lab-scale combustors (cf. Sec. 2.1 and 2.3) operated at either thermoacoustically stable or unstable conditions. These time series originate from sampling (i) the dynamic pressure via several transducers at the combustor face-plates or (ii) flame CL recordings from the perturbed combustion. The latter time series can be both, either volume integrated scalar or two-dimensional image time series. In order describe the unsteady quantities of a thermoacoustic system (e.g. acoustic pressure or perturbed heat release) the following decomposition is established:

$$\phi(\mathbf{x},t) = \bar{\phi}(\mathbf{x}) + \phi'(\mathbf{x},t) + \breve{\phi}(\mathbf{x},t) \tag{3.1}$$

In this equation, $\phi$ consists of a superposition of mean $\bar{\phi}$, and fluctuating $\phi' + \breve{\phi}$ components, which are a functions of space $\mathbf{x}$ and time $t$. The latter fluctuating components are governed by deterministic, i.e. thermoacoustic oscillations, denoted by $\phi'$ or by stochastic, i.e. noise due to turbulence effects, denoted by $\breve{\phi}$. The principal aim of post-processing the raw data is to retrieve the deterministic signal $\phi'$ with which the thermoacoustic stability state, modal dynamics and general characteristics of the concerned systems are identified. The most fundamental analysis is the identification of acoustic modes and respective pulsation intensities via the Fourier transform. This form of spectral analyses allows to specify frequency bands that constitute the stable/unstable transverse acoustic mode of interest. A combination of (i) narrow-band filtering of the signal with specified frequency bands constituting the unstable frequency and (ii) the Hilbert transform (cf. Sec. 3.1.1) of the time series is then used for investigations of thermoacoustic stability and modal dynamics (cf. Sec. 3.1.2). In addition, the polar decomposition of the signal is the basis for the flame CL image processing discussed in Section 3.2.

### 3.1.1 Band-limited Hilbert Transform

The Hilbert transform allows to represent a measured time series $\phi(t)$ by a complex-denoted analytical signal

$$\Phi(t) = \phi(t) + i\tilde{\phi}(t). \tag{3.2}$$

In this representation, the measured time series $\phi(t)$ is the projection of the analytical signal onto the real axis and is related to $\tilde{\phi}(t)$ via the Hilbert transform $\mathcal{H}[\phi(t)]$. The Hilbert transform

$$\mathcal{H}[\phi(t)] = \tilde{\phi}(t) = \frac{1}{\pi}\int_{-\infty}^{\infty}\frac{\phi(\tau)}{t-\tau}d\tau \tag{3.3}$$

is defined as a convolution integral of $\phi(t)$. Conceptually, a Hilbert transformation shifts the Fourier coefficients in the complex space by a quarter-cycle, i.e. converts the real component into the imaginary counterpart. Afterwards, the shifted Fourier component is added back on the original component followed by an inverse Fourier transform to retrieve the complex denoted time series representation [116,117].

The determination of $\Phi(t)$ and its projections via the Hilbert transform has been established as a central analysis method within identification and analysis of oscillatory thermoacoustic systems [35,47,48,98,118,119]. With this, the initial signal can be investigated from the perspective of a rotating vector (phasor) in the complex plane as schematically shown in Figure 3.1 (a). The advantage of this method is observable from the polar decomposition of Equation 3.2 by conversion to an exponential or trigonometric notation, via

$$\Phi(t) = A(t)e^{i\varphi(t)} = A(t)\cdot\cos\varphi(t) + i\cdot A(t)\cdot\sin\varphi(t). \tag{3.4}$$

These notations provide access to an instantaneous envelope amplitude $A(t)$ and phase $\varphi(t)$ of the measured time series (cf. Fig. 3.1 (b)), which are particularly useful for investigation of the thermoacoustic feedback.

The **envelope amplitude** $A(t) = \pm|\Phi(t)|$ encloses the oscillating signal. It is given by the instantaneous phasor length. The envelope amplitude $A(t)$ allows to identify e.g. the temporal mode dynamics and damping/growth rates of a thermoacoustic system as demonstrated in [47,120].

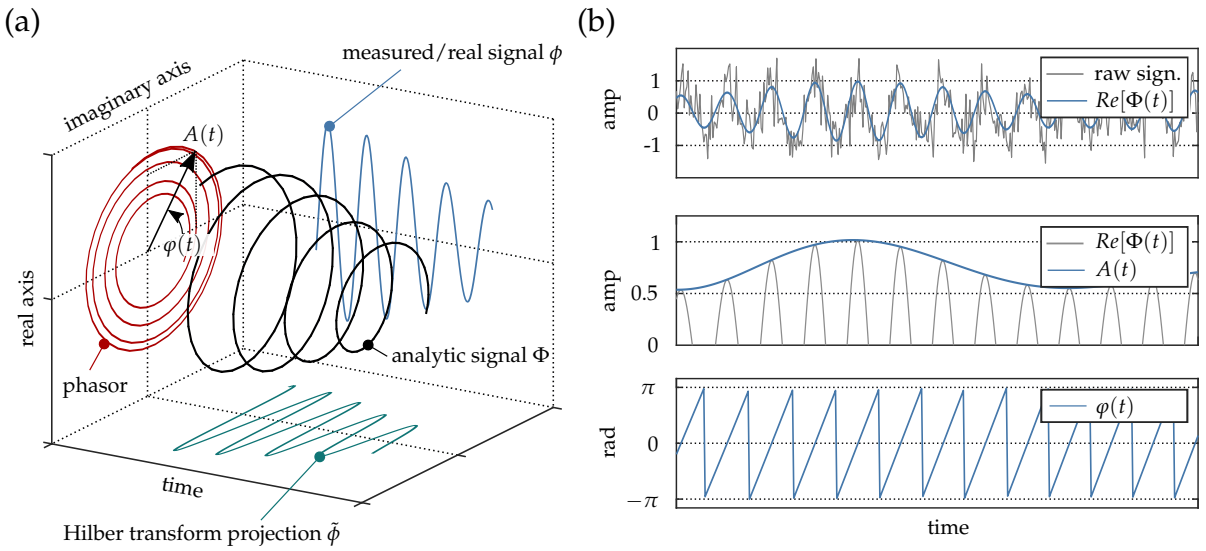


**Figure 3.1:** (a) Analytic signal representation with projection of the real, i.e. measured, signal, imaginary signal and phasor diagram in the complex plane (adapted from [117]), (b) sample time series of a raw unfiltered signal, its bandpass filtered Hilbert transformed counterpart $Re[\Phi(t)]$, envelope amplitude $A(t)$ and phase $\varphi(t)$.

Moreover, the envelope signal of the acoustic pressure time traces is used to decompose different intensity states of the thermoacoustic feedback loop in order to study its pulsation amplitude dependence (cf. Ch. 6). In addition to this, the root-mean-square of the envelope amplitude $rms(A)$ is a reliable measure to quantify the oscillation amplitude. This allows to qualitatively characterize different thermoacoustic stability states without the need for e.g. direct identification of thermoacoustic growth rates (cf. procedure in Sec. 3.1.2 and application in Ch. 4).

The **instantaneous phase** $\varphi(t) = \arctan \frac{\tilde{\phi}(t)}{\phi(t)}$ provides the rotation velocity of the phasor that represents the oscillation signal. In general, $\varphi(t)$ allows to identify the phase-shift (delay) between different signals or to derive the instantaneous oscillation frequency $\omega(t) = \frac{d\varphi(t)}{dt}$. The phase-shift can be used to reconstruct the acoustic mode from spatially distributed pulsations probes in the control volume (cf. Sec. 3.1.2), or to identify the phase relation of pressure and heat release oscillations. The temporal frequency information is beneficial to investigate the amplitude dependent system dynamics during limit-cycle oscillations (cf. Ch. 6). Particularly for this work, $\varphi(t)$ is utilized to receive phase locked ensemble averages

from the flame CL data. The instantaneous phase information of pressure time traces sampled synchronously with flame CL data allows to visualize coherent flame oscillation patterns associated with the instantaneous acoustic field. With these visualizations, insight into the physical flame response mechanisms is generated (cf. Sec. 5).

In order to analyze the pressure and heat release oscillations associated with the unstable transverse modes of the combustors, the Hilbert transform is obtained only for a narrow frequency-band of the dynamic signal. Thus, the Hilbert transform of $\phi(t)$ is combined with signal band-pass filtering around the transverse resonance frequency $f_T$ of a specified bandwidth $df$. This is a common procedure to retrieve an interpretable complex signal representation of data governed by either strong background noise or multi-frequency components. An implementation example is provided by [118]. In this reference the band-limited Hilbert transform is notated by

$$\mathcal{H}[x(t)] = F^{-1}[F\{\phi(t)\} \cdot \Theta(f_q - f_T + df) \cdot (1 - \Theta(f_q - f_T - df))], \quad (3.5)$$

where $F$ denotes the Fourier transform, $F^{-1}$ its inverse, $\Theta$ the Heaviside function and $f_q$ the Nyquist frequency.

### 3.1.2 Identification of Thermoacoustic Stability States and Modal Dynamics

First of all, thermoacoustic stability states are qualitatively characterized via the envelope amplitude root-mean-square $rms(A)$ of the polar-decomposed pressure time traces. Thermoacoustically unstable combustor operation points are associated with considerable pulsation amplitudes. Operation parameter dependencies on the thermoacoustic stability can thus be studied by evaluating associated pulsation amplitudes in the fashion of a bifurcation diagram. In addition, the probability density function (PDF) of the filtered acoustic signal $P(p')$ and its envelope $P(A)$ is taken as a further qualitative indicator for the thermoacoustic stability state of the system. While thermoacoustically stable operation points are governed by a normal pressure density distribution, changing operation parameters of the combustor towards the thermoacoustically unstable op-

eration regime converges the pressure density distribution into a bimodal shape, which is illustrated in Figure 3.2 (a). The amplitude density distribution, illustrated in Figure 3.2 (b), can be characterized by a mean away from zero and positive skewness, which indicates the onset of instability. A limit-cycle oscillation shows a normal shaped amplitude distribution with a mean at high pulsation amplitudes. With reference to the PDFs in Figure 3.2 and associated pulsation amplitudes, three stability states can occur:

1. The stable state reveals a unimodal pressure PDF, low pulsation amplitudes and a narrow amplitude PDF with negative skewness.
2. The marginally unstable state reveals a pressure PDF mode which is slightly off zero. Pulsation amplitudes are moderate and the amplitude PDF shows a positive skewness with increasing width.
3. The unstable state reveals a distinct pressure PDF bimodality and considerable pulsation amplitudes. The amplitude PDF is normally distributed with moderate width.

Second of all, modal dynamics, i.e. temporal behavior of the acoustic field, are analyzed based on the pressure time series obtained from the spatially distributed pulsation probes at the combustor face-plates. The acoustic field in the cylindrical A$^2$EV combustion chamber shows either

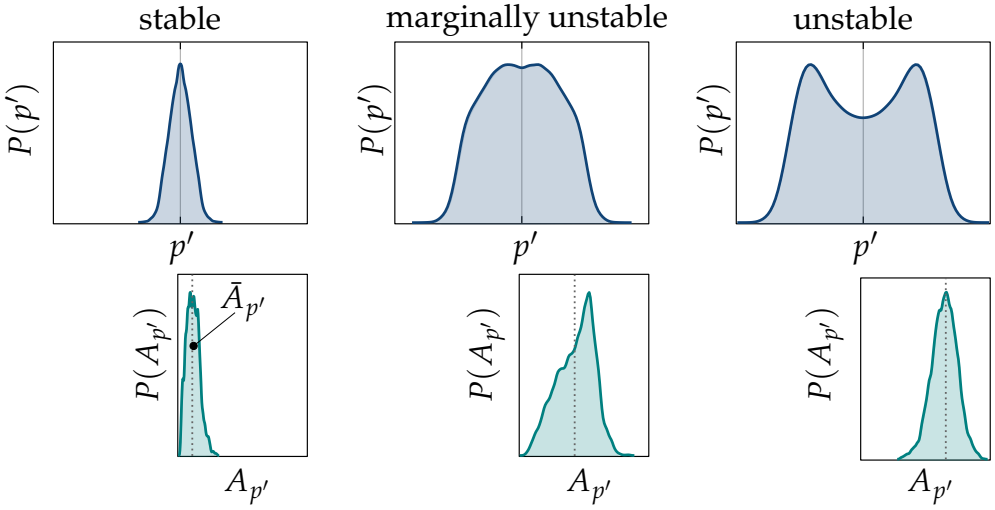


**Figure 3.2:** Probability density distributions $P(p')$ and $P(A_{p'})$ for three thermoacoustic stability states, referred to as stable, marginally unstable and unstable.

a standing, rotating or mixed type first transverse mode [38, 99, 115]. The associated transverse acoustic field at the swirl-combustor face-plate can thus be described via

$$p'(\theta,t) = \eta_F(t)\sigma(x,r)e^{-i\theta} + \eta_G(t)\sigma(x,r)e^{i\theta} + \text{c.c.}, \tag{3.6}$$

where complex-denoted Fourier coefficients $\eta_F(t)$ and $\eta_G(t)$ represent a clockwise (cw) and counter-clockwise (ccw) travelling transverse mode, respectively [99, 115]. The longitudinal and radial mode distribution is described by $\sigma(x,r)$, while c.c. denotes the complex conjugate counterparts of the two terms in this equation. The complex conjugate counterparts are required to ensure that the resulting time domain pressure signal $p'(\theta,t)$ is of real value, which is in accordance with the theory of Fourier series [121]. Studying the dynamics of the transverse acoustic field at the swirl-combustor face-plate in terms of its spinning character only requires a fixed axial $x$ and radial $r$ position, irrespective of the mode's longitudinal variability. Resolving the longitudinal dependence would further require FEM methods introduced in [38, 44] or longitudinally arranged additional sensors. Hence, the measured pressure oscillation time traces from the azimuthally distributed pulsation probes $p'(\theta,t)$ at the combustor face-plate are used to identify the complex time-dependent Fourier coefficients $\eta_F(t)$ and $\eta_G(t)$ of the cw and ccw rotating modes via solving Equation 3.6 in a least-square sense [35, 99, 122]. The Fourier coefficients are further decomposed via

$$f(t) = F(t)e^{i\omega t + i\theta_F(t)}, \tag{3.7}$$

$$g(t) = G(t)e^{i\omega t + i\theta_G(t)}, \tag{3.8}$$

where $F(t)/G(t)$ and $\theta_F(t)/\theta_G(t)$ are slowly varying amplitudes and phases. Depending on the oscillation intensity of the superposed Fourier coefficients $F(t)$ and $G(t)$, the resulting acoustic mode dynamics are of either standing ($F(t) = G(t)$), rotating ($F(t) >> G(t)$ resp. $F(t) << G(t)$) or mixed type ($F(t) > G(t)$ resp. $F(t) < G(t)$) character [99]. For a thermoacoustically stable system, it is observed that the $F(t)$ and $G(t)$ intensity is dominated by the stochastic nature of combustion noise [35]. Eventually, with increasing pulsation amplitude, the ccw rotating $G(t)$ mode settles into a stable limit-cycle oscillation and the cw rotating mode remains at low intensity. This is due to the swirling flow of the A$^2$EV com-

bustor (which is in ccw direction) and associated higher damping of the mode that travels against the swirl direction [98]. By relating the cw and ccw rotating mode dynamics, the spin-ratio

$$S(t) = \frac{G(t) - F(t)}{G(t) + F(t)} \tag{3.9}$$

can be retrieved as a function of time [122]. Looking at the probability density distribution of this time series allows to reveal whether the modal dynamics is of standing, mixed, or rotating dynamics. These modal dynamics are exemplarily shown in Figure 3.3 for a stable (a) and an unstable (b) operation point via a PDF of $Re(\eta_F(t))$ and $Re(\eta_G(t))$. Figure 3.3 (c) shows the density distribution of the resulting spin-ratio for the stable (a) and unstable (b) operation point indicating standing and predominantly ccw spinning modal dynamics, respectively. Evaluation of the modal dynamics for different A$^2$EV swirl-combustor operation conditions and thermoacoustic stability states (cf. Sec. 4) is carried out utilizing the PDF mean $\bar{S}$ (solid line in Fig. 3.3 (c)) and its standard deviation (dashed lines in Fig. 3.3 (c)).

Due to the rectangular geometrical nature of the reheat combustor, rotating mode dynamics are non-existing. Thus, the acoustic field is gov-

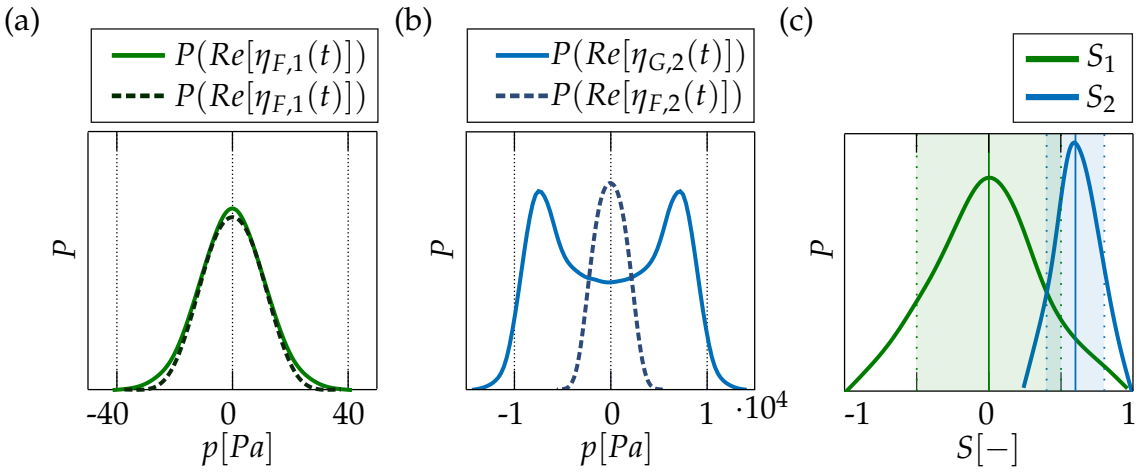


**Figure 3.3:** PDF's of the Fourier coefficients $Re(\eta_F(t))$ and $Re(\eta_G(t))$ for (a) stable and (b) unstable combustor operation, and (c) PDF of the spin-ratio $S(t)$ for the former operation points, with PDF mean $\bar{S}$ (solid line) and deviation (dashed line).

erned by a single transverse mode only, regardless of the stability state. This significantly eases analyses of modal dynamics as the acoustic field and its time variate characteristics can be directly reconstructed by (i) relating the instantaneous phase and amplitude time series of the installed pulsation probes (cf. Fig. 2.7) to each other or by (ii) comparing these time series to shape functions of the acoustic field. The time series analysis via the band-limited Hilbert transform and classification of the stability types using probability density functions equally applies for the swirl and the reheat combustor.

## 3.2 Investigation of the Non-Compact Flame Response

Identification of the physical flame response mechanisms to transverse and HF pressure pulsations relies on decomposition procedures of the recorded flame images. In general, the flame CL time series is composed of mean $\bar{I}(\mathbf{x})$ and oscillating $I'(\mathbf{x})$ as well as fluctuating $\breve{I}(\mathbf{x})$ components, as given per Equation 3.1. The overall aim of the decomposition procedures described in the following is to extract the coherent flame patterns $I'(\mathbf{x})$ from these image data only. Coherence information between the acoustic field and the perturbed flame is retrieved from the synchronously recorded signal of the pressure pulsations. The resulting distributions that visualize the coherent flame response to the acoustic oscillations are then used for interpretation of respective non-compact feedback mechanisms in Chapter 5.

For investigation of the non-compact flame response, Section 3.2.1 outlines the procedure to retrieve the modulated flame heat release patterns from perturbed flames. Aspects of cut-plane visualization and quantification of modulated heat release distributions are presented in Sections 3.2.2 and 3.2.3. Further details in terms of methods to retrieve amplitude dependent effects of the flame response is introduced in Section 3.2.4.

Parts of these method descriptions have been previously published by the author in [114,115].

### 3.2.1 Decomposition of the Oscillating Heat Release Field

Local flame modulations driven by the harmonically oscillating transverse acoustic field are revealed during thermoacoustically unstable operation of the investigated swirl and reheat combustors. The deterministic flame modulation is decomposed from the recorded image time series by conditional averaging of image ensembles related to a certain phase or amplitude interval of associated pressure signals [118, 123–125]. These conditional, i.e. ensemble, averages are achieved via synchronous sampling of the acoustic pressure with the flame CL. This allows to assign each individual flame image with a respective conditional state of the acoustic field. The conditional states are provided by an instantaneous envelope amplitude $A_n$, phase $\varphi_n$, or frequency $\omega_n(\varphi)$ resulting from the application of the previously introduced polar-decomposition to the acoustic pressure time traces (cf. Sec. 3.1.1). Conditional states from the governing multi-dimensional transverse acoustic mode are derived only from a single reference sensor located at the combustor face-plate. This procedure is precise enough, as the acoustic mode shape and its dynamics are a priori assessed by comparing the pressure readings of the pulsation probe array with shape functions of the transverse modes [38, 59].

Assignment of the acoustic signal to the flame CL data is achieved by its superposition with synchronization signals of the image acquisition unit as schematically shown in Figures 2.12 and 3.4. These synchronization signals are TTL[1] time traces indicating the image intensifier gating, i.e. the exposure time (cf. Fig. 2.12 (2) and 3.4 (b)), and the camera recording sequence (cf. Fig. 2.12 (1)). While the image intensifier signal provides the instance of time $t_n$ at which an image $I_n$ is taken with an exposure time $t_{ex}$, the record sequence provides a time stamp at the beginning and end of the entire acquisition procedure.

In order to gain a sufficient signal-to-noise ratio of the conditional averages visualizing the HF thermoacoustic heat release oscillations, the following points were taken into account:

- Image acquisition frequencies must not be a multiple of the targeted heat release oscillation frequency. In addition, a sufficient number

[1] Transistor-Transistor-Locic (TTL)

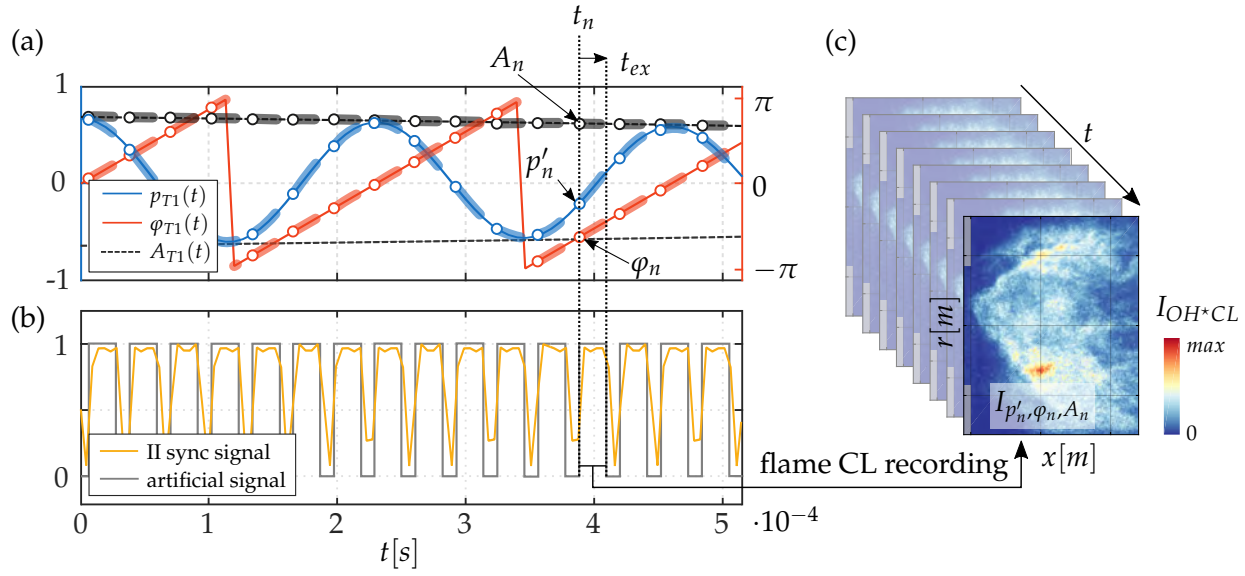


**Figure 3.4:** (a) Analytical signal of the filtered acoustic pressure time trace showing instantaneous pressure $p'$, phase $\varphi$ and envelope $A$, (b) discretely sampled image intensifier (II) synchronization signal and fitted artificial counterpart, (c) flame OH$^\star$ CL recording time series with sample image in front, which is taken at $t_n$ with an exposure time $t_{ex}$ and is associated to $p'_n$, $\varphi_n$ and $A_n$. The thick lines starting from points at e.g. $p'_n$, $\varphi_n$ and $A_n$ in (a) indicate the II exposure time and related ranges of the acoustic signal.

of samples (images) is required to allow for an appropriate phase-resolution. Besides improving the quality of the results, these measures also assure that each image is taken at a random phase and thereby prevent averaging errors, such as aliasing effects.

- For avoidance of systematic measurement errors due to hardware limited resolution of the discretely sampled synchronization signals, a higher resolved artificial intensifier exposure signal is fitted to the original/measured counterpart (cf. Fig. 3.4) in a least-square sense or via auto-correlation. The artificial exposure signal reproduces the exact exposure time and sampling frequency of the intensified camera settings. This allows to retrieve an accurate time stamp for correlation of the flame image with the associated acoustic oscillation.

- Short exposure times $t_{ex}$ are needed in order to receive a sharp snapshot image of the flame motion. Reducing the exposure time (at constant lens aperture), however, requires an increase of the intensifier gain, which is accompanied by an increase of signal noise. Hence, a

compromise between short exposure times and reduced intensification gain needs to be made for an improved signal-to-noise ratio at the cost of the image sharpness. Also, increasing exposure times reduce the accuracy of associated instantaneous acoustical states. This is less critical for conditional averages, but needs to be considered for the displacement reconstruction outlined in Section 3.3. Capturing the HF combustion dynamics of the swirl and reheat flames required exposure times of $\approx 60\mu$s.

The diagnostics deliver (i) flame images, (ii) corresponding synchronization signals, and (iii) pulsation probe measurements. These are utilised for the decomposition and visualization of coherent heat release modulations associated with the targeted pulsation frequency. Conditional averages $\langle I \rangle_{\varphi_n}$ can be calculated from all images in a phase interval/ensemble $[\varphi_n, \varphi_{n+c}]$, which is then repeated for all phase intervals resembling the thermoacoustic oscillation cycle. Moreover, a distributed Fourier coefficient

$$I_{\mathcal{F}}(\mathbf{x}, \varphi) = \frac{1}{N} \sum_{n=1}^{N} I_n(\mathbf{x}) \cdot e^{i\varphi_n(A_n)} \tag{3.10}$$

can be calculated from the entire image series, where $N$, $I_n$, $\varphi_n$, $A_n$ denote the total number of images, individual image, as well as respective phase angle and envelope amplitude from the associated dynamic pressure data. Both methods qualify for visualizing the oscillating heat release. While conditional averages are useful for a direct analysis of occurring phenomena without any a-priori assumption of an underlying periodicity of the signal, the complex-denoted distributed Fourier coefficient additionally allows for further post-processing of the oscillatory phenomena via tomographic reconstructions. These latter reconstructions are necessary for an unambiguous analysis of the swirling flame. The determination of a Fourier coefficient is possible because the observed heat release perturbations show a constant angular frequency. In accordance with the above given directions on the data acquisition setup, it is also assumed that the phase angle $\varphi_n$ is uniformly distributed in the sampled data.

Both of the foregoing described methods to decompose the oscillatory heat release distributions are equally applicable to both, the swirl and reheat experiments.

### 3.2.2 Tomographic Cut-Plane Reconstruction of the Swirl Flame

Phase-locked ensemble averages and distributed Fourier coefficients from the previously introduced methods are retrieved from line-of-sight integrated flame CL data. However, due to the quasi two-dimensional nature of the reheat flame, these distributions can be utilized without further data processing to unambiguously investigate underlying flame modulation phenomena. In contrast to the two-dimensional reheat combustor setup, the rotational shape of the $A^2EV$ swirl flame requires a cut-plane reconstruction of the distributed heat release oscillation with additional post-processing. Principally, time averaged line-of-sight swirl flame data can be inverse Abel transformed to obtain its de-convoluted information. However, as this method relies on rotationally symmetric distributions, it is not suitable for phase-locked time averaged data exhibiting transverse modulations. Moeck *et al.* [126] provided a review of tomographic reconstruction algorithms based on the Radon transform alongside with methodological descriptions for application to perturbed flames stabilized by swirling flow. The three-dimensional structure of a test object is reconstructed based on its projections from different viewing angles. In general, these projections are achieved by observing the fixed object from multiple viewing angles. This is either implemented by multiple cameras positioned around the object or by moving a single camera to multiple positions to obtain the different projections. For the specific swirl combustor setup, it can be advantageously used that the object under investigation, i.e. the flame perturbed by the first transverse acoustic mode, rotates around its axis and shows uniformly distributed phase angles. Thereby, only a simple optical setup with a single camera is necessary to gain the required spatial information. Utilizing the distributed Fourier coefficient from the phase resolved image processing, the projection of the perturbed flame for any viewing angle $\varphi$ can be obtained. Following the recommendations in [126], a Chebychev Zernike polynomial expansion is utilized

for tomographic reconstruction due to its superior noise resistance. The corresponding flame structure

$$I_{\mathcal{R}}(x, r_s, \varphi) = e^{i\varphi} \sum_{n=0}^{\infty} A_n(x) Z_{1+2n}^1 r_s \tag{3.11}$$

is described as a series of Zernike polynomials $Z$ with initially unknown expansion coefficients $A_k$ ($r_s$ denotes the normalized radius $r_s = \frac{r}{R}$). The missing expansion coefficient

$$A_n(x) = 2\frac{n+1}{\pi} \int_{-1}^{1} I_{\mathcal{F}}(x, r_s) U_{2n+1}(r_s) dr_s, \tag{3.12}$$

can be obtained by application of the Fourier coefficient $I_{\mathcal{F}}$ from the phase-resolved flame CL measurements and utilizing the second order Chebychev polynomials $U$.

### 3.2.3 Quantification of the Flame Response

Besides obtaining a qualitative distribution of the perturbed heat release rate induced by the transverse acoustic field, quantification of the local flame response is of interest for e.g. validation of derived analytical source terms in [38] or assessment of the combustor's linear stability[2]. In order to quantitatively characterize the oscillating heat release distribution, a proper scaling of the formerly obtained tomographic reconstruction is required. For this purpose, the investigated turbulent, lean and perfectly premixed combustion is considered as an open stationary thermodynamic system with complete chemical reaction in the flame region. Balancing the power over the observation area consequently delivers the net heat release rate $\dot{Q}_{th}$ by combustion. Assuming that the mean flame CL intensity indicates the steady heat release distribution allows to introduce a constant proportionality factor

$$K = \frac{\dot{Q}_{th}}{\int_{dV} \bar{I}(\mathbf{x}) dV} \tag{3.13}$$

[2] A comprehensive linear stability assessment would further require a quantification of the underlying damping rate and inclusion of possible further driving mechanisms.

to fulfill the above stated energy balance. With this $K$-factor, two-dimensional cut-plane data of the flame can be scaled to obtain the local heat release rate

$$\dot{q}(\mathbf{x}) = K \cdot \bar{I}(\mathbf{x}). \tag{3.14}$$

This method can be applied to the A$^2$EV swirl combustor with good confidence for two reasons. First, as the combustion is fully premixed, the distributed OH$^\star$ CL intensity can be assumed to be proportional to the thermal power [111, 127], which is exemplarily illustrated in Figure 3.5 for measurements of the swirl flame. Second, induced deviations on the OH$^\star$ CL emissions in different regions of the flame due to local strain rate effects [110] have negligible impact on the quantification method of the flame response.

It is important to point out that the advantage of the swirl flame setup for scaling the flame CL images does not apply to the reheat flame. This inapplicability is mainly due to the combustor operation in technically premixed mode, i.e. it exhibits a non-homogeneous air-fuel equivalence ratio distribution. These flow inhomogeneities induce systematic errors when OH$^\star$ CL is correlated with heat release [110], which is why appli-

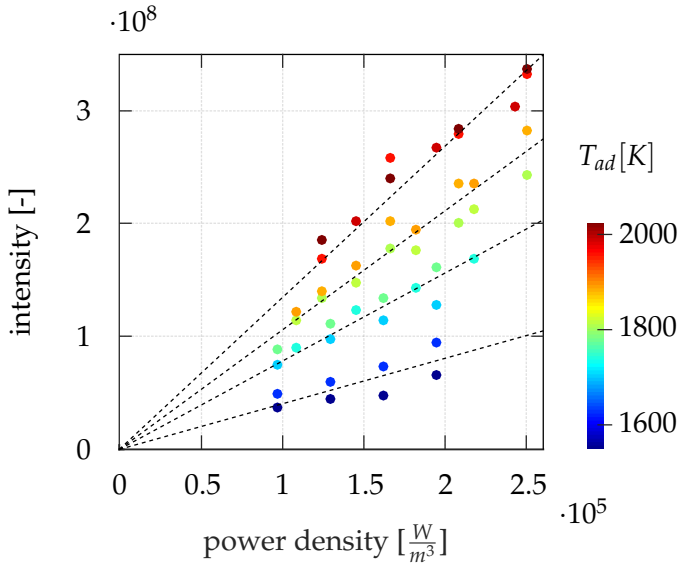


**Figure 3.5:** Proportionality of measured OH$^\star$ CL intensity with thermal power of the swirl-stabilized flame run in perfectly premixed mode. The color code represents the adiabatic flame temperature evaluated from the operation parameters.

cation of the scaling method to the reheat flame discussed above only allows for qualitative conclusions or requires to consider the local equivalence ratio distribution. The latter can be accounted for by e.g. combined $OH^\star$ and $CH^\star$ CL measurements of the flame as described in [113].

The distributed heat release rate oscillations $\dot{q}'(\mathbf{x})$ allow to quantify the flame response by evaluating either the Rayleigh index or the flame driving rates (cf. Ch. 1). However, both methods further require access to the three-dimensional acoustic field $p'(\mathbf{x})$, interacting with the local heat release. These acoustic field variables are obtained by solving the acoustic conservation equations via a discretized FEM in a non-compact thermoacoustic analysis framework. This framework was developed by Hummel *et al.* [38,44] and allows, among others, for computations based on experimentally obtained mean heat release $\bar{q}(\mathbf{x})$ and temperature $\bar{T}(\mathbf{x})$ distributions. Besides obtaining the acoustic field variables, the FEM framework is also applied within this work to (i) directly compute linear flame driving rates (cf. Sec. 6.1), as well as (ii) numerical counterparts of the distributed heat release oscillations for validation of analytical source terms (cf. Sec. 5.1.7). A developed framework to approximate the required mean temperature distribution from experimental data is outlined in Appendix A. Details on computation of thermoacoustic variables via the FEM framework are provided in [38].

### 3.2.4 Amplitude Dependent Flame Response

The previously introduced methods for decomposition of the deterministic heat release oscillations (cf. Sec. 3.2.1) rely on connecting the flame CL measurements with the instantaneous phase of the pressure time traces from the interfering transverse acoustic mode. In the same fashion, conditional averages evaluated for other distinct flame or acoustic conditional states have proven to provide valuable insight for further analysis of the flame dynamics. For the swirl stabilized flame, it is for example observed that the time series of the acoustic pressure reveal a slowly varying envelope amplitude $A(t)$ (amplitude beating). The amplitude modulation is intense for marginally unstable operation points and settles into more constant envelope amplitudes towards limit-cycle oscillations. Sample

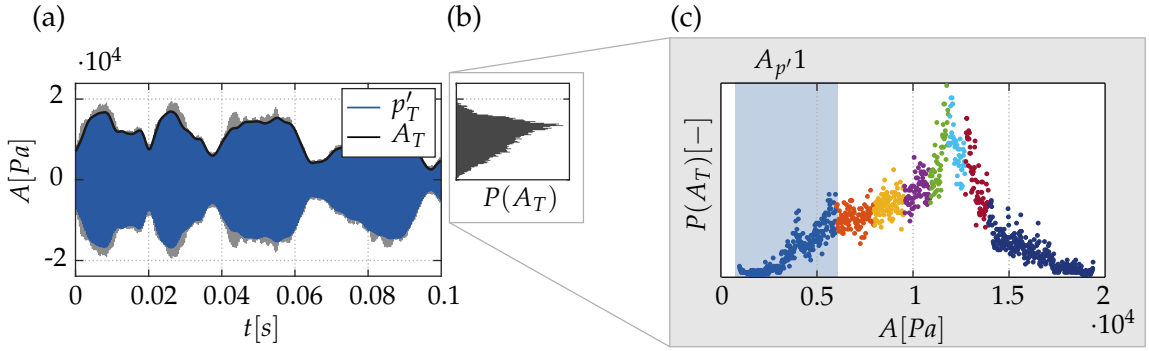


**Figure 3.6:** (a) Sample polar decomposed pressure signal $p'_T$ with envelope amplitude $A_T$ and (b) related probability density distribution $P(A_T)$, (c) probability density distribution $P(I(A_T))$ constituting the OH* CL chemiluminescence measurements (dots) related to the instantaneous pressure envelope amplitude $A_T$. Different colors indicate ensembles of selected amplitude range, e.g. $A_{p'}1$ highlighted in blue.

time series are provided in Figure 3.6 (a). To understand the underlying flame dynamics, coherent heat release distributions for different phase and amplitude conditions can be visualized according to Equation 3.10. In order to retrieve the flame response occurring only for a certain pulsation amplitude, its density distribution is partitioned into several amplitude levels for which conditional averages or distributed Fourier coefficients are then evaluated. A sample density distribution of the envelope for such an analysis is provided in Figure 3.6 (b), which is composed of the envelope amplitude associated with each flame CL image taken synchronously to the reference pressure data. Different colors show the grouping into 8 amplitude levels to obtain an amplitude average flame CL distribution $\bar{I}_A$. Instead of specifying certain amplitude ranges, the number of images $N$ taken for each range is set constant. This is done in order to obtain a sufficient signal-to-noise ratio for e.g. evaluating the distributed amplitude dependent Fourier coefficient but has the consequence of varying ranges of the individual amplitude levels, as can be seen in Figure 3.6 (c).

Evaluation of amplitude dependent flame response can be equally applied for the swirl and reheat flame.

## 3.3 Reconstruction of Flame Displacement

A characteristic observation for the thermoacoustically unstable swirl combustor is a distinct transverse and oscillatory flame motion, as reported in [57–59]. This displacement effect is visualized from experimental data to further study the phenomenology in Chapter 5. The visualization method relies on synchronous measurements of (i) the line-of-sight flame CL, (ii) the Mie-scattering from flow particles for validation purposes and (iii) the acoustic pressure during thermoacoustically unstable combustor operation. Instantaneous flame displacement fields are identified by cross-correlating the spatial flame structure from two subsequent flame chemiluminescence images. This identification is repeated for the entire time series of images to yield a respective series of covariance matrices. The oscillation cycle of the heat release modulation is then identified by phase-conditional averages and local scaling of these matrices. Finally, the reconstructions of only the flame displacement fields allows to further decompose the entire heat release modulation (cf. Sec. 3.2) to visualize remaining heat release fluctuations and associated mechanisms. These evaluations have so far only been carried out for the swirl-stabilized flame as this flame displacement effect could not yet be clearly identified for the second-stage reheat flame.

In order to validate conclusions drawn from the investigations of the flame displacement, acoustic particle image velocimetry (PIV) reference fields are retrieved from synchronous flow-particle Mie-scattering measurements [128]. These flow field reconstructions generally provide a more accurate insight into the oscillatory flame motion as a two dimensional profile, i.e. sectional image, of the flame can be detected from the density gradient across the reaction zone. Advantages of the rather non-intuitive reconstruction of the displacement field from flame chemiluminescence data compared to the application of acoustic PIV are: (i) Greatly reduced complexity of the diagnostic apparatus, (ii) direct post-processing of the occurring flame CL, which is available for numerous operation conditions, and (iii) the exclusion of any a-priori assumption of flame coupling with the acoustic velocity.

Two main differences between measurements of flame CL and acoustic PIV for the reconstruction of the displacement field need to be taken into account. First, the measured quantity is the displacement of the flame reaction zone that must not necessarily coincide with the acoustic velocity magnitude (identified from acoustic PIV). Second, instantaneous line-of-sight integrated flame CL fields are processed instead of planar cut-plane data from laser measurements. The latter introduces a systematic measurement error, which is assessed in Sec. 5.1.4. Instead of tracking a tracer particle pattern, as utilized in PIV methods [129–131], the basis for the displacement field reconstruction is the local deformation of the recorded time-variate flame structure, i.e. the local flame intensity distribution. The evaluation of the spatial covariance of subsequent flame images is presented in Section 3.3.1. This method provides the basis for reconstructing the oscillatory displacement field (cf. Sec. 3.3.2), and thereupon the oscillatory heat release distribution (cf. Sec. 3.3.3). Handling of the Mie-scattering images and PIV postprocessing for reference fields is not discussed due to the availability of reports in the literature [57, 129–131].

The method of reconstructing the oscillating heat release distribution due to flame displacement is principally applicable to both, the swirl and reheat combustors. Parts of these method descriptions have been previously published by the author in [128].

### 3.3.1 Spatial Covariance of Subsequent Flame Images

Starting point for the spatial covariance identification are the instantaneous line-of-sight integrated flame CL images $I(\mathbf{x}, t)$ (cf. Fig. 3.7 (a) - raw image), which are accompanied by noise from the image intensification. In order to improve the efficiency of the displacement field reconstruction, the image contrast is enhanced followed by smoothing of the raw image. Contrast enhancement is applied via contrast-limited adaptive histogram equalization (CLAHE), which optimizes the identification of the flame displacement in areas of low signal intensity. As only the acoustically induced motion of the flame brush is of interest, the resulting image is smoothed to accentuate the global flame structure instead of local intensity peaks (Fig. 3.7 (a) - smoothed image). Afterwards, the images

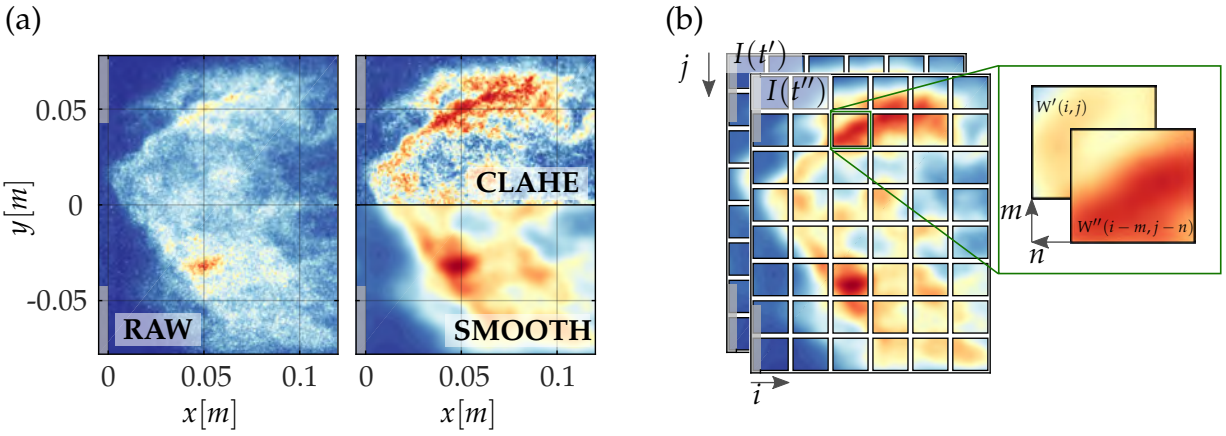


**Figure 3.7:** (a) Conditioning of the raw image with smoothing and contrast enhancement, (b) cross-correlation of two subsequent flame images with indication of windowing.

are divided into uniform interrogation windows $W$ (sub-images), shown in Figure 3.7 (b). Each of these windows yields one displacement vector and thereby allows for a spatial resolution of the flame displacement. The window size is optimized for high displacement field resolution, while maintaining a sufficient data basis for the reconstruction of the local displacement vector.

The spatial covariance of two subsequent flame CL images $I(\mathbf{x}, t')$ and $I(\mathbf{x}, t'')$ recorded with a sufficiently short time lag $t_r = t'' - t' = \frac{1}{f_s}$ is evaluated by obtaining the correlation matrix

$$\mathcal{C}(m,n) = \sum_i \sum_j W'(i,j) W''(i-m, j-n) \tag{3.15}$$

for each window pair $W'(i,j)$ and $W''(i,j)$, where $i,j$ are the window and $m,n$ the correlation coordinates. The cross-correlation function in Equation 3.15 is a statistical approach that evaluates the pattern matching for an individual window pair [132, 133]. A displacement of $W'$ towards $W''$ with the highest probable pattern agreement yields a peak in the correlation matrix. This peak is located and transformed to a distance. The correlation function is applied to all windows of the image pair to obtain a displacement vector field $D(\mathbf{x})$. The evaluation procedure is then repeated for all consecutive image pairs of the recording sequence in order to obtain a time series of instantaneous flame displacement fields $D(\mathbf{x}, t)$.

At this point it is important to note that the evaluation of the spatial covariance field of an image pair yields a vector field, which depends on (i) the local heat release intensity of the turbulent flame brush, (ii) the flame motion impacted by the mean fluid flow, (iii) the transverse flame motion with the acoustic oscillation, as well as (iv) systematic errors associated with applying the correlation function [133]. These latter systematic errors have shown to be negligible for the flame displacement reconstruction.

### 3.3.2 Reconstruction of the Oscillatory Displacement Field

In order to extract only the acoustically induced periodic flame motion, mean displacement fields are calculated from (i) the entire time span $\bar{D}_T$, and (ii) ensembles of images $\bar{D}_{\varphi_n}$ corresponding to the same acoustic phase signal $\varphi_n$ within a chosen bin width $\varphi'' - \varphi'$. The bin width specifies the phase resolution for the post-processing procedure, and is dependent on the required quality in terms of signal-to-noise ratio of the ensemble-average image. The phase signal is obtained from the bandpass filtered dynamic pressure time traces sampled with a reference sensor installed at location P1 of the face plate of the swirl-combustor (cf. Fig. 2.1). Resulting sample images are shown in Figure 3.8 (a). To decompose the oscillating information from the resulting phase-conditioned displacement

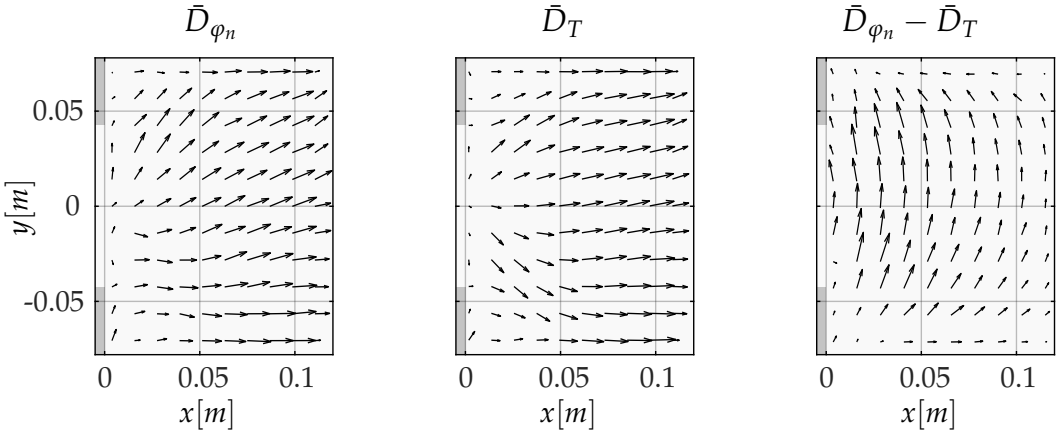


**Figure 3.8:** Sample vector fields from the covariance analysis of flame CL measurements showing phase-locked ensemble average $\hat{D}_{\varphi_n}$, time average $\hat{D}_T$ and difference image $\bar{D}_{\varphi_n} - \bar{D}_T$ for illustration of oscillatory displacement.

field, the mean contribution is then subtracted from each ensemble average $\bar{D}_{\varphi_n} - \bar{D}_T$ (cf. Fig. 3.8 (b)).

The previously obtained phase-locked averaged displacement fields contain the information of the flame motion starting within a phase bin $\varphi_n$ for the time lag between recording the subsequent images $t_r$. This makes it necessary to consider that different time lags result, depending on the time resolution of either $t_\varphi = \frac{1}{f_{T1} N_\varphi}$ or $t_r$. In the case presented in this work $t_r$ exceeds $t_\varphi$. As the quantity and field of oscillatory displacement is of interest, calculation of the displacement magnitude requires a scaling with the time lag within each phase bin

$$\tilde{D}_{\varphi_n} = \frac{\bar{D}_{\varphi_n}}{t_r f_{T1} N_\varphi}, \tag{3.16}$$

where $N_\varphi$ is the number of phase intervals. In the next step, the phase resolved flame displacement is transformed to

$$\mathcal{D}(\mathbf{x}, \varphi) = \frac{1}{N_\varphi} \sum_{n=1}^{N_\varphi} \tilde{D}_{\varphi_n}(\mathbf{x}) \cdot e^{i\varphi_n}, \tag{3.17}$$

from the individual phase-locked fields $\tilde{D}_{\varphi_n}(\mathbf{x})$ related to the phase bin $\varphi_n$, similar to a Fourier coefficient (cf. Sec. 3.2).

The previous steps are appropriate for identification of a qualitative displacement field. However, the introduction of systematic errors complicate a quantitative analysis and results in an underestimation of the displacement magnitude. Errors mainly result from (i) the evaluation of line-of-sight integrated flame CL images to retrieve planar information of the acoustically induced displacement (ii) phase-conditioned averaging and (iii) the stochastic/turbulent flame (intensity) dynamics. Up to this point, the retrieved flame displacement fields $\mathcal{D}(\mathbf{x}, \varphi)$ can be used to indicate the most probable flame motion direction (in $x, r$ coordinates), but do not qualify to retrieve the local flame displacement magnitude.

In order to quantitatively reproduce the flame motion, instantaneous flame images at phase positions $\varphi = 0^\circ$ and $180^\circ$ are used to identify the maximum transversal displacement of the flame front. For this, two flame images consecutively taken at $0^\circ$ and $180^\circ$ are binarized to only extract

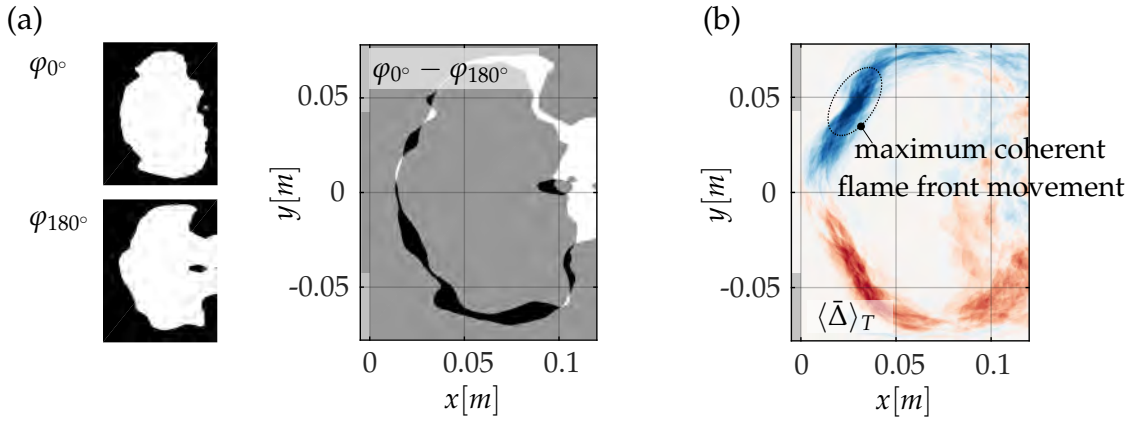


**Figure 3.9:** Evaluation of a scaling factor for the peak displacement obtained from (a) difference images of the binarized flame structure $\langle\Delta\rangle_T$ at phase position $\varphi = 0°, 180°$, (b) illustration of the resulting distribution of the maximum coherent flame front motion.

the global flame front. Afterwards, a difference image of the two former masks is calculated (cf. Fig. 3.9 (a)). Averaging a number of these difference images over the measurement sequence delivers the maximum oscillatory flame motion $\langle\Delta\rangle_T$, as shown in Figure 3.9 (b). From this, a scaling factor is extracted from the marked area close to the outer recirculation zone. This factor is the sum of the local absolute displacement and this specific area is chosen as it is of inherent interest for later identification of the flame/heat release modulation. The constant proportionality factor is then applied for calibration of $\mathcal{D}(\mathbf{x}, \varphi)$ so that the locally extracted magnitude is conserved in a quantitatively correct manner in the entire displacement field.

### 3.3.3 Reconstruction of the Heat Release Modulations

The final step is the visualization of the oscillating heat release field induced by the displacement field as indicated in Figure 3.10. Starting point for identification of the modulated heat release is the time averaged inverse Abel transformed flame image, i.e. the mean heat release field, and the previously obtained displacement field. It is assumed from experimental observations that the local heat release oscillation phenomenologically results from the acoustically induced transverse motion of the flame

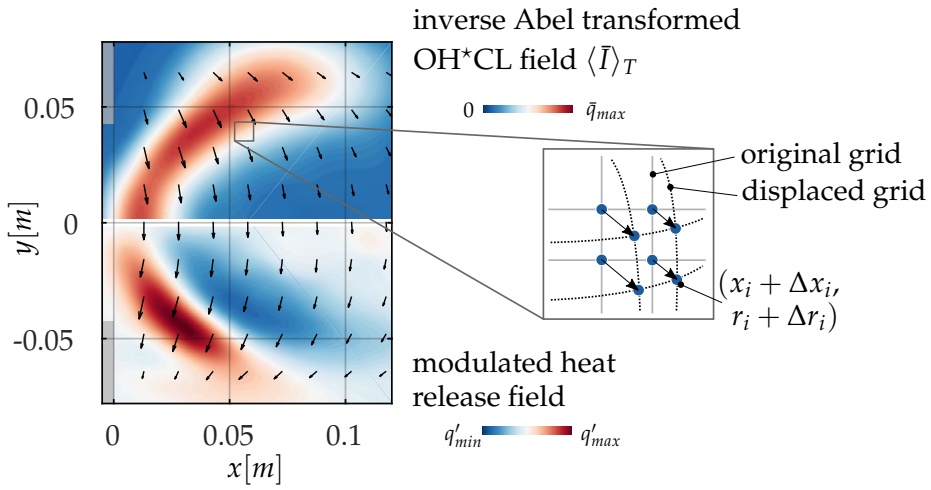


**Figure 3.10:** Evaluation of the oscillating heat release field from the displacement vector field based on the time averaged and inverse Abel transformed flame CL data.

brush off its mean position. To reconstruct this oscillating field from the experiments, the coarse displacement field $\mathcal{D}(\mathbf{x}, \varphi)$ is interpolated to a grid that matches the resolution of the heat release map given from the flame CL measurements. The displacement at the wall is set to zero to represent a no-slip wall condition. Afterwards, the $x$ and $r$ coordinates of each pixel in the mean heat release field are transformed in accordance to the local displacement field (schematic in Fig. 3.10), i.e. via

$$\dot{q}'_{\Delta}(x, y) = \bar{q}(x + \Delta x, y + \Delta y) - \bar{q}(x, y). \tag{3.18}$$

This results in the superposed mean and oscillating heat release field at a certain phase condition. In a final step, the heat release information from the deformed mesh is interpolated back to the original grid and the mean heat release field is subtracted (Fig. 3.10, lower image half). As a result, the oscillating heat release induced by the displacement effect is obtained in the cut-plane through the burner axis. Resulting heat release oscillation fields and quantitative comparison of these results with counterparts obtained from acoustic PIV displacement fields are provided in Section 5.1.4 alongside with a discussion of systematic measurement errors.

# 4 Acoustic Combustor Response to Unsteady Heat Release

This chapter comprises the results of the system response investigations in the HF regime of both, the laboratory swirl and reheat laboratory combustors. Specifically, dynamic pressure time traces recorded at the combustor's face-plate are analyzed to reveal the thermoacoustic stability characteristics through the methods introduced in Chapter 3. Moreover, fundamental characteristics of the acoustic mode dynamics and interference phenomena of flame and acoustics are assessed. The results with reference to the swirl and reheat combustor are consecutively discussed in Sections 4.1 and 4.2. The findings established in this chapter are essential for the identification and discussion of the non-compact linear flame response mechanisms applying to both of the combustor types in Chapter 5 and 6.

Parts of these discussions have been previously published by the author in [96, 114, 115].

## 4.1 Swirl Combustor

The HF thermoacoustic instability occurring within the $A^2EV$ swirl combustor was previously studied by Schwing *et al.* [57–60] and Hertweck *et al.* [62, 63]. In particular, these studies provide a comprehensive view on operational parameters that govern the $A^2EV$ combustor's thermoacoustic instability propensity. To complement this view, the present work focusses on individual representative operation conditions in order to (i) clarify thermoacoustic stability characteristics (cf. Sec. 4.1.1), as well as (ii) to further elaborate the characteristic system response (cf. Sec. 4.1.2 - 4.1.4).

### 4.1.1 Thermoacoustic Stability States

During investigations of the swirl combustor, it was observed that its thermoacoustic stability depends on the swirl intensity [60]. Taking advantage of this effect, characteristic interactions of the flame with the acoustic field can be studied under different thermoacoustic stability states (i.e. by varying the swirl numbers), excluding the effect of thermal power $Q_{th}$ on the flame driving. Thereby, the effect of other influencing factors on the thermoacoustic stability, such as the spatial distribution of the heat release with different burner configurations can be unambiguously explored. Thus, the following discussions refer to either a low swirl (LS) or a high swirl (HS) configuration, for which the swirl-number [12] accounts to $S_n = 0.58$ or 0.74, respectively. In practice, $S_n$ is modified by altering the A$^2$EV swirler slot height to $h = 14\,\mathrm{mm}$ (LS) or $h = 11\,\mathrm{mm}$ (HS). All results are obtained with an inlet air mass flow rate $\dot{m}_a = 0.1$ or $0.12\,\mathrm{kg/s}$ preheated to $T_a = 473\,\mathrm{K}$. In order to investigate the thermal power dependence of the system dynamics (at the end of this section), the air-fuel equivalence ratio $\lambda$ is varied within the range of $1.0 - 2.0$.

Three selected dynamic pressure time series are analyzed that reveal characteristics to exemplify thermoacoustic stability states (cf. Sec. 1.2), which are illustrated in Figure 4.1. The underlying time series are obtained for an LS configuration and decreasing air-fuel equivalence ratio $\lambda$, which implies an increase of thermal power $Q_{th}$. For interpretation of each individual operation point, the raw acoustic pressure $p'$ and analytical[1] $p'_{T1}$ time series are provided alongside with the envelope amplitude $A_{T1}$. These time series are supplemented with probability density distributions $P(p'_{T1})$ and $P(A_{T1})$, as well as frequency spectra for a more detailed analysis.

Figure 4.1 (a) shows the system response during stable combustor operation with low thermal power $Q_{th} = 164\,\mathrm{kW}$. The raw acoustic pressure is predominantly noise driven, i.e. reveals no deterministic oscillations on first sight, and the analytic signal representation $p'_{T1}$ is characterized

[1] In the following, the term analytical signal/time series implies the combined (i) polar decomposition and (ii) bandpass filtering around the transverse mode frequency of interest (indicated in blue color in the frequency spectra in Figure 4.1) of the raw acoustic pressure time series according to the methods introduced in Section 3.1.

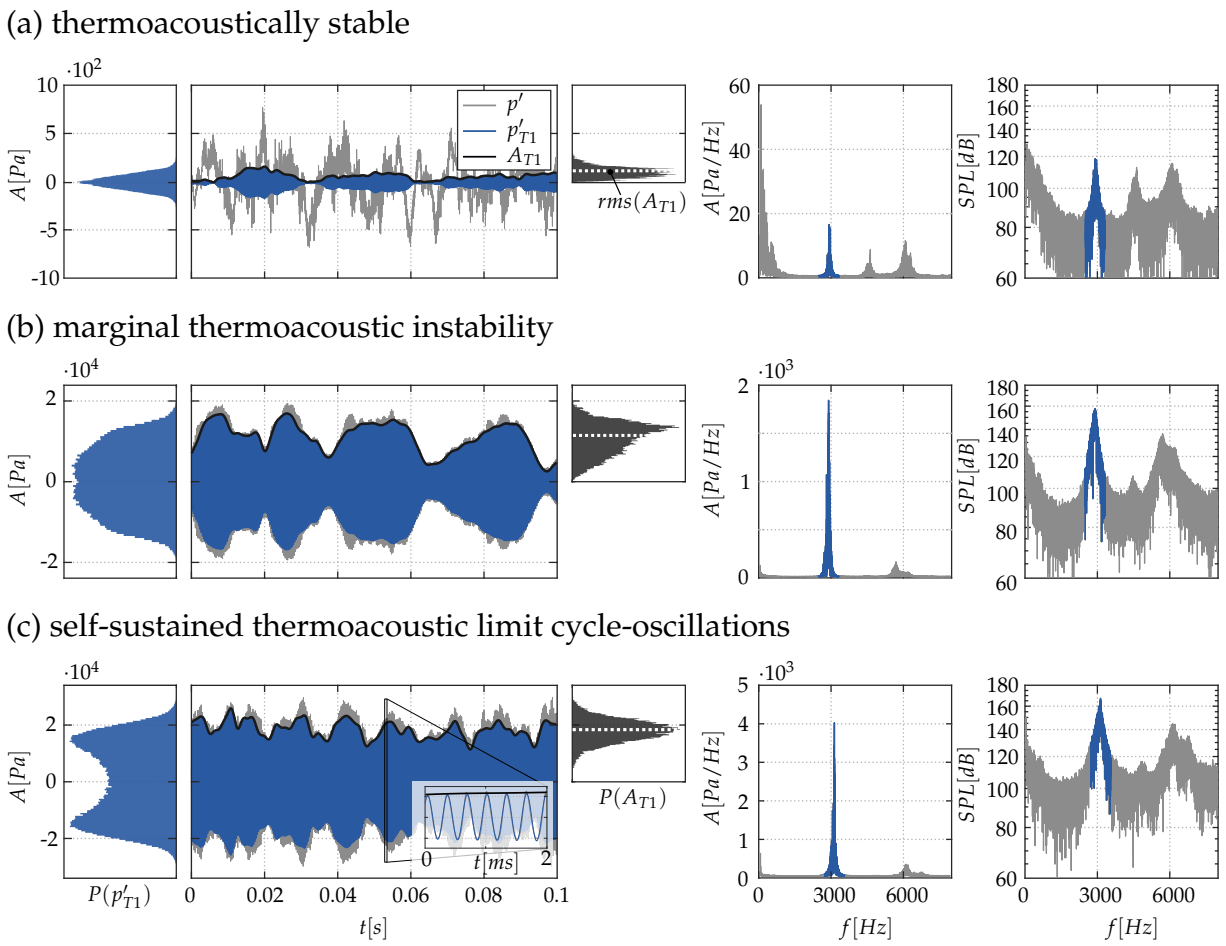


**Figure 4.1:** From left to right: Probability density distribution of the analytical pressure signal $P(p'_{T1})$, raw $p'$ and analytical $p_{T1}$ time series of the acoustic pressure with envelope $A_{T1}$, density distribution of the envelope $P(A_{T1})$ with indicated root-mean-square of $A(p'_{T1})$ and frequency spectra of $p'$ with normal and logarithmic y-axis.

by a low pulsation amplitude. These kinds of noise driven, linearly stable operation points reveal a unimodal distribution $P(p')$ of the acoustic pressure oscillations [47,99,119]. With regard to the frequency spectra, a peak at the first transverse resonance is visible but does not reach a significant level.

In contrast to the stable combustor operation (cf. Fig. 4.1 (a)), Figures 4.1 (b) and (c) show the dynamic pressure of a marginal instability and a fully developed limit-cycle oscillation, respectively. The thermal power $Q_{th}$ of these operation points are 193 and 232 kW. Both thermoacoustic (in-)stability states show considerable pulsation amplitudes, represented by

root-mean-square values of the envelope amplitude $rms(A)$ (dashed lines in $P(A_{T1})$ inserts in Figure 4.1). A characteristic that is effectively used for the distinct classification of a thermoacoustic stability state [20,35,119,134] is the distribution of the probability density functions $P(p'_{T1})$ and $P(A_{T1})$. First of all, this is the transition of the pressure distribution $P(p'_{T1})$ from a normal to a bimodal shape from stable conditions towards limit-cycle oscillations. Second of all, the amplitude probability density distribution $P(A_{T1})$ reveals a shift of the mean value from low towards higher amplitudes from the stable to the limit-cycle situation. At the same time, the shape of the amplitude probability densities transitions from (i) a negatively skewed distribution with a relatively thin width (stable) over (ii) a positively skewed one with increased width (marginal) to (iii) a normally shaped distribution with a relatively moderate width (limit-cycle). The associated frequency spectra show distinct peaks at approximately 3000 Hz, which can be allocated to the first transverse acoustic mode [57, 58, 60]. In contrast to stable combustor operation, the spectrum is dominated by a mono-frequent pulsation during thermoacoustically unstable conditions. To illustrate the intensity of the pulsations, the spectra on the right in Figure 4.1 show the sound pressure levels retrieved at the burner face-plate. Sound pressure levels reach up to 160 dB[2] for the fully developed limit-cycle oscillations, which underline the significance of these HF pulsations if translated into mechanical vibrations and associated fatigue of affected hardware components [20, 135]. Thus, the occurrence of such pressure pulsations needs to be avoided for smooth operation of gas turbines (cf. Ch. 1).

### 4.1.2 Effect of Swirl on the Acoustic Response

The previously categorized (in)stability states resulted from variation of the air-fuel equivalence ratio $\lambda$ and thus variation of the thermal power $Q_{th}$. This section now focusses on comparing the impact of the swirl intensity on the thermoacoustic stability, while $\lambda$ and $Q_{th}$ are kept constant. Figure 4.2 (a) shows the acoustic system response for the LS configuration and 4.2 (b) the HS counterpart. Both operation points have a thermal

[2]Note for comparison to other typical sources of sound: Aircraft engine at takeoff in 100 m distance $120 - 140$ dB, pneumatic chipper 100 dB, average street traffic $80 - 90$ dB.

power of $Q_{th} = 208\,\mathrm{kW}$ at $\lambda = 1.4$. As can be observed from the root-mean-square of the pulsation amplitude level $rms(A_{T1})$, as well as the pressure and amplitude distributions $P(p'_{T1})$ and $P(A_{T1})$, both operation points exhibit a self-sustained HF thermoacoustic instability. For the LS configuration the pressure pulsations are at a moderate amplitude level and reveal an intense modulation, i.e. beating, of the envelope. These pulsation characteristics are similar to the previously discussed marginal instability (cf. Fig. 4.1 (b)), i.e. slightly exceeding the linear regime. Interestingly, changing the swirl intensity towards an HS configuration significantly alters the thermoacoustic properties of the burner. The increased swirl leads to strong limit-cycle oscillations associated with high pulsation amplitudes and a more constant envelope amplitude, i.e. modulations are less distinct. The difference between both configurations is confirmed by the characteristic pressure distribution $P(p'_{T1})$ revealing a clear bimodal shape for the high swirl configuration with respect to a less distinct distribution for decreased numbers of swirl. The main implication of

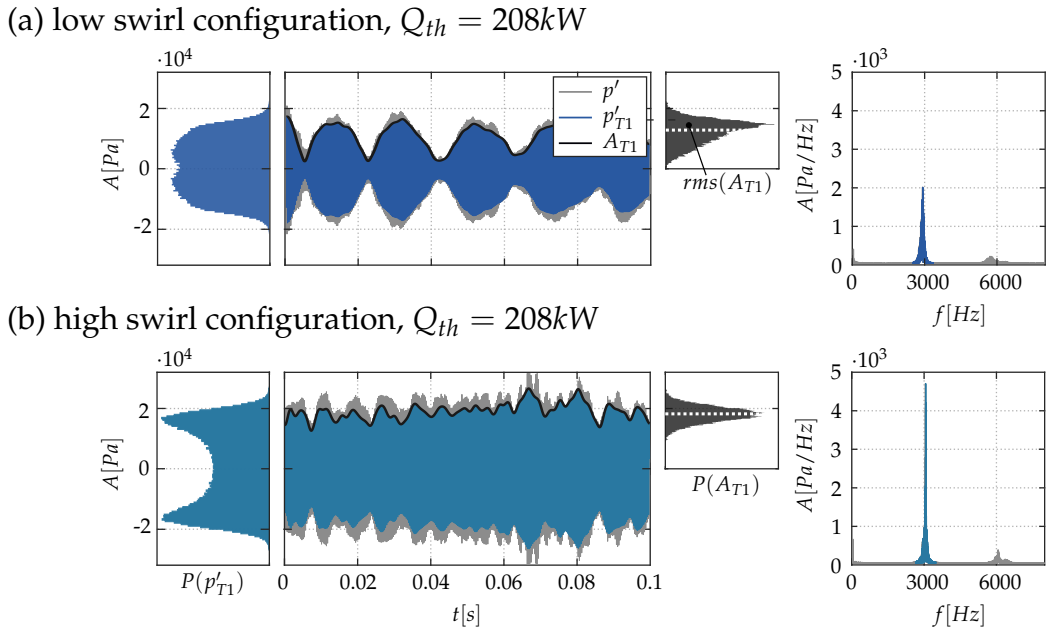


**Figure 4.2:** Comparison of two swirl configurations at otherwise equal operation conditions. From left to right: Density distribution of the analytical pressure signal $P(p_{T1})$, raw $p$ and analytical $p_{T1}$ time series of the acoustic pressure with envelope $A_{T1}$, density distribution of the envelope $P(A_{T1})$ with indicated root-mean-square of $A(p_{T1})$, frequency spectrum of $p$.

the previous section is that the LS configuration is less prone to thermo-acoustic instabilities than the HS configuration.

### 4.1.3 Combined Effects of Swirl and Thermal Power on the Acoustic Response

Further insight is generated by a combined view of the effect of changing the air-fuel equivalence ratio $\lambda$, which effectively translates into varying thermal power $Q_{th}$, and differing swirl-numbers $S_n$ onto the thermo-acoustic system dynamics. Sample results are provided in Figure 4.3 (a,b). They show the pulsation amplitude indicated by the root-mean-square of the envelope amplitude $rms(A)$ plotted over the air-fuel equivalence ratio as a bifurcation diagram. Figure 4.3 (c,d) shows the spin-ratios at the concerned operation points, which are addressed in the following section. Both graphs of Figure 4.3 (a,b) show a continuous rise of the pulsation

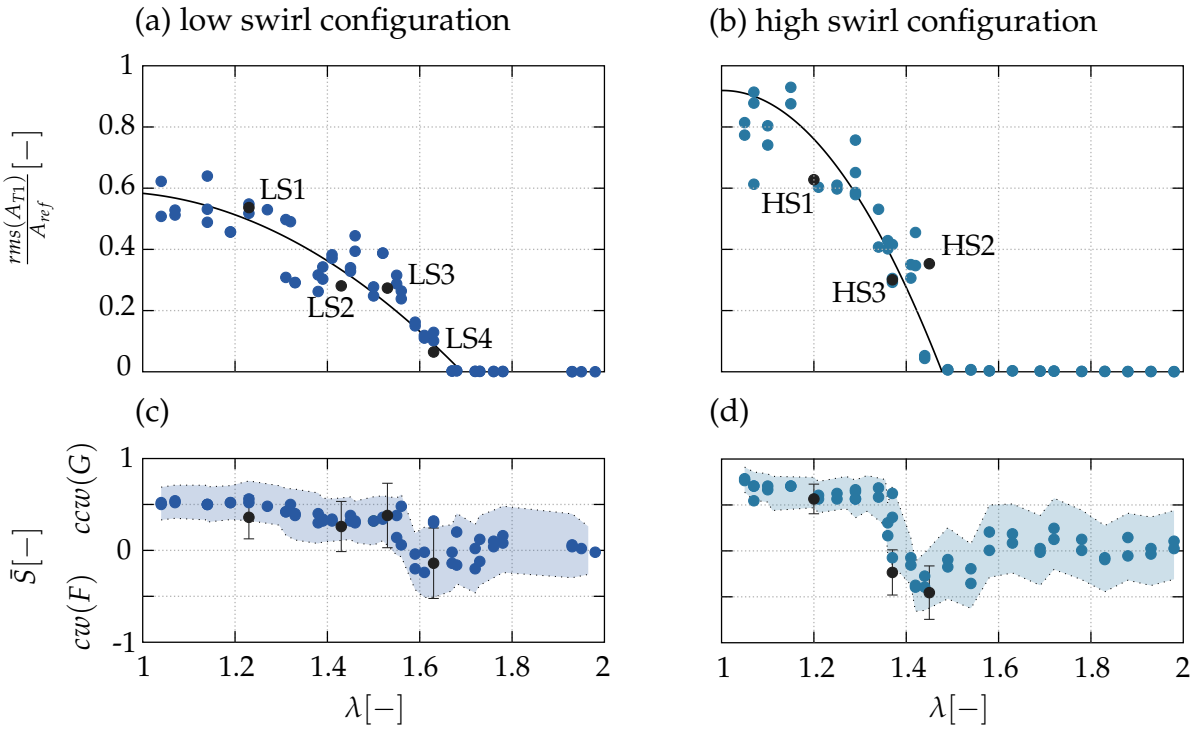


**Figure 4.3:** Bifurcation diagram for air-fuel equivalence ratio over the pulsation amplitude for the LS configuration (a) and HS configuration (b) (upper diagrams) and spin-ratio of the reconstructed first transverse mode - ccw is in swirl direction, cw is against swirl direction (lower diagrams).

amplitude at the critical air-fuel equivalence ratio representing the onset of instability. The amplitude rise follows a monotonically increasing function from bifurcation[3]. The HS setup converges into an instability at significantly lower air-fuel equivalence ratio $\lambda$ with respect to the LS setup (cf. Fig. 4.3). This observation supports the results presented in the previous Section 4.1.2 as well as of the conclusions in [59, 63]. Furthermore, two characteristics are observed, which were not discovered in previous works. First, the HS configuration reveals significantly higher pulsation amplitudes in the unstable regime. Second, both configurations show a different initial slope of the bifurcation curve at the onset of instability. The initial slope is steeper for the HS configuration and indicates a more rapid rise at pulsation intensity and thereby system instability.

To conclude, the categorization of A$^2$EV thermoacoustic stability states needs to consider both, (i) the onset of an instability in terms of critical air-fuel equivalence ratio, and also the (ii) amplitudes of the pressure pulsations. Hence, the marginally unstable LS operation points reveal an early onset of instability with respect to the critical air-fuel equivalence ratio, while the HS configuration has a larger stable operation window but significantly higher pulsation amplitudes for unstable conditions. To shed light onto the underlying mechanisms leading to this behavior, further detailed investigations of the thermoacoustic feedback are conducted for several representative unstable operation points with different air-fuel equivalence ratios in Section 6.1. The air-fuel equivalence ratios and pressure pulsation levels of those operation points are highlighted and annotated in Figure 4.3 (a, b) for both swirl configurations.

### 4.1.4 Acoustic Mode Dynamics

This section provides a parametric reconstruction of the occurring modal dynamics for the entire operation range in order to reveal a further thermoacoustic characteristic of the A$^2$EV swirl burner. These dynamics are shown in Figure 4.3 (c,d). As introduced in Section 3.1, the distribution of the spin-ratio $S$ (cf. Eq. 3.9) of the transverse acoustic mode is evalu-

[3]Note that the data was obtained by decreasing the air-fuel equivalence ratio from $\lambda = 2.0$ to 1.0, i.e. starting in the stable and ending in the unstable regime. An investigation of the detailed hysteresis behavior of the system can be found in [59].

ated for different air-fuel equivalence ratios, i.e. thermoacoustic stability states. In Figures 4.3 (c,d) the highest density and the standard deviation of the spin-ratio density distribution (cf. Fig. 3.3) are provided for each operation point.

At thermoacoustically stable operation conditions ($\lambda_{HS} > 1.47$, $\lambda_{LS} > 1.65$), the amplitudes $F(t)$ and $G(t)$ are equal, which results in a standing mode with a spin-ratio distribution $P(S)$ of zero [99, 136]. However, the dominance of stochastic flame noise at these conditions leads to a wide deviation of the spin-ratio distribution. In the marginally unstable region ($1.35 < \lambda_{HS} < 1.47$, $1.55 < \lambda_{LS} < 1.65$), the spin-ratio $S$ reveals both, predominantly counter swirl-wise and swirl-wise spinning acoustic modes. This signifies that the mean of the spin-ratio distribution $P(S)$ takes non-zero values, which can be both positive and negative. In these scenarios, the direction of rotation is random as the oscillation dynamics are mainly governed by uncorrelated combustion noise. Proceeding further towards stoichiometric combustion ($\lambda_{HS} < 1.35$, $\lambda_{LS} < 1.55$), the limit-cycle of the system reproducibly settles into the swirl-wise spinning mode $G$. Ultimately, the cause for these mode dynamics is a loss of degeneracy between the counter-rotating $F$ and $G$ modes and associated non-linear mode interactions. In addition, for the HS configuration the spin-ratio distribution mean is larger and the width narrower, which is due to increased loss of degeneracy with respect to the LS configuration. Details on mode interactions and loss of degeneracy can be found in [38, 98].

### 4.1.5 Summary and Conclusions - Swirl Combustor Response

The following conclusions can be drawn from the investigations of the A$^2$EV swirl combustor's acoustic response:

1. At specific combustor configurations, an instability of the first transverse acoustic mode in the 3000 Hz regime occurs. By varying the thermal power, all thermoacoustic stability states (stable, marginally unstable and limit-cycle oscillations) can be observed.

2. The thermoacoustic instability propensity significantly depends on the swirl number. While LS configurations show a higher tendency

towards developing an HF instability in terms of the critical air-fuel equivalence ratio $\lambda$ at instability onset, HS configurations reveal significantly higher pulsation amplitudes in the unstable regime. Hence, the onset of instability and the pulsation intensity need to be considered for the assessment of the thermoacoustic characteristics of the burner.

3. Thermoacoustically unstable operation conditions are always governed by a spinning transverse acoustic mode, which rotates in the direction of the swirling flow.

## 4.2 Reheat Combustor

This section discusses the acoustic responses of the reheat combustor. Two characteristic thermoacoustic dynamics are observed that reveal a distinct non-compact thermoacoustic feedback. These responses are associated with (i) a week thermoacoustic pulsation resulting from an intermittend/marginal instability in the 1600 Hz regime (cf. Sec. 4.2.1), as well as (ii) a self-excited and self-sustained limit-cycle oscillation[4] at approximately 3000 Hz (cf. Sec. 4.2.2).

### 4.2.1 Acoustic Response at the $\mathbf{T_{1y}}$ Resonance Frequency

Figure 4.4 (a) shows the frequency spectrum of a representative dynamic pressure time trace measured at the reheat combustor face-plate (cf. Fig. 2.7). The combustor was operated with a vitiator air-fuel ratio $\lambda_{VIT} = 2.41$, leading to a hot gas inlet temperature of $T_{RC,in} = 1487\,\mathrm{K}$ and a thermal power of the reheat combustion stage of $Q_{th,RC} = 603\,\mathrm{kW}$. The propane content in the fuel is $x_{C_3H_8} = 15\,\%$. The frequency spectrum shows two characteristic properties: (i) A widespread response in the LF regime and (ii) a distinct high frequency peak. The LF response appears at approximately $150 - 250\,\mathrm{Hz}$ and relates to the first longitudinal mode

[4] Thermoacoustic stability states and related characteristics of the acoustic pressure time series as discussed in Section 4.1 and indicated in Figure 4.1 are principally equal also for this combustor type. Hence, a repetitive discussion is omitted here.

$L_1$ as demonstrated in [80]. Varying either the pressure loss of the reheat combustor inlet orifice or the reheat combustor outlet nozzle area ratio (cf. Fig. 2.7) influences the amplitude and frequency of the longitudinal response. In the presented case high attenuation of the longitudinal acoustics is achieved, as intended for the specific combustor design (cf. Sec. 2.2). The reason why these longitudinal frequency peaks still occur is the forcing via (i) significant noise levels from the high power densities and (ii) possible feedback with the auto-igniting flame. It is assumed that synchronization effects with the combustion of the first-stage, as for example described in [75], are negligible. This is due to the first-stage combustor's high pressure losses alongside additional acoustic attenuation from the secondary air injection nozzles.

Desirable for the study of the non-compact HF flame response is the weak but clearly observable acoustic response at 1600 Hz, as it accurately matches the theoretical cut-on frequency in transverse y-direction (cf. Eq. 2.5). To allocate this HF peak to an acoustic mode, Figure 4.4 (b) shows the phase difference of the pulsation probes at the combustor face-plate to the reference sensor $P_{ref}$. For this illustration, the analytic signals (cf. Sec. 3.1) are retrieved from the raw pressure time series, which are bandpass filtered around the desired frequency (frequency band is indicated by green color in Fig. 4.4 (a)). This is followed by a calculation of the phase differ-

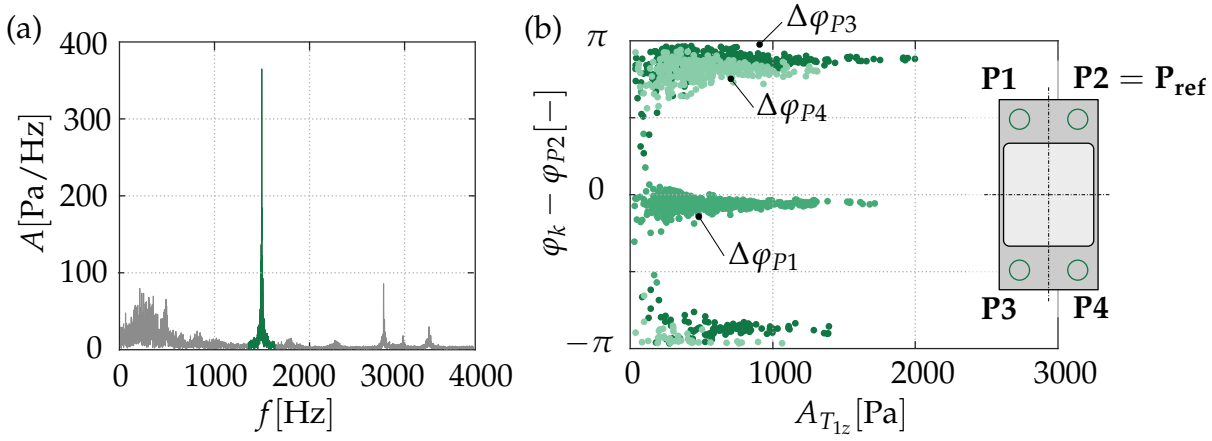


**Figure 4.4:** (a) Frequency spectrum of the dynamic pressure for marginal (in)stability obtained with $\lambda_{VIT} = 2.41$, $Q_{th,RC} = 602\,\text{kW}$ and $x_{C_3H_8} = 15\,\%$, (b) phase difference $\varphi_k - \varphi_{ref}$ of the pulsation probes at location P1, P3 and P4 relative to the reference sensor at location P2 of the reheat combustor face-plate over the pulsation amplitude.

ence $\varphi_k - \varphi_{P_{2,ref}}$ of the three remaining pressure sensors to the reference at location P2 (cf. insert in Fig. 4.4 (b)). All sensors show nearly constant phases over the pulsation amplitude and a phase shift of $\Delta\varphi = 180^\circ$ between the upper and lower sensor pair. The latter phase shift is a clear indicator for the fact that the oscillation frequency can be related to the first transverse combustor mode oriented in y-direction $T_{1y}$ (cf. coordinates of the reheat combustor provided in Fig. 2.7). While this mode identification relies only on the measured transducer data at the face-plate, the assumed mode shape and missing information of the longitudinal mode extend is confirmed by/retrieved from solving the respective FEM acoustic conservation equations, as presented in [80]. In addition, the $T_{1y}$ frequency response is independent of geometric modifications in downstream direction, i.e. independent of modifications of the outlet nozzle geometry [96]. This is a further indicator for a pure transverse mode (cf. Sec. 2.2.2), since it is known for decaying in axial direction as a result of the temperature gradient induced by the flame heat release [62, 105]. A parametric study revealed that the $T_{1y}$ response is not related to any specific geometrical combustor inlet or outlet configuration.

To further illustrate the low and high frequency combustor response, corresponding raw $p'$ and analytical $p'_{L_1}$ pressure time traces with envelope amplitude $A_{L_1}$, as well as the density distributions of the pressure $P(p'_{L_1})$ and envelope $P(A_{L_1})$ are provided in Figure 4.5 (a). The same is given for the $T_{1y}$ mode in Figure 4.5 (b). Filter bandwidths are $f_b \pm 250Hz$ around the frequencies of interest (cf. colored frequency band in spectra of Fig. 4.5). The LF fluctuations represent thermoacoustically stable conditions and appear to be primarily noise driven. This can be concluded from the resulting pressure density distribution $P(p'_{L_1})$, which shows a clear uni-modal shape. In contrast to this, the pressure density distribution $P(p'_{T_{1y}})$ for the first transverse combustor mode in Figure 4.5 (b) shows a clear trend towards a bimodal shape, which indicates a marginal thermoacoustic instability where acoustic damping and flame driving quantitatively balance. The related amplitude distribution $P(A_{T_{1y}})$ shows moderate trends, e.g. shifting mean and skew, towards a thermoacoustic instability. In contrast to this, the associated analytical time series $p'_{T_{1y}}$ show a dynamic growth of amplitude to a considerable level followed by an amplitude decrease (cf. envelope $A$ in Fig. 4.5 (a)). This can be interpreted

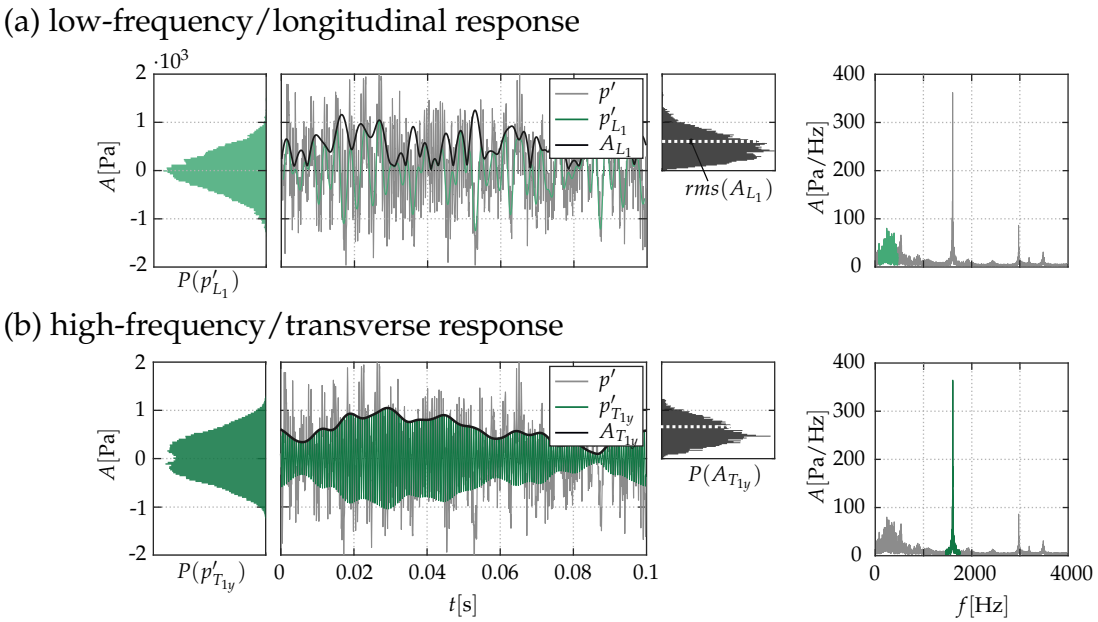


**Figure 4.5:** Comparison of the low frequency and high frequency combustor response. From left to right in the upper row (a): Probability density distribution of the analytical pressure signal $P(p'_{L_1})$, raw $p'$ and analytical $p_{L_1}$ time series of the acoustic pressure with envelope $A_{L_1}$, density distribution of the envelope $P(A_{L_1})$ with indicated root-mean-square of $A(p'_{L_1})$, and frequency spectra of $p'$ highlighting the frequency band for the band-limited Hilbert transform. The same is given for the $T_{1y}$ frequency in the lower row (b).

as another characteristic precursor for an onset of instability. However, a self-excited and sustained instability of the $T_{1y}$ mode was not observed for any of the examined operation conditions. Nevertheless, such marginal thermoacoustic (in)stability states represent ideal conditions for the application of external acoustic forcing. This forcing would add further monofrequent acoustic energy to the system to amplify the flame dynamics. This is appealing for investigations of the thermoacoustic feedback in an open-loop configuration for future studies [37]. It should be pointed out that a comprehensive framework (e.g. hardware, workflow, control schemes, post-processing methods) for such studies has been readily established in the course of the presented work. First campaigns were carried out and sample results were produced, which can be found alongside the description of the workflow in Appendix B.

### 4.2.2 Limit-Cycle Oscillations at the $T_{1z}$ Resonance Frequency

Specific reheat combustor configurations exist, which feature clear limit-cycle oscillation occurring at a frequency of approximately 3000 Hz. One of the main design goals of the reheat combustor experiment (cf. Ch. 2) was to achieve the occurrence of this HF instability. The system response of such a naturally unstable operation point is illustrated in Figure 4.6, where (a) shows the frequency spectrum and (b) the phase difference of all four sensors located at the reheat combustor face-plate to the reference sensor $P_{ref}$. Figure 4.6 (c) shows the corresponding raw acoustic pressure $p'$ and analytic[5] $p'_{T_{1z}}$ pressure time series measured at combustor face-plate location P2 (cf. Fig. 4.4) alongside their pressure and amplitude density distributions $P(p'_{T_{1z}})$ and $P(A_{T_{1z}})$. The data is retrieved for a vitiator air-fuel ratio $\lambda_{VIT} = 2.35$, translating into a reheat inlet temperature of $T_{RC,in} = 1507\,\mathrm{K}$. The thermal power of the second-stage reheat combustor is elevated to $Q_{th} = 769\,\mathrm{kW}$ and propane content in the fuel is $x_{C_3H_8} = 15\,\%$ per mass. Additionally, an orifice with an area blockage of 0.4 is applied at the reheat combustor inlet and a diffusor with a rounded rim (cf. Fig. 2.9) is installed at the sudden area expansion, i.e. combustion

[5]Filter bandwidths are $f_b \pm 250\,\mathrm{Hz}$ around the dominant transverse frequency $f = 3030\,\mathrm{Hz}$.

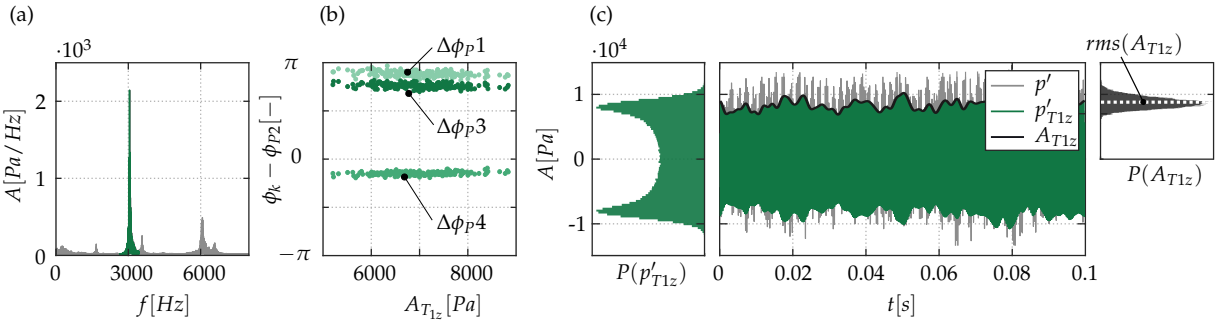


**Figure 4.6:** (a) Frequency spectrum of the dynamic pressure for the limit-cycle oscillations, (b) phase difference $\varphi_k - \varphi_{ref}$ of the pulsation probes at location P1, P3 and P4 relative to the reference sensor at location P2 of the reheat combustor face-plate over the pulsation amplitude, (c) probability density distribution of the analytical pressure signal $P(p'_{T_{1z}})$, raw $p'$ and analytical $p_{T_{1z}}$ time series of the acoustic pressure with envelope $A_{T_{1z}}$, and density distribution of the envelope $P(A_{T_{1z}})$ with indicated root-mean-square of $A(p'_{T_{1z}})$.

chamber face-plate. The combustor outlet is equipped with a nozzle (cf. Sec. 2.3.2).

The resulting frequency spectrum shows an isolated mono-frequent peak at 3030 Hz with a considerable amplitude. All previously observed frequency responses in the low- and high-frequency regime (cf. Fig. 4.4) remain at low amplitude levels. In accordance with Equation 2.4, this frequency indicates either an oscillation of the second transverse mode in y-direction $T_{2y}$, or the first transverse mode in z-direction $T_{1z}$. To unambiguously identify the mode type, phase differences of the individual pulsation probes at the combustor face-plate array are shown in Figure 4.6 (b). These are evaluated in the same way as outlined in the previous Section 4.2.1. The phase shift between the left (P1, P3) and right (P2, P4) located sensors indicate the first transverse acoustic mode oriented in z-direction $T_{1z}$ (cf. coordinates of the reheat combustor, Fig. 2.7). The pressure time series in Figure 4.6 (c) and corresponding density distributions reveal all characteristics of a saturated limit-cycle oscillation. The analytic pressure signal $p'_{T_{1z}}$ shows an oscillation with a considerable pulsation amplitude. Uncorrelated flow and flame noise levels are less significant in contrast to the previously discussed $T_{1y}$ acoustic response. Additionally, the pressure and the amplitude density distribution show a clear bimodal shape and a characteristic single-sided normal distribution, respectively. In contrast to the limit-cycle oscillations of the A$^2$EV swirl burner (cf. Fig. 4.1), it can also be observed that modulations of the envelope amplitude $A$, i.e. beating, are weaker. This can be mainly attributed to the absence of any rotating acoustic mode dynamics in the rectangular shaped reheat combustion chamber.

### 4.2.3 Effect of Reheat Combustor Configuration on the Thermoacoustic Instability Propensity

The previously introduced acoustic responses to the unsteady heat release at the $T_{1y}$ and $T_{1z}$ modes occurred for specific reheat combustor settings in terms of operational conditions and geometrical configuration. The question of which effect these configurations (i.e. thermal power, propane

blend, combustor geometry) have on the occurrence of the observed instabilities is addressed in the following:

**High thermal power levels** particularly impact the frequency response in the 3000 Hz regime. Specifically, it is observed that the $T_{1z}$ mode is thermoacoustically unstable beyond a certain thermal power level $Q_{th} > 690\,\mathrm{kW}$. The power dependence results from increased flame driving with rising power, which leads to an increase in the specific acoustic energy transfer from the flame to the mode [21, 44]. In contrast to this, the $T_{1y}$ response occurs reliably even in the low thermal load range but does not reveal characteristics of a limit-cycle oscillation for the investigated operation conditions.

**Increased propane content** in the natural gas fuel showed no impact on the $T_{1y}$ response. However, for the $T_{1z}$ mode, the instability propensity increases with the propane content. This suggests that flame driving is governed by modulation of the auto-ignition delay, because it has been found that auto-ignition is more likely to occur when fuel is blended with higher hydrocarbons (cf. Ch. 1) [24, 72, 137]. Adding propane to the fuel thus results in a more reactive auto-ignition zone leading to higher sensitivity of the flame response to pressure and temperature fluctuations. This effect can be inferred from Figure 4.7, which shows the pulsation amplitude of the $T_{1z}$ acoustic mode plotted over the air-fuel equivalence ratio $\lambda_{RC}$ (alters the thermal power) of the reheat stage. Different colors/symbols show different propane mass concentrations $x_{C_3H_8}$ in the fuel. It can be observed that $x_{C_3H_8} = 15\,\%$ leads to a significantly increased instability tendency of the reheat combustor in contrast to the $x_{C_3H_8} = 10\,\%$ case. However, increasing the propane content to $x_{C_3H_8} = 25\,\%$ does not show a further increase in the thermoacoustic instability propensity.

**Geometrical modifications** of the reheat combustor in- and outlets (i.e. inlet orifice and exhaust gas nozzle) as well as the diffusor geometry at the combustor face-plate have little effect on the $T_{1y}$ response. The same accounts for the $T_{1z}$ mode instability, except for the diffusor geometry. It is observed that a rounded diffusor rim ultimately leads to the limit-cycle oscillations of the reheat combustor. However, the effect of the diffusor geometry could not yet be clarified conclusively. It is assumed that acoustic attenuation is reduced by impacting the acoustically induced vortex

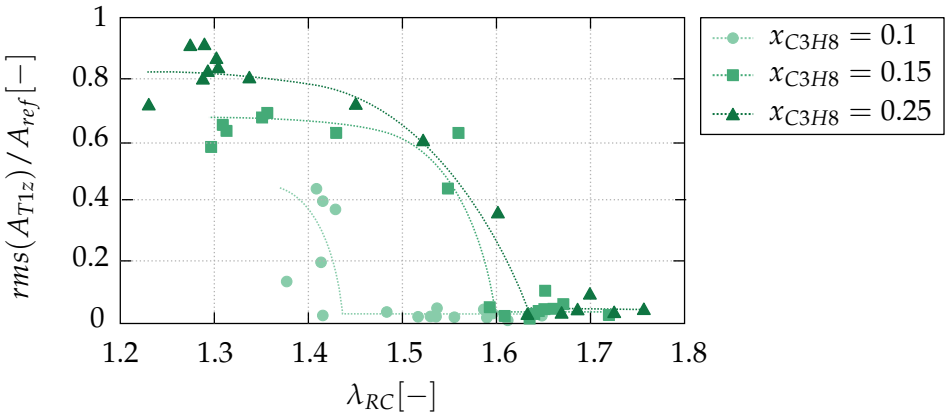


**Figure 4.7:** Bifurcation diagram of air-fuel equivalence ratio over the pulsation amplitude for different propane blends with natural gas fuel.

shedding at the mean flow separation point. Whether this assumption is correct or not, however, needs to be clarified in future work by e.g. acoustic PIV measurements of the shear layer zone.

Finally, an interesting observation is the presence of two potentially unstable modes, i.e. $T_{1y}$ and $T_{1z}$. A marginal response of the $T_{1y}$ mode is observed at moderate thermal power levels (cf. Fig. 4.4). From increasing the thermal power of the combustion, it can be concluded that this $T_{1y}$ response is intensified until it converges into a limit-cycle oscillation. However, this $T_{1y}$ instability does not occur, and instead, a self-excited $T_{1z}$ limit-cycle oscillation appears. Thus, it can be implied that the combustor contains two linearly unstable modes. The same has been observed in industrial gas turbine engines [22] and hampers effective mitigation strategies of thermoacoustic pulsations. This observation renders the lab-scale reheat combustor ideal for an investigation of the physical mechanisms behind multimodal interactions in future work.

### 4.2.4 Summary and Conclusions - Reheat Combustor Response

The section above focussed on the acoustic response of the reheat combustor. The key objectives of its discussion were (i) to establish a general characterization of the thermoacoustic behavior of the commissioned reheat combustor experiment and (ii) to identify suitable operation condi-

tions for the study of non-compact flame response phenomena as shown in the next chapter. Specifically, the following phenomena were observed:

1. Limit-cycle oscillations of the $T_{1z}$ mode occur at (i) high thermal power, (ii) elevated propane content in the natural gas fuel, and (iii) rounded diffusor rim of the reheat combustor.

2. Marginal instability of the $T_{1z}$ mode without a clear dependency on (i) thermal power, (ii) propane content, and (iii) geometry modifications was observed.

3. Suitability of the marginally unstable $T_{1y}$ mode for external acoustic forcing studies in an open-loop configuration was identified and a roadmap for future investigations established.

4. The limit-cycle and marginally unstable $T_{1z}$ and $T_{1y}$ responses imply that the reheat combustor features multiple linearly unstable modes. This reflects a common characteristic also found in industrial combustors. Thereby, the reheat experiment presents an ideal setup to pursue further research work on this industrially relevant issue of multimodal interactions.

# 5 Non-Compact Flame Response

This chapter discusses the observed non-compact flame modulations associated with the previously introduced system responses (cf. Ch. 4) of both, the swirl (cf. Sec. 5.1) and the reheat (cf. Sec. 5.2) combustor. The key objectives for the two setups are to identify the phenomenological and physical occurrences of the non-compact flame driving that cause the HF pressure pulsations.

## 5.1 Swirl Stabilized Flame

First, general phenomenological observations in terms of local modulations of the flame heat release with the acoustic pressure are presented in Sections 5.1.1 and 5.1.2. Decompositions of the modulated heat release fields, treated in Sections 5.1.3-5.1.5, allow to comprehend the associated physical mechanisms. Afterwards, the flame modulations for the low- and high-swirl configurations are compared to each other in Section 5.1.6. Experimentally obtained heat release oscillation fields are used to validate analytical source term expressions in Section 5.1.7.

### 5.1.1 General Observations

The investigation of the flame response relies on operating the swirl combustor in the thermoacoustically unstable regime[1]. In this regime, both the marginally unstable and saturated limit-cycle conditions were assessed by evaluating highly time resolved acoustic and flame CL signals as well as by decomposing coherent flame oscillation patterns from these mea-

[1] Results are obtained by investigating the naturally unstable regime in a closed-loop configuration only. Externally forced flame responses have not been explicitly studied within this work. An example for an externally forced flame response can be found in [115].

surements. This section focusses on the marginally unstable low-swirl operation point indicated in Figure 4.2 (a). These conditions allow the flame modulation to be studied at low amplitudes, which represent the onset of instability, a topic of major interest in engineering [20, 21].

As discussed in Chapter 4, the swirl combustor develops a thermoacoustic instability of the first transverse acoustic mode in the combustion chamber, which oscillates at a frequency of $f_{T1} \approx 3000\,\text{Hz}$. In Figure 5.1 (a) the sample frequency spectrum of the acoustic pressure for a marginal instability (cf. Fig. 4.2) is supplemented with the corresponding frequency spectrum of the flame OH$^\star$ CL fluctuations (cf. Sec. 2.4 for details of the diagnostics). Due to the perfectly premixed operation mode of the A$^2$EV combustor, the OH$^\star$ CL data can be taken as an indicator of the spatio-temporal dynamics of the combustion heat release. In order to obtain the given frequency spectra of the heat release fluctuations, the symmetry of the acoustic modes/non-compact feedback in the HF regime must be taken into account. The investigated first transverse acoustic field is axially antisymmetric, i.e. $p'(y) = -p'(-y)$. As a result, typically obtained time series of the volume integral of the instantaneous heat release oscillations

$$\int_V \int_t I'_{CL}(\mathbf{x}, t) dV dt \approx 0 \tag{5.1}$$

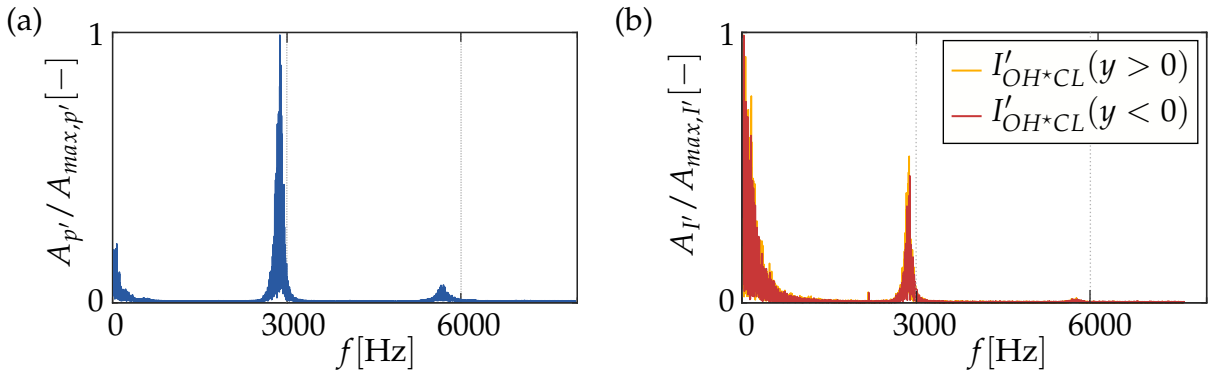


**Figure 5.1:** Frequency profile of the (a) pressure and (b) heat-release oscillations (indicated by the flame OH$^\star$ CL signal integrated over the upper $y > 0$ and lower $y < 0$ flame volume). Signals are obtained for an A$^2$EV operation point exhibiting a marginal thermoacoustic instability of the first transverse acoustic mode in the combustion chamber.

would always approximate to zero (e.g. by recording the global flame CL with a photomultiplier). Hence, investigating the flame response to the first transverse acoustic mode requires consideration of only half of the flame volume, i.e.

$$\tilde{I}'_{CL}(y < 0) \quad \text{or} \quad \tilde{I}'_{CL}(y > 0), \tag{5.2}$$

where

$$\tilde{I}'_{CL}(y) = \int_z \int_x I'_{CL}(x, y, z) dx dz. \tag{5.3}$$

This is necessary to resolve the local, i.e. non-compact, oscillations which would otherwise be masked by their axially opposing counterpart. The spectra of the heat release fluctuation in Figure 5.1 (b) are obtained from time series of the integrated upper and lower half of the flame CL data. It can be observed that the heat release oscillations respond at the frequency of the acoustic pulsations with a significant amplitude compared to the stochastic fluctuations close to the 0 Hz regime. In addition to this, absolute intensities of the heat release response are equal for both flame halves. This non-compactness, i.e. multi-dimensionality, of the heat release oscillations comprises one of the main differences to longitudinal LF thermoacoustic oscillations. In the latter, heat release oscillations are usually considered compact and have no spatial variability in transverse direction.

The time series of the integrated heat release fluctuations allow the visualisation of further characteristics of the non-compact flame acoustic interaction. These are presented in Figure 5.2 (a,b). Each marker in this figure represents an $OH^\star$ CL image, volume integrated over the upper flame half, i.e. $\tilde{I}'_{CL}(y > 0)$. In addition, these are linked to the synchronously recorded acoustic pressure signal at the $A^2EV$ probe location $P1$ (cf. Fig. 2.1). Figure 5.2 (a) shows the $OH^\star$ CL oscillation amplitude $\tilde{I}'(y > 0)/I_{\max}$ over the phase $\varphi_{p'}$ of the acoustic pressure signal. The color code indicates the associated pressure amplitude. Both, the acoustic and flame signals, are bandpass filtered around the frequency of the first transverse combustor mode. The insert shows the oscillation of the acoustic pressure at probe location $P1$ for high (red curve) and low (blue curve) pulsation amplitudes.

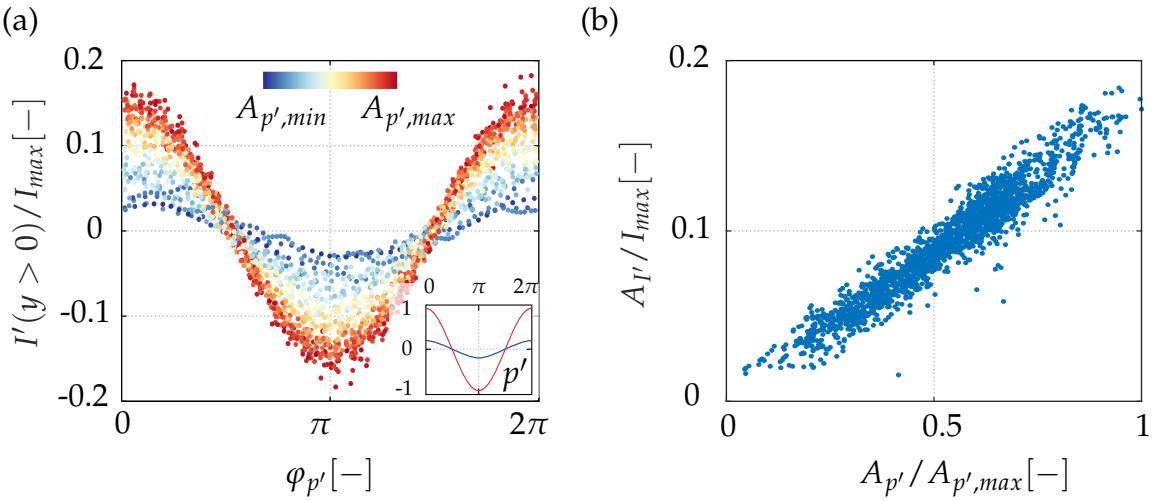


**Figure 5.2:** (a) Integral flame heat release intensity oscillations from OH* CL recordings over the pressure phase measured at A$^2$EV face-plate position P1, color coded with pressure envelope amplitude. Insert in (a) shows the corresponding pressure oscillation at location P1. (b) Amplitude of the heat release intensity oscillations over the pressure pulsation amplitude.

First, Figure 5.2 indicates that the heat release perturbations exhibit a constant angular frequency. Second, relating the flame and acoustic signal shows that the heat release oscillations directly respond to the acoustic pulsations, both in terms of phase and amplitude. The pressure oscillation in the insert shows that the heat release oscillates in-phase with the acoustic pressure (both signals show an antinode at $\varphi = \pi$). This in-phase situation is independent of the pulsation amplitude, as revealed from the color coding with the envelope amplitude. It can be additionally observed that the heat release oscillation amplitude spreads over a certain range. This is interesting, as the color coding shows high heat release oscillation amplitudes to be associated with high pressure pulsations. This coherence is further visualized in Fig. 5.2 (b), showing the amplitude relation of flame and acoustic oscillations at the frequency of the first transverse acoustic mode. During the investigated naturally unstable operation, flame intensity oscillations are linearly proportional to the acoustic pressure amplitudes even at high modulation intensity.

### 5.1.2 Phase-Conditional Heat Release Oscillations

The previous results provided general insight into the time series characteristics of the oscillating heat release during unstable swirl combustor operation. The following investigations focus on phase-locked ensemble averaged OH* CL distributions. It is of primary interest to find out how the flame locally responds to the instantaneous transverse acoustic field. To simplify interpretations, time averaged OH* CL distributions are provided first in Figure 5.3. The raw OH* CL measurement in Figure 5.3 (a) is line-of-sight integrated. As the time averaged swirl flame appears to be rotationally symmetric, deconvolution via the inverse Abel transform allows to visualize the two-dimensional cut-plane of the CL distribution in Figure 5.3 (b). This view shows a typical V-shaped swirl flame brush with high local CL in the inner shear layer. The flame OH* CL intensity towards the outer recirculation zone remains at very low levels, which is a typical characteristic of the A$^2$EV burner [61].

In a subsequent step, line-of-sight ensemble averages are obtained from the OH* CL images dependent on the acoustic pressure phase. Phase-locked ensemble averaging is carried out for a total of 12 phase intervals, representing the thermoacoustic oscillation cycle. Figure 5.4 shows example results of phase-locked averages. The images correspond to the bins with an average pressure phase of $\varphi_{p'} = 0, \frac{1}{2}\pi, \pi$ and $\frac{3}{2}\pi$, respectively. The provided conditional averages belong to the pressure data shown in

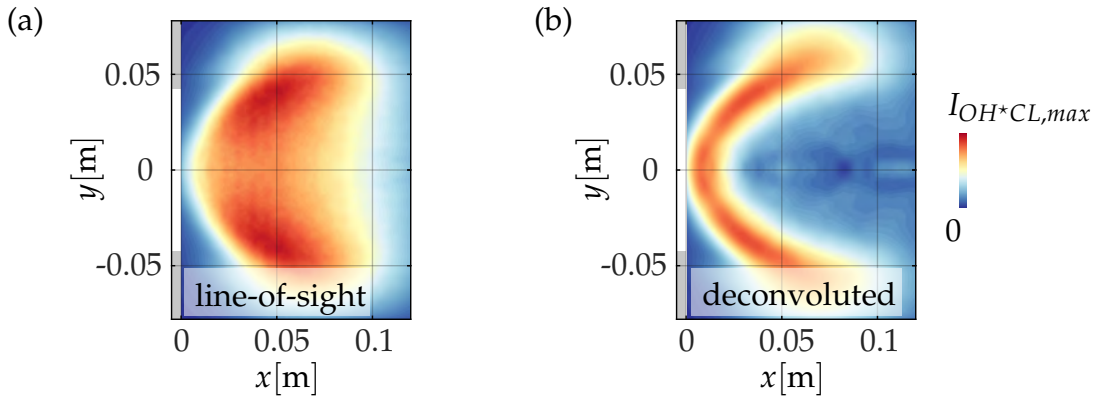


**Figure 5.3:** (a) Line-of-sight integrated and time averaged OH* CL recording, (b) deconvolution of (a) via inverse Abel transform.

Figure 4.2 (a) alongside the synchronously recorded OH* CL image series. This comprises 23 536 frames captured with an acquisition frequency $f_I = 15\,000$ frames/s. Due to the differing frequencies of the acoustic oscillation and the image acquisition, the phase angle $\varphi_{p'}$ is uniformly distributed in the sampled data. For each phase-locked average, 800 individual frames are selected, which are associated with a pressure phase within a specified interval of $\Delta\varphi \approx \pm 5°$ (cf. Fig. 3.4). To predominantly capture the linear flame response, images with a high corresponding pressure envelope amplitude $A_{p'} > 0.75 \cdot A_{p',max}$ are excluded from the analysis to avoid inclusion of non-linear saturation effects. In addition to this, the time averaged distribution $\bar{I}$ (cf. Fig. 5.3 (a)) is subtracted from each conditional average $I_\varphi$ to visualize the fluctuating heat release component, i.e.

$$I' = I_\varphi - \bar{I}. \tag{5.4}$$

The location of the reference pulsation probe is annotated with $P1$ in the first image. Hence, each conditional average can be interpreted as a line-of-sight distribution of the fluctuating OH* CL signal at specific instants of the transverse pressure field in the vicinity of the face-plate.

The resulting oscillation cycle confirms the characteristics also observed in Section 5.1.1. The distributed heat release oscillations indicate that the flame responds in-phase with the acoustic pressure. For the phase-locked distributions belonging to $\varphi_{p'} = 0$ and $\pi$, the acoustic pressure is at its

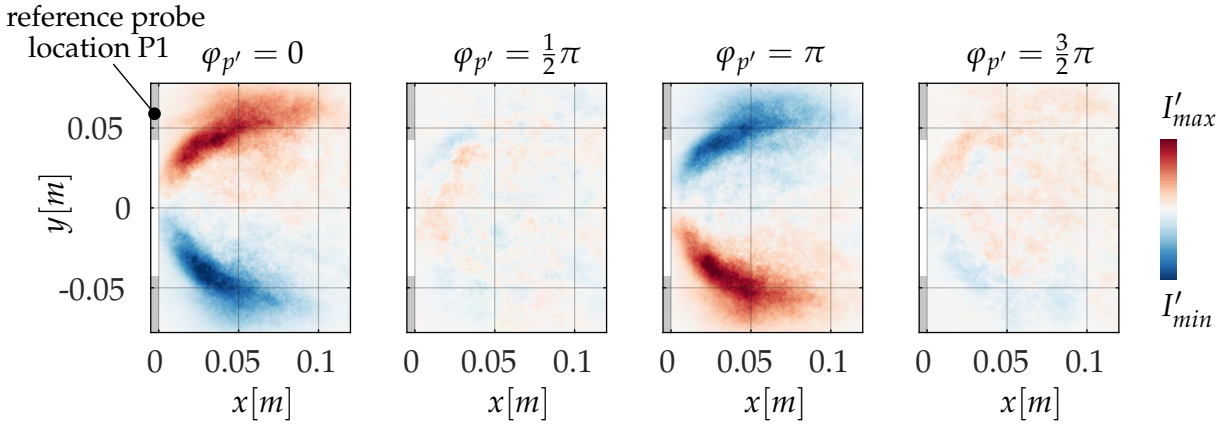


**Figure 5.4:** Phase-locked ensemble averaged OH* CL images (line-of-sight integrated) for four different phase bins of the associated acoustic pressure signal at reference location P1.

maximum and minimum at the upper and lower image half, respectively. Furthermore, the local heat release fluctuations are of opposite phase in the upper and lower zones and are close to zero for $\varphi_{p'} = \frac{1}{2}\pi$ and $\frac{3}{2}\pi$, which shows the previously discussed axial antisymmetry. The resulting pattern would thus lead to a zero heat release oscillation if integrated over the entire flame volume (cf. Eq. 5.1) and demonstrates that the HF thermoacoustic heat release oscillations are non-compact. This is a major difference to the LF situation (cf. Ch. 1), which is why the spatial distribution of the flame response needs to be taken into account for thermoacoustic system analysis.

Concluding the foregoing evaluation, Figure 5.5 shows (i) the standard error (error bars and shaded region) with (ii) the average oscillation intensity obtained from the upper and lower half of each of the 12 phase-locked ensemble averages. Both, the oscillation amplitude and its variance demonstrate that stochastic fluctuations of the heat release are small compared with the coherent flame response to the transverse pressure pulsations. For all phase bins evaluated, the standard error of the intensity fluctuations is an order of magnitude lower than the average oscillation intensity. Alongside with the observed constant angular frequency of the coherent heat release perturbations, these properties justify to further advance the post-processing of the obtained flame images (cf. procedure details in Ch. 3).

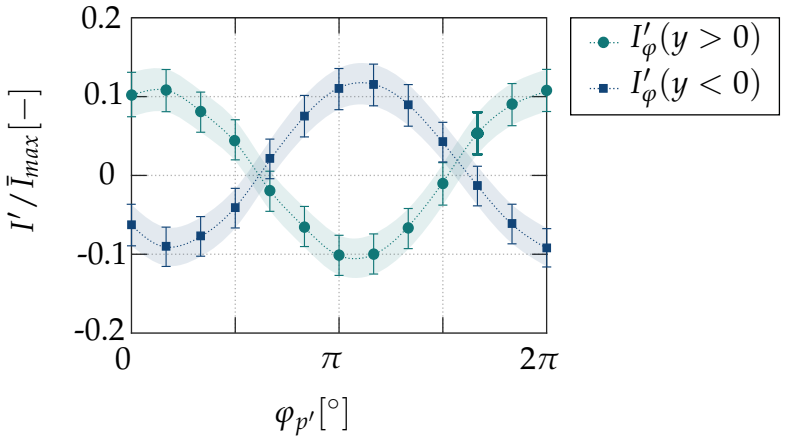


**Figure 5.5:** Oscillation intensity obtained from line-of-sight phase-locked averaged OH* CL distributions integrated over the upper and lower flame half. Shaded region indicates standard error.

### 5.1.3 Tomographic Reconstruction of the Distributed Heat Release Oscillations

To investigate the flame feedback phenomena in more detail, two-dimensional cut-plane views of the oscillating heat release are of interest. This is achieved by tomographic reconstructions of the perturbed flame. Starting point for the tomographic reconstruction (cf. Ch. 3) is the evaluation of the distributed Fourier coefficient. Sample results of the real part and phase of the Fourier coefficient $Re(I_{\mathcal{F}})$ and $\angle(I_{\mathcal{F}})$ are illustrated in Figure 5.6 (a), which originate from the data set used in Section 5.1.2. The Fourier coefficient comprises the amplitude and phase distribution of the line-of-sight integrated heat release oscillations through different viewing angles. The acquisition of the different viewing angles is straightforward with the A$^2$EV setup, since the modulated swirl flame and the associated transverse acoustic mode rotate around the central axis and can therefore

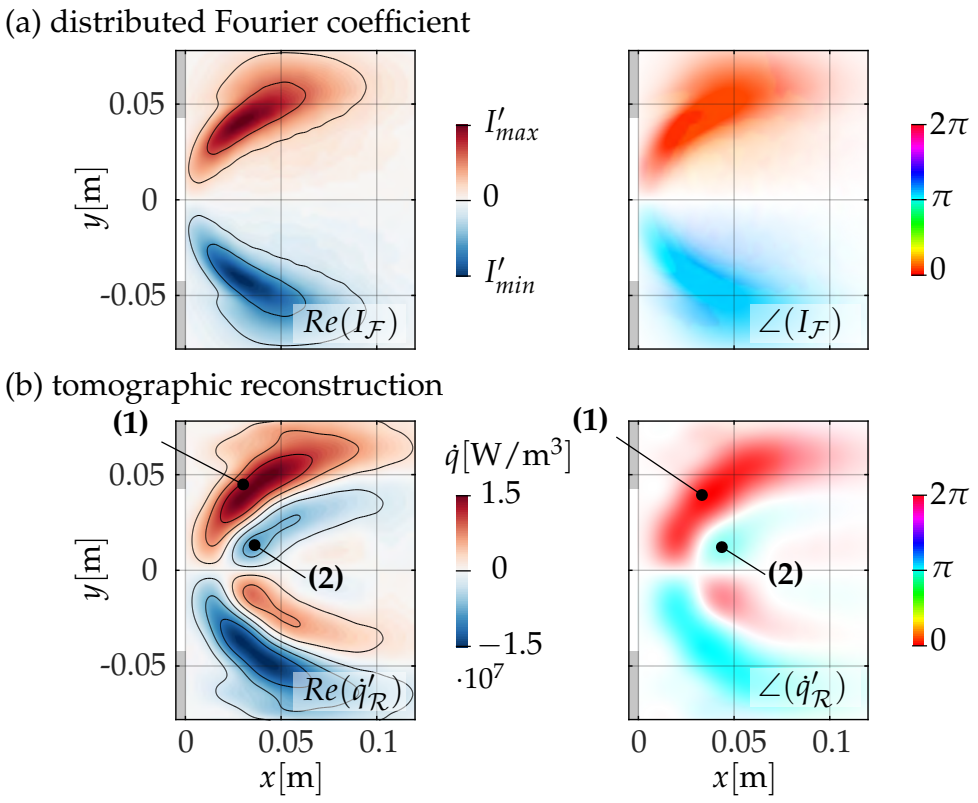


**Figure 5.6:** Real part and amplitude weighted phase of (a) the distributed Fourier coefficient as well as (b) the tomographic reconstruction (scaled with the K-factor (cf. Eq. 3.13)) of the modulated swirl flame.

be captured by means of the fixed camera. In principle, the Fourier coefficient provides the same information as the phase-locked conditional averages (cf. Fig. 5.4) and can therefore be used equivalently up to this point. However, the Fourier coefficient is necessary as input for the further post-processing via the Radon transform (cf. Ch. 3).

Evaluating the Radon transform allows to reconstruct the three-dimensional structure of the perturbed flame and thereby to obtain two-dimensional cut-plane views of the heat release oscillations. To obtain also a quantitative estimate, the resulting maps are scaled with the K-factor (cf. Eq. 3.13). The resulting real part $Re(\dot{q}'_{\mathcal{R}})$ and phase $\angle(\dot{q}'_{\mathcal{R}})$ distributions of the tomographic reconstruction are shown in Figure 5.6 (b). These distributions can be interpreted as follows: Structures with opposing phases can be identified on both, the upper and lower image half of Figure 5.6 (b) in the vicinity of the inner flow recirculation zone. Consequently, the 180 ° phase shift translates into positive and negative local heat release oscillations. Red regions in Figure 5.6 (b) locally add energy to the total heat release (cf. Fig. 5.3 (b)) and vice versa for blue regions. Heat release oscillations are most intense close to the face-plate in the inner shear layer (cf. (1) in Fig. 5.6 (b)), where the first transverse acoustic mode reveals locally elevated acoustic pressures. For the upper half of the image, negative heat release oscillation regions can be observed in the downstream flame root of the inner recirculation zone (cf. (2) in Fig. 5.6 (b)). Positive and negative heat release oscillations occur in the upper and lower part of the image. However, the positive heat release outperforms the negative contribution in the upper image half and vice versa for the lower half. Under consideration of the transverse pressure field and the positive acoustic pressure at reference location $P1$, this results in a positive Rayleigh integral (cf. Eq. 1.1) and leads to a situation where the heat release oscillations add energy to the acoustic field.

The previous results illustrated the cut-plane view through the locally modulated swirl flame. The applied decomposition approach results in the visualization of the overall heat release modulation. Previous works [59, 67, 69] suggest that the non-compact thermoacoustic feedback results from a superposition of different individual flame response phenomena. A clear pattern, which is already recognizable in the raw $OH^{\star}$ CL data, is the periodic flame displacement [57]. At this point the question

arises, whether the results are governed only by this displacement phenomenon or whether they are composed of further contributing mechanisms. For this reason, the distributed heat release perturbations caused by the transversal displacement of the flame is only evaluated on the basis of a covariance analysis as presented in the following section.

### 5.1.4 Extraction of the Flame Displacement

The observation of a periodic transverse motion of the flame brush with the pressure pulsation frequency (first described in [57]) motivates the extraction of displacement vectors from the flame OH$^\star$ CL measurement. An example of this flame motion is shown in Figure 3.9. In order to obtain the coherent flame motion, instantaneous OH$^\star$ CL images are binarized to extract only the flame structure from which a difference image is obtained afterwards as described in detail in Chapter 3. The resulting motion of the binarized flame images is visualized in Figure 3.9 (b). The distribution illustrates a significant flame displacement off its mean position in transverse y-direction.

Figure 5.7 shows the previously introduced line-of-sight integrated heat release oscillations from the phase-locked averaged OH$^\star$ CL images (cf. Fig. 5.4). In addition to this, these images now contain the vectors of the temporal flame motion. To identify the superposed vector fields, image post-processing was performed as outlined in Section 3.3. For improved visualization, the oscillating velocity is shown instead of the displacement vector, which is linked by $\mathbf{u}' = \partial\Delta'/\partial t$ and results in a 90 $^\circ$ phase shift. From this oscillation cycle, the flame motion off its mean position towards the positive pressure antinode and the displacement in-phase with the acoustic pressure can be observed. It can be concluded that there is a significant displacement of the fluid flow (and thus the reaction zone) with the transverse acoustic velocity. The link to the acoustic velocity is further confirmed by the spatial variability of the displacement field obtained through the flame motion, which shows a bend in transverse direction and decrease of the vector length towards the upper/lower combustor zone at the face-plate. This coincides with acoustic field variables of the transverse acoustic mode shown in e.g. [114].

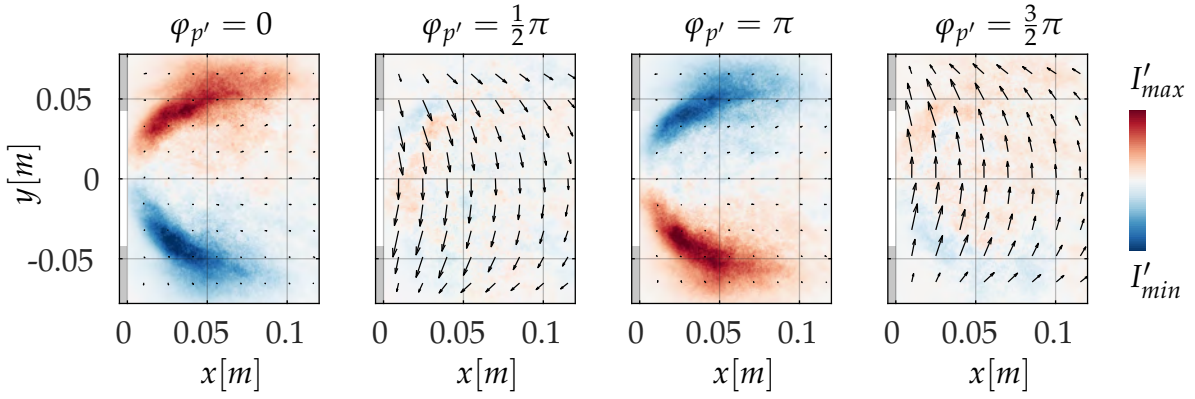


**Figure 5.7:** Oscillation cycle of the line-of-sight integrated heat release superposed with related velocity vector fields $\mathbf{u}' = \delta\Delta'/\delta t$ indicating the flame displacement/motion. Vector fields are obtained from through OH*CL image covariance analysis.

Figures 5.8 (a,b) show the phase and amplitude dependence of the displacement effect in the same fashion as introduced in Section 5.1.1 (cf. Fig. 5.2). For illustration, the flame displacement is evaluated in y-direction for each time step, i.e. each individual covariance reconstruction of an image pair, in a small sub-region containing the flame front (cf. Fig. 3.9 (b)). This allows to correlate the oscillations and the derived magnitude of the flame displacement with the acoustic pressure amplitude and phase. Two dis-

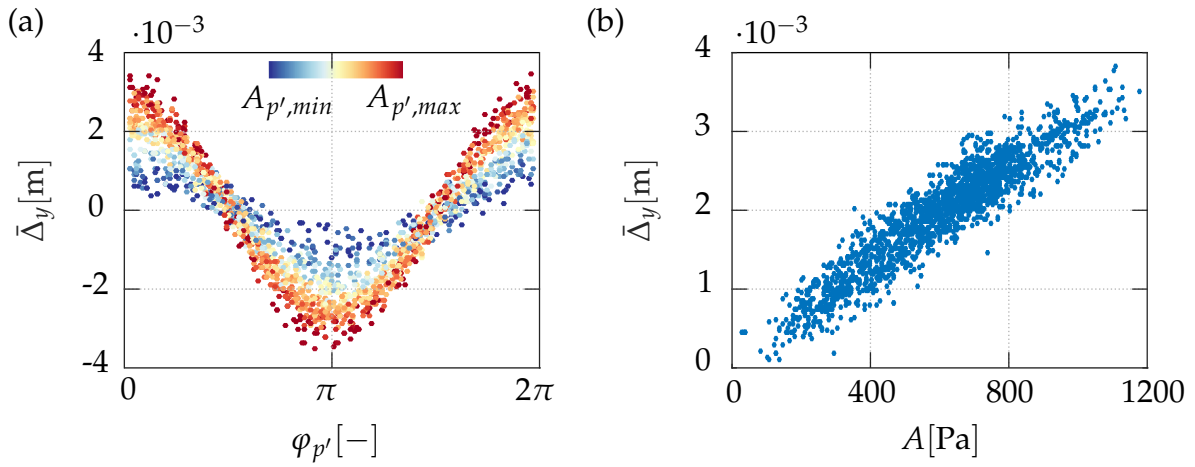


**Figure 5.8:** (a) Flame displacement oscillations from OH*CL image covariance analysis over the pressure phase measured at A$^2$EV face-plate position P1, color coded with related pressure envelope amplitude, (b) amplitude of the flame displacement over the pressure envelope amplitude.

tinct features are observable, which are (i) a linear proportionality of the y-displacement magnitude to the acoustic pressure amplitude as well as (ii) the characteristic oscillatory motion of the displacement as already observed for the overall heat release oscillations in Fig. 5.2. These preceding observations support the assumption of flame coupling with the acoustic velocity by an in-phase periodic heat release displacement, which is a non-compact thermoacoustic driving mechanism.

In the following, the flame displacement fields are used to visualize the heat release oscillations due to the displacement mechanism. These are reconstructed by locally displacing the mean heat release field (cf. Fig. 5.3) by the displacement vector field (cf. Sec. 3.3). The real part $Re(\dot{q}'_\Delta)$ and the phase $\angle(\dot{q}'_\Delta)$ distribution resulting from the complex denoted reconstruction are provided in Figure 5.9. The results show a flame displacement towards the pressure maximum within the upper image half. Indicated by the dashed lines (cf. Fig. 5.9 (1)), a shift of the mean flame off its axis hence increases the local heat release towards the outer and reduces it towards the inner recirculation zone. In other words, displacing the mean flame locally adds heat in regions of positive gradients, and vice versa. This results in heat release oscillations with opposing phases in each flame half leading to thermoacoustic driving and damping according to Rayleigh's criterion (cf. Eq. 1.1). It can be further observed that the resulting heat release distribution in Fig. 5.9 (a) differs from the general heat release oscil-

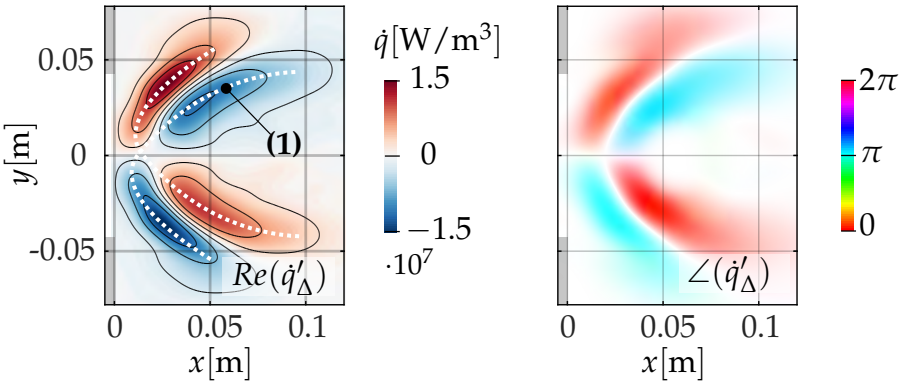


**Figure 5.9:** Distributed heat release oscillations resulting from local flame displacement of the mean heat release field: Left hand side shows the real part (scaled with the K-factor (cf. Eq. 3.13)) and the right hand side the associated amplitude weighted phase.

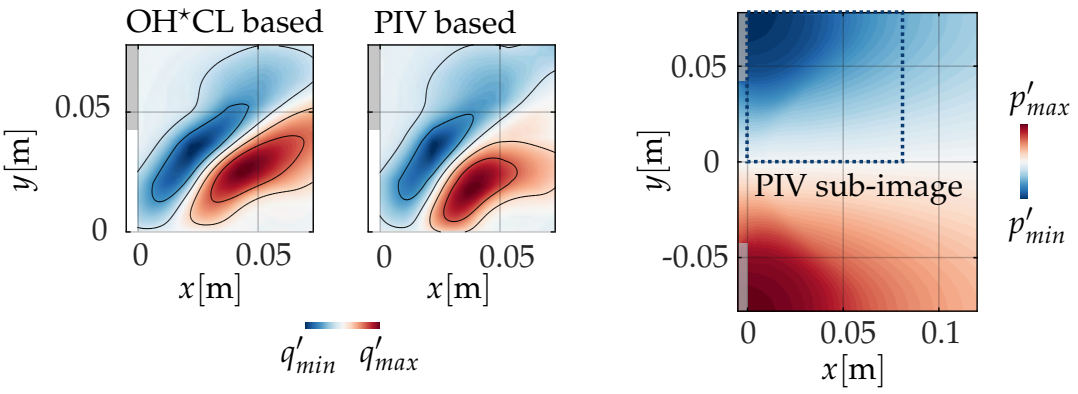


**Figure 5.10:** Resulting spatial heat release oscillations based on OH*CL recordings and acoustic PIV data along with sample acoustic pressure distribution to indicate regions of flame acoustics interaction, as well as PIV sub-image position.

lation map obtained via the tomographic reconstruction (cf. Fig. 5.6 (a)). This is highest towards the positive pressure antinode and the negative contribution towards the centerline is less significant in contrast to the heat release distribution governed by the displacement field. This underlines the assumption that the swirl flame response is composed of multiple interacting non-compact flame response mechanisms. This observation is further discussed in Section 5.1.5.

Retrieving the heat release oscillation by flame displacement on basis of the perturbed flame CL images (instead of PIV velocity fields) is motivated by (i) a simpler measurement setup, (ii) the advantage given when evaluating the flame motion instead of the acoustic velocity (thus independent of any a priori root cause assumption), and (iii) the availability of a broad experimental data base. In order to compare (and validate) these results to the flow field displacement governed by the acoustic velocity, acoustic particle image velocimetry (PIV) is carried out synchronous to the flame CL and acoustic pressure measurements. Due to measurement constraints of the PIV setup, only a small sub-image is recorded for evaluation. Resulting heat release oscillation fields of the OH*CL and acoustic PIV based displacement patterns are provided in Fig. 5.10. It can be seen that the patterns of the heat release oscillations are consistent with both measurement methods. Differences occur mainly at the downstream position at the inner shear layer zone. These can be attributed to the mislead-

ing information from correlating line-of-sight integrated, unsteady flame chemiluminescence data according to the OH* CL images. However, taking the transverse pressure field into account for the flame response, the zone with larger errors loses importance because local pressure fluctuations are low. The heat release oscillations occurring in the vicinity of the outer recirculation zone towards the face-plate are nearly equal to those obtained from acoustic PIV measurements. These regions are of inherent interest as high pressure pulsation intensities, and thereby strong interactions of flame and acoustics, are observed here. In conclusion, both methods, the OH* CL measurements and acoustic PIV, used to analyze the heat release oscillations by acoustic displacement, lead to the same result. However, the advantage of the OH* CL measurements is that they do not require any a priori assumptions. Thus, it is possible to use the flame CL based results as an unambiguous confirmation of the PIV based observation of flame displacement with acoustic velocity.

### 5.1.5 Thermoacoustic Response due to Flame Displacement and Deformation

From the preceding investigations, two heat release oscillation patterns have been obtained. These are (i) the overall heat release oscillations via tomographic reconstructions and (ii) the heat release oscillations from acoustic flame displacement via the covariance analysis. Both rely on recorded flame OH* CL image series. The tomographic reconstruction can be interpreted as the superposition of all flame modulation effects. Thus, from the discrepancies between the two heat release oscillation patterns, a remaining residual can be obtained by subtracting the displacement flame modulation pattern $Re(\dot{q}'_{\Delta})$ from the overall, i.e. tomographically reconstructed, heat release oscillation $Re(\dot{q}'_{\mathcal{R}})$. The subtraction $Re(\dot{q}'_{\mathcal{R}} - \dot{q}'_{\Delta})$ yields a remaining field $Re(\dot{q}'_{\rho})$. The two original distributions, as well as the subtraction are shown in Figure 5.11.

In accordance with the findings presented in [38, 44, 67] the remaining fluctuating heat release field portrays the spatial interference of the transverse acoustic pressure oscillations with a periodical flame deformation. The flame's up- and downward motion induced by the displacement field

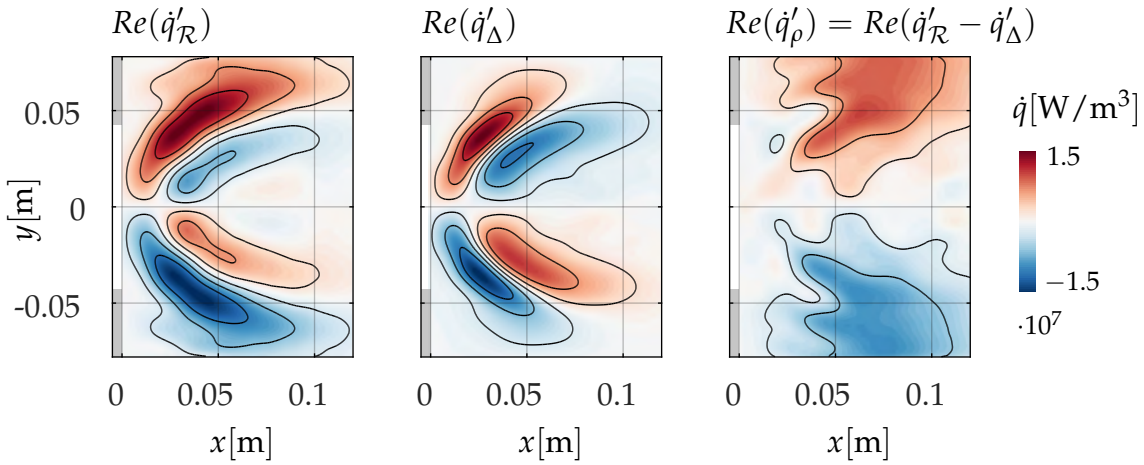


**Figure 5.11:** Heat release oscillation fields obtained via tomographic reconstruction, covariance analysis, and substraction of the former two fields.

causes a local compression and expansion of the heat release field towards the outer recirculation zones. Interaction of the transverse acoustic pressure field with the deforming flame leads to an increased volumetric heat release rate for the locally compressed region and vice versa for the expanding flame region. This effect is demonstrated by the red area (with positive values) in the $Re(\dot{q}'_{\rho})$ field of Figure 5.11, spatially coherent with the high local pressure of the transverse acoustic mode. The opposing effect can be observed for the blue area in the lower half of the field. Hence, with the periodic deformation of the flame, a thermoacoustic feedback loop in agreement with Rayleigh's criterion (cf. Eq. 1.1) is established. In addition to observing this phenomenon, it is interesting to find that the obtained oscillating heat release fields in Figure 5.11 both qualitatively and quantitatively agree with analytic expressions for the displacement and deformation mechanisms in [38, 44]. This validation is further addressed in Section 5.1.7.

To conclude the above discussions, the interactions of three basic phenomena were observed and for the first time successfully visualized from experimental data obtained with the A$^2$EV swirl combustor:

1. Transverse displacement of the flame brush by the acoustic velocity.
2. Local deformation of the flame shape due to the acoustic displacement field.

3. Increased/decreased volumetric heat release rates at regions of high compression/expansion of the deformed flame.

### 5.1.6 Impact of the Swirl Number on Non-Compact Flame Response

The observations of the acoustic response of the A$^2$EV swirl combustor in Chapter 4 revealed a dependence of the thermoacoustic stability on the swirl number (cf. Figs. 4.2 and 4.3). However, the swirl influence on the thermoacoustic driving of the flame has not yet been discussed. Inspection of the distributed heat release oscillations associated with both swirl configurations yield different thermoacoustic driving potentials. For this purpose the distributed Rayleigh indices are calculated (cf. Eq. 1.2). The input variables are the oscillating heat release fields $\dot{q}'(\mathbf{x})$ from tomographic reconstruction and acoustic mode shape $p'(\mathbf{x})$ from FEM computations [44], all of which are provided in Figure 5.12.

The Rayleigh indices reflect the typical characteristics of the heat release oscillation pattern of the swirl flame (cf. Sec. 5.1.5) for both, the HS and LS operation point. Specifically, the thermoacoustic response of the HS flame results in a driving potential increase of 35 %, which is obtained by spatially integrating the Rayleigh indices. The reason for this can be mainly attributed to the altered flame shape, and thereby the heat re-

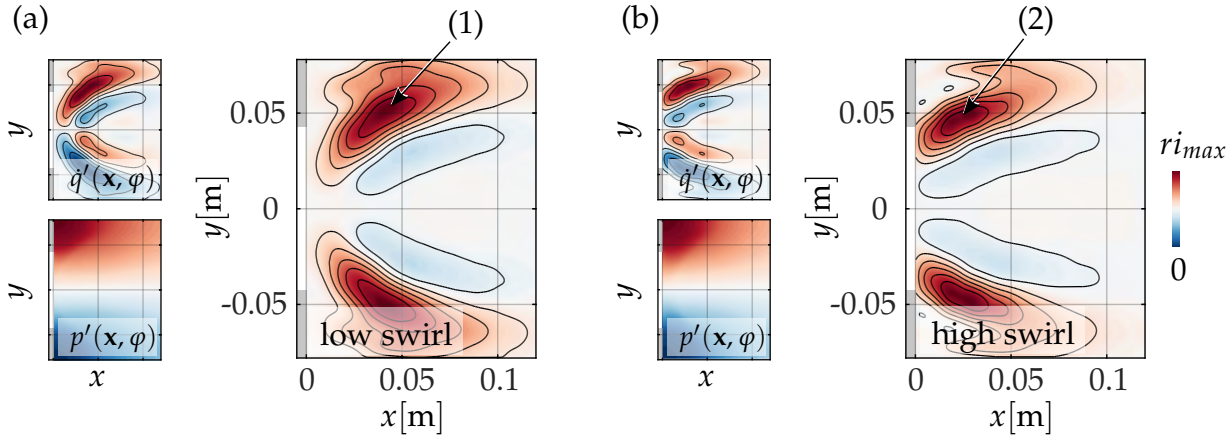


**Figure 5.12:** Distributed Rayleigh indices for the low (a) and high (b) swirl configuration alongside the distributed heat release and the pressure field of the first transverse acoustic mode.

lease oscillation field for differing swirl numbers. With increasing swirl the flow field shifts the heat release towards the face-plate into a region of higher acoustic pressure, which leads to increasing thermoacoustic feedback. This shifted heat release is highlighted in (1,2) in Figure 5.12. As thermal power remains constant, the more compact interaction zone of flame and acoustics results in an increased specific acoustic energy transfer. Thus, driving is enhanced.

These observations of the Rayleigh indices lead to the conclusion that the macroscopic heat release distribution has an important impact on the resulting $A^2EV$ swirl flame driving. This can explain the difference of the thermoacoustic stability states associated with the two swirl configurations even though the thermal power is equal. Further analyses of the impact of the macroscopic heat release distribution on non-compact swirl flame driving are presented in Chapter 6.

It is important to point out that the impact of changing the swirl on acoustic damping of the transverse mode has not been considered here. Numerical investigations of the swirl combustor experiment in [43] obtain periodic vortex shedding at the mean flow separation point as the main damping effect. However, while the swirl number has an effect on acoustic damping due to vortex shedding, it is not clear whether increasing swirl leads to higher or lower damping rates in the specific case. From an integral perspective, it can be expected that the pressure loss for the HS configuration is increased and leads to higher absolute flow velocities at the burner outlet. Lastly, damping due to wall friction might also have an effect [42]. A conclusive evaluation of the swirl impact on the thermoacoustic instability with the focus on acoustic damping is left for future work.

### 5.1.7 Analytical Source Term Expressions and Their Validation

Performance enhancement of existing gas turbines by combustor retrofits or the development of novel/modern combustion systems are examples for engineering tasks, which require advanced design tools enabling robust a priori thermoacoustic stability assessments of the combustors [37]. One essential component towards such tools are linear thermoacoustic

source term expressions (or respective flame transfer functions) to account for the linear flame response in such systems. Especially for the non-compact HF regime, validated flame response descriptions have not been available. This is why analytic formulations of non-compact linear thermoacoustic source terms have been derived from first principles by Hummel *et al.* [38, 44]. These source term expressions are based on the phenomenological observations of the non-compact flame modulation of the A$^2$EV swirl combustor presented in this thesis as well as in previous works [57–60, 62, 63, 69].

An analytically useful expression of non-compact source terms relates acoustic pressure fluctuations to the heat release perturbations. The proposed feedback mechanisms are periodic flame displacement as well as oscillating compression and expansion of the flame's local reaction zone, i.e. flame deformation. The experimentally observed flame response phenomena for the swirl flame are shown in Figure 5.13. This illustration shows the idealized and acoustically modulated swirl flame (black line (1)) at four different phases of the thermoacoustic oscillation cycle.

For flame displacement, it is assumed that the acoustic velocity drives the flame up- and downwards. The flame is periodically displaced off its centerline, while the maximum displacement is in-phase with the acoustic pressure (cf. Fig. 5.13 (a,c)). Equally, the flame motion is maximum at

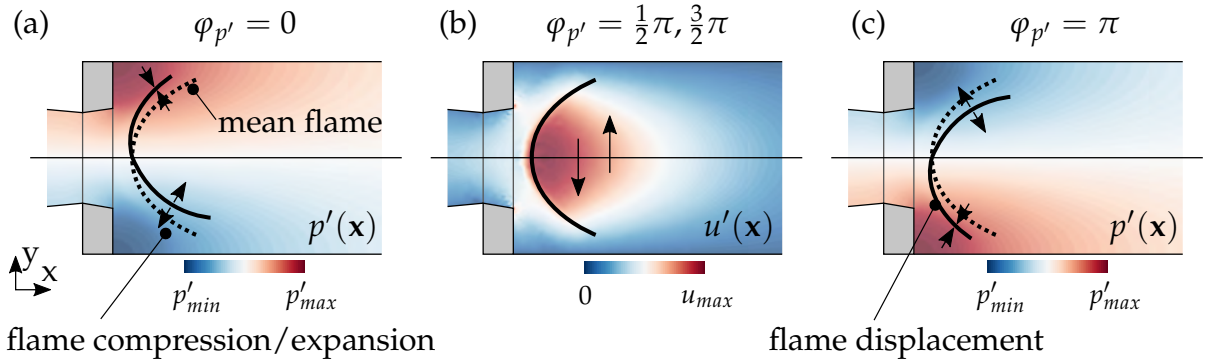


**Figure 5.13:** Representation of the non-compact thermoacoustic driving mechanisms via flame displacement and deformation throughout an oscillation cycle. Illustrated are the modulated (continuous line) and the mean (dashed line) swirl flame at instances of maximum local pressure at $\varphi = 0$ and $\pi$ and maximum transverse velocity at $\varphi = \frac{1}{2}\pi$ and $\frac{3}{2}\pi$ of the first transverse mode (adapted from [38, 59]).

the pressure node, i.e. at the velocity antinode, as shown in Figure 5.13 (b). On a local scale, this means that the heat release intensity oscillates around its mean quantity, resulting in flame zones, which thermoacoustically generate and absorb acoustic energy according to the Rayleigh criterion (cf. Fig. 5.9). The resulting spatio-temporal heat release modulation is described by

$$\dot{q}'_{\Delta}(\mathbf{x},t) = -\nabla\bar{\dot{q}}(\mathbf{x}) \cdot \Delta'(\mathbf{x},t), \tag{5.5}$$

where $\nabla\bar{\dot{q}}$, and $\Delta'(\mathbf{x},t)$ denote the gradient field of mean heat release and the acoustic displacement field, respectively. The latter is linked to the acoustic velocity by $\mathbf{u}' = \frac{\partial\Delta'}{\partial t}$. The net effect (i.e. Rayleigh integral in Eq. 1.1) of this displacement mechanism can be of driving or absorbing character, which is dependent on the macroscopic flame structure as demonstrated in [80]. For the investigated swirl flame, all combustor operation conditions lead to driving by this mechanism [38, 44].

The root cause of thermoacoustic driving by local compression and expansion of the reaction zone is the gradient associated with the displacement $\Delta'(\mathbf{x},t)$. It spatially deforms the flame and thus increases the heat release intensity in compressed regions and vice versa (cf. Fig. 5.13 (a,c)). Hence, the heat release perturbations by this mechanism are formally related to the acoustic pressure oscillations $p'$ by

$$\dot{q}'_{\rho}(\mathbf{x},t) = p'(\mathbf{x},t) \cdot \frac{\bar{\dot{q}}(\mathbf{x})}{\gamma\bar{p}(\mathbf{x})}, \tag{5.6}$$

where $\bar{\dot{q}}$, $\bar{p}$ and $\gamma$ respectively denote the time averaged quantities of heat release, pressure and ratio of specific heats.

The proposed analytical models specifically account for the in-phase flame acoustics interaction and the non-compactness of the perturbed heat release. In order to demonstrate the validity of Equations 5.5 and 5.6, the spatial distribution and intensity of the fluctuating heat release from experiments and from theoretical source terms have to be equal. This applies to both, the individual and the superposed theoretical heat release oscillation fields via the displacement $\dot{q}'_{\Delta}(\mathbf{x},t)$ and deformation $\dot{q}'_{\rho}(\mathbf{x},t)$ mechanism, i.e.

$$\dot{q}'_{\mathcal{R},exp}(\mathbf{x},t) = \dot{q}'_{\Delta}(\mathbf{x},t) + \dot{q}'_{\rho}(\mathbf{x},t). \tag{5.7}$$

The required field variables of $\bar{q}$ and $\gamma$ needed to compute the oscillating heat release via the above introduced Equations 5.5 and 5.6, are based on experimentally obtained $OH^{\star}$ CL data and thereof derived temperature distributions (cf. Apdx. A). In principle, these variables could also be obtained by means of the reactive CFD solution for an exclusively numerical solution. Derivation of the input variables based on experimental data for a large number of operation points, however, is much faster, as shown in [44]. With this input, the heat release distributions based on the flame displacement and the deformation source term are computed, which is carried out by employing the analysis method presented in [38, 44]. The input is scaled through the measured average pressure amplitude $rms(A)$ and the thermal heat release of the flame $\dot{Q}_{th}$. Thus, resulting oscillation field variables are not linked to the measured fluctuating heat release distribution, but only depend on the mean quantities.

Figure 5.14 shows the numerically obtained heat release oscillation field for the (a) superposed , (b) displacement and (c) deformation flame modulation of the LS configuration discussed throughout the previous sections. Added to this information are the related oscillation fields from experiments (cf. Fig. 5.11). First, the overall heat release modulation pattern is well described by these linear and non-compact thermoacoustic source terms and only minor deviations from the experimental counterparts are visible. Furthermore, also the individual patterns from flame displacement and deformation are conserved by the analytical descriptions, and confirm the assumption of in-phase acoustic pressure and velocity coupling with the flame. Second, the local intensity of the theoretically obtained heat release fluctuations matches with the experimental counterpart. This leads to the conclusion, that the observed mechanisms appropriately describe the linear and non-compact swirl flame response to transverse pressure pulsations. This allows robust calculation of growth rates and distributed source terms for further analyses. In addition to this, the results indicate that LF thermoacoustic mechanisms dominated by convective time delays are negligible for HF thermoacoustic response of the swirl flame. This is due to the low-pass character of convective driving effects [37, 51, 52, 138]. A fundamental assessment of this low-pass behavior for two different flame types in the framework of HF thermoacoustic instabilities can be found in [38].

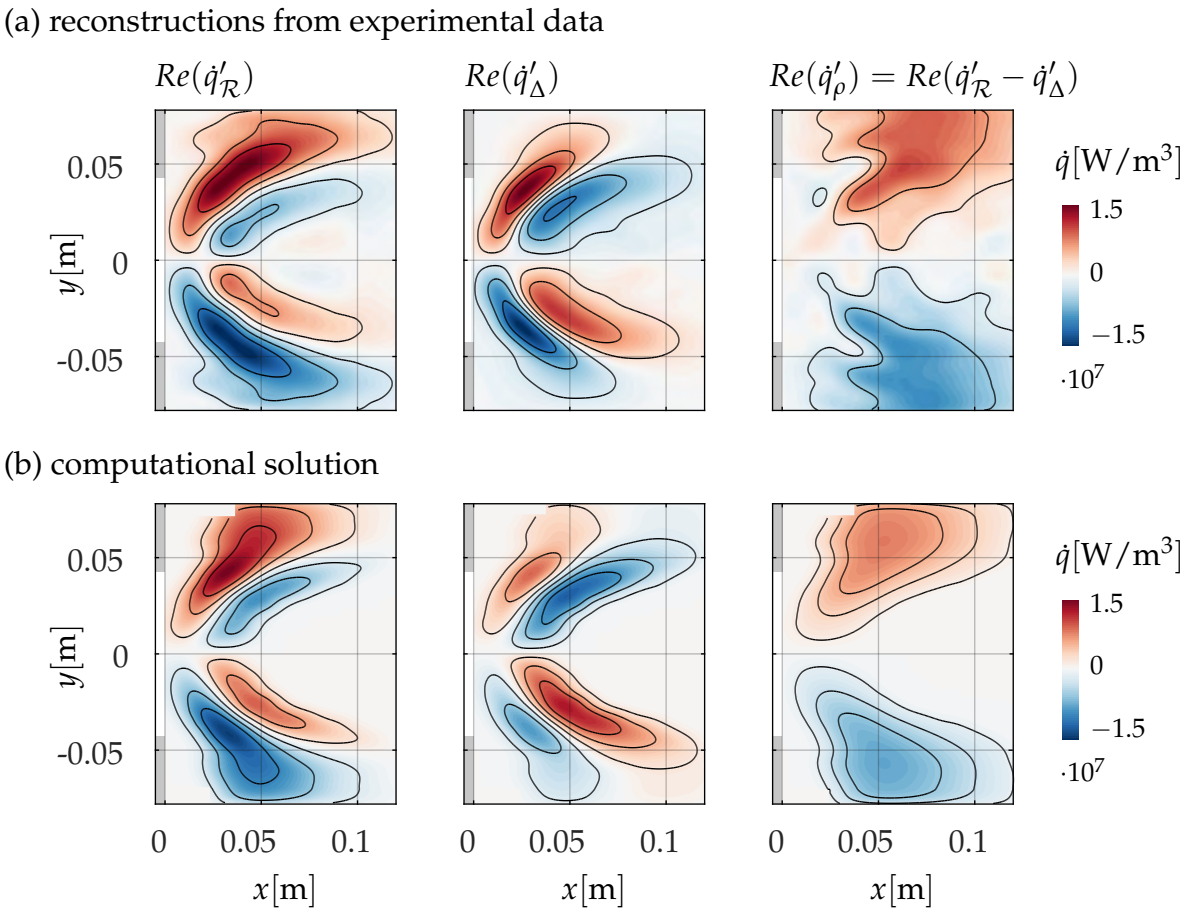


**Figure 5.14:** (a) Experimentally obtained fields of the oscillating heat release from non-compact flame response to transverse pressure pulsations, (b) numerically obtained counterparts of the heat release oscillation field employing the displacement and deformation source terms (cf. Eq. 5.5 and 5.6).

Another interesting observation from the flame driving computations in [38, 44] is a significantly different contribution of both source terms. The displacement driving contributes $\approx$ 25 % to the total driving rate while the deformation effect is dominating with $\approx$ 75 %. The low contribution from the flame displacement in contrast to the flame deformation is due to the local phase of the heat release oscillations in relation to the acoustic pressure. This leads to a combined acoustic driving and damping effect for the in and out of phase situation, respectively. Even though the flame displacement has little effect, it causes the deformation mechanism, so that both are physically linked to each other and need to be both considered. Note that the relative contribution of the individual

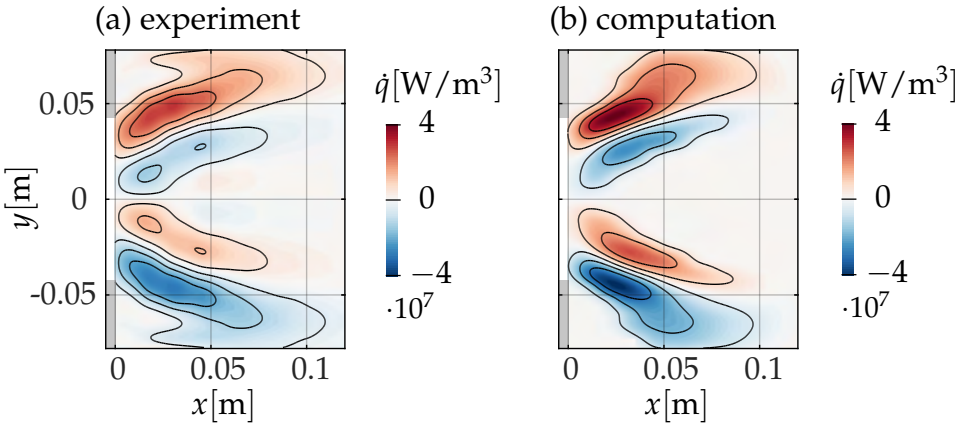


**Figure 5.15:** (a) Experimentally obtained oscillating heat release field (tomographic reconstruction, scaled with the K-factor), compared to the (b) computationally obtained counterpart for the high-swirl A$^2$EV combustor configuration.

driving mechanisms is specific to the herein treated A$^2$EV combustor and can differ for other systems.

Finally, Figure 5.15 shows the comparison of the experimental and numerical heat release oscillation patterns for the previously discussed high swirl configuration (cf. Sec. 5.1.6), highlighting the limitations of using linear source term expressions. While the macroscopic high swirl flame modulation pattern qualitatively agrees, the numerically obtained local intensities of the heat release oscillations are overpredicted by approximately 30%. Neglecting measurement and computation inaccuracies, this effect may originate from the non-linearity associated with the fully developed limit-cycle of the present HS case. The LS configuration (cf. Fig. 5.14) exhibited marginal instability, which is why these experiments are expected to be more suitable for comparison with linear models. Only for the low swirl configuration, it can be assumed that non-linear amplitudes and saturation mechanisms are not equally dominant as for the high swirl configuration shown in Figure 5.15. For the high swirl configuration, limit-cycle amplitudes are approximately 50% higher. This means that non-linear driving saturation mechanisms are more dominant and would consequently need to be accounted for. Hence, the mismatch between the computed flame response and the reconstructions from experimental data (governed by saturated limit-cycle pulsations) is to be expected due to the applied linear framework neglecting any non-linear

saturation mechanisms. Note that an investigation of non-linear effects is carried out in Chapter 6 with the assessment of the pulsation amplitude dependent swirl flame response.

### 5.1.8 Summary and Conclusions - Swirl Flame Response

The previous section was concerned with the flame driving mechanisms of the $A^2EV$ swirl combustor. In addition, experimentally obtained heat release oscillation fields were used to validate analytical source terms. The key findings of this investigation are:

1. The swirl flame response is governed by local, i.e. non-compact, and in-phase coupling with the acoustic pressure.
2. Physical mechanisms that govern flame driving are associated with periodical displacement and deformation of the heat release zone.
3. The macroscopic flame structure (e.g. impacted by the swirl number) has a significant impact on the flame driving.
4. Analytical source term expressions for flame displacement and deformation allow to reproduce the macroscopic heat release oscillation patterns, as well as the local flame response intensity. The latter is limited to the linear regime only.

## 5.2 Partly Auto-Ignition Stabilized Reheat Flame

This section discusses the dynamics of the partly auto-ignition stabilized flame in the reheat combustor (cf. Ch. 2). Section 5.2.1 describes the reheat flame characteristics at thermoacoustically stable conditions. The observed flame modulations associated with the $T_{1y}$ and $T_{1z}$ acoustic modes are subject of Sections 5.2.2 and 5.2.3, respectively. In Section 5.2.4, findings are summarized and recommendations for future work are given.

### 5.2.1 General Reheat Flame Characteristics

As described in Chapter 2, inlet temperatures in the reheat combustor are significantly higher than for the aerodynamically stabilized swirl flame. This means that auto-ignition of the fuel can occur within its residence time in the reheat combustor. These inlet temperatures are achieved with a first combustion stage operated at lean conditions followed by a dilution of the exhaust gas with additional cold air. The elevated inlet temperature yields a mixed flame stabilization pattern characterized by (i) flame propagation and (ii) auto-ignition (cf. Fig. 2.3). Instead of a swirling flow that governs the aerodynamic flame stabilization (cf. Fig. 2.2), delta wings in the combustor mixing section induce large scale vortices in the flow that increase fuel-air mixing and produce beneficial flow features in the combustor (cf. Sec. 2.3.3). Flow recirculation through backward facing steps further promotes flame stabilization by deflagrative propagation (cf. Fig. 2.10).

A key objective of the reheat combustor design (cf. Ch. 2) was to reproduce the characteristic flame features in engine combustors at atmospheric and lab-scale conditions. These mean flame features are the basis for the subsequent investigations of the HF thermoacoustic flame response mechanisms. Figure 5.16 shows the time averaged line-of-sight integrated $CH^\star$ CL images of a representative reheat flame from a lateral[2] (a) and upstream (b) view of the combustion zone. The standard deviation $\sigma(\bar{I})$ is indicated in Figure 5.16 (c) and (d). The reason for capturing the $CH^\star$ CL at $431nm$ instead of the $OH^\star$ CL at $307nm$ is the better visualization of the heat release zone especially in the reactive turbulent shear layer. Visualization is improved due to higher transmission of the applied $CH^\star$ bandpass filters in contrast to the $OH^\star$ filters, allowing reduced intensification gain even at high image sampling rates, i.e. short exposure times.

[2] A benefit of the quasi two-dimensional reheat combustion chamber design is that tomographic reconstructions of flame cut-plane views (as e.g. performed by Radon transforms for the $A^2EV$ swirl flame) can be omitted here. The design and flow field are chosen so that the flame shape and underlying dynamics are approximately constant in line-of-sight direction from the lateral view. Hence, images of the flame are already quasi two-dimensional (cf. experimental setup in Sec. 2).

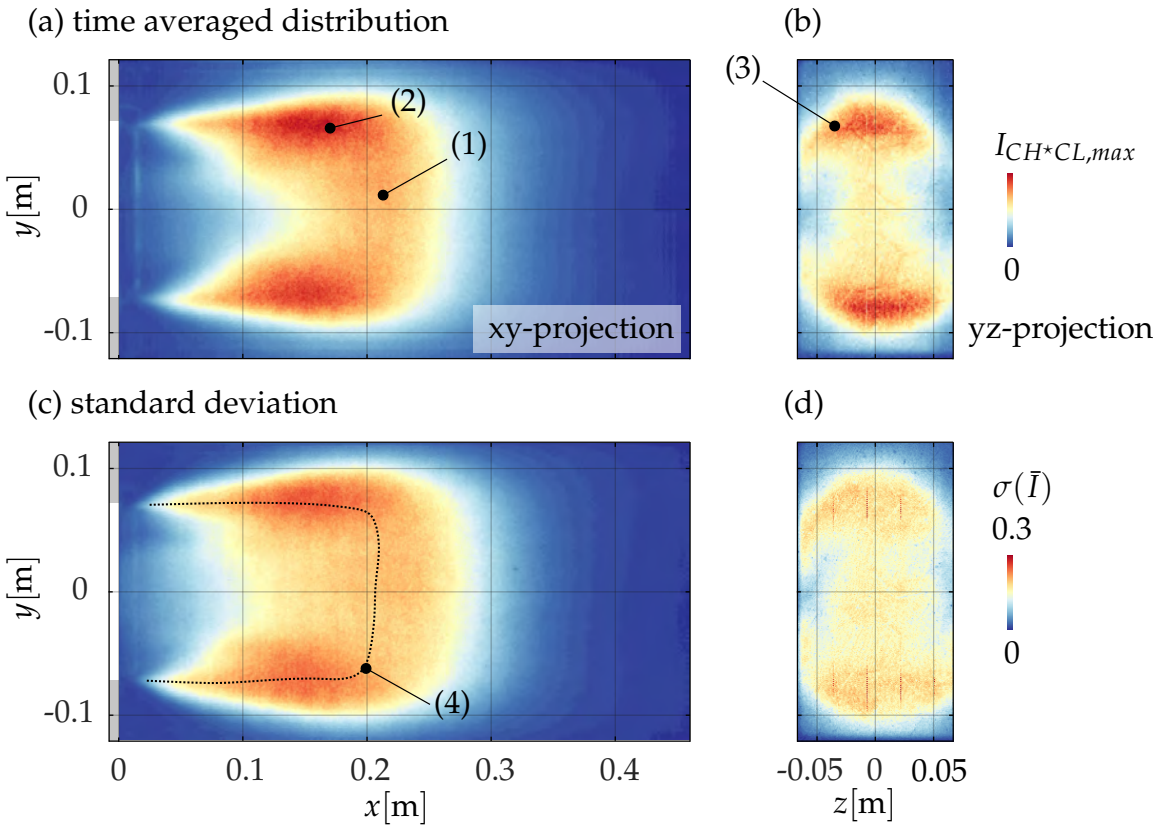


**Figure 5.16:** Time averaged CH* CL recording of a the (a) xy-projection and (b) yz-projection of the reheat flame for a representative operation point with respective standard deviation of the mean in (c) and (d).

From these images, the following observations were made and demonstrate that the combustor experiment is suitable to reproduce realistic reheat flame features:

1. A symmetric flame shape with a homogeneous core flame zone (cf. Fig. 5.16 (1)) enclosed by upper/lower flame zones (cf. Fig. 5.16 (2)) anchored at the diffusor edges of the sudden area expansion is generated.

2. The homogeneous core flame zone shows auto-ignition characteristics, as also demonstrated in e.g. [73,97]. In line with this, the heat release zone shows a characteristic bend towards the upper and lower flame zone (cf. dashed line (4) in Fig. 5.16, indicating the location of maximum heat release intensity in x-y-direction) [30,90].

3. An increased standard deviation $\sigma(\bar{I})$ and an axial spread of the distribution can be observed at the core flame region, which further implies auto-ignition in this zone. The increased standard deviation is caused by the axially fluctuating core flame. This is assumed to be due to the sensitivity of the auto-ignition delay to temperature and pressure fluctuations and the stochastic occurrence of auto-ignition kernels [139–142].

4. The upper and lower flame zones anchored at the diffusor edge indicate flame stabilization by deflagrative propagation.

5. The upstream view shows high intensity in the shear layer zones (cf. Fig. 5.16 (3)) and characteristic patterns originating from the delta wing flow mixers (cf. Fig. 2.10).

It is important to point out that the auto-ignition dominated core flame zone is partly governed by stochastic effects, i.e. spontaneous occurrence of ignition kernels [73,139–142]. This manifests in lower CH$^\star$ CL intensity towards the centerline in Figure 5.16 (a), and the wide distribution of the standard deviation $\sigma(\bar{I})$ in Figure 5.16 (c). Due to this effect, the time averaged flame CL intensity can easily be misinterpreted as low reactivity in this core zone compared to the upper/lower deflagration dominated flame zones. To better visualize the reheat flame features and prevent misinterpretations, the flame heat release zone is split into three areas. These areas are the two, upper and lower, flame propagation dominated zones ($pr$) and a core zone in which auto-ignition ($ai$) is expected to dominate the combustion process (cf. Fig. 5.17 (a)). Based on the volume integrals of the CH$^\star$ CL intensity, the heat release ratio in the auto-ignition

$$ai = \frac{\int_{V_{ai}} I(\mathbf{x}) dV}{\int_{V_{tot}} I(\mathbf{x}) dV} \tag{5.8}$$

and the propagation zones

$$pr = \frac{\int_{V_{pr}} I(\mathbf{x}) dV}{\int_{V_{tot}} I(\mathbf{x}) dV} \tag{5.9}$$

are evaluated, where $V_{ai}$, $V_{pr}$ and $V_{tot}$ label the auto-ignition, propagation and total heat release region, respectively. Second, the identification of the

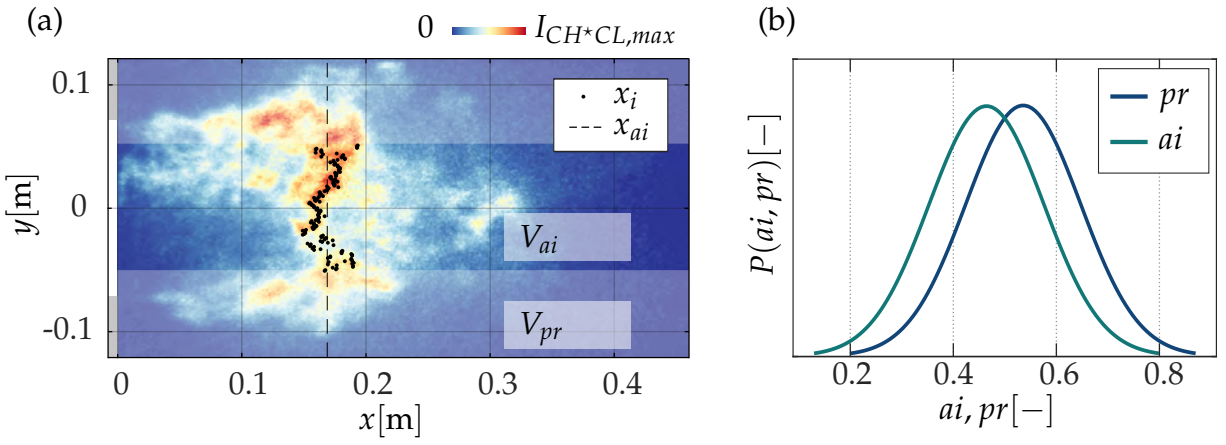


**Figure 5.17:** (a) Raw CH* CL image sectionized in upper/lower and center zones in which flame propagation and auto-ignition dominate flame stabilization, respectively. Dots and dashed line indicate the instantaneous flame position $x_i$ and the mean instantaneous position $x_{ai}$. (b) Probability density distribution of the auto-ignition and propagation ratio $P(ai)$ and $P(pr)$ according to Equations 5.8 and 5.9.

axial location of maximum CH* CL intensity in the auto-ignition section allows to further characterize the fluctuating core zone.

Figure 5.17 shows (a) an example instantaneous flame image with the *ai* and *pr* zones and the identified axial heat release location $x_{ai}$ in the *ai* zone. Figure 5.17 (b) illustrates the probability density distributions $P(ai)$ and $P(pr)$ of the auto-ignition *ai* and propagation *pr* ratio resulting from the image time series.

While the time average in Figure 5.16 implies less intense heat release in the core flame region, the distribution of the intensity ratio in the propagation *pr* and auto-ignition *ai* zone in Figure 5.17 (b) reveals an almost equal contribution to the heat release. Depending on the operation conditions (e.g. inlet temperature, fuel blend, thermal power, and air-fuel equivalence ratio), the heat release is slightly higher either in the auto-ignition zone or the outer primarily propagation stabilized zones. Specifically, elevated inlet temperatures, increased propane content, high mass flows/thermal power, and near stoichiometric reheat combustion conditions favor auto-ignition. This observation is supported by the probability density distribution $P(x_{ai})$ of the axial core flame location in Figure 5.18 (a). The distribution reveals that the auto-ignition heat release is

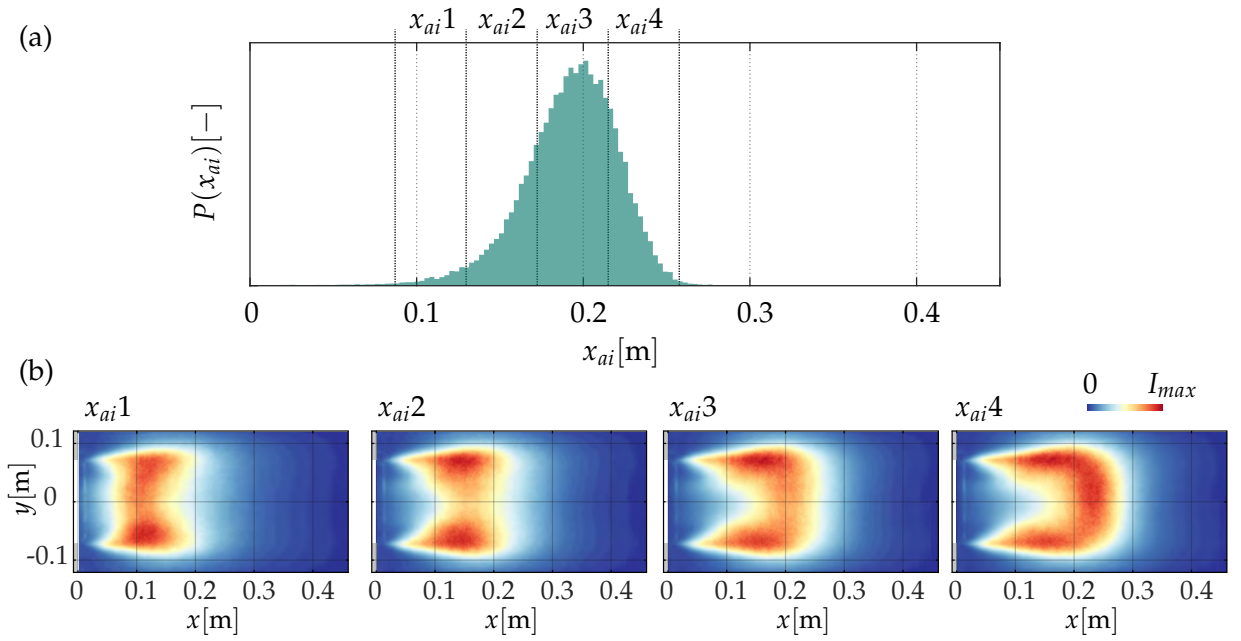


**Figure 5.18:** (a) Probability density distribution of the axial position $P(x_{ai})$ of the auto-ignition flame zone and (b) conditional average of the CH* CL data for different ensembles of the axial flame position $x_{ai}1$ - $x_{ai}4$

mainly located at $x \approx 0.2m$ but deviates from this location in up- and downstream direction. The flame front motion, responsible for the width of the distribution, can be attributed to stochastic modulations of the auto-ignition delay [139–142]. Furthermore, the axial location of the auto-ignition flame front can be manipulated by increasing/decreasing the reheat inlet temperature [96]. This is an effective measure to control/alter the heat release distribution, and thereby to effectively investigate its effect on the thermoacoustic feedback.

Conditional averages $\bar{I}(\mathbf{x}, x_{ai})$ for different ranges of axial core flame positions $x_{ai}1 - x_{ai}4$ are provided in Fig. 5.18 (b) and show the resulting fluctuation of the auto-ignition zone. It can be concluded from frequency analyses (using the fast Fourier transform) of the measurement data that the axially deviating core flame zone neither originates from (i) LF fuel- and air-feed oscillations nor from (ii) any coupling effects with HF acoustic oscillations in the burner. Thus, the core flame zone fluctuations seem not to have a significant effect on the HF flame response, as discussed in the following Sections 5.2.2 and 5.2.3.

### 5.2.2 Non-Compact Flame Response at the $T_{1y}$ Resonance Frequency

A weak thermoacoustic response of the reheat combustor is observed at a pulsation frequency of approximately 1600 Hz (cf. Figs. 4.4 and 4.5 (b)). Underlying coherent heat release oscillation patterns are visualized by correlating the CL measurements with the synchronously sampled acoustic pressure signal, bandpass filtered around the $T_{1y}$ modal frequency (cf. Ch. 3). Afterwards, distributed Fourier coefficients are obtained analogously to the A$^2$EV swirl flame investigations (cf. Sec. 5.1.2). Figure 5.19 shows the real part $Re(I_{\mathcal{F}})$ and the amplitude weighted phase $\angle(I_{\mathcal{F}})$ of the distributed Fourier coefficient obtained from the CH$^\star$ CL data. The associated analytical pressure time series $p_{T_{1y}}$ are recorded at sensor position $P1$ in the upper reheat combustion chamber half.

The distributed heat release oscillations (cf. Fig. 5.19) show a sequence of zones with alternating high and low intensity starting from the sudden area expansion. Through this deterministic reheat flame dynamics for the $T_{1y}$ mode, the following characteristics can be identified: First, by comparing the oscillation field with the flame zones visible in the time averaged CL image (cf. Fig. 5.16 (a)), the heat release oscillation sequence spatially correlates with the propagation stabilized flame. More specifically, it occurs along the reactive shear layer between the flow recirculation

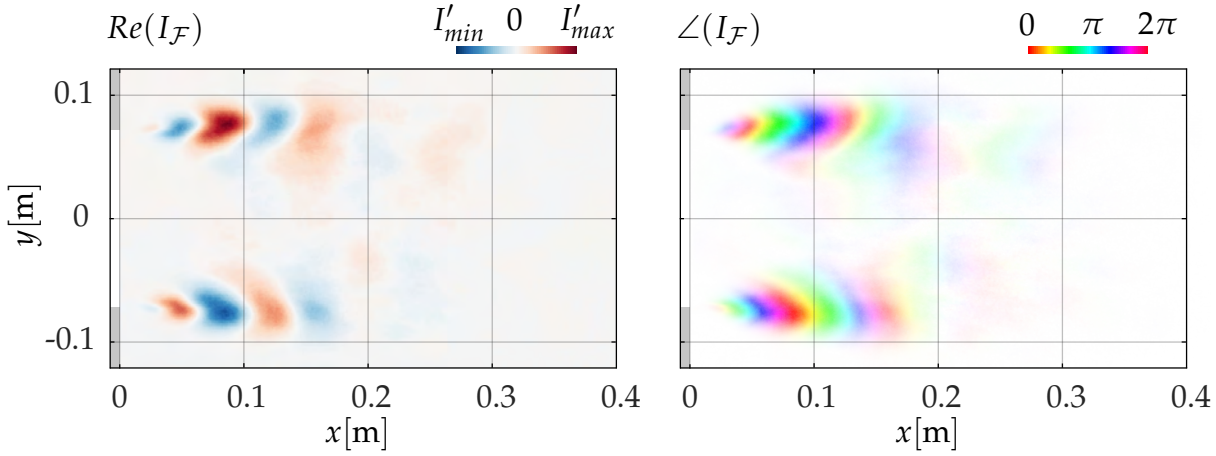


**Figure 5.19:** Heat release oscillations from CH$^\star$CL measurements of the perturbed reheat flame visualized via $Re(I_{\mathcal{F}})$ and $\angle(I_{\mathcal{F}})$ (amplitude weighted) of the distritbuted Fourier coefficient related to the unstable $T1_y$ frequency.

and the bulk flow. The auto-ignition dominated flame zone in the bulk flow towards the combustor centerline shows no distinct coherent flame modulations. This observation holds true also if the previously observed fluctuation of the auto-ignition flame zone (cf. Fig. 5.17) is taken into account by evaluating only image ensembles with equal axial flame location $x_{ai}$. Second, the coherent heat release modulations in the shear layer are anti-symmetric, i.e. counter-phased with respect to the burner centerline. This is a typical characteristic for flame responses related to the first transverse resonance of the burner. The shedding frequency of the heat release pattern is $f_{q'} = f_{T_{1y}}$. Hence, a positive and a negative heat release zone (cf. respective red and blue patches in Fig. 5.19) are formed during each oscillation cycle of the acoustic mode. Third, the moving phase and the transport velocity $u_{q'} = \partial x_{q'}/\partial t$ (determined by tracking the heat release patches from a time series of images) indicate downstream convection of the heat release zones originating from the mean flow separation point at the diffusor edge.

The origin of the heat release pattern can be associated with acoustically induced shedding of vortices that cause wrinkling of the flame front in the propagation flame zones. This is visible from inspecting the phase-locked ensemble averages (cf. Ch. 3), samples of which are given in Figure 5.20 for different phase bins. These ensemble averages show a distinct wave form modulation of the heat release zone in the upper/lower shear layer, which is in accordance to findings of Zellhuber *et al.* who investigated this phenomenon numerically [67].

A periodic transverse displacement of the flame, as suggested in [69] and also observed for the A$^2$EV swirl flame, could not be observed during the experiments. The phase-locked ensemble averages (cf. Fig. 5.20) do not reveal any significant flame displacement either. This observation is confirmed by a covariance analyses conducted in the same manner as for A$^2$EV swirl flame (cf. Sec. 5.1.4), which, however, did not yield any meaningful results. It is unclear at this stage, whether the observed heat release oscillation pattern in Figure 5.19 consists of (i) only the periodic formation of heat release patches due to flame wrinkling at the reactive shear layer or (ii) indeed also a heat release modulation by transverse flame displacement as suggested in [69]. It is possible that the displacement cannot be visualized with the applied methods due to the interac-

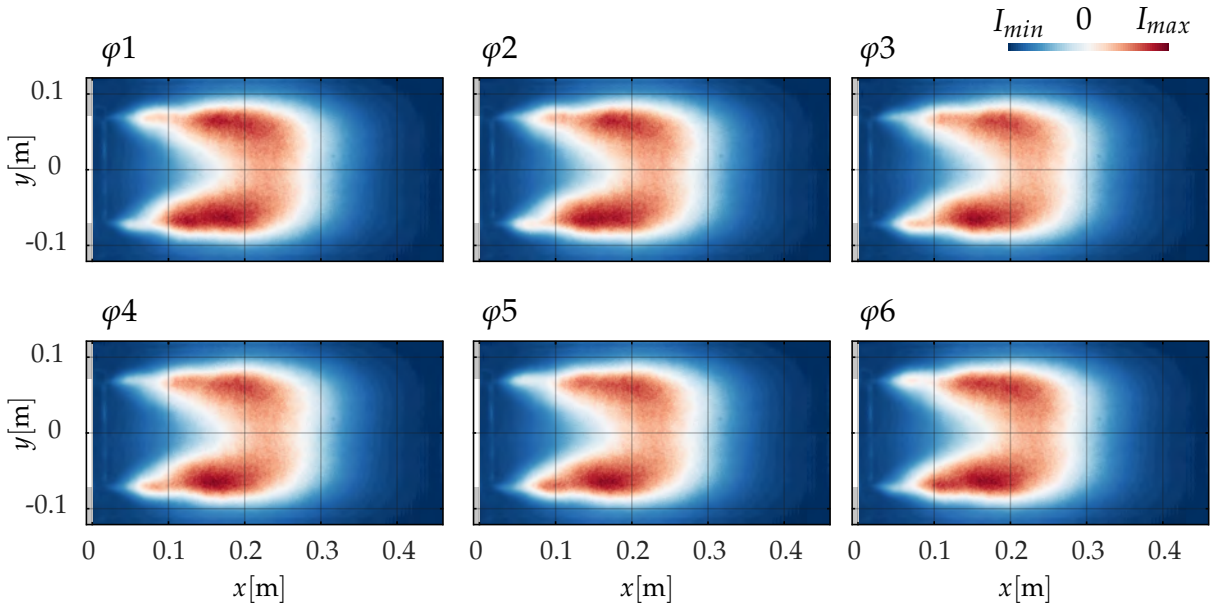


**Figure 5.20:** Phase-locked ensemble averages for six phase situations $\varphi 1 - 6$ of the $T_{1y}$ thermoacoustic oscillation cycle.

tion of multiple flame response mechanisms leading to the observed heat release pattern, or simply due to the low pulsation amplitudes for the tested configurations of the reheat experiment.

A remaining question is to what extend the observed heat release pattern in the reactive shear layer drives the $T_{1y}$ acoustic mode. Hence, it is of particular interest, if the net effect of the heat release oscillations is positive and which phase relationship between heat release and pressure exists. Whether a positive significant net effect is present is questionable due to the alternating amplitudes in the modulated zones (cf. red and blue patches in upper/lower shear layer in Fig. 5.19) and the marginal instability.

Figure 5.21 shows the heat release fluctuations $I'$, from spatial integration over the upper half of the image (cf. Fig. 5.19). The phase $\varphi_{p'}$ is retrieved from the synchronously measured pulsation probe time series. An oscillation of the integrated heat release with the acoustic pressure can be observed. In addition, the color coding shows that the heat release intensity is proportional to the pressure amplitude. At low pressure amplitudes there is no distinct oscillation pattern (cf. blue dots cluster around zero amplitude) while the heat release oscillations towards higher

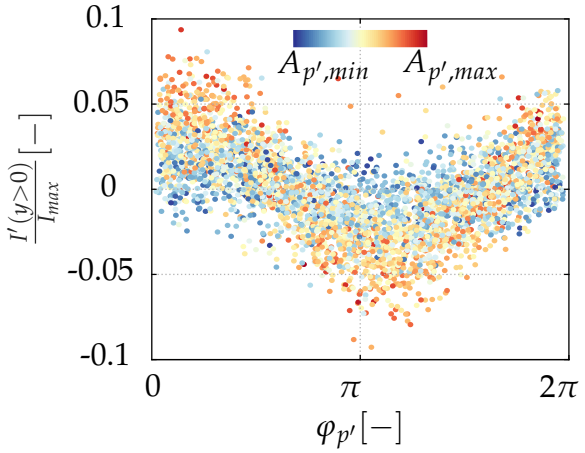


**Figure 5.21:** Integral flame heat release intensity oscillations from CH* CL data over the phase from synchronous acoustic pressure measurements, the color code shows pressure envelope amplitudes.

pressure amplitudes show a clearer oscillatory behavior in-phase with the dynamic pressure. However, in contrast to the flame response of the marginally unstable A$^2$EV operation conditions investigated in Section 5.1.1 (cf. Fig. 5.2), oscillations show significantly lower amplitudes and higher scatter.

To further follow up on the question of the driving extend of the vortex shedding phenomenon, the local Rayleigh index $ri(\mathbf{x})$ (cf. Eq. 1.2) is calculated. In order to visualize in detail the spatial behavior of the oscillations, the propagation flame region is subdivided into axial integration zones for which the individual/local Rayleigh integral (cf. Eq. 1.1) is calculated (analogous to [67,69]). The Rayleigh index field and the integration zones (detail (1)) are illustrated in Figure 5.22 (a) alongside with the Rayleigh integrals and the associated cumulative sum plotted over the combustor's x-axis in Figure 5.22 (b) and (c), respectively. The local heat release fluctuations $q'$ to calculate the Rayleigh index are qualitatively described by the distributed Fourier coefficient $I'_{\mathcal{F}}$ from the CH* CL data. The acoustic mode $p'$ (visualization in [80]) is obtained by means of FEM computations, where the required temperature distribution is approximated from experimental data (cf. details in [80]). The anti-symmetry of the heat release oscillation sequence with respect to the burner centerline (cf. Fig. 5.19) and the underlying transverse acoustic field result in a symmetric distribution of the Rayleigh index. From the cumulative Rayleigh inte-

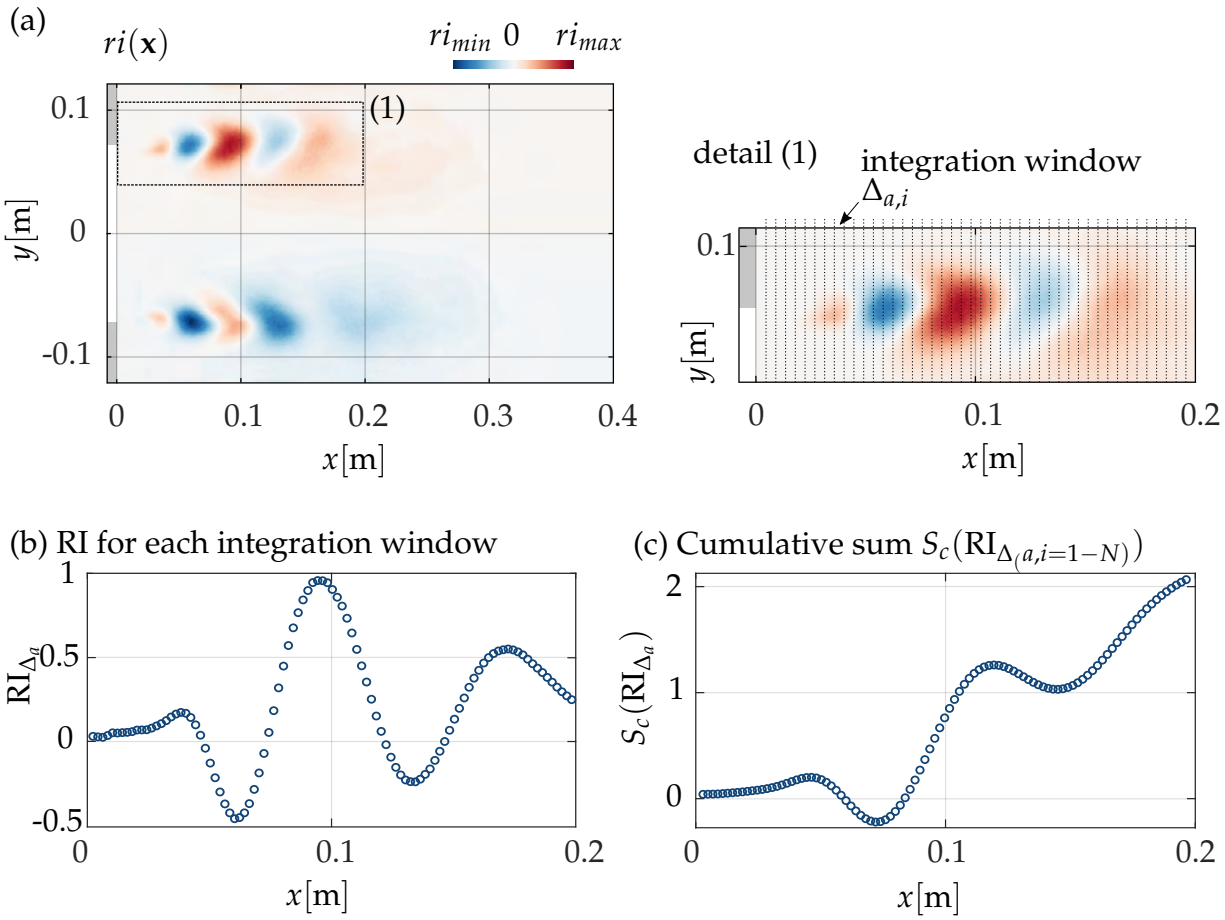


**Figure 5.22:** (a) Distributed Rayleigh index $ri(\mathbf{x})$ (normalized with $ri_{max}$) with schematic illustration of integration sub-windows for visualization of local flame driving behavior, (b) Rayleigh integral $\mathrm{RI}_{\Delta_a}$ for each integration sub-window and (c) cumulative sum $S_c$ of individual $\mathrm{RI}_{\Delta_a}$.

grals, it can be observed that the driving character of the locally positive Rayleigh indices outperforms the energy sinks in the blue zones. Thus, the total Rayleigh integral is positive, for both, the sub-window (1) and the entire volume. Therefore, the observed effect can be considered as a further driving mechanism that is specific for the flame stabilization by deflagrative propagation with distinct reaction in the shear layer. However, the data does not allow for quantitative assessment of the driving strength and hence the effectiveness remains unclear. This needs to be addressed in future studies to show the relevance of this vortex shedding phenomenon in contrast to the displacement and deformation mechanisms.

The previously presented results allow the following physical interpretations with respect to the thermoacoustic feedback associated with the $T_{1y}$ mode:

1. Vortex shedding originating from the flow separation point at the sudden area expansion is induced by the transverse acoustic velocity oscillations, in accordance with [38,43,57,69]. The vortices entrain hot product gases into the cold educt flow and vice versa [76]. As a consequence, heat release in the reactive shear layer is modulated. It is interesting to note that similar observations have been made for the $A^2EV$ swirl combustor from evaluating acoustic PIV images [57, 69]. However, in contrast to the reheat flame, the swirl stabilized counterpart shows no heat release modulation in the perturbed shear layer (towards the outer recirculation zone), which is due to flame quenching from the high local stretch rates [61]. Thus, in the $A^2EV$ burner configuration, vortex shedding only accounts for acoustic damping as demonstrated in [38, 43, 45].

2. Acoustic pressure oscillations are expected to modulate the local reaction progress in the reactive shear layer governed by deflagrative flame propagation.

3. An additional heat release modulation by local displacement of the flame as predicted in [69] might be present. However, this mechanism cannot be unambiguously identified from the decompositions of the line-of-sight $CH^\star$ CL data of the marginally unstable operation point.

### 5.2.3 Non-Compact Flame Response at the $T_{1z}$ Resonance Frequency

The lab-scale reheat combustor exhibits a self-sustained limit-cycle with considerable pulsation amplitudes at a frequency of $f = 3050\,\mathrm{Hz}$. The investigations of the acoustic response in Chapter 4 showed that these pulsations are associated with the $T_{1z}$ acoustic mode. In order to visualize the underling non-compact flame response to the HF acoustic pulsations, phase-locked ensemble averages are obtained from CL images and the synchronously recorded pressure time traces. The latter of which are band

pass filtered around $f = 3050\,\mathrm{Hz}$. These reveal a coherent flame response that spatially correlates with the acoustic pressure field of the $T_{1z}$ mode. Figure 5.23 shows phase-locked CH* CL averages from which the mean image is subtracted, i.e. $I_{\phi,n} - \bar{I}$, recorded from upstream view into the combustor against main flow direction. Six individual phase bins are provided, which resolve the line-of-sight integrated heat release oscillation cycle of the reheat flame. Observations from these recordings are:

1. Alternating areas of increased/decreased heat release intensity in z-direction towards the combustion chamber side walls.
2. Increased overall oscillation intensity in areas of vortical flow structures originating from the vortex generators in the combustor mixing tube (cf. dashed lines in Fig. 5.23 (a)).
3. Highest local heat release intensity oscillations in close vicinity of the combustor side walls, where the acoustic pressure is maximum, i.e. at the pressure anti-node. No oscillations of the heat release near the vertical centerline of the combustor, i.e. at the acoustic velocity anti-node/pressure node.

Based on these observations, two possible scenarios would explain the physical cause of the flame driving:

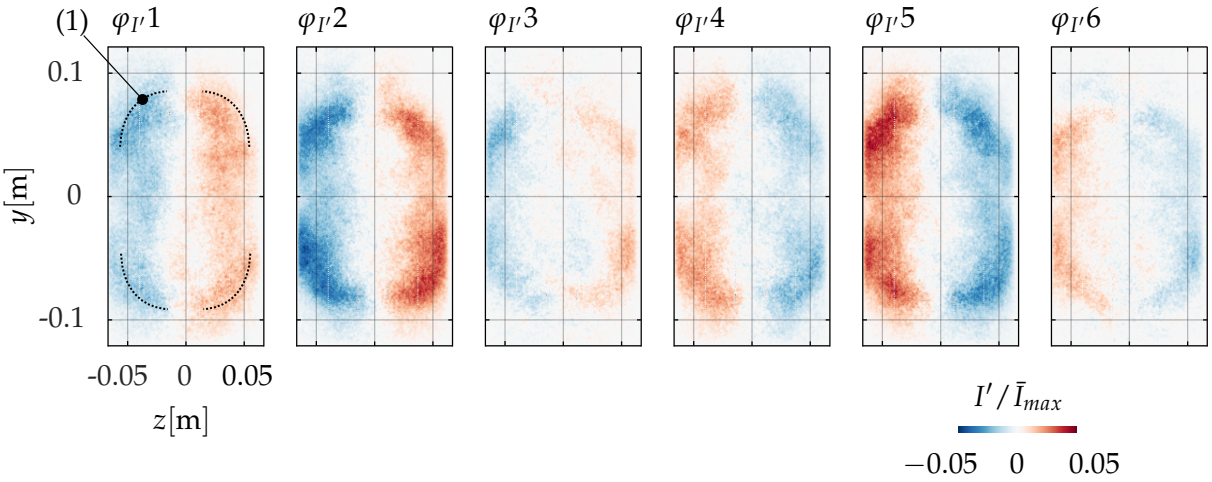


**Figure 5.23:** Oscillation cycle of the flame CH* CL recordings from backwards facing view via ensemble averages from six phase conditions $\varphi_{I'}1 - \varphi_{I'}6$.

First, a **modulation of the auto-ignition delay** $\tau_{ign}$ with the acoustic pressure can cause the observed spatial heat release oscillation pattern. The reasons for this are the maximum heat release fluctuations at the combustor side walls, where pressure pulsations of the distributed $T_{1z}$ acoustic mode are largest and lead to highest modulations of $\tau_{ign}$ [68]. In addition to this, the oscillation intensity is zero at the vertical combustor centerline, i.e. at the node of the $T_{1z}$ acoustic field so that modulations of $\tau_{ign}$ do not occur. Moreover, the assumption of a modulation of the auto-ignition delay is strengthened by the observation of highest local heat release oscillation intensity towards the upper/lower areas with vortical flow structures (cf. dashed lines in Fig. 5.23 (1)). It is shown in [72, 97] that the downstream zones of the upper and lower propagation stabilized flame in the reheat combustor also reveal auto-ignition. Hence, an increased modulation intensity in these regions can be implied. Furthermore, elevating the propane (higher hydrocarbon) content in the fuel, i.e. reducing the auto-ignition delay $\tau_{ign}$, increases the susceptibility to develop the observed thermoacoustic instability (cf. Fig. 4.7).

Second, **flame displacement and deformation** cannot be per se excluded as another cause of the heat release pattern. Shifting the yz-projection of the mean flame shape in Figure 5.16 (b) in transverse z-direction overlaid with an associated flame deformation towards the combustor walls would lead to (i) a heat release oscillation pattern that is positive/negative towards the pressure anti-nodes and zero at the pressure node and (ii) a deformation of the flame towards the outer walls, which increases the local heat release oscillation at the pressure anti-nodes (cf. Fig. 5.23). This is supported by the observation of a slight transverse flame displacement with the acoustic field. A further investigation of these flame dynamics by means of a covariance analysis (cf. Ch. 3), however, has not yielded clear results. Accordingly, further studies are necessary to unambiguously identify the physical mechanism behind the observed dynamics.

The previous observations from the view in upstream direction clearly indicate a modulation of the reheat flame with the $T_{1z}$ mode. To complement this analysis the associated lateral view of the modulated flame is provided in Figure 5.24 in comparison with the upstream view. Apart from uncorrelated heat release fluctuations in downstream direction, this

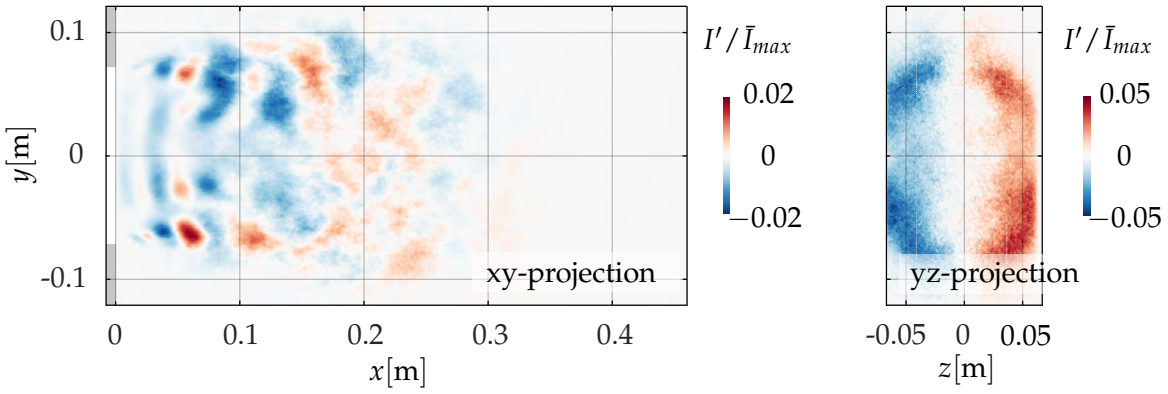


**Figure 5.24:** Line-of-sight distribution of the oscillating flame CH* CL signal $I'$ from lateral (xy-projection) and backwards view (yz-projection).

lateral view shows small scale structures in the wake of the diffusor. These structures cannot be unambiguously associated to any specific acoustic mode type of the combustor, which is in contrast to a distinct oscillatory pattern for the view in upstream direction. It is rather assumed that small vortices are formed from shedding processes at the diffusor edges due to the $T_{1z}$ mode leading to the observable heat release oscillation pattern. Furthermore, (i) low local intensities in contrast to those from the cross sectional view in upstream direction (cf. yz-projection in Fig. 5.24) and (ii) a periodicity of the heat release oscillations render the observed effect insignificant for the driving of the $T_{1z}$ acoustic mode.

### 5.2.4 Summary and Future Work - Reheat Flame Response

In conclusion, the following observations and findings result from the investigated non-compact reheat flame response:

1. Weak thermoacoustic driving of the $T_{1y}$ mode is mediated by acoustically induced vortex shedding in the reactive shear layer and convectively transported heat release oscillations. An amplification of this phenomenon by local modulation of the auto-ignition delay is assumed. The significance of (i) this vortex shedding induced driving phenomenon, (ii) the impact of the damping due to the vortex shedding process as well as (iii) the role of auto-ignition need to be

addressed in future studies to further comprehend the underlying physical mechanisms.

2. The self-sustained limit-cycle oscillations of the $T_{1z}$ acoustic mode yield a distinct oscillating heat release pattern. The observed pattern suggests both, a modulation of the auto-ignition delay $\tau_{ign}$ with the acoustic pressure and a feedback due to flame displacement and deformation to occur. This first effect constitutes a further non-compact reheat flame specific thermoacoustic driving mechanism, while displacement and deformation driving confirm previously identified mechanisms for the swirl flame (cf. Sec. 5.1.5).

3. Numerical investigations presented in [72, 97, 137] revealed a clear dominance of auto-ignition over propagation stabilization of the reheat flame with increasing combustor operation pressure. This would consequently increase the impact of auto-ignition flame modulation within industrial high-pressure applications, as this phenomenon is already observed at atmospheric conditions where the auto-ignition delay is larger. This assumption is supported by an observed increase of the thermoacoustic instability propensity of the laboratory reheat combustor with elevated propane content in the fuel.

These foregoing points summarize first investigations of the newly commissioned reheat combustor and the associated non-compact HF flame response. Further investigations of the flame perturbations in the reactive shear layer and modulation of the auto-ignition delay are needed to assess their contribution to the non-compact thermoacoustic feedback. Specifically, the following recommendations for future studies are as follows:

1. Flame CL measurements from all lateral sides would add beneficial information to unambiguously reconstruct the multi-dimensional heat release oscillation patterns.

2. Laser induced diagnostics (particle image velocimetry, laser induced fluorescence) allow for direct visualization of unsteady flow and heat release patterns in two-dimensional cut-planes to investigate auto-ignition, vortex shedding and displacement/deformation phenomena.

3. Comprehensive analysis of the local and integral Rayleigh indices or respective driving rate computations are needed to assess the contribution of the individual driving mechanisms.

4. Development of a strategy (e.g. by combination with CFD and FEM computations) to clearly distinguish between auto-ignition and propagation stabilized flame zones in the experimental data will make it possible to quantify the effect of auto-ignition delay modulation on the flame driving.

5. The effect of transverse fuel staging (cf. Fig. 2.8) on the auto-ignition core flame interaction with the $T_{1z}$ or $T_{2y}$ modes in the thermoacoustically unstable regime should be explored.

# 6 Influence of Flame Shape Effects on Swirl Combustor Dynamics

In the previous chapters the focus was to comprehend the non-compact flame response to transverse acoustic pressure pulsations. In this chapter, further investigations are carried out using the $A^2EV$ swirl combustor. The purpose of these investigations is to increase physical insight and understanding of general characteristics of HF thermoacoustic oscillations in swirl stabilized combustors. First, the pulsation amplitude dependent flame dynamics are studied in Section 6.1. The idea behind this analysis is to comprehend the flame dynamics that dominate flame driving from low to high pulsation amplitudes. Specifically, it is observed that a modulating pulsation amplitude is linked to a changing flame shape. Hence, the goal of this study is to understand the influence of this flame shape effect on the combustor dynamics. Second, this study is followed by a parametric investigation on the effect of the mean spatial heat release distribution on flame driving in Section 6.2. The motivation for this work is the observation that the thermoacoustic stability depends on the swirl number (cf. Sec. 5.1.6), indicating a significant effect of the flame shape on the non-compact and in-phase interference with the pressure pulsations. To further vary the flame shape, the $A^2EV$ burner geometry can modified to investigate the flame response for different spatial distributions of the heat release.

The following investigations are carried out for the swirl flame response, while an analogous investigation of the reheat flame response is left for future work. The presented approaches and results show directions for future investigations to unveil the detailed flame dynamics also for the reheat combustor.

## 6.1 Pulsation Amplitude Dependent Swirl Flame Response

The motivation for the analysis of non-compact flame response mechanisms to HF pressure pulsations in Chapter 5 was to identify linear thermoacoustic source term descriptions. Such descriptions allow to predict the initial growth of a constructive flame acoustics interference, but do not account for non-linear saturation effects of flame driving (cf. Ch. 1). Hence, flame dynamics associated with different pulsation amplitudes during moderate or intense limit-cycle oscillations were taken into account for the linear analyses. However, it is observed for the swirl combustor that the pressure pulsations throughout a thermoacoustic instability reveal a significant amplitude modulation, i.e. beating (cf. Fig. 4.1). These oscillation dynamics are strongest for a marginal instability, but settle into more constant envelope amplitudes towards limit-cycle oscillations.

The question arises whether the modulated pulsation amplitude is associated with the linear flame response or whether it is due to non-linear saturation of flame driving. In [38, 98], it was shown that the amplitude beating during a transverse instability is linked to the underlying modal dynamics (cf. Sec. 3.1.2). In addition to this, a characteristic flame response related to different pulsation amplitude levels is observed in the experiments. In order to more deeply investigate this phenomenon, the flame dynamics are analyzed for different pulsation amplitude levels in Section 6.1.1. Afterwards, the effect on flame driving is analyzed by evaluating the pulsation amplitude dependence of the thermoacoustic driving rates in Section 6.1.2. This is done by employing the analytical source terms of local flame displacement and deformation (cf. Sec. 5.1.7) in a non-compact stability assessment based on the numerical solution of the acoustic Helmholtz equation [44].

Parts of this study have been previously published by the author in [115].

### 6.1.1 Amplitude Dependent Heat Release Distribution

In order to study the effect of the pulsation amplitude on the thermoacoustic feedback, heat release distributions are extracted from flame OH*CL data for different acoustic amplitude levels. To specify the amplitude levels, the density distribution of the corresponding analytic pressure time series envelope is split into eight bins. An example of such a distribution with the amplitude bins is provided in Figure 3.6 alongside with the description of the method (cf. Ch. 3). To assess the impact of changing intensity of the thermoacoustic instability, different operation conditions are considered. These comprise two sets of operation points with different thermal power, associated to a low and high swirl configuration. The selected operation points are highlighted as LS1-4 and HS1-3 in Figure 4.3.

Representative conditional averages for different pulsation amplitude levels retrieved from the LS2 configuration are shown in Figure 6.1. The upper row (a) of Figure 6.1 shows the line-of-sight integrated conditional averages $\bar{q}(\mathbf{x}, A)$ with increasing amplitude of the associated pressure pulsations $A_{p'}$ from left to right. Associated views of the deconvoluted average heat release $\bar{q}_{\mathcal{A}}(\mathbf{x}, A)$ and the dynamic component $Re(q'_{\mathcal{R}}(\mathbf{x}, A, \varphi))$ are shown in the middle (b) and bottom (c) row, respectively. The other operation points (LS1-4 and HS1-3) exhibit the same general trends, which is why a repetitive discussion is omitted. Tracking the flame deformation observable from the time average heat release distributions from low towards high oscillation amplitudes reveals a general flame compression and a flame contraction towards the axial centerline. This effect is most notable from the flame brush reaching to the combustion chamber walls at low pulsation amplitudes, whereas the heat release is concentrated towards the inner recirculation zones with increasing pulsation levels. This volume contraction is associated with a local increase of the heat release rate.

As discussed in Section 5.1, the thermoacoustic feedback can be described by a superposition of (i) flame displacement with the acoustic velocity and (ii) flame deformation interfering with the acoustic pressure. Considering the distribution of the acoustic field variables for the asso-

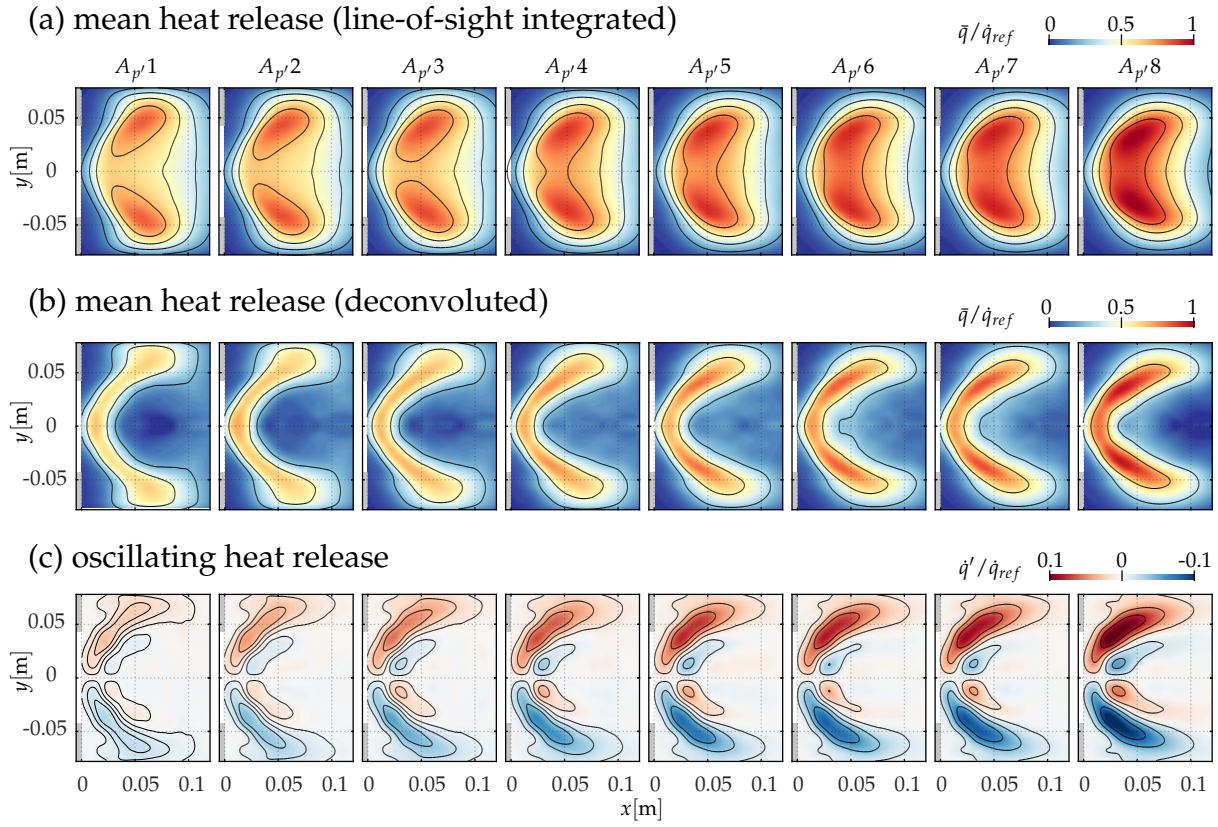


**Figure 6.1:** Top: Mean line-of-sight OH*CL distributions of the flame related to the amplitude of the dynamic pressure pulsation $A_{p'}$ given from the dynamic pressure envelope; Middle: Inverse Abel transformations of the mean OH*CL images; Bottom: Oscillating heat release fields obtained from tomographic reconstructions via the Radon transform. Pulsation amplitudes increase from left to right.

ciated first transverse mode, (i) the acoustic velocity is highest towards the combustor's axial centerline and (ii) the acoustic pressure is highest towards the combustion chamber walls in the vicinity of the area expansion. Investigating the change of the oscillating heat release distribution with increasing oscillation amplitude in Figure 6.1 (c) leads to the following assumptions: For low pulsation amplitudes, the oscillating heat release indicates that a significant part of the flame is exposed to regions in which the acoustic pressure is high. Hence, interpreting this in accordance with the Rayleigh criterion, thermoacoustic feedback by local, in-phase interactions is favored for heat release distributions with low amplitude oscillations. The flame contracts towards the nodal line of the acoustic

pressure field for increasing pulsation amplitudes, which would imply a decrease of flame driving.

In order to ensure that previously observed flame dynamics are governed by flame shape effects and do not impact the integral heat release, volume integrals for both the mean $\bar{Q}_A = \int_V \bar{q}/\bar{q}_{max} dV$ and oscillating field $\dot{Q}'_A = \int_V \dot{q}'/\dot{q}'_{max} dV$ are determined for each amplitude level. The results are shown in Figure 6.2 (a). First, the net heat release $\bar{Q}_A$ does not change in spite of the change in flame volume. Second, the measured heat release oscillation intensity $\dot{Q}'_A$ from the self-sustained thermoacoustic response increases proportional to the pulsation amplitude.

Figure 6.2 (b) shows the frequency response for the discussed operation point, which is retrieved from the time derivative of the phase $\varphi_{p'}(t)$ from the analytical signal representation of the pressure data. For the unstable operation point increasing amplitudes are associated with decreasing oscillation frequencies. The corresponding amplitude locked averages of the mean heat release fields in Figure 6.1 indicate that this change in frequency can be attributed to the flame contraction and the heat intensity shift towards the axial centerline. It can be assumed that the changing heat release distribution leads to a temporal change of the temperature distribution in the recirculation area towards lower mean temperatures for high pulsation amplitudes. This reduction of the mean temperature is

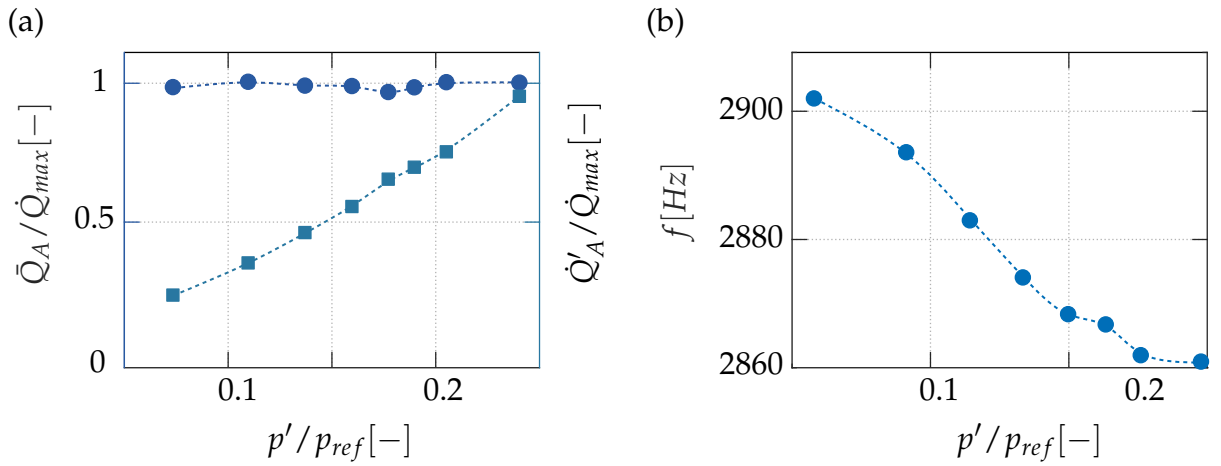


**Figure 6.2:** (a) Integral heat release of the amplitude ensemble averaged flame $\bar{Q}_A$ and integral heat release of the flame oscillations $\dot{Q}'_A$ (normalized with the maximum heat release), (b) frequency response over the pulsation amplitude.

expected to be caused by the increased axial extent of the flame. Hence, this effect reduces the average speed of sound with which the acoustic mode propagates and thereby alters the frequency. This decreasing frequency also impacts flame driving, as implicated by Equation 5.5. Specifically, the acoustic displacement in this expression can be related to the acoustic velocity/pressure by

$$\hat{\Delta} = \frac{\hat{\mathbf{u}}}{i\omega} \sim \frac{\nabla \hat{p}}{\omega^2}, \tag{6.1}$$

which increases with decreasing frequency as well as increasing pressure amplitude.

Figure 6.3 shows the effect of thermal power on the pulsation amplitude dependent flame shape variation. First, line-of-sight integrated OH*CL conditional averages are shown for the low (Fig. 6.3 (a)) and high (Fig. 6.3 (b)) pulsation amplitude bin from the low swirl operation points LS1-4 (cf. Fig. 4.3). Second, in order to highlight the pulsation amplitude dependent flame contraction, the spatial difference between both distributions - i.e. $\bar{I}_{A_{\max}} - \bar{I}_{A_{\min}}$ is shown in Figure 6.3 (c). As expected, the flame shape generally changes with thermal power due to changing reactivity. In addition to this, the previously discussed flame contraction with increasing pressure pulsation amplitude can be observed for all operation points. This effect becomes more visible from the difference images that demonstrate the distinct shift of the heat release towards the centerline. While this effect is observable for all thermoacoustically unstable operation points, it is becomes stronger with increasing pulsation amplitudes. This can be attributed to the increasing magnitude of the acoustic displacement with increasing pulsation amplitudes. With the acoustic first transverse mode distribution in mind, the resulting pattern in Figure 6.3 (c) supports the assumption that the contributions of the individual thermoacoustic driving mechanisms change with different pulsation amplitudes. The flame shape observed for low amplitudes favors driving by flame deformation, while the flame shape at high pulsation amplitudes favors driving by flame displacement.

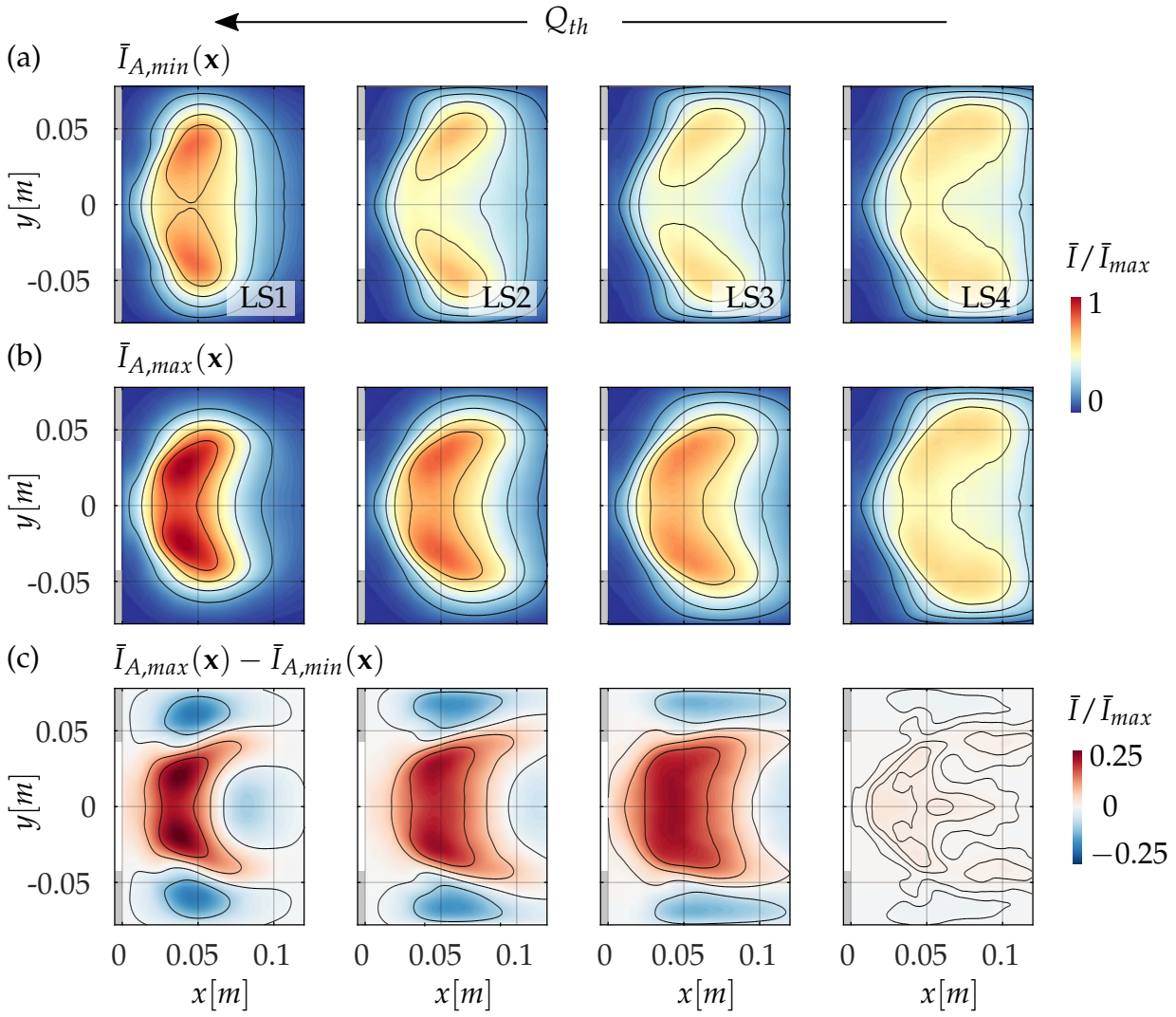


**Figure 6.3:** Mean OH* CL distributions for (a) min $\bar{I}_{A_{\min}}$ and (b) max $\bar{I}_{A_{\max}}$ pressure amplitude level for LS1-4 (cf. Fig. 4.3) and (c) difference image $\bar{I}_{A_{\max}} - \bar{I}_{A_{\min}}$.

### 6.1.2 Quantification of the Amplitude Dependent Driving Rate

With the experimentally determined heat release distributions for different pulsation amplitude levels, corresponding driving rates can be computed to quantify the amplitude dependence of the flame response. Specifically, the driving rates of displacement $\beta_\Delta(A)$ and density $\beta_\rho(A)$ mechanisms are evaluated for each amplitude level. This is done by solving the modal eigenvalues employing Equations 5.5 and 5.6 in a non-compact FEM computation, based on the acoustic Helmholtz equation [44]. The resulting driving rates provide a measure for the acoustic en-

ergy generation by the flame (cf. discussion in [38]). Conceptually, these amplitude dependent driving rates are evaluated in the sense of a non-compact flame-describing function approach.

All resulting driving rates are shown in Figure 6.4. The different rows of plots show the deformation $\beta_\rho(A)$ and displacement $\beta_\Delta(A)$ driving rates as well as their superposition $\beta_{\rho,\Delta}(A) = \beta_\rho(A) + \beta_\Delta(A)$ over the measured pulsation amplitude for the LS and HS cases, respectively.

First, the driving rates $\beta_\rho(A)$ from flame deformation show the previously inferred trends to be more intense at low pulsation amplitudes, i.e. at conditions where the heat release is exposed to the region of high acoustic pressure. With increasing amplitude the driving decreases, which is due to the flame contraction to the centerline. These trends are equally found for the LS and HS configurations. Second, the displacement driving rates $\beta_\Delta(A)$ behave in the opposite manner, i.e. increase with elevating amplitudes. This trend also confirms the observations from the heat release distributions discussed in the previous sections. The heat release zone migrates towards the center where the acoustic displacement effect is at maximum. Moreover, it can be observed that the displacement driving saturates towards high oscillation amplitudes, which is equally observed for LS and HS configurations. These observations can be explained with help of the Rayleigh integral by assuming a simple cosine and sine distribution for the transversal pressure and velocity mode, respectively. This is schematically shown in Figure 6.5 for $p'(r)$, $u'(r)$ and $u' \cdot p'$ over the combustor radius $r$ from $-R$ to $R$. Additionally, three different theoretical flame positions $1-3$ are indicated. Flame position 1 would imply pure thermoacoustic driving due to flame deformation, while displacement effects are zero (high values of $p'$ while $u'$ is zero). This condition is an idealized representation of a low amplitude heat release situation where the flame expands towards the outer recirculation zone. Moving the flame towards the burner centerline decreases driving by flame deformation to zero at flame position 3 (local Rayleigh index: $p'q'_\rho \sim p'^2$). At the same time, the displacement effect starts to act as the acoustic velocity $u'$ increases until the maximum is reached at flame position 2. The displacement effect decreases beyond this point towards zero at the centerline 3 (local Rayleigh index: $p'q'_\Delta \sim p'u'$). This simplified scheme agrees with the experimental observations in Figure 6.1. The flame shift

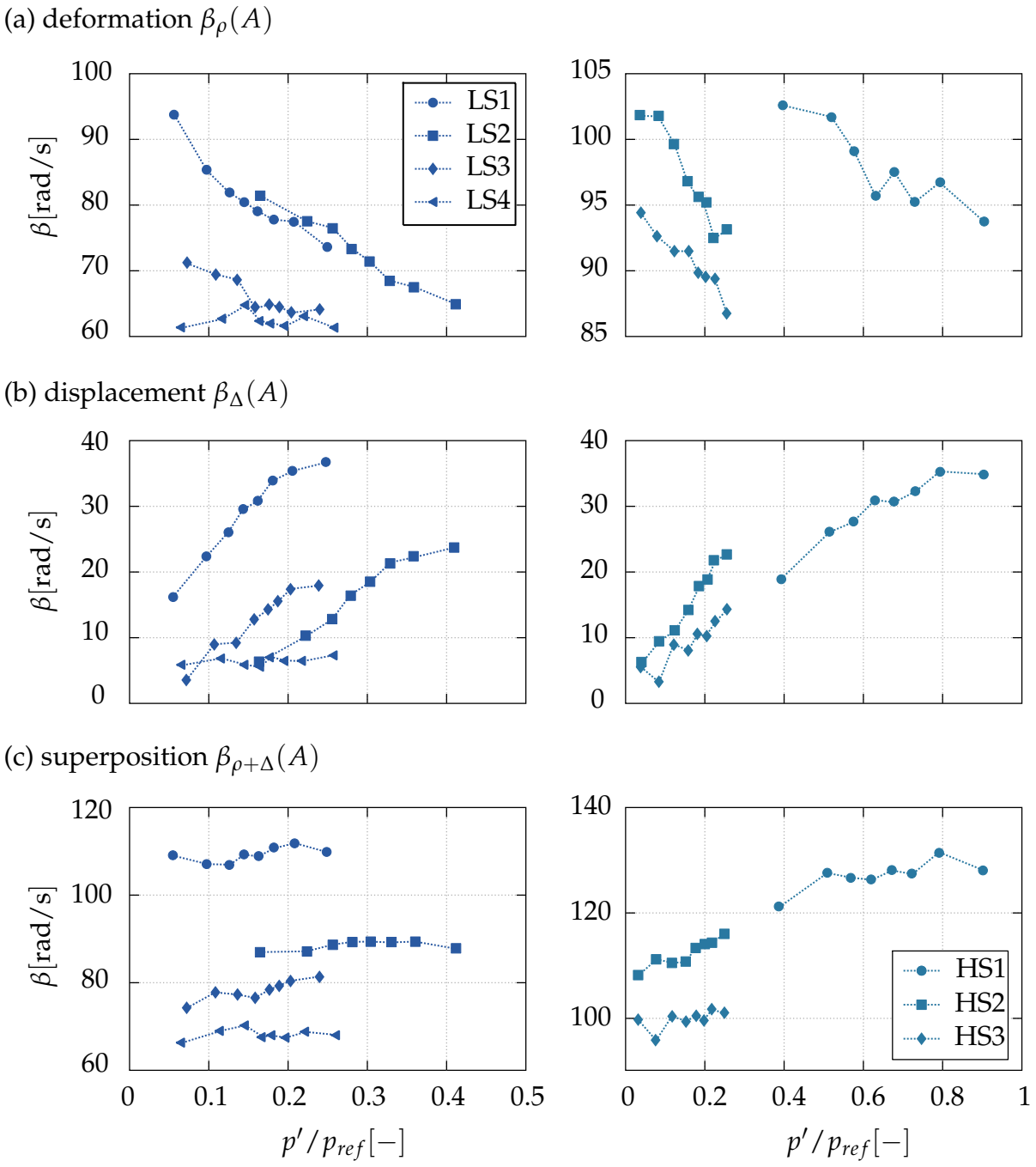


**Figure 6.4:** Amplitude dependent driving rates for (a) flame deformation $\beta_\rho(A)$, (b) flame displacement $\beta_\Delta(A)$ and (c) their superposition $\beta_{\rho,\Delta}(A)$; left column shows low swirl (LS) configuration results, and right column the high swirl (HS) configuration results.

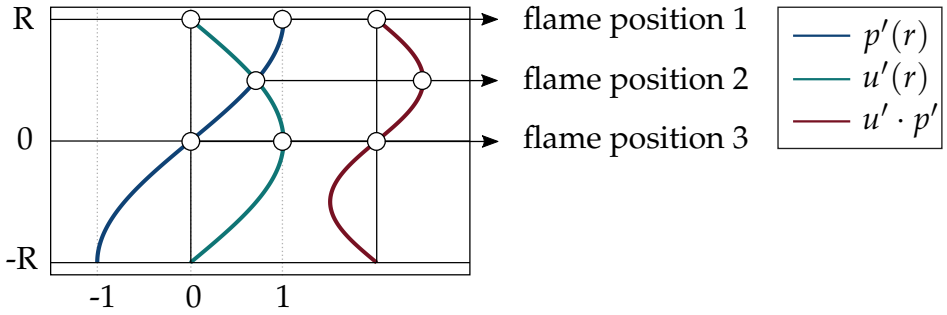


**Figure 6.5:** Schematic of acoustic pressure $p'$ and velocity $u'$ over the combustor radius and indicative flame positions 1-3 that lead to different contributions of thermoacoustic driving.

towards the centerline for high oscillation amplitudes results in an initial increase of the displacement strength, which, however, decreases beyond the flame position 2. Finally, the bottom line of plots (c) of Figure 6.4 shows the superposition of both contributions, the total driving rate $\beta_{\rho,\Delta}(A) = \beta_\rho(A) + \beta_\Delta(A)$. It is observed that the decrease of deformation and simultaneous increase of displacement driving compensate each other for increasing amplitude levels. These observations are true for LS and HS operation points. Based on these observations, it can be concluded that the deformation source term predominates for low amplitudes at which a significant share of heat is released in the vicinity of the outer recirculation area. As this thermoacoustic source decreases, the contraction of the flame favours the thermoacoustic driving by flame displacement.

### 6.1.3 Summary and Conclusions - Pulsation Amplitude Dependent Swirl Flame Response

From the investigation of the amplitude dependent swirl flame response, the following conclusions can be drawn:

1. The turbulent swirl flame brush contracts towards the combustor center with increasing pulsation amplitude.

2. Thermoacoustic driving contribution by the different mechanisms changes with the variation of the heat release distribution. Deformation is at its highest with low pulsation amplitudes and an expanded

flame reaching the combustor walls. Deformation driving decreases with increasing pulsation amplitude and flame contraction, while the previously low displacement driving increases.

3. It could not be confirmed that saturation of the flame driving is linked to the pulsation amplitude dependent flame shapes. This might, however, be an issue of sampling data from self-sustained thermoacoustic oscillations. Ultimately, the hypothesis of a saturating effect of the observed flame contraction would need to be tested at thermoacoustically stable combustor operation with external forcing beyond the herein observed amplitude level, i.e. by effectively identifying the flame describing function.

## 6.2 Impact of Macroscopic Swirl Flame Structure on the Thermoacoustic Response

This section deals with the impact of the macroscopical flame structure caused by geometrical modifications of the swirl burner on the linear thermoacoustic stability of the first transverse acoustic mode. In the analyses in Sections 4.1 and 5.1.6, a distinct impact of the swirl intensity on the thermoacoustic instability propensity was observed. In particular, a changing heat release distribution due to changing swirl intensity was identified in Section 5.1.6 as the cause of different pulsation intensities. In Section 6.1 different pulsation levels revealed a change in the macroscopic flame shape. This changing flame shape resulted in a shift from thermoacoustic driving by flame displacement to deformation, yet driving through flame deformation always exceeds flame displacement (cf. Ch. 5). These observations motivated a parametric analysis with the aim to better understand the dependence of the thermoacoustic instability on the flame shape.

The $A^2EV$ swirl combustor (cf. Fig. 2.1) provides the possibility to modify [85,87,88]

1. the axial flow momentum by adjusting the opening area at the swirler cone tip $\Delta_{A,SC}$,

2. the swirl intensity by varying the tangential slot height $h$ of the swirler cone, and
3. the diffusor opening angle $\alpha$ from the mixing tube to the combustion chamber at the sudden area expansion.

The effect of the diffusor geometry on the thermoacoustic stability was already studied by Hertweck *et al.* [62, 63]. In these investigations, a significant impact of the diffusor angle $\alpha$ on the macroscopic heat release distribution and thereby the thermoacoustic stability of the A$^2$EV swirl combustor was reported. To extend this view, a parametric analysis of possible correlations between the thermoacoustic instability propensity and either axial flow momentum and/or swirl intensity is carried out in the following. First of all, the effect of the first two geometric burner modifications on the heat release distribution is outlined in Section 6.2.1. Furthermore, parameters are defined to describe the flame macrostructure in a simple way. Second, the effect of the geometric combustor modifications on the thermoacoustic stability is discussed in Section 6.2.2.

### 6.2.1 Combustor Geometry Impact on Mean Heat Release Distribution

Modifications of the A$^2$EV swirl combustor geometry translate into a changing mean flow field that consequently impacts the resulting macroscopic flame shape. The effect of axial flow momentum and swirl intensity on the resulting flow field was studied in [84–87, 89]. In general, (i) an increased axial flow momentum moves the flow stagnation point downstream and (ii) an increased swirl intensity leads to a reduced axial extend of the flow expansion, i.e. the reattachment point of the flow recirculation after the sudden area expansion moves upstream.

In order to directly study the effect of changing axial flow momentum and swirl intensity on the resulting flame structure, two parameters describing the time averaged deconvoluted swirl flame brush are defined. These are (i) the flame opening angle $\gamma_f$ and (ii) the axial location of the flow stagnation point $x_f$, as are illustrated in Figure 6.6. In order to obtain these parameters, the axial location of the maximum OH$^\star$ CL intensity along the y-axis of the flame brush is evaluated for each x-position to

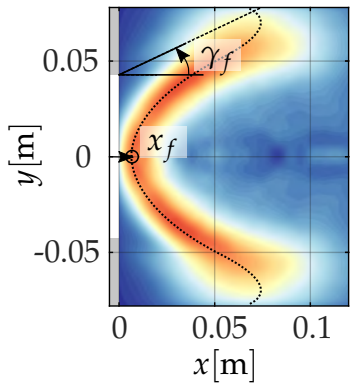


**Figure 6.6:** Flame opening angle $\gamma_f$ and the axial position of the flame stagnation point $x_f$ for an example CL image of the A$^2$EV swirl flame.

which a polynomial curve is fitted afterwards. The flame opening angle $\gamma_f$, based on this polynomial fit, is defined by the angle between the two solid lines in Figure 6.6. The flow stagnation point $x_f$ is determined from the intersection of the polynomial curve with the combustor central axis.

The impact of thermal power is considered with varying the air and fuel mass flow rates. Combinations of the following operation parameters are investigated:

- air mass flow rate $\dot{m} = 0.10, 0.12\,\mathrm{kg/s}$
- air-fuel equivalence ratio $\lambda = 1.2, 1.4, 1.6, 1.8$
- swirler cone tip area blockage $\Delta_{A,SC} = 0, 0.37, 0.49, 0.7$
- swirler slot height $h = 9, 11, 14\,\mathrm{mm}$

When the geometry is modified, an important aspect is that high blockage of the swirler cone tip opening $\Delta_{A,SC}$ leads to a low axial flow momentum at the burner centerline. Decreasing the swirler tangential slot height $h$ increases the tangential/swirl momentum in the flow.

The effects of the previously introduced modifications of the combustor geometry on the flame shape are shown in Figure 6.7. The impact of the swirl intensity on the mean heat release distribution for different air-fuel equivalence ratios is shown in Figure 6.7 (a). A modification of the air mass flow rate from $\dot{m} = 0.1$ to $0.12\,\mathrm{kg/s}$ does not lead to signifi-

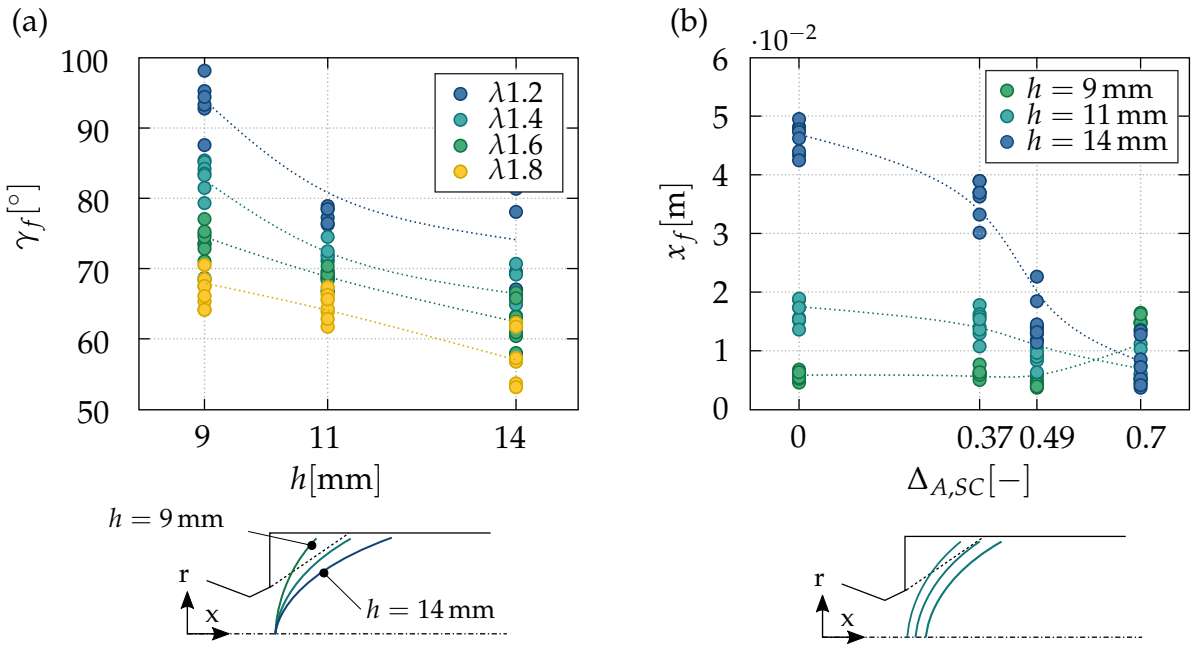


**Figure 6.7:** (a) Swirl flame opening angle $\gamma_f$ dependency on the swirl number from altering the A$^2$EV swirler's tangential slot height $h$, (b) swirl flame stagnation point position $x_f$ on the burners central axis for different area blockage ratios $\Delta_{A,SC}$ at the swirler cone tip. Schematics illustrate the effective change of the macroscopic flame structure with modified burner geometries.

cant changes of the macroscopic flame structure, which is why this is not explicitly shown. The investigation indicates an increasing flame opening angle $\gamma_f$ with increasing swirl intensity. This is to be expected as the flame brush stabilizes in the turbulent shear layer of the flow recirculation zones, which are impacted by the tangential flow momentum [84,85]. This is reflected by large flame opening angles, i.e. compact heat release zones towards the combustor face-plate for low values of the air-fuel equivalence ratio $\lambda$. The impact of the swirler cone tip opening on the heat release distribution strongly depends on the swirl intensity, as illustrated in 6.7 (b). For low swirl intensity, the flow stagnation point is sensitive to the axial flow momentum near the burner axis. This sensitivity decreases with increasing swirl, until no direct correlation of axial flow momentum and location of the corresponding flame stagnation point is observed anymore. Hence, the heat release distribution is modified not only with changing air and fuel flow, but also show a distinct sensitivity to the specific swirler geometry. The following Section 6.2.2 discusses the impact of the resulting heat release distributions on the thermoacoustic stability.

### 6.2.2 Impact of the mean Heat Release Distribution on Thermoacoustic Stability

The correlation of the mean heat release distribution and resulting linear driving rates, due to thermoacoustic driving through flame displacement and deformation, is shown in Figure 6.8. Note that the previously discussed amplitude dependence of the flame shape is not considered here. The axial location of the flame stagnation point $x_f$ is plotted over the flame opening angle $\gamma_f$. For each operation point the linear driving rates $\beta_{\rho+\Delta}$ are determined with the previously mentioned non-compact evaluation tool [44], employing the source terms for flame displacement (cf. Eq. 5.5) and deformation (cf. Eq. 5.6). Looking only at the distribution of the operation points in Figure 6.8, large flame opening angles correlate with an axial location of the stagnation point close to the face-plate. In contrast, decreasing opening angles of the flame brush scatter over a wider range of flame stagnation point locations. As shown in Section 6.2.1, especially the downstream located stagnation points are associated with configurations of $h = 9\,\text{mm}$ and $14\,\text{mm}$ (cf. Fig. 6.8). The linear driving rates are indicated by the color coding of each operation point. From this color coding, a clustering of high flame driving can be observed for high flame

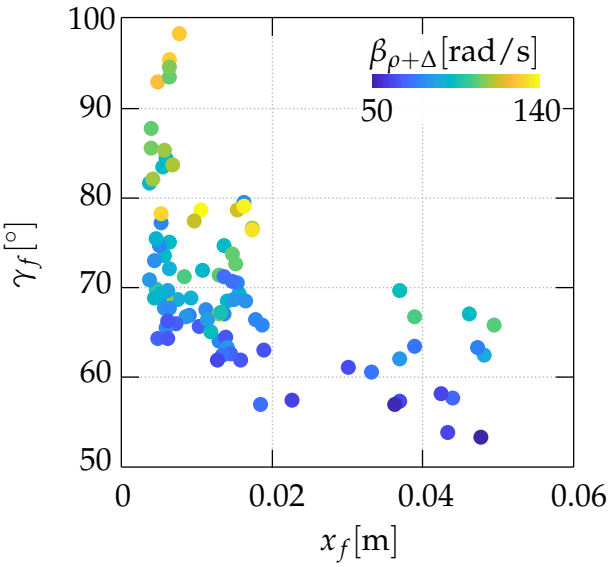


**Figure 6.8:** Swirl flame opening angle $\gamma_f$ over axial position of the flow stagnation point at the combustor centerline $x_f$, colors show the linear thermoacoustic driving rate $\beta_{\rho+\Delta}$ through flame deformation and displacement.

opening angles and upstream located stagnation points. Vice versa, low flame opening angles correlate with distinctly decreasing flame driving.

Figure 6.9 (a) shows the effect of the mean heat release distribution on the first transverse mode oscillation frequency. Additionally, Figure 6.9 (b) shows the thermoacoustic stability states, separated into stable (point) and unstable (triangles) points dependent on a threshold value of the measured pressure pulsation amplitude. The color coding labels each operation point with the respective thermal power $Q_{th}$. In addition, all operation points with a related thermal power of the combustion exceeding $Q_{th} = 230\,\mathrm{kW}$ are highlighted with black outlines. These results show some interesting trends in line with the driving rate analysis in Section 6.1. First, a clear dependency of the thermal power on the oscillation frequency can be observed, as already shown in [59]. This can be observed from the clustering of operation points with high thermal power density in the area of high oscillation frequency. However, Figure 6.9 (b) also indicates that there is a number of operation points with high thermal

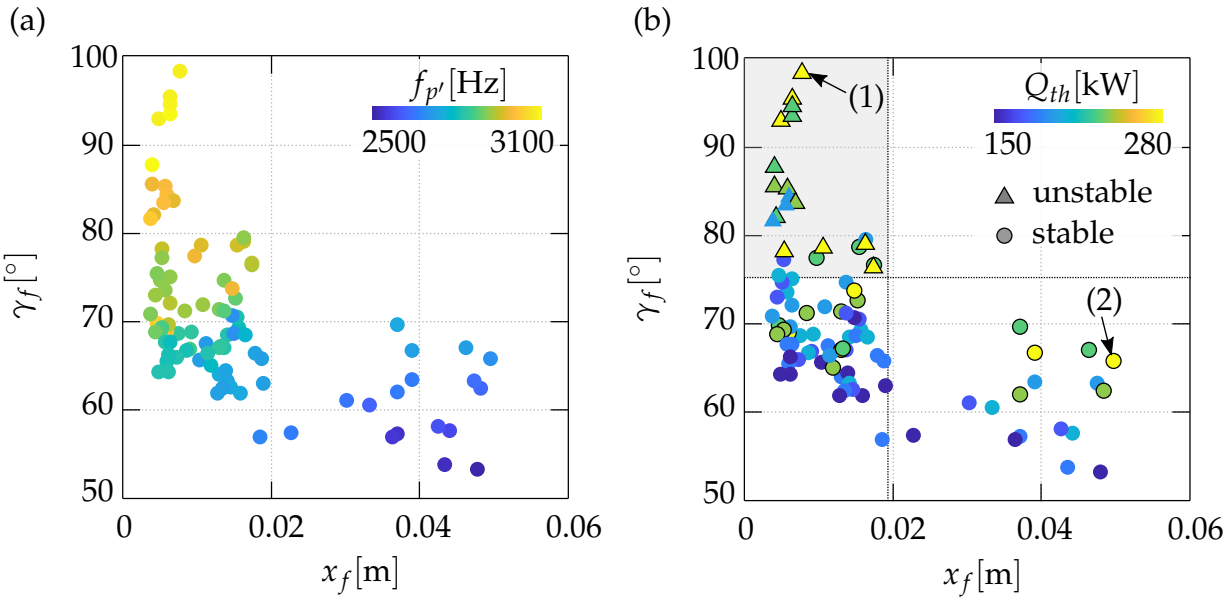


**Figure 6.9:** Swirl flame opening angle $\gamma_f$ over axial position of the swirl flame stagnation point at the combustor centerline $x_f$: colors show (a) the oscillation frequency $f_{p'}$ of the associated acoustic pressure and (b) the thermal power $Q_{th}$. Points and triangles in diagram (b) show thermoacoustically stable and unstable operation conditions, respectively. Black outlines of the points in diagram (b) illustrate all operation conditions with a thermal power $Q_{th} > 230\,\mathrm{kW}$.

power that are associated with moderate or low pulsation frequencies. Hence, elevated temperatures from high thermal power and a characteristic distribution of the heat release lead to high oscillation frequencies. High power densities can be associated with an increase of the speed of sound due to the increased adiabatic flame temperature. In contrast to this, the flame shape effectively impacts the slope of the temperature gradient. This is why lower oscillation frequencies are observed for flames with downstream located stagnation points and low flame opening angles, i.e. decreasing power density (cf. scatter of blue points at $x_f \approx 0.04$ but $Q_{th} > 230\,\mathrm{kW}$ in Fig. 6.9 (a) and (b), respectively). Second, it can be observed in particular from Figure 6.9 (b) that compact flames, i.e. large opening angles and upstream located stagnation point, exhibit a higher tendency to be thermoacoustically unstable compared with flames exhibiting low opening angles and downstream located stagnation points. This is illustrated with the gray area, indicating a clustering of thermoacoustically unstable operation points. While this zone also governs a large number of operation points with high thermal power, it is interesting to observe that the thermal power does not necessarily correlate with a increased thermoacoustic instability propensity for the considered cases. Specifically, operation points exceeding a thermal power of $Q_{th} > 230kW$ are highlighted with black outlines and are distributed independent of the cluster of stable and unstable operation points (cf. (1) and (2) in Fig. 6.9 (b)). This is also reflected in the driving rates (cf. Fig. 6.8), where high thermal power densities do not necessarily correlate with a high flame driving potential. The same trend can be observed for the whole range of moderate to high thermal power operation points. While generally high power densities cause an increased susceptibility to thermoacoustic pulsations, the results of the foregoing parametric study imply that the flame shape can be used as a measure to reduce this susceptibility even at high power densities.

### 6.2.3 Summary and Conclusions - Impact of Macroscopic Swirl Flame Structure on the Thermoacoustic Response

The following conclusions with respect to the non-compact flame response can be drawn from the results shown in this section:

1. For non-compact thermoacoustic combustion instabilities, the spatial distribution of the heat release has a significant effect on the flame driving, which agrees with [63].

2. A spatially compact swirl flame brush located close to the combustor face-plate shows the highest driving potential. This observation is in accordance with findings in [92, 143].

3. The stability of the $A^2EV$ transverse mode can be influenced by modification of the heat release distribution through variations of the burner geometry (e.g. slot height for varying swirl intensity, cone tip opening for varying axial flow momentum). A similar effect was observed with varying the diffusor opening angle at the sudden area expansion, as reported in [62, 63]. Notice, in contrast to the stability characteristics of the $A^2EV$ experiment, fuel/air staging concepts for improved thermoacoustic stability of real engines (e.g. shown in [10,20,82,144]) take into account multiple linearly unstable modes. This is because (i) a modified heat release pattern stabilizes a certain target resonance, but (ii) might lead to a different acoustic mode becoming unstable due to the changed heat release distribution [22].

# 7 Summary and Outlook

The main subject of this thesis were experimental investigations of high-frequency (HF) thermoacoustic combustion instabilities associated with sequential gas turbine systems. In times where substantial transformations of the energy infrastructure is taking place, advanced combined cycle gas turbine (CCGT) power plants are ascribed a crucial role to compensate for volatile renewable energy sources. Hence, the development of combustion systems focuses on increased operational flexibility and improved sustainability in terms of efficiency and low emissions. Thermoacoustic oscillations present a major challenge as occurring instabilities limit the operational range, cause an increased hardware fatigue, and require costly mitigation strategies. Thus, a deep understanding of the processes that cause the instabilities is required in order to achieve improved combustor designs. While low-frequency thermoacoustic instabilities have been studied extensively, HF instabilities are less understood. However, recent advancements of combustion systems gave rise to increasingly frequent occurrence of HF pulsations. Thus, this work investigates such HF non-compact and transverse thermoacoustic feedback phenomena in two different combustion systems, featuring an aerodynamically stabilized swirl flame and a partly auto-ignition stabilized reheat flame, respectively. Both of these systems are relevant in gas turbines with sequential combustion for power generation. The study of thermoacoustic instabilities in these combustor types helps to improve the understanding of non-compact thermoacoustic feedback mechanisms. This understanding is generated by addressing three specific research objectives in the thesis:

1. Design and construction of a laboratory sequential reheat combustor featuring a partly auto-ignition stabilized flame that develops an HF thermoacoustic instability.

2. Characterization and generation of understanding of the HF acoustic response in the swirl as well as the reheat combustor.

3. Visualization and analysis of the mechanisms behind the flame feedback on HF transverse pressure pulsations in swirl and reheat combustors.

Two lab-scale combustors were used for the experimental investigations. While the swirl combustor was readily available from previous research projects, the reheat combustor with vitiator was designed and commissioned in the framework of the thesis project. A flat and rectangular reheat combustor design was found to favor the desired properties, namely the reproduction of (i) HF combustion dynamics and (ii) a reheat flame realistically representing industrial scenarios. This geometric design allowed to distinguish between heat release zones dominated by flame propagation and auto-ignition. Such a clear distinction is important in order to separately assess the contribution of these flame zones to the thermoacoustic driving. The reheat combustor exhibited the development of an HF transverse instability which successfully completed the first research objective.

In order to reach the second goal, the acoustic pressure responses of the swirl and reheat combustors were investigated during HF transverse instabilities. The swirl combustor was investigated first and it was shown that the swirl number has a decisive impact on the HF thermoacoustic instability. Specifically, and in contrast to low swirl configurations, increased swirl numbers lead to (i) significantly higher pulsation amplitudes, but (ii) later onset of the instability in terms of the equivalence ratio. Further to this, investigations of modal dynamics at different stability states yielded further insight and understanding of the nature of HF oscillations: Limit-cycle oscillations are governed by spinning transverse modes, whereas for low pulsation amplitudes mixed type standing and spinning modes were observed. Second, the newly designed reheat combustor was tested for several operation conditions, with which distinct pressure pulsations at two different frequencies were revealed. These frequencies are associated with the $T_{1y}$ and $T_{1z}$ acoustic modes, where the former shows marginal instability characteristics and the latter exhibited self-sustained limit-cycle oscillations. It could be shown that the occur-

rence of limit-cycle oscillations is favored by high power densities and by blending the natural gas fuel with propane. The observation that propane addition to the fuel promotes the instability propensity supports the assumption that auto-ignition induced combustion is present and that it influences the non-compact HF flame response.

To achieve the third objective, the flame response mechanisms associated with the HF transverse pressure pulsation were analyzed. Investigations of the modulated swirl flame showed that non-compact HF thermoacoustic driving occurs through local displacement and deformation of the heat release zone in-phase with the acoustic pressure. In addition to this, flame shape effects on the combustion dynamics were investigated. First, it was observed that pulsation amplitude modulations are linked to the flame shape, which results in a changing contribution of displacement and deformation to flame driving. Second, modifying the heat release distribution by adjusting the burner geometry, i.e. flow field, leads to different HF instability propensities of the system. Hence, it was possible to (i) visualize and understand the swirl flame driving mechanisms, (ii) validate analytical source terms, and (iii) further comprehend the relation of heat release distribution and swirl flame dynamics. In the reheat combustor, the flame response to the $T_{1y}$ mode showed a modulation of the reactive shear layer due to periodic vortex shedding. The limit-cycle oscillations governed by the $T_{1z}$ mode revealed a heat release pattern indicative of flame modulation via the local auto-ignition delay, as well as via displacement and deformation coupling. An unambiguous identification of the driving mechanism of the $T_{1z}$ mode could not be obtained and needs to be addressed in future studies. While the assumption that displacement and deformation play a role in flame driving are in line with the observations from the swirl combustor, the auto-ignition delay modulation is a driving mechanism that is specific to the reheat flame.

The successful construction of an unstable reheat combustor together with the experimental investigations of the non-compact thermoacoustic feedback in the swirl and the reheat combustors contributed to expand understanding of causes and consequences of HF thermoacoustic instabilities. Nevertheless, open questions remain that need to be addressed in future research. From the swirl flame investigations, linear flame dynamics were derived, while saturation phenomena of the flame driving

within limit-cycle oscillations were not obtained. From investigations of the pulsation amplitude dependent dynamics, a decrease of displacement driving at high pulsation amplitudes was observed. This study should be extended by applying external forcing in an approach equal to measuring flame describing functions to unveil physical saturation mechanisms. The next step that should follow the reheat combustor studies presented in this thesis is the further investigation of the physical flame response mechanisms. Especially the relevance of the observed auto-ignition effect during limit-cycle oscillations needs to be explored further. This would help to confirm or extend existing theoretical analyses of the reheat flame dynamics. Furthermore, the physical mechanisms behind multimodal interaction in thermoacoustic systems are of growing interest due to industrial relevance. The reheat combustor comprises an ideal laboratory setting for such investigations due to the observation of two linearly unstable acoustic modes which dominate at different operation conditions. Unambiguously understanding the reheat flame response and expanding the comprehension of non-compact flame dynamics from linear driving towards non-linear saturation mechanisms would allow to draw a clear picture of HF instabilities in lean-premixed swirl and reheat combustors. This would ultimately contribute to the enhancement of the technical and economic efficiency of advanced gas turbine systems.

# A Temperature Field Approximation

The computation of thermoacoustic variables (such as the flame driving rate $\beta$) via solving the acoustic conservation equations with an FEM framework described in [38, 44] requires mean heat release and temperature fields as input. For the investigations presented in this thesis, these input fields are obtained from experimental data to ease parametric analyses. The mean heat release is provided by measured flame chemiluminescence (CL) images. Averaging these image time series and deconvolution via the inverse Abel transform provides the required two-dimensional field. As the swirl combustor is run in fully premixed mode, the assumption that heat release is proportional to the flame CL images can be made with good confidence (cf. Ch. 3). Transferability of this method to the reheat case is described below.

In order to obtain realistic acoustic mode shapes via FEM computations, the mean temperature field governed by the combustion heat release is of importance. As this cannot be measured straightforwardly, a reconstruction based on a numerical reference field is applied. A reactive fluid dynamics (CFD) solution of the $A^2EV$ swirl burner (readily available from [61]) provides mean heat release, temperature, and hydroxyl radical distributions. An extended flamelet generated manifold model that considers various stretch rates and heat losses [61] is applied in the CFD and leads to an accurate agreement of the results with the experimental observations. Hence, the solution provides a flame CL field that matches the experimental counterpart at the reference operation condition. Additionally, it provides the corresponding mean temperature distribution $\bar{T}_{\mathrm{CFD}}$, which conserves the impact of the specific flow and heat release features (e.g. recirculation zones and flow stagnation). To now retrieve the mean temperature distribution for another operation condition, the reference flame CL solution is fitted to the newly measured mean and deconvoluted flame CL image, which delivers a set of scaling parameters. Applying these parameters to the numerically extracted $\bar{T}_{\mathrm{CFD}}$ solu-

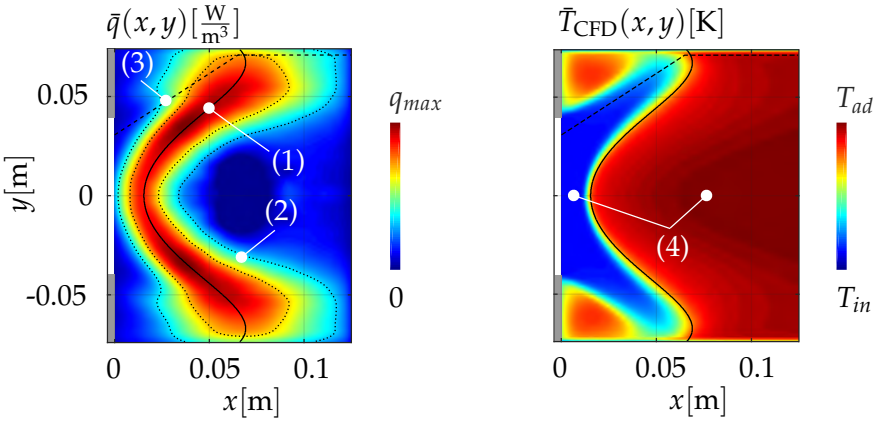


**Figure A.1:** Sample flame CL distribution indicating the mean heat release $\bar{q}$ and reconstructed temperature distribution $\bar{T}_{CFD}$ from the CFD reference.

tion thus results in a representation of the underlying temperature field of the flame CL measurement. In order to gain physically meaningful results, the $\bar{T}_{CFD}$ reconstruction accounts for the (1) flame center of mass, (2) swirl flow expansion, (3) reaction zone thickness, and (4) combustor inlet and flame temperatures. All of these characteristics are denoted in the example in Figure A.1. As a measure of accuracy, eigenfrequencies of the acoustic field computations utilizing the reconstructed temperature field are compared with the corresponding frequency of the experimental Fourier spectrum from dynamic pressure measurements. Frequencies match with less than 5% deviation for a wide variety of stable and unstable operation points as demonstrated in [38, 44].

This procedure is only applicable to a limited extent to the data of the reheat burner. This is due to its operation in technically premixed mode and the specific flow features (cf. Ch. 2 and 3) that hinder a direct indication of heat release by flame CL. Hence, a corresponding CFD solution would need to account for the exact visible hydroxyl radical distribution, which was not available for this work. Instead, acoustic mode computations of the reheat combustor (presented in [80]) used for this work, are based on an artificial mean temperature field considering the associated flame CL distribution and LES results presented in [30]. Numerically obtained eigenfrequencies still match with less then 5% deviation [80] for the transverse acoustic oscillations compared to the experimental data.

# B External Forcing of High-Frequency Pressure Pulsations

Investigations presented in this work are based on experimental data obtained by naturally stable/unstable combustor operation. External forcing has not been applied here, but the following long term goals reaching beyond the scope of the present thesis motivated the development of an external forcing unit including necessary workflows: (i) The study of saturation phenomena and their presentation in terms of flame describing function. (ii) The opportunity to externally force thermoacoustic pulsations in the reheat combustor if no natural instability occurs.

External acoustic forcing of HF transverse modes is most effective at locations at which the targeted mode naturally occurs and where oscillation amplitudes are largest. In addition to this, the three-dimensionality of the mode requires proper phase shifting of the excitation signals if more than one forcing unit is applied. Specifically, in contrast to up- or downstream forcing for LF longitudinal thermoacoustic systems, HF transverse modes require placement of the forcing unit in close vicinity to the burner faceplate. Attenuation of e.g. the first transverse acoustic mode in up- and downstream direction due to the combustor geometry and temperature conditions would render forcing at other combustor positions mostly ineffective (assuming that convectively driven flame response mechanisms are negligible). Figure B.1 shows a sketch of the reheat combustor with applied forcing units positioned at the chamber walls.

A forcing unit consists of a mid to high frequency compression driver (e.g. Monacor KU-516), an air purge, and an impedance tube. The air purge prevents the driver membrane from overheating by hot gas entrainment, while the purge flow is set low enough to not impact combustion. An impedance tube of variable length connects the driver with the combustor. The impedance tube length is adjusted to $\Delta L$ to match a resonance

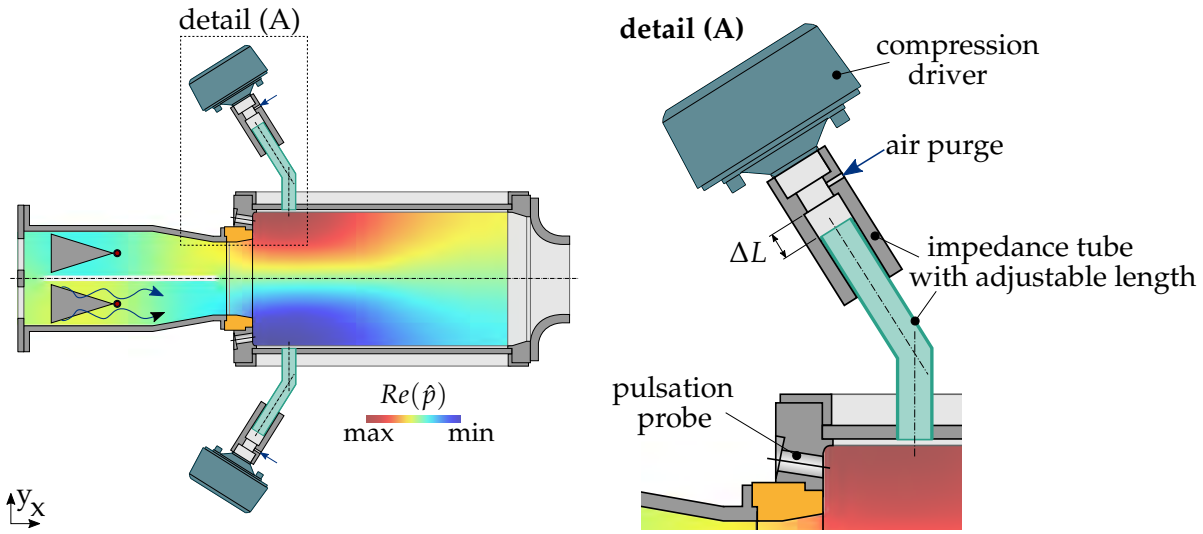


**Figure B.1:** Sketch of the reheat combustor with external forcing applied to the upper and lower combustor liner with detailed view of the forcing unit.

frequency of the forcing unit with the targeted acoustic mode frequency of the combustor. The harmonic forcing signal for each driver is a phase-sensitive mono-frequent sine wave, whose frequency is set equal to the naturally occurring frequency of the targeted mode at the specific operation conditions. Phase-sensitive in this context means that the phase of the individual forcing signal is aligned with the spatial distribution of the mode if more than one forcing unit is applied. It is challenging for the practical application of the forcing units that the natural frequency of the targeted transverse mode depends on the local temperature in close vicinity of the flame - i.e. some local temperature in between incoming hot-gas flow and actual flame temperature. Hence, slight deviations of the combustor inlet conditions already result in a significant change of the resonance frequency. The A$^2$EV swirl combustor reveals an almost constant first transverse mode frequency for a fixed operation condition. However, for the reheat combustor, the sequential setup and the necessity to control the auto-igniting flame position in the combustion chamber via the inlet temperature leads to significant variations of the resonance frequency during operation. This is why an online frequency tracking method was established to effectively force acoustic pulsations in the reheat combustor. This frequency tracking methods is applied during combustor operation by (i) recording short sequences of the acoustic pressure signals at

the combustor face-plate (cf. detail in Fig. B.1) followed by (ii) an extraction of the actual resonant frequency, (iii) which is then directly fed back to the acoustic driver(s). Obtaining the resonant frequency is realized by fitting a Lorenz curve to the measured frequency spectrum for a sufficiently small time window or by evaluation of the mean frequency from the band-pass filtered analytical signal representation utilizing the Hilbert transform. Both methods yield sufficient accuracy during combustor operation.

Results from non-forced (a) and forced (b) reheat combustor operation are provided in Figure B.2 for a vitiator air-fuel ratio $\lambda_{VIT} = 2.27$, translating into a reheat inlet temperature of $T_{RC,in} = 1536\,\mathrm{K}$. The thermal power of the second-stage reheat combustor is $Q_{th} = 640\,\mathrm{kW}$ and propane content in the fuel is $x_{C_3H_8} = 15\,\%$ per mass. Without external forcing the spectrum exhibits a distinct peak at the $T_{1y}$ eigenfrequency, but low pulsation amplitudes. To obtain the results shown in Figure B.2 (b), four external forcing units are applied, two at the upper and two at the lower

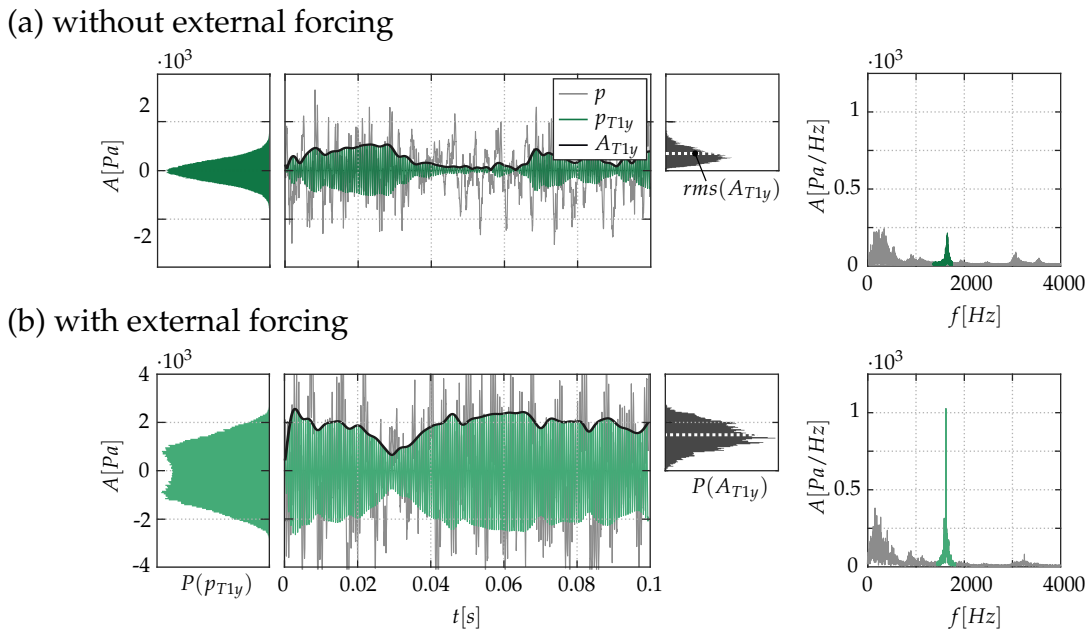


**Figure B.2:** Comparison of the non-forced (a) and forced (b) combustor response. From left to right: Probability density distribution of the analytical pressure signal $P(p'_{T1y})$, raw $p'$ and analytical $p_{T1y}$ time series of the acoustic pressure with envelope $A_{T1y}$, density distribution of the envelope $P(A_{T1y})$ with indicated root-mean-square of $A(p'_{T1y})$, and frequency spectra of $p'$.

liner position as shown in Figure B.1. The forcing signal has a phase shift of 180° between the upper and lower pair of drivers to account for the acoustic field of the $T_{1y}$ mode. The acoustic pressure data of the forced case shows that the $T_{1y}$ frequency reveals significantly higher pulsation amplitudes, both, in the time series and in the frequency spectrum. Furthermore, the pressure time series PDF show typical characteristics of a marginal instability (cf. Ch. 4). However, pulsation amplitudes with external forcing applied are always lower than observed limit-cycle oscillation amplitudes in these combustors. Hence, for an investigation of flame saturation mechanisms, further improvements of the methodology would be necessary. Apart from this, with the forcing unit, thermoacoustic feedback mechanism studies in the swirl and reheat combustors can be extended in future work to e.g. assessing flame response mechanisms also at higher transverse modes, which do not appear to be naturally unstable.

# Previous Publications

Wesentliche Teile dieser Dissertation wurden von dem Autor bereits standardmäßig vorab als Konferenz- und Journalbeiträge veröffentlicht [42, 44, 63, 80, 96, 98, 105, 107, 114, 115, 120, 128]. Alle Vorveröffentlichungen sind entsprechend der gültigen Promotionsordnung ordnungsgemäß gemeldet. Sie sind deshalb nicht zwangsläufig im Detail einzeln referenziert. Vielmehr wurde bei der Referenzierung eigener Veröffentlichungen Wert auf Verständlichkeit und inhaltlichen Bezug gelegt.

Significant parts of this thesis were already published by the author in conference proceedings and journal papers [42, 44, 63, 80, 96, 98, 105, 107, 114, 115, 120, 128]. All these publications are registered according to the valid doctoral regulations. However, not all of them are quoted explicitly everywhere. Whether these personal prior printed publications were referenced depends on maintaining comprehensibility in providing all necessary context.

# Supervised Student Theses

Im Rahmen dieser Dissertation entstanden am Lehrstuhl für Thermodynamik, Technische Universität München in den Jahren 2014 bis 2018 unter wesentlicher wissenschaftlicher, fachlicher und inhaltlicher Anleitung des Autors die im Folgenden aufgeführten studentischen Arbeiten. Ergebnisse aus diesen Arbeiten können in Teilen in das vorliegende Dokument eingeflossen sein. Der Autor dankt hiermit explizit allen ehemals betreuten Studenten für ihr Engagement bei der Unterstützung des hier behandelten Forschungsprojekts.

Associated with this Ph.D. thesis, a number of student theses were supervised by the author of the present work. These theses were prepared at the Lehrstuhl für Thermodynamik, Technische Universität München in the years 2014 to 2018 under the close supervision of the present author. Parts of these supervised theses may be incorporated into the present thesis. The author would like to express his sincere gratitude to all formerly supervised students for their commitment and support of this research project.

| Student | Titel/Thesis |
|---|---|
| Egon Ye | Auslegung und Simulation eines statischen Mischers für eine vorgemischte Verbrennung in einer Gasturbinenbrennkammer, Bachelor's Thesis, October 2014 |
| Ruben Gleiter | Numerische Untersuchung der Mischstrecke eines SEV-Experiments zur Optimierung des Strömungs- und Mischungsfelds in der Brennkammer, Bachelor's Thesis, October 2015 |
| Alexander Kröper | Konzeption, Auslegung und numerische Simulation einer Temperaturstufung für einen Prüfstand mit sequentieller Verbrennung, Bachelor's Thesis, November, 2015 |
| Frederik Schillert | Charakterisierung eines zweistufigen Verbrennungsprüfstands mittels Reaktornetzwerke, Semester Thesis, September 2015 |
| Martin Eser | Thermomechanical Design of a Second Stage Model Combustor with Analytical and Numerical Methods, Bachelor's Thesis, May 2016 |
| Jan Kaufmann | Untersuchung von hochfrequenten transversalen thermoakustischen Instabilitäten in Gasturbinenbrennern mit mager-vorgemischter, drallstabilisierter Verbrennung, Master's Thesis, April 2017 |
| Andreas Ewald | Inbetriebnahme eines sequentiellen Verbrennungsprüfstands zur experimentellen Analyse der Verbrennungsdynamik, Master's Thesis, July 2017 |
| Michael Bertsch | Experimental Investigation of the Flame Dynamics of High-Frequency Thermoacoustic Oscillations in an Atmospheric Reheat Combustor, Master's Thesis, August 2018 |
| Matthias Lang | Experimentelle Charakterisierung eines Aktuators zur Anregung transversaler thermoakustischer Verbrennungsinstabilitäten, Bachelor's Thesis, August 2018 |

# Bibliography


[1] UN General Assembly, 2015. "Transforming our World: The 2030 Agenda for Sustainable Development". *A/RES/70/1 available from undocs.org/A/RES/70/1*.

[2] Umweltbundesamt UBA, 2017. "Data on the Environment 2017: Indicator Report". *available from https://www.umweltbundesamt.de/publikationen/data-on-the-environment-2017*.

[3] International Energy Agency IEA/OECD, 2018. "Perspectives for the energy transition". *available from www.iea.org/publications/freepublications/publication/*.

[4] International Energy Agency IEA/OECD, 2018. "Electricity information 2018: Overview". *available from webstore.iea.org/electricity-information-2018-overview*.

[5] Feldhaus, P., Fürstenwerth, D., Gohl, M., Schröter, B., and Vahlenkamp, T., 2010. "Transformation of Europe's Power System until 2050, Inclusding Specific Considerations for Germany". *https://www.mckinsey.com [accessed 10.04.2019]*.

[6] Teske, S., Sawyer, S., Schaefer, O., Pregger, T., Simon, S., and Naegler, T., 2015. "Energy (R)Evolution - A Sustainable World Energy Outlook 2015". *Report 5th Edition - World Energy Scenario*.

[7] Gonzalez-Salazar, M. A., Kirsten, T., and Prchlik, L., 2018. "Reveiew of the Operational Flexibility and Emissions of Gas- and Coal-Fired Power Plants in a Future with Growing Renewables". *Renewable and Sustainable Energy Reviews,* **82**, pp. 1497–1513.

[8] American Physical Society Panel on Public Affairs, 2011. "Integrating Renewable Electricity on the Grid". *APS Physics*.

[9] Güthe, F., Hellat, J., and Flohr, P., 2007. "The Reheat Concept: The Proven Pathway to Ultra-Low Emissions and High Efficiency and Flexibility". In Proceedings of the ASME Turbo Expo, no. GT2007-27846.

[10] Karim, H., Natarajan, J., Narra, V., Cai, J., Rao, S., Kegley, J., and Citeno, J., 2017. "Staged Combustion System for Improved Emissions Operability and Flexibility for 7HA Class Heavy Duty Gas Turbine Engine". In Proceedings of the ASME Turbo Expo, no. GT2017-63998.

[11] Pennell, D., Bothien, M., Ciani, A., Grante, V., Singla, G., Thorpe, S., Wickstroem, A., Oumejjoud, K., and Yauinto, M., 2017. "An Introduction to the Ansaldo GT36 Constant Pressure Sequential Combustor". In Proceedings of the ASME Turbo Expo, no. GT2017-64790.

[12] Lefebvre, A. H., and Ballal, D. R., 1998. *GAS Turbine Combustion: Alternative Fuels and Emissions, Third Edition*. CRC Press.

[13] Eroglu, A., Flohr, P., Brunner, P., and Hellat, J., 2009. "Combustor Design for Low Emissions and Long Lifetime Requirements". In Proceedings of the ASME Turbo Expo, no. GT2009-59540.

[14] Steinbach, C., Ruck, T., Lloyd, J., Jansohn, P., Döbbling, K., Sattelmayer, T., and Strand, T., 1998. "ABB's Advanced EV Burner - A Dual Fuel Dry Low NOx Burner for Stationary Gas Turbines". In Proceedings of the ASME Turbo Expo, no. 98-GT-519.

[15] Düsing, K. M., Ciani, A., Benz, U., Eroglu, A., and Knapp, K., 2013. "Development of GT24 and GT26 (Upgrades 2011) Reheat Combustor, Achieving Reduced Emissions and Increased Fuel Flexibility". In Proceedings of the ASME Turbo Expo, no. GT2013-95437.

[16] Joos, F., Brunner, P., Schulte-Werning, B., Syed, K., and Eroglu, A., 1996. "Development of the Sequential Combustion System for the ABB GT24/GT26 Gas Turbine Family". In Proceedings of the ASME

Turbo Expo, no. 96-GT-315.

[17] Joos, F., Brunner, P., Stalder, M., and Tschirren, S., 1998. "Field Experience of the Sequential Combustion System for the GT24/GT26 Gas Turbine Family". In Proceedings of the ASME Turbo Expo, no. 98-GT-220.

[18] Düsing, K. M., Ciani, A., and Eroglu, A., 2011. "Effect of Mixing Quality on NOx Emissions in Reheat Combustion of GT24 & GT26 Engines". In Proceedings of the ASME Turbo Expo, no. GT2011-45676.

[19] Winkler, D., Geng, W., Engelbrecht, G., Stuber, P., Knapp, K., and Griffin, T., 2017. "Staged Combustion Concept for Increased Operational Flexibility of Gas Turbines". In Proceedings of the 1st Global Power and Propulsion Forum GPPF 2017, no. GPPF-2017-64.

[20] Lieuwen, T. C., 2012. *Unsteady Combustor Physics*. Cambridge University Press.

[21] Culick, F., 2006. "Unsteady Motions in Combustion Chambers for Propulsion Systems". *Number AC/323(AVT-039)TP/103 in RTO AGARDograph AG-AVT-039*.

[22] Schuermans, B., Bothien, M., Maurer, M., and Bunkute, B., 2015. "Combined Acoustic Damping-Cooling System for Operational Flexibility of GT24/26 Reheat Combustors". In Proceedings of the ASME Turbo Expo, no. GT2015-42287.

[23] Bothien, M. R., Noiray, N., and Schuermans, B., 2012. "A Novel Damping Device for Broadband Attenuation of Low-Frequency Combustion Pulsations in Gas Turbines". In Proceedings of the ASME Turbo Expo, no. GT2012-68873.

[24] Ciani, A., Eroglu, A., Güthe, F., and Paikert, B., 2010. "Full-Scale Atmospheric Test of Sequential Combustion". In Proceedings of the ASME Turbo Expo, no. GT2010-22891.

[25] Sattelmayer, T., Felchin, M. P., Haumann, J., Hellat, J., and Styner, D., 1992. "Second-Generation Low-Emission Combustors for ABB Gas Turbines: Burner Development and Tests at Atmospheric Pressure".

*Journal of Engineering for Gas Turbines and Power,* ***114***(1), pp. 118–125.

[26] Stuttaford, P., Rizkalla, H., Oumejjoud, K., Demougeot, N., Bosnoian, J., Hernandez, F., Yaquinto, M., Mohammed, A. P., Terrell, D., and Weller, R., 2016. "FlameSheet$^{TM}$ Combustor Engine and Rig Validation for Operational and Fuel Flexibility With Low Emissions". In Proceedings of the ASME Turbo Expo, no. GT2016-56696.

[27] Rizkalla, H., Hernandez, F., KeshavaBhattu, R., and Stuttaford, P., 2018. "FlameSheet$^{TM}$ Combustor Extended Engine Validation for Operational Flexibility and Low Emissions". In Proceedings of the ASME Turbo Expo, no. GT2018-75764.

[28] Turns, S. R., 2012. *An Introduction to Combustion: Concepts and Applications*. McGraw-Hill.

[29] Poyyapakkam, M., Wood, J., Mayers, S., Ciani, A., Güthe, F., and Syed, K., 2012. "Hydrogen Combustion Within a Gas Turbine Reheat Combustor". In Proceedings of the ASME Turbo Expo, no. GT2012-69165.

[30] Kulkarni, R., Bunkute, B., Biagioli, F., Duesing, K. M., and Polifke, W., 2014. "Large Eddy Simulation of ALSTOM´s Reheat Combustor using Tabulated Chemistry and Stochstic-Fields Combustion Model". In Proceedings of the ASME Turbo Expo, no. GT2014-26053.

[31] Schulz, O., and Noiray, N., 2017. "Combustion Regimes in Sequential Combustors". In Proceedings of the 1st Global Power and Propulsion Forum GPPF 2017, no. GPPF-2017-83.

[32] Healy, D., Curran, H., Dooley, S., Simmie, J., Kalitan, D., Petersen, E., and Bourque, G., 2008. "Methane/Propane Mixture Oxidation at High Pressures and at High, Intermediate and Low Temperatures". *Combustion and Flame,* ***155***(3), pp. 451–461.

[33] Noiray, N., 2019. "Thermoacoustic Coupling in a Combustion Chamber". *http://www.caps.ethz.ch/research/thermoacoustics.html accessed on 01.04.2019*.

[34] Bauerheim, M., Nicoud, N., and Poinsot, T., 2016. "Progress in Analytical Methods to Predict and Control Azimuthal Combustion Instability Modes in Annular Combustors". *Physics of Fluids,* ***28***, pp. 021303–1–27.

[35] Noiray, N., and Schuermans, B., 2013. "On the Dynamic Nature of Azimuthal Thermoacoustic Modes in Annular Gas Turbine Combustion Chambers". *Proceedings of the Royal Society A: Mathematical, Physical and Engineering Sciences,* ***469***(2151), pp. 20120535–15.

[36] Lieuwen, T. C., and Yang, V., 2006. *Combustion Instabilities in Gas Turbine Engines: Operational Experience, Fundamental Mechanisms, and Modeling*. Progress in Astronautics and Aeronautics. American Institute of Aeronautics and Astronautics American Institute of Aeronautics and Astronautics.

[37] Schuermans, B., 2003. "Modelling and Control of Thermoacoustic Instabilities". PhD Thesis, Ècole Polytechnique Fédérale de Lausanne.

[38] Hummel, T., 2019. "Modeling and Analysis of High-Frequency Thermoacosutic Oscillations in Gas Turbine Combustion Chambers". PhD Thesis, Technische Universität München.

[39] O'Connor, J., Acharya, V., and Lieuwen, T., 2015. "Transverse Combustion Instabilities: Acoustic, Fluid Mechanic, and Flame Processes". *Progress in Energy and Combustion Science,* ***49***, pp. 1–39.

[40] Rayleigh, 1878. "The Explanation of Certain Acoustical Phenomena 1". *Nature,* ***18***(455), pp. 319–321.

[41] Polifke, W., 2004. "Combustion Instabilities". *VKI Lecture Series*.

[42] Romero, P., Hummel, T., Berger, F. M., Schuermans, B., and Sattelmayer, T., 2017. "Damping due to the Acoustic Boundary Layer in High-Frequency Transverse Modes". In Proceedings of the 24th International Congress of Sound and Vibration.

[43] Hofmeister, T., Hummel, T., Schuermans, B., and Sattelmayer, T., 2019. "Modeling and Quantification of Acoustic Damping Induced by Vortex Shedding in Non-Compact Thermacoustic Systems". In

Proceedings of the ASME Turbo Expo, no. GT2019-90241.

[44] Hummel, T., Berger, F. M., Hertweck, M., Schuermans, B., and Sattelmayer, T., 2017. "High-Frequency Thermoacoustic Modulation Mechanisms in Swirl-Stabilized Gas Turbine Combustors - Part II: Modeling and Analysis". *Journal of Engineering for Gas Turbines and Power,* ***139***(7), pp. 071502–10.

[45] Hummel, T., Hofmeister, T., Schuermans, B., and Sattelmayer, T., 2017. "Modeling and Quantification of Acoustic Damping Induced by Vortex Shedding in Non-Compact Thermoacoustic Stystems". In Proceedings of the 24th International Congress on Sound and Vibration.

[46] Dowling, A. P., 1997. "Nonlinear Self-Excited Oscillations of a Ducted Flame". *Journal of Fluid Mechanics,* ***346***, pp. 271–290.

[47] Noiray, N., 2016. "Linear Growth Rate Estimation From Dynamics and Statistics of Acoustic Signal Envelope in Turbulent Combustors". *Journal of Engineering for Gas Turbines and Power,* ***139***(4), pp. 041503–11.

[48] Noiray, N., and Denisov, A., 2017. "A Method to Identify Thermoacoustic Growh Rates in Combustion Chambers from Dynamic Pressure Time Series". *Proceedings of the Combustion Institute,* ***36***(3), pp. 3843–3850.

[49] Bellows, B. D., Bobba, M. K., Forte, A., Seitzman, J. M., and Lieuwen, T., 2007. "Flame Transfer Function Saturation Mechanisms in a Swirl-Stabilized Combustor". *Proceedings of the Combustion Institute,* ***31***(2), pp. 3181–3188.

[50] Bellows, B. D., Bobba, M. K., Seitzman, J. M., and Lieuwen, T., 2007. "Nonlinear Flame Transfer Function Characteristics in a Swirl-Stabilized Combustor". *Journal of Engineering for Gas Turbines and Power,* ***129***(4), pp. 954–961.

[51] Schimek, S., Cosic, B., Moeck, J., Terhaar, S., and Paschereit, C., 2015. "Amplitude-Dependent Flow Field and Flame Response to Axial and Tangential Velocity Fluctuations". *Journal of Engineering for Gas*

*Turbines and Power,* ***137***(8), pp. 081501–10.

[52] Wassmer, D., Schuermans, B., Paschereit, C. O., and Moeck, J. P., 2016. "An Acoustic Time-of-Flight Approach for Unsteady Temperature Measurements: Characterization of Entropy Waves in a Model Gas Turbine Combustor". *Journal of Engineering for Gas Turbines and Power,* ***139***(4), pp. 041501–8.

[53] Hauser, M., Lorenz, M., and Sattelmayer, T., 2011. "Influence of Transversal Acoustic Excitation of the Burner Approach Flow on the Flame Structure". *Journal of Engineering for Gas Turbines and Power,* ***133***(4), pp. 041501–8.

[54] Hauser, M., Wagner, M., and Sattelmayer, T., 2012. "Transformation of Transverse Acoustic Velocity of the Burner Approach Flow Into Flame Dynamics". In Proceedings of the ASME Turbo Expo, no. GT2012-69051.

[55] O'Connor, J., and Lieuwen, T., 2011. "Further Characterization of the Disturbance Field in a Transversely Excited Swirl-Stabilized Flame". In Proceedings of the ASME Turbo Expo, no. GT2011-45221.

[56] Saurabh, A., and Paschereit, C. O., 2013. "Combustion Instability in a Swirl Flow Combustor With Transverse Extensions". In Proceedings of the ASME Turbo Expo, no. GT2013-95732.

[57] Schwing, J., Noiray, N., and Sattelmayer, T., 2011. "Interaction of Vortex Shedding and Transverse High-Frequency Pressure Oscillations in a Tubular Combustion Chamber". In Proceedings of the ASME Turbo Expo, no. GT2011-45246.

[58] Schwing, J., Grimm, F., and Sattelmayer, T., 2012. "A Model for the Thermo-Acoustic Feedback of Transverse Acoustic Modes and Periodic Oscillations in Flame Position in Cylindrical Flame Tubes". In Proceedings of the ASME Turbo Expo, no. GT2012-68775.

[59] Schwing, J., 2013. "Über die Interaktion von transversalen akustischen Moden, Strömung und drallstabilisierter Flamme in zylindrischen Flammrohren". PhD Thesis, Technische Universität München.

[60] Schwing, J., and Sattelmayer, T., 2013. "High-Frequency Instabilities in Cylindrical Flame Tubes: Feedback Mechanism and Damping". In Proceedings of the ASME Turbo Expo, no. GT2013-94064.

[61] Klarmann, N., Sattelmayer, T., Geng, W., and Magni, F., 2016. "Impact of Flame Stretch and Heat Loss on Heat Release Distributions in Gas Turbine Combustors: Model Comparison and Validation". In Proceedings of the ASME Turbo Expo, no. GT2016-57625.

[62] Hertweck, M., 2016. "Einfluss der Flammenposition auf transversale hochfrequente akustische Moden in zylindrischen Brennkammern". PhD Thesis, Technische Universität München.

[63] Hertweck, M., Berger, F. M., Hummel, T., and Sattelmayer, T., 2017. "Impact of the Heat Release Distribution on High-Frequency Transverse Thermoacoustic Driving in Premixed Swirl Flames". *International Journal of Spray and Combustion Dynamics,* ***9***(3), pp. 143–154.

[64] Buschhagen, T., Gejji, R., Philo, J., Tran, L., Bilbao, J. E. P., and Slabaugh, C. D., 2019. "Self-Excited Transverse Combustion Instabilities in a High Pressure Lean Premixed Jet Flame". *Proceedings of the Combustion Institute,* ***37***(4), pp. 5181–5188.

[65] Buschhagen, T., Gejji, R., Philo, J., Tran, L., Bilbao, J. E. P., and Slabaugh, C. D., 2018. "Experimental Investigation of Self-Excited Combustion Instabilities in a Lean, Premixed, Gas Turbine Combustor at High Pressure". *Journal of Engineering for Gas Turbines and Power,* ***140***(11), pp. 111503–9.

[66] Zellhuber, M., Meraner, C., Kulkarni, R., Polifke, W., and Schuermans, B., 2013. "Large Eddy Simulation of Flame Response to Transverse Acoustic Excitation in a Model Reheat Combustor". *Journal of Engineering for Gas Turbines and Power,* ***135***(9), pp. 091508–9.

[67] Zellhuber, M., 2013. "High Frequency Response of Auto-Ignition and Heat Release to Acoustic Perturbations". PhD Thesis, Technische Universität München.

[68] Zellhuber, M., Schuermans, B., and Polifke, W., 2014. "Impact of Acoustic Pressure on Autoignition and Heat Release". *Combustion*

*Theory and Modelling,* ***18***(1), pp. 1–31.

[69] Zellhuber, M., Schwing, J., Schuermans, B., Sattelmayer, T., and Polifke, W., 2014. "Experimental and Numerical Investigation of Thermoacoustic Sources Related to High-Frequency Instabilities". *International Journal of Spray and Combustion Dynamics,* ***6***(1), pp. 1–34.

[70] Scarpato, A., Zander, L., Kulkarni, R., and Schuermans, B., 2016. "Identification of Multi-Parameter Flame Transfer Function for a Reheat Combustor". In Proceedings of the ASME Turbo Expo, no. GT2016-57699.

[71] Bothien, M., Lauper, D., Yang, Y., and Scarpato, A., 2017. "Reconstruction and Analysis of the Acoustic Transfer Matrix of a Reheat Flame From Large-Eddy Simulations". In Proceedings of the ASME Turbo Expo, no. GT2017-64188.

[72] Schulz, O., and Noiray, N., 2018. "Autoignition Flame Dynamics in Sequential Combustors". *Combustion and Flame,* ***192***, pp. 86–100.

[73] Ebi, D., Doll, U., Schulz, O., Xiong, Y., and Noiray, N., 2019. "Ignition of a Sequential Combustor: Evidence of Flame Propagation in the Autoignitable Mixture". *Proceedings of the Combustion Institute,* ***37***(4), pp. 5013–5020.

[74] Weilenmann, M., Xiong, Y., Bothien, M. R., and Noiray, N., 2018. "Background Oriented Schlieren of Fuel Jet Flapping under Thermoacoustic Oscillations in a Sequential Combustor". In Proceedings of the ASME Turbo Expo, no. GT2018-75517.

[75] Bonciolini, G., and Noiray, N., 2018. "Synchronization of Thermoacoustic Modes in Sequential Combustors". In Proceedings of the ASME Turbo Expo, no. GT2018-75531.

[76] Rogers, D. E., and Marble, F. E., 1956. "A Mechanism for High-Frequency Oscillation in Ramjet Combustors and Afterburners". *Journal of Jet Propulsion,* ***26***(6), pp. 456–462.

[77] Elias, I., 1959. "Acoustical Resonances Produced by Combustion of a Fuel-Air Mixture in a Rectangular Duct". *The Journal of the Acoustical Society of America,* ***31***(3), pp. 296–304.

[78] Ghani, A., Poinsot, T., Gicquel, L., and Staffelbach, G., 2015. "LES of Longitudinal and Transverse Self-Excited Combustion Instabilities in a Bluff-Body Stabilized Turbulent Premixed Flame". *Combustion and Flame,* ***162***(11), pp. 4075–4083.

[79] Schadow, K., and Gutmark, E., 1992. "Combustion Instability Related to Vortex Shedding in Dump Combustors and their Passive Control". *Progress in Energy and Combustion Science,* ***18***(2), pp. 117–132.

[80] Romero, P., Berger, F. M., Hummel, T., Schuermans, B., and Sattelmayer, T., 2018. "Numerical Design of a Novel Reheat Combustor Experiment for the Analysis of High-Frequency Flame Dynamics". In Proceedings of the ASME Turbo Expo, no. GT2018-77034.

[81] Döbbeling, K., Hellat, J., and Koch, H., 2005. "25 Years of BBC/ABB/ALSTOM Lean Premix Combustion Technologies". In Proceedings of the ASME Turbo Expo, no. GT2005-68269.

[82] Bothien, M. R., Pennell, D. A., Zajadatz, M., and Döbbeling, K., 2013. "On Key Features of the AEV Burner Engine Implementation for Operational Flexibility". In Proceedings of the ASME Turbo Expo, no. GT2013-95693.

[83] Zajadatz, M., Pennel, D., Bernero, S., Paikert, B., Zoli, R., and Döbbeling, K., 2012. "Development and Implementation of the AEV Burner for the ALSTOM GT13E2". In Proceedings of the ASME Turbo Expo, no. GT2012-68471.

[84] Mayer, C., Sangl, J., Sattelmayer, T., Lachaux, T., and Bernero, S., 2011. "Study on the Operational Window of a Swirl Stabilized Syngas Burner Under Atmospheric and High Pressure Conditions". *Journal of Engineering for Gas Turbines and Power,* ***134***(3), pp. 031506–11.

[85] Mayer, C., 2012. "Konzept zur vorgemischten Verbrennung wasserstoffhaltiger Brennstoffe in Gasturbinen". PhD Thesis, Technische Universität München.

[86] Sangl, J., Mayer, C., and Sattelmayer, T., 2011. "Dynamic Adaption of Aerodynamic Flame Stabilization of a Premix Swirl Burner to Fuel Reactivity Using Fuel Momentum". *Journal of Engineering for Gas Turbines and Power,* ***133***(7), pp. 071501–11.

[87] Sangl, J., 2011. "Erhöhung der Brennstoffflexibilität von Vormischbrennern durch Beeinflussung der Wirbeldynamik". PhD Thesis, Technische Universität München.

[88] Bade, S., Wagner, M., Hirsch, C., Sattelmayer, T., and Schuermans, B., 2013. "Design for Thermoacoustic Stability: Procedure and Data Base". In Proceedings of the ASME Turbo Expo, no. GT2013-94131.

[89] Seidel, V., 2014. "Numerische und experimentelle Untersuchung der Aerodynamik und Verbrennungsstabilität eines Vormischbrenners". PhD Thesis, Technische Universität München.

[90] Schulz, O., Doll, U., Ebi, D., Droujko, J., Bourquard, C., and Noiray, N., 2019. "Thermoacoustic Instability in a Sequential Combustor: Large Eddy Simulation and Experiments". *Proceedings of the Combustion Institute,* ***37***(4), pp. 5325–5332.

[91] Hardi, J. S., 2012. "Experimental Investigation of High Frequency Combustion Instability in Cryogenic Oxygen-Hydrogen Rocket Engines". PhD Thesis, The University of Adelaide, Australia.

[92] Bibik, O., Lubarsky, E., Shcherbik, D., Hadjipanayis, M., and Zinn, B., 2008. "Rotational Traveling of Tangential Wave in Multi-Injectors LRE Combustor Simulator". In Proceedings of the 44th AIAA Aerospace Sciences Meeting and Exhibit, no. AIAA 2008-1001.

[93] Pomeroy, B., and Anderson, W., 2016. "Transverse Instability Studies in a Subscale Chamber". *Jorunal of Propulsion and Power,* ***32***(4), pp. 939–947.

[94] Richecoeur, F., Scouflaire, P., Ducruix, S., and Candel, S., 2006. "High-Frequency Transverse Acoustic Coupling in a Multiple-Injector Cryogenic Combustor". *Journal of Propulsion and Power,* ***22***(4), pp. 790–799.

[95] Méry, Y., Hakim, L., Scouflaire, P., Vingert, L., Ducruix, S., and Candel, S., 2013. "Experimental Investigation of Cryogenic Flame Dynamics under Transverse Acoustic Modulations". *Comptes Rendus Mécanique,* ***341***(1-2), pp. 100–109.

[96] Berger, F. M., Hummel, T., Romero, P., Schuermans, B., and Sattelmayer, T., 2018. "A Novel Reheat Combustor Experiment for the Analysis of High-Frequency Flame Dynamics - Concept and Experimental Validation". In Proceedings of the ASME Turbo Expo, no. GT2018-77101.

[97] Aditya, K., Gruber, A., Xu, C., Lu, T., Krisman, A., Bothien, M. R., and Chen, J. H., 2019. "Direct Numerical Simulation of Flame Stabilization Assisted by Autoignition in a Reheat Gas Turbine Combustor". *Proceedings of the Combustion Institute,* ***37***(2), pp. 2635–2642.

[98] Hummel, T., Berger, F. M., Schuermans, B., and Sattelmayer, T., 2016. "Theory and Modelling of Non-Degenerate Transversal Thermoacoustic Limit Cycle Oscillations". In Proceedings of the Symposium: Thermoacoustic Instabilities in Gas Turbines and Rocket Engines- Industry Meets Academia, Munich, Germany, no. GTRE-038.

[99] Hummel, T., Hammer, K., Romero, P., Schuermans, B., and Sattelmayer, T., 2017. "Low-Order Modeling of Nonlinear High-Frequency Transversal Thermoacoustic Oscillations in Gas Turbine Combustors". *Journal of Engineering for Gas Turbines and Power,* ***139***(7), pp. 071503–11.

[100] Bechert, D. W., 1980. "Sound Absorption caused by Vorticity Shedding, Demonstrated with a Jet Flow". *Journal of Sound and Vibration,* ***70***(3), pp. 389–405.

[101] Marble, F., and Candel, S., 1977. "Acoustic Disturbance from Gas Non-Uniformities Convected through a Nozzle". *Journal of Sound and Vibration,* ***55***(2), pp. 225–243.

[102] Freitag, E., Konle, H., Lauer, M., Hirsch, C., and Sattelmayer, T., 2006. "Pressure Influence on the Flame Transfer Function of a Premixed Swirling Flame". In Proceedings of the ASME Turbo Expo,

no. GT2006-90540.

[103] Kolb, M., 2016. "Influence of the Injector Geometry on Mixing and Lift-Off of Premixed Jet Flames in Hot Cross Flow". PhD Thesis, Technische Universität München.

[104] Freitag, E., 2008. "On the Measurement and Modelling of Flame Transfer Functions at Elevated Prssure". PhD Thesis, Technische Universität München.

[105] Schulze, M., Hummel, T., Klarmann, N., Berger, F. M., Schuermans, B., and Sattelmayer, T., 2016. "Linearized Euler Equations for the Prediction of Linear High-Frequency Stability in Gas Turbine Combustors. ". *Journal of Engineering for Gas Turbines and Power,* ***139***(3), pp. 031510–10.

[106] Eroglu, A., Döbbeling, K., Joos, F., and Brunner, P., 1999. "Vortex Generators in Lean-Premix Combustion". *Journal of Engineering for Gas Turbines and Power,* ***123***(1), pp. 41–49.

[107] Berger, F. M., Eser, M., and Sattelmayer, T., 2016. "Thermomechanical Design of a Gas Turbine Reheat Combustor Experiment Using Finite Element Analysis". In Proceedings of the 2016 COMSOL Conference, Munich.

[108] Sardeshmukh, S., Bedard, M., and Anderson, W., 2017. "The use of OH* and CH* as Heat Release Markers in Combustion Dynamics". *International Journal of Spray and Combustion Dynamics,* ***9***(4), pp. 409–423.

[109] Güthe, F., Guyot, D., Singla, G., Noiray, N., and Schuermans, B., 2012. "Chemiluminescence as Diagnostic Tool in the Development of Gas Turbines". *Applied Physics B,* ***107***(3), pp. 619–636.

[110] Lauer, M., and Sattelmayer, T., 2010. "On the Adequacy of Chemiluminescence as a Measure for Heat Release in Turbulent Flames with Mixture Gradients". *Journal of Engineering for Gas Turbines and Power,* ***132***(6), pp. 061502–8.

[111] Hardalupas, Y., and Orain, M., 2004. "Local Measurements of the Time-Dependent Heat Release Rate and Equivalence Ratio using

Chemiluminescent Emission from a Flame". *Combustion and Flame,* ***139***(3), pp. 188–207.

[112] Lauer, M., Zellhuber, M., Sattelmayer, T., and Aul, C., 2011. "Determination of the Heat Release Distribution in Turbulent Flames by a Model Based Correction of OH* Chemiluminescence". *Journal of Engineering for Gas Turbines and Power,* ***133***(12), pp. 121501–8.

[113] Guyot, D., Güthe, F., Schuermans, B., Lacarelle, A., and Paschereit, C. O., 2010. "CH*/OH* Chemiluminescence Response of an Atmospheric Premixed Flame Under Varying Operation Conditions". In Proceedings of the ASME Turbo Expo, no. GT2010-23135.

[114] Berger, F. M., Hummel, T., Hertweck, M., Kaufmann, J., Schuermans, B., and Sattelmayer, T., 2017. "High-Frequency Thermoacoustic Modulation Mechanisms in Swirl-Stabilized Gas Turbine Combustors - Part I: Experimental Investigation of the Local Flame Response". *Journal of Engineering for Gas Turbines and Power,* ***139***(7), pp. 071501–9.

[115] Berger, F. M., Hummel, T., Schuermans, B., and Sattelmayer, T., 2018. "Pulsation-Amplitude-Dependent Flame Dynamics of High-Frequency Thermoacoustic Oscillations in Lean-Premixed Gas Turbine Combustors". *Journal of Engineering for Gas Turbines and Power,* ***140***(4), pp. 041507–10.

[116] Hahn, S. L., 1996. *Hilbert Transforms in Signal Processing*. Artech House.

[117] Feldman, M., 2011. "Hilbert Transform in Vibration Analysis". *Mechanical Sysetms and Signal Processing,* ***25***(3), pp. 735–802.

[118] Güthe, F., and Schuermans, B., 2007. "Phase-Locking in Post-Processing for Pulsating Flames". *Measurement Science and Technology,* ***18***(9), pp. 3036–3042.

[119] Noiray, N., and Schuermans, B., 2013. "Deterministic Quanities Characterizing Noise Driven Hopf Bifurcations in Gas Turbine Combustors". *International Journal of Non-Linear Mechanics,* ***50***, pp. 152–163.

[120] Hummel, T., Berger, F. M., Stadlmair, N., Schuermans, B., and Sattelmayer, T., 2017. "Extraction of Linear Growth and Damping Rates of High-Frequency Thermoacoustic Oscillations from Time Domain Data". *Journal of Engineering for Gas Turbines and Power,* ***140***(5), pp. 051505–10.

[121] Kreiyszig, E., 2007. *Advanced Engineering Mathematics*. Wiley, Hoboken , USA.

[122] Bourgouin, J., Durox, D., Moeck, J., Schuller, T., and Candel, S., 2013. "Self-Sustained Instabilities in an Annular Combustor Coupled by Azimutal and Longitudinal Acoustic Modes". In Proceedings of the ASME Turbo Expo, no. GT2013-95010.

[123] Temme, J. E., Allison, P. M., and Driscoll, J. F., 2014. "Combustion Instability of a Lean Premixed Prevaporized Gas Turbine Combustor Studied using Phase-Averaged PIV". *Combustion and Flame,* ***161***(4), pp. 958–970.

[124] Stöhr, M., Sadanandan, R., and Meier, W., 2011. "Phase-Resolved Characterization of Vortex–Flame Interaction in a Turbulent Swirl Flame". *Experiments in Fluids,* ***51***(4), pp. 1153–1167.

[125] Gounder, J. D., Boxx, I., Kutne, P., Wysocki, S., and Biagioli, F., 2014. "Phase Resolved Analysis of Flame Structure in Lean Premixed Swirl Flames of a Fuel Staged Gas Turbine Model Combustor". *Combustion Science and Technology,* ***186***(4-5), pp. 421–434.

[126] Moeck, J., Bourgouin, J.-F., Durox, D., Schuller, T., and Candel, S., 2013. "Tomographic Reconstruction of Heat Release Rate Perturbations Induced by Helical Modes in Turbulent Swirl Flames". *Experiments in Fluids,* ***54***(4), pp. 1498–1515.

[127] Güthe, F., Lachner, R., Schuermans, B., Biagioli, F., Geng, W., Inauen, A., Schenker, S., Bombach, R., and Hubschmid, W., 2006. "Flame Imaging on the ALSTOM EV-Burner: Thermo Acoustic Pulsations and CFD-validation". In Proceedings of the 44th AIAA Aerospace Sciences Meeting and Exhibit, no. AIAA 2006-437.

[128] Berger, F. M., Kaufmann, J., Schuermans, B., and Sattelmayer, T., 2017. "Identification of Flame Displacement from High-Frequency Thermoacoustic Pulsations in Gas Turbine Combustors". In Proceedings of the 24th International Congress of Sound and Vibration.

[129] Fischer, A., Bake, F., Heinze, J., Diers, O., Willert, C., and Röhle, I., 2009. "Off-Line Phase-Averaged Particle Image Velocimetry and OH Chemiluminescence Measurements Using Acoustic Time Series". *Measurement Science and Technology,* ***20***(7), pp. 075403–10.

[130] Pfadler, S., Beyrau, F., and Leipertz, A., 2007. "Flame Front Detection and Characterization using Conditioned Particle Image Velocimetry (CPIV)". *Optics Express,* ***15***(23), pp. 15444–56.

[131] Westerweel, J., 1997. "Fundamentals of Digital Particle Image Velocimetry". *Measurement Science and Technology,* ***8***(12), pp. 1379–1392.

[132] Thielicke, W., and Stamhuis, E. J., 2014. "PIVlab - Towards User-Friendly, Affordable and Accurate Digital Particle Image Velocimetry in MATLAB". *Journal of Open Research Software,* ***2***(e30), pp. 1–10.

[133] Huang, H., Dabiri, D., and Gharib, M., 1997. "On Errors of Digital Particle Image Velocimetry". *Measurement Science and Technology,* ***8***(897), pp. 1427–1440.

[134] Lieuwen, T., 2005. "Online Combustor Stability Margin Assessment Using Dynamic Pressure Data". *Journal of Engineering for Gas Turbines and Power,* ***127***(3), pp. 478–482.

[135] Sewell, J., Sobieski, P., and Beers, C., 2004. "Application of Continuous Combustion Dynamics Monitoring in Large Industrial Gas Turbines". In Proceedings of the ASME Turbo Expo, no. GT2004-54310.

[136] Hummel, T., Temmler, C., Schuermans, B., and Sattelmayer, T., 2015. "Reduced-Order Modeling of Aeroacoustic Systems for Stability Analyses of Thermoacoustically Noncompact Gas Turbine Combustors". *Journal of Engineering for Gas Turbines and Power,* ***138***(5), pp. 051502–11.

[137] Schulz, O., Jaravel, T., Poinsot, T., Cuenot, B., and Noiray, N., 2017. "A Criterion to Distinguish Autoignition and Propagation Applied to a Lifted Methane–Air Jet Flame". *Proceedings of the Combustion Institute,* ***36***(2), pp. 1637–1644.

[138] Wassmer, D., Schuermans, B., Paschereit, C. O., and Moeck, J. P., 2017. "Measurement and Modeling of the Generation and the Transport of Entropy Waves in a Model Gas Turbine Combustor". *International Journal of Spray and Combustion Dynamics,* ***9***(4), pp. 299–309.

[139] Fleck, J. M., Griebel, P., Steinberg, A. M., Stöhr, M., and Aigner, M., 2010. "Experimental Investigation of a Generic, Fuel Flexible Reheat Combustor at Gas Turbine Relevant Operating Conditions". In Proceedings of the ASME Turbo Expo, no. GT2010-22722.

[140] Fleck, J., Griebel, P., Steinberg, A., Stöhr, M., Aigner, M., and Ciani, A., 2012. "Autoignition Limits of Hydrogen at Relevant Reheat Combustor Operating Conditions". *Journal of Engineering for Gas Turbines and Power,* ***134***(4), pp. 041502–8.

[141] Fleck, J. M., Griebel, P., Steinberg, A. M., Arndt, C. M., Naumann, C., and Aigner, M., 2013. "Autoignition of Hydrogen/Nitrogen Jets in Vitiated Air Crossflows at Different Pressures". *Proceedings of the Combustion Institute,* ***34***(2), pp. 3185–3192.

[142] Schulz, O., and Noiray, N., 2019. "Combustion Regimes in Sequential Combustors: FLame Propagation and Autoignition at Elevated Temperature and Pressure". *Combustion and Flame,* ***205***, pp. 253–268.

[143] Lubarsky, E., Hadjipanayis, M., Shcherbik, D., Bibik, O., and Zinn, B., 2008. "Control of Tangential Combustion Instability by Asymmetric Baffle". In Proceedings of the 46th AIAA Aerospace Sciences Meeting and Exhibit, no. AIAA 2008-955.

[144] Samarasinghe, J., Culler, W., Quay, B. D., Santavicca, D. A., and O'Connor, J., 2017. "The Effect of Fuel Staging on the Structure and Instability Characteristics of Swirl-Stabilized Flames in a Lean Premixed Multinozzle Can Combustor". *Journal of Engineering for Gas Turbines and Power,* ***139***(12), pp. 121504–10.